



UNIVERSITAT DE  
BARCELONA

## Timing the chemical evolution of the dense gas in high-mass star forming regions

Gemma Busquet Rico

**ADVERTIMENT.** La consulta d'aquesta tesi queda condicionada a l'acceptació de les següents condicions d'ús: La difusió d'aquesta tesi per mitjà del servei TDX ([www.tdx.cat](http://www.tdx.cat)) i a través del Dipòsit Digital de la UB ([diposit.ub.edu](http://diposit.ub.edu)) ha estat autoritzada pels titulars dels drets de propietat intel·lectual únicament per a usos privats emmarcats en activitats d'investigació i docència. No s'autoritza la seva reproducció amb finalitats de lucre ni la seva difusió i posada a disposició des d'un lloc aliè al servei TDX ni al Dipòsit Digital de la UB. No s'autoritza la presentació del seu contingut en una finestra o marc aliè a TDX o al Dipòsit Digital de la UB (framing). Aquesta reserva de drets afecta tant al resum de presentació de la tesi com als seus continguts. En la utilització o cita de parts de la tesi és obligat indicar el nom de la persona autora.

**ADVERTENCIA.** La consulta de esta tesis queda condicionada a la aceptación de las siguientes condiciones de uso: La difusión de esta tesis por medio del servicio TDR ([www.tdx.cat](http://www.tdx.cat)) y a través del Repositorio Digital de la UB ([diposit.ub.edu](http://diposit.ub.edu)) ha sido autorizada por los titulares de los derechos de propiedad intelectual únicamente para usos privados enmarcados en actividades de investigación y docencia. No se autoriza su reproducción con finalidades de lucro ni su difusión y puesta a disposición desde un sitio ajeno al servicio TDR o al Repositorio Digital de la UB. No se autoriza la presentación de su contenido en una ventana o marco ajeno a TDR o al Repositorio Digital de la UB (framing). Esta reserva de derechos afecta tanto al resumen de presentación de la tesis como a sus contenidos. En la utilización o cita de partes de la tesis es obligado indicar el nombre de la persona autora.

**WARNING.** On having consulted this thesis you're accepting the following use conditions: Spreading this thesis by the TDX ([www.tdx.cat](http://www.tdx.cat)) service and by the UB Digital Repository ([diposit.ub.edu](http://diposit.ub.edu)) has been authorized by the titular of the intellectual property rights only for private uses placed in investigation and teaching activities. Reproduction with lucrative aims is not authorized nor its spreading and availability from a site foreign to the TDX service or to the UB Digital Repository. Introducing its content in a window or frame foreign to the TDX service or to the UB Digital Repository is not authorized (framing). Those rights affect to the presentation summary of the thesis as well as to its contents. In the using or citation of parts of the thesis it's obliged to indicate the name of the author.

UNIVERSITAT DE BARCELONA

DEPARTAMENT D'ASTRONOMIA I METEOROLOGIA

**Timing the chemical evolution  
of the dense gas in high-mass  
star-forming regions**

Memòria presentada per  
**Gemma Busquet Rico**  
per optar al grau de  
Doctora en Ciències Físiques  
Barcelona, desembre 2010



PROGRAMA DE DOCTORAT D'ASTRONOMIA I METEOROLOGIA  
UNIVERSITAT DE BARCELONA

BIENNI 2005–2007

Memòria presentada per **Gemma Busquet Rico** per optar al grau  
de Doctora en Ciències Físiques

DIRECTORS DE LA TESI

Dr. Robert Estalella

Dr. Paul T. P. Ho



## Agraïments-Agradecimientos-Acknowledgments

To start with, I would like to express my gratitude to my advisors, Robert Estalella and Paul Ho. Thank you so much for the help, orientation and dedication received during these years. Gràcies Robert per haver-me introduït en el món de la radio astronomia i la formació estel·lar, així com per tot el teu suport científic. Thanks Paul for your availability and for always being here despite the huge distance between Barcelona and Taiwan/Boston.

Vull agrair molt sincerament tota l'ajuda rebuda per part de l'Aina en molts aspectes del contingut i desenvolupament d'aquest treball, que ha estat com una co-directora i fins i tot més. Moltes gràcies per ensenyar-me la bona manera de fer ciència!

I'm deeply grateful to Qizhou Zhang. Thanks for your guidance during the stays in the Center for Astrophysics (CfA). I really appreciate all the time you spent on me. I would say that you are my advisor too.

Vull expressar també el meu agraïment a tots els membres del grup de *Radio*. Agraeixo tota l'ajuda rebuda per part d'en Josep Miquel Girart, en Chema Torrelles, la Rosario López, la Maite Beltrán i l'Inma Sepúlveda. Per descomptat, vull donar les gràcies als estudiants i post-docs d'en Robert i en Josep Miquel: en Josep Maria, en Felipe, en Pau, en Marco, i molt molt especialment a l'Álvaro, que sempre ha estat disposat a ajudar-me i a discutir molts dels aspectes d'aquest treball.

From the CfA, I would like to specially thank Qizhou's and Paul's students: Keping, Yang, Roberto, Baobab, and Ke. I also appreciate the kindness of Nimesh Patel and the discussions with Thushara Pillai. Thank you also to Margaret Simonini, Jennifer Barnett, and Muriel Hodges, who helped me with all the paperwork.

From the University College London (UCL) I would like to thank Serena Viti for introduce me in a new field, the chemical models, and to Estelle, Magda, and Zainab, who kindly answered all my questions about the chemical model.

Vull agrair a tots els membres del Departament d'Astronomia i Meteorologia de la Universitat de Barcelona el suport rebut durant tots aquests anys. Gràcies a la gent de secretaria, en JR, la Montse, i la Rosa, per tota l'ajuda en els tràmits burocràtics, a la gent de suport, en Gaby i en Jordi, per ajudar-me en tots els problemes informàtics. També vull donar les gràcies a la Rosa, la Carme, en Pol, en

Javi Moldón, en Víctor, en Sinue, la Laura, la Maria, en Jordi, la Teresa, l'Albert, en Pere, en Javi Castañeda, l'Adolfo, l'Héctor...bé, a tots els DAMeros. Gràcies per totes les bones estones compartides dins i fora del departament!

Gracias también a Daniel Tafoya (mi compañero de despatxo del CfA), a Ramiro, Sergio Martín, Daniel Espada, y Javier Rodón. Javier, muchísimas gracias por toda tu ayuda y colaboración, por estar siempre disponible a compartir conocimientos y contrastar resultados.

També vull donar les gràcies a tot un grup de persones que sempre han estat al meu costat. A la meva família, especialment als meus pares, la meva germana, i a en Dídac. Moltes gràcies Dídac per haver-me recolzat durant tot aquests anys! i al grup d'amics: Buri, Jessica, Laia, Gerard, Cris, Ignasi, Juano, Pati, Cristian, Lu i Charlie, que durant els viatges al CfA i UCL sempre heu estat al meu costat. Merci a tots!!

Finalment, moltes gràcies a tots els que d'una manera o altra heu col·laborat en la realització d'aquesta tesi.

Moltíssimes gràcies a tothom!

Thank you so much to all of you!

*A en Dídac*

*...a vegades allargava la mà  
per atrapar les partícules de llum  
que flotaven a l'aire,  
però els meus dits no tocaven res*

*Norwegian Wood (Tokio Blues)  
Haruki Murakami*



# Contents

|  |           |
|--|-----------|
| <b>Resum de la tesi</b>  | <b>xi</b> |
| <b>1 Introduction</b>  | <b>1</b>  |
| 1.1 The birth sites of high-mass stars . . . . .   | 1         |
| 1.1.1 Fragmentation . . . . .  | 3         |
| 1.1.2 Stages of massive star formation . . . . .   | 4         |
| 1.2 The relevance of chemistry in high-mass star-forming regions . . . . .                       | 4         |
| 1.2.1 N-bearing chemistry . . . . .  | 7         |
| 1.2.2 Deuterated species . . . . .   | 9         |
| 1.2.3 Column density ratios as tracers of chemical evolution . . . . .                           | 10        |
| 1.3 The aim and structure of the thesis . . . . .  | 13        |
| 1.3.1 Goal of the thesis . . . . .   | 13        |
| 1.3.2 Strategy: why $\text{NH}_3$ and $\text{N}_2\text{H}^+$ at high angular resolution? . . .   | 13        |
| 1.3.3 Thesis organization and status of the different projects constituting the thesis . . . . . | 14        |
| <b>2 G14.2–0.60: an example of a large Infrared Dark Cloud at the onset of star formation</b>    | <b>17</b> |

---

|          |  |           |
|----------|--|-----------|
| 2.1      | Introduction . . . . .   | 17        |
| 2.2      | Observations . . . . .   | 18        |
| 2.2.1    | APEX observations . . . . .  | 18        |
| 2.2.2    | FCRAO observations . . . . .   | 19        |
| 2.2.3    | Effelsberg observations . . . . .  | 19        |
| 2.2.4    | VLA observations . . . . .   | 20        |
| 2.2.5    | SMA observations . . . . .   | 21        |
| 2.3      | Preliminary results and analysis . . . . .   | 22        |
| 2.3.1    | Dust emission . . . . .  | 22        |
| 2.3.2    | Dense gas emission . . . . .   | 36        |
| 2.3.3    | SMA dust emission . . . . .  | 50        |
| 2.3.4    | The mass spectrum of the clumps . . . . .  | 55        |
| 2.4      | Discussion . . . . .   | 57        |
| 2.4.1    | On the behavior of the $\text{NH}_3/\text{N}_2\text{H}^+$ ratio in IRDCs . . . . .                                     | 57        |
| 2.4.2    | Filamentary structures . . . . .   | 58        |
| 2.4.3    | High-mass star formation in IRDC G14.2–0.60 . . . . .  | 59        |
| 2.4.4    | Fragmentation and cluster formation . . . . .  | 61        |
| 2.5      | Conclusions . . . . .  | 63        |
| <b>3</b> | <b>The <math>\text{NH}_3/\text{N}_2\text{H}^+</math> abundance ratio in a sample of high-mass star-forming regions</b> | <b>67</b> |
| 3.1      | Introduction . . . . .   | 67        |
| 3.2      | Observations . . . . .   | 68        |

---

|          |   |            |
|----------|---|------------|
| 3.2.1    | Very Large Array observations . . . . .   | 68         |
| 3.2.2    | CARMA observations . . . . .  | 70         |
| 3.2.3    | BIMA observations . . . . .   | 71         |
| 3.2.4    | SMA observations . . . . .  | 72         |
| 3.3      | IRAS 00117+6412 . . . . .   | 72         |
| 3.3.1    | Description . . . . .   | 72         |
| 3.3.2    | Results . . . . .   | 73         |
| 3.4      | IRAS 22134+5834 . . . . .   | 76         |
| 3.4.1    | Description . . . . .   | 76         |
| 3.4.2    | Results . . . . .   | 77         |
| 3.5      | IRAS 20126+4104 . . . . .   | 80         |
| 3.5.1    | Description . . . . .   | 80         |
| 3.5.2    | Results . . . . .   | 81         |
| 3.6      | Analysis . . . . .  | 86         |
| 3.6.1    | Physical parameters of dense gas . . . . .  | 86         |
| 3.6.2    | NH <sub>3</sub> and N <sub>2</sub> H <sup>+</sup> fractional abundances . . . . .         | 98         |
| 3.7      | Brief discussion . . . . .  | 100        |
| 3.7.1    | General properties of the dense gas . . . . .   | 100        |
| <b>4</b> | <b>N<sub>2</sub>H<sup>+</sup> depletion in the massive protostellar cluster AFGL 5142</b> | <b>103</b> |
| 4.1      | Introduction . . . . .  | 104        |
| 4.2      | Observations . . . . .  | 106        |

---

|          |  |            |
|----------|--|------------|
| 4.3      | Results . . . . .  | 107        |
| 4.3.1    | Continuum emission . . . . .   | 107        |
| 4.3.2    | Molecular line emission: $\text{N}_2\text{H}^+$ . . . . .  | 109        |
| 4.4      | Analysis . . . . .   | 115        |
| 4.4.1    | Column density maps . . . . .  | 115        |
| 4.4.2    | The $\text{NH}_3/\text{N}_2\text{H}^+$ abundance ratio map . . . . .   | 119        |
| 4.5      | Chemical modeling . . . . .  | 122        |
| 4.5.1    | The UCL_CHEM model . . . . .   | 122        |
| 4.5.2    | Results . . . . .  | 123        |
| 4.6      | Discussion . . . . .   | 130        |
| 4.7      | Conclusions . . . . .  | 134        |
| <b>5</b> | <b>The <math>\text{NH}_2\text{D}/\text{NH}_3</math> ratio toward pre-protostellar cores around<br/>the UCHII region in IRAS 20293+3952</b> | <b>137</b> |
| 5.1      | Introduction . . . . .   | 138        |
| 5.2      | Observations . . . . .   | 139        |
| 5.3      | Results . . . . .  | 140        |
| 5.4      | Discussion and summary . . . . .   | 144        |
| <b>6</b> | <b>General discussion and conclusions</b>  | <b>147</b> |
| 6.1      | On the behavior of the $\text{NH}_3/\text{N}_2\text{H}^+$ ratio . . . . .  | 147        |
| 6.1.1    | $\text{NH}_3$ and $\text{N}_2\text{H}^+$ column densities . . . . .  | 148        |
| 6.1.2    | Column densities against temperature . . . . .   | 150        |

---

|       |  |            |
|-------|--|------------|
| 6.1.3 | The $\text{NH}_3/\text{N}_2\text{H}^+$ ratio . . . . . | 153        |
| 6.2   | Open questions . . . . .                               | 162        |
| 6.3   | Conclusions . . . . .                                  | 162        |
|       | <b>Bibliography</b>                                    | <b>165</b> |
|       | <b>A Appendix</b>                                      | <b>189</b> |



# Resum de la tesi:

## Datant l'evolució química del gas dens en regions de formació estel·lar d'alta massa

### Introducció

En la nostra galàxia, la Via Làctea, les estrelles es formen en els braços espirals i a prop del centre galàctic. Les estrelles neixen en condensacions de gas i pols, en els anomenats núvols moleculars. Tradicionalment els núvols moleculars s'han classificat en dues categories segons la seva massa: núvols moleculars gegants i núvols foscos. Els núvols foscos tenen masses  $\sim 10^3 M_{\odot}$ , tamanyes d'uns pocs parsecs i temperatures molt baixes ( $\sim 10 - 20$  K). Per altra banda, els núvols moleculars gegants tenen masses  $\sim 10^4 - 10^6 M_{\odot}$ , tamanyes d'unes desenes de parsecs i temperatures  $\sim 20$  K. Tot i aquesta es la classificació tradicional, recentment els satèl·lits *Infrared Space Telescope* (ISO) i *Midcourse Space Experiment* (MSX) han identificat una nova classe de núvols, els anomenats núvols foscos en l'infraroig. Aquests núvols són molt massius, densos i freds, normalment amb formes filamentàries, i representen el lloc on neixen les estrelles d'alta massa. Aleshores, segons la divisió tradicional entre núvols foscos i núvols moleculars gegants, aquesta nova població de núvols foscos en l'infraroig pot representar les parts més denses dels núvols moleculars gegants o bé les primeres etapes de l'evolució del núvol.

L'estructura dels núvols moleculars és inhomogènia i consisteix regions en de més alta densitat, els anomenats "clumps", que a la vegada es fragmenten en es-

estructures més petites i denses, anomenats nuclis denses. Aleshores, la fragmentació és un procés jeràrquic. Per explicar aquest procés de fragmentació s'han proposat diferents mecanismes: rotació, turbulència, i camps magnètics. Tanmateix, cap de les simulacions actuals és capaç de reproduir les dades observacionals i per tant actualment encara no està clar quin d'aquests mecanismes determina la fragmentació d'aquests núvols. Per tant, per tal d'estudiar el procés de fragmentació que dona lloc a la formació de cúmuls d'estrelles és necessari observar les primeres etapes evolutives dels núvols moleculars, és a dir, els núvols foscos en l'infraroig.

Les estrelles es formen doncs en les parts més denses dels núvols moleculars. Abans de la formació d'un objecte protoestel·lar, els nuclis pre-protoestel·lars estan caracteritzats per temperatures baixes i densitats altes. En aquestes condicions gran part de les molècules desapareixen de la fase gas en els centres d'aquests nuclis denses. En concret, les molècules amb carboni i oxigen es congelen sobre els grans de pols, mentre que les molècules que contenen nitrogen, com per exemple el  $\text{NH}_3$  i el  $\text{N}_2\text{H}^+$ , sobreviuen fins a densitats molt més elevades. Així doncs, tant la molècula de  $\text{NH}_3$  com la de  $\text{N}_2\text{H}^+$  juntament amb la pols són els millors traçadors del gas més dens. Una vegada neix la protoestrella, aquesta escalfa el material del seu voltant formant un "nucli molecular calent". Aquests nuclis presenten una química molt rica ja que els mantells de gel dels grans de pols s'evaporen i es creen molècules molt complexes. Tanmateix, per tal d'explicar les abundàncies d'aquestes espècies és necessari tenir en compte tan la química en fase gas com la química que té lloc en la superfície dels grans de pols. Un altre fenomen que té lloc durant les primeres etapes evolutives d'una protoestrella és la presència de fluxes moleculars molt energètics i col·limats que provoquen canvis químics importants en el seu entorn.

A partir de treballs observacionals, principalment realitzats en regions de formació estel·lar de baixa massa, s'han proposat diversos quocients de densitat columnar com a bons traçadors de l'evolució química dels nuclis denses, i per tant poden ser utilitzats com a un "rellotge químic". Entre tots aquests quocients, el més estudiat es el quocient  $\text{NH}_3/\text{N}_2\text{H}^+$  (Caselli et al. 2002a; Hotzel et al. 2004; Friesen et al. 2010; Miettinen et al. 2010). Tots aquests treballs mostren que el quocient  $\text{NH}_3/\text{N}_2\text{H}^+$  és baix en nuclis que contenen objectes protoestel·lars embeguts mentre que en nuclis sense formació estel·lar el quocient és alt. En el règim d'alta massa, Palau et al. (2007) també troba una tendència similar en els nuclis de massa intermitja que envolten la regió ultracompacte IRAS 20293+3952.

---

Altres quocients de densitats columnars són el de  $\text{SiO}/\text{C}^{34}\text{S}$ ,  $\text{CN}/\text{N}_2\text{H}^+$  (Fuente et al. 2005b), o bé el quocient  $\text{C}^{18}\text{O}/\text{N}_2\text{H}^+$  (Tafalla and Santiago 2004). Aquest darrer és especialment important per les primeres etapes evolutives dels nuclis densos ja que permet diferenciar nuclis pre-protoestel·lars molt joves on les molècules encara no s'han condensat sobre els grans de pols i per tant, aquest quocient seria inicialment alt i aniria disminuint a mesura que el nucli pre-protoestel·lar evoluciona de manera que la condensació de les molècules es fa més evident. Per altra banda, la fracció de deuteració també es considerat un bon traçador d'evolució. Inicialment la fracció de deuteració augmenta en l'etapa pre-protoestel·lar i decreix a partir de la formació de la protoestrella (Crapsi et al. 2005; Emprechtinger et al. 2009). Finalment, quocients entre molècules amb sofre són de gran utilitat durant l'etapa protoestel·lar amb presència de nuclis moleculars calents (Herpin et al. 2009).

## Objectius i estructura de la tesi

L'objectiu d'aquest treball és estudiar l'evolució de les propietats químiques del gas dens en les primeres etapes de formació estel·lar. Hem extès la comparació de les molècules de  $\text{NH}_3$  i  $\text{N}_2\text{H}^+$  a través del quocient  $\text{NH}_3/\text{N}_2\text{H}^+$  en nuclis densos associats amb regions de formació estel·lar d'alta massa començada per Palau et al. (2007). En aquest estudi es pretén veure si les diferències entre aquestes dues molècules són degudes a que els nuclis s'han format en diferents temps, i per tant relacionat amb l'evolució química del gas dens, o bé perquè les altes temperatures i les interaccions dels fluxes moleculars i/o la radiació ultraviolada afecten l'evolució del medi.

Les molècules de  $\text{NH}_3$  i el  $\text{N}_2\text{H}^+$  són dos traçadors de gas dens àmpliament utilitzades per diverses raons. En primer lloc, les dues molècules sobreviuen en fase gas fins a densitats  $\geq 10^6 \text{ cm}^{-3}$  (e. g., Flower et al. 2006). A més, tant la molècula de  $\text{NH}_3$  com la de  $\text{N}_2\text{H}^+$  presenten estructura hiperfina, permetent-nos obtenir així informació sobre l'opacitat del gas observant tan sols una única transició. L'ús de la molècula de  $\text{NH}_3$  ens permetrà obtenir una mesura de la temperatura dels gas degut a que les dues transicions d'inversió dels estats rotacionals més baixos es poden observar simultàneament ja que tenen freqüències molt similars. Ara bé, com ja hem vist anteriorment les estrelles de massa intermitja/alta es formen en mode cúmul i com que estem interessats en caracteritzar cada nucli dens de forma individual, típicament amb tamanys de l'ordre 0.03–0.2 pc, necessitem ser capaços de resoldre'ls

per a distàncies d'uns pocs kiloparsecs. Per tant, hem seleccionat una mostra de regions situades a distàncies  $< 3$  kpc de tal manera que per poder resoldre l'emissió dels diferents nuclis necessitem assolir resolucions angulars  $\sim 3'' - 5''$ , i això només es pot dur a terme mitjançant interferòmetres.

Aquesta tesi és el resultat de diferents treballs duts a terme principalment entre el 2006 i el 2010. Durant aquest període hem observat l'emissió de les molècules de  $\text{NH}_3$  i  $\text{N}_2\text{H}^+$  utilitzant interferòmetres en quatre regions de formació estel·lar d'alta massa, i mitjançant telescopis d'una única antena hem observat l'emissió de la pols i dels gas dens en tot un núvol fosc en l'infraroig. A més d'utilitzar el quocient  $\text{NH}_3/\text{N}_2\text{H}^+$  també hem utilitzat la fracció de deuteració com a bon traçador de l'evolució dels nuclis densos. L'estructura de la tesi és la següent:

En primer lloc, en el capítol 1 fem una introducció a la formació estel·lar i a la química d'aquestes regions. En el capítol 2 presentem els resultats pel núvol fosc en el infraroig G14.2–0.60. Amb l'objectiu d'estudiar les propietats físiques i químiques del núvol a gran escala hem observat la regió utilitzant primer telescopis d'una única antena per traçar l'emissió de la pols, del  $\text{N}_2\text{H}^+$ , i del  $\text{NH}_3$ . La molècula de  $\text{NH}_3$  també s'ha observat amb l'interferòmetre Very Large Array (VLA, New Mexico, US) per poder estudiar l'estructura del núvol a les escales dels nuclis densos. El següent pas ha estat observar una regió concreta del núvol utilitzant l'interferòmetre Submillimeter Array (SMA, Mauna Kea, Hawaii) per investigar els pocés de fragmentació i la formació dels cúmuls estel·lars.

A continuació, en els capítols 3 i 4, presentem els resultats per a 4 regions de formació estel·lar d'alta massa, observades en  $\text{NH}_3$  i  $\text{N}_2\text{H}^+$  amb els interferòmetres VLA, Combined Array for Research on Millimeter Astronomy (CARMA, Cedar Flat, California, US), i Berkley-Illinois-Maryland Array (BIMA, Hat Creek, California). A més de presentar els resultats observacionals en el capítol 4 hem aplicat el model químic UCL\_CHEM per tal de poder explicar les diferències observades del quocient  $\text{NH}_3/\text{N}_2\text{H}^+$ . En el capítol 5 presentem els resultats per la regió de formació estel·lar de massa intermitja/alta que s'ha observat en amoníac deuterat ( $\text{NH}_2\text{D}$ ) amb el Plateau de Bure Interferometer (PdBI, Alpes, France) per tal d'estudiar la fracció de deuteració així com la relació d'aquesta amb el quocient  $\text{NH}_3/\text{N}_2\text{H}^+$ . Finalment, en el capítol 6 fem una discussió global dels resultats obtinguts per les regions estudiades tenint en compte també regions de la literatura i donem les conclusions generals d'aquest treball.

## G14.2–0.60: un exemple d'un gran núvol fosc en l'infraroig a l'inici de la formació estel·lar

G14.2–0.60 és un núvol fosc en l'infraroig que està situat a una distància de 2.3 kpc. La majoria dels estudis en aquesta regió s'han centrat en la font IRAS més brillant, IRAS 18153-1651, que té una lluminositat de  $1.1 \times 10^4 L_{\odot}$  (Jaffe et al. 1981), i la font IRAS 18152-1658. Aquesta darrera, situada uns  $7'$  al sud té una lluminositat de  $3900 L_{\odot}$  i està associada amb emissió centimètrica (Jaffe et al. 1982). Observacions amb telescopis d'una única antena mostren que IRAS 18153-1651 presenta emissió de màser d'aigua (Comoretto et al. 1990; Jaffe et al. 1981; Palagi et al. 1993), i emissió de gas dens traçat per les molècules de CS i  $\text{NH}_3$  (Plume et al. 1992; Anglada et al. 1996; Bronfman et al. 1996). Un estudi més recent de màsers de  $\text{H}_2\text{O}$  amb el VLA (Wang et al. 2006) revela emissió màser en 9 posicions diferents del núvol, indicant que en certes parts dels núvol ja s'ha iniciat el procés de formació estel·lar.

Amb l'objectiu d'estudiar les propietats físiques i químiques de G14.2–0.60 vam observar primer tot el núvol utilitzant telescopis d'una única antena. L'emissió de la pols a  $870 \mu\text{m}$  s'ha observat amb el bolometre LABOCA, instal·lat en el telesopi Atacama Pathfinder EXperiment (APEX, Llano de Chajnantor, Chile). La molècula de  $\text{N}_2\text{H}^+$  s'ha observat amb el Five College Radio Astronomy Observatory (FCRAO) mentre que l'amoniac l'hem observat amb el telescopi de 100 m Effelsberg i amb alta resolució angular utilitzant el VLA. Finalment, vam seleccionar una petita regió del tot el núvol i vam observar la seva emissió a 1.2 mm amb l'interferòmetre SMA. Aquest conjunt d'observacions ens permetrà estudiar l'estructura i la cinemàtica de tot el núvol a escales  $\sim 0.02 - 0.05$  pc així com també els processos de fragmentació i la formació dels cúmuls d'estrelles.

L'emissió de la pols a  $870 \mu\text{m}$  mostra estructures filamentàries formades per diversos fragments compactes que resegueix molt bé l'absorció a  $8 \mu\text{m}$  (veure Fig. 2.1). El núvol s'extén uns  $21'$  ( $14$  pc a la distància de la regió). Hem identificat 74 nuclis amb masses entre 11 i  $1000 M_{\odot}$  i tamanys entre  $0.2-1.2$  pc. Per tal d'evaluar si aquests nuclis formaran o no estrelles d'alta massa hem utilitzat dues eines diferents. En primer lloc, hem aplicat el criteri de Krumholz and McKee (2008), el qual estableix una densitat superficial  $\Sigma$  mínima de  $0.7-1.5 \text{ g cm}^{-2}$  per formar una estrella de  $10-200 M_{\odot}$ , respectivament. Pels nuclis de G14.2–0.60 hem obtingut una densitat superficial  $\sim 0.01 - 0.5 \text{ g cm}^{-2}$ , molt per sota de valor teòric de  $0.7 \text{ g cm}^{-2}$ . Aquest

resultat implica que cap dels nuclis de G14.2–0.60 formarà una estrella d’alta massa (d’acord al criteri de Krumholz and McKee (2008)). Tanmateix, aquest nucli no són homogenis sinó que contenen nuclis més densos i petits que no podem resoldre amb APEX. De fet, les observacions d’un d’aquests nuclis amb el SMA mostren que aquest es fragmenta en vàries condensacions o fragments amb valors de la densitat superficial clarament per sobre del límit teòric. Per tant, per poder aplicar el criteri de Krumholz and McKee (2008) és necessari assolir resolucions espacials característiques dels nuclis densos. Per altra banda, hem utilitzat la relació empírica entre la massa i el radi proposada recentment per Kauffmann and Pillai (2010). A partir d’aquesta relació trobem que només 10 dels 74 nuclis poden formar estrelles d’alta massa, entre ells el nucli estudiat amb el SMA on es detecten fonts amb masses superiors a  $10 M_{\odot}$ .

El gas dens traçat per la molècula de  $\text{NH}_3$  mostra diversos nuclis compactes formant estructures extenses i filamentàries amb una morfologia semblant a la de la pols (veure Fig. 2.6). Aquests filaments contenen cadenes de nuclis densos, separats aproximadament la mateixa distància. Els filaments apareixen molt estructurats, en alguns casos fins i tot es veuen filaments paral·lels. L’emissió de  $\text{NH}_3$  està essencialment a la mateixa velocitat, i en general es veuen petites variacions de velocitat al llarg d’un filament, indicant que la seva presència és intrínseca de l’estructura del núvol i no el resultat de factors evolutius com per exemple a l’activitat estel·lar.

Hem obtingut el quocient  $\text{NH}_3/\text{N}_2\text{H}^+$  convolucionant l’emissió de  $\text{NH}_3$  a la mateixa resolució que la molècula de  $\text{N}_2\text{H}^+$ , observada amb una resolució angular de  $58''$ . Els valors que hem obtingut estan en el rang 425–693. En aquesta regió podem intuir una certa tendència entre els valors del quocient i l’estat evolutiu dels nuclis al llarg d’un dels filaments. Ara bé, els valors del quocient són molt més alts que els valors que es troben en altres treballs, ja que per G14.2–0.60 estem considerant escales molt més grans que en les regions de la literatura o les estudiades en els següents capítols, de manera que en G14.2–0.60 tenim la contribució de diversos nuclis densos. De fet, observacions amb alta resolució de la molècula de  $\text{N}_2\text{H}^+$  mostren que aquesta es detecta marginalment o no es detecta en alguns núvols foscos, essent G14.2–0.60 un d’ells. Aquest fet ens fa pensar que l’emissió de  $\text{N}_2\text{H}^+$  prové de regions molt més fredes, difuses i extenses que només es detecten amb baixa resolució i no amb interferòmetres, un resultat totalment oposat al que s’ha observat en regions de formació estel·lar on les molècules de  $\text{N}_2\text{H}^+$  i  $\text{NH}_3$  són detectades en les regions més denses dels nuclis. Per tant, caldria dur a terme més observacions interferomètriques

per tal d'esbrinar quin és el comportament del  $\text{N}_2\text{H}^+$  en aquests núvols foscos en l'infraroig.

Finalment, l'emissió de la pols a 1.2 mm observada amb l'interferòmetre SMA amb una resolució angular de  $1''.5$  ( $\sim 0.02$  pc) mostra 16 fonts amb masses entre 0.5 i  $16 M_\odot$ , i amb una separació de 0.05 pc. Gràcies a la sensibilitat i a la resolució assolida amb el SMA hem pogut contrastar els nostres resultats observacionals amb els models teòrics actuals. En el model d'acreció competitiva de Bonnell and Bate (2002) els núvols es fragmenten en nuclis amb masses de Jeans de  $\sim 0.5 M_\odot$ . Tot i que les nostres observacions ens permeten detectar condensacions de  $0.3 M_\odot$ , la majoria de les fonts tenen masses molt superiors a  $1 M_\odot$ . Per altra banda, l'escalfament produït per objectes joves embeguts pot fer augmentar la massa de Jeans mitjançant un augment de la temperatura (e. g., Krumholz 2006). Tanmateix, els valors de temperatura obtinguts a partir de la molècula de  $\text{NH}_3$  per aquestes fonts no pot explicar les masses observades. Així doncs, tant la turbulència com els camps magnètics semblen tenir un paper molt important en G14.2–0.60.

## El quocient $\text{NH}_3/\text{N}_2\text{H}^+$ en una mostra de regions de formació estel·lar d'alta massa

En aquest capítol mostrem els resultats del quocient  $\text{NH}_3/\text{N}_2\text{H}^+$  en una petita mostra de regions de formació estel·lar d'alta massa que ha estat seleccionada a partir de les mostres de Sridharan et al. (2002) i Molinari et al. (1996). Les regions són: IRAS 00117+6412, IRAS 20126+4104 i IRAS 22134+5834. Les tres regions contenen nuclis densos en estats evolutius diferents. IRAS 20126+4104 està associada amb un nucli molecular calent, en canvi les altres dues regions tracen una regió UCH II que pràcticament s'ha després del gas molecular. A més a més les tres regions estan associades amb fluxes moleculars, i contenen tant nuclis pre-protostel·lars com nuclis protostel·lars.

Hem observat aquestes regions en  $\text{NH}_3$  utilitzant el VLA, mentre que l'emissió de  $\text{N}_2\text{H}^+$  s'ha observat utilitzant amb els interferòmetres BIMA i CARMA per les regions IRAS 20126+4103 i IRAS 22134+5834, respectivament. Les observacions de  $\text{N}_2\text{H}^+$  per la regió IRAS 00117+6412 s'han obtingut de la literatura (Palau et al. 2010). També hem observat l'emissió en el continu a 0.85 mm en la regió

IRAS 20126+4104 fent servir el SMA.

L'emissió del continu a 0.85 mm mostra dues condensacions de pols. D'aquestes dues condensacions, la més intensa està associada a la font IRAS 20126+4104 i té una massa de  $28 M_{\odot}$ , mentre que l'altre condensació té una massa de  $11\text{--}4 M_{\odot}$  (estimada pel rang de temperatures 10–20 K).

L'anàlisi de l'obtenció dels paràmetres físics del  $\text{NH}_3$  i  $\text{N}_2\text{H}^+$  s'ha fet de la mateixa manera que en el cas de la regió AFGL 5142 (veure capítol 4). Hem trobat que la temperatura en els nuclis pre-protostel·lars és 16 K, força més alta que la temperatura típica dels nuclis de baixa massa (e. g., Tafalla et al. 2002; Crapsi et al. 2007) però semblant als resultats obtinguts en regions d'alta massa (e. g., Li et al. 2003; Palau et al. 2007). Aquest resultat indicaria que aquests nuclis contenen o bé un objecte molt jove embegut o bé que estan escalfats externament. De fet, en les regions IRAS 00117+6412 i IRAS 22134+5834 hem trobat evidències d'escalfament extern en les proximitats de la regió UCH II amb un gradient de temperatura que augmenta a mesura que ens anem acostant a la regió UCH II. Pel que fa a la densitat columnar de  $\text{NH}_3$  hem pogut veure una certa tendència del gas per la qual els nuclis més freds tenen densitats columnars de  $\text{NH}_3$  més elevades. A més a més també s'observa que els valors més baixos de densitat columnar de  $\text{NH}_3$  estan associats a les regions on la temperatura és més alta, que pot ser degut al pas d'un flux molecular o al front de ionització de l'estrella més massiva.

En les tres regions trobem variacions significatives del quocient  $\text{NH}_3/\text{N}_2\text{H}^+$  entre els diversos nuclis que constitueixen la regió. Per exemple, el nucli associat amb un objecte jove de Classe 0/I en la regió IRAS 00117+6412 presenta valors baixos del quocient, al voltant de 100, mentre que els altres nuclis tenen valors molt més alts del quocient. Per la regió IRAS 22134+5834 trobem un resultat similar. En aquesta regió tots els nuclis detectats en  $\text{NH}_3$  i  $\text{N}_2\text{H}^+$  semblen tenir propietats característiques dels nuclis pre-protostel·lars, és a dir, que no tenen formació estel·lar associada, i els valors del quocient  $\text{NH}_3/\text{N}_2\text{H}^+$  estan entre 50 i 600. És important destacar que els valors més baixos estan associats amb aquells nuclis afectats per la radició ultraviolada. Per aquestes dues regions els valors del quocient  $\text{NH}_3/\text{N}_2\text{H}^+$  són consistents amb els resultats obtinguts en estudis previs (Caselli et al. 2002a; Hotzel et al. 2004; Palau et al. 2007; Friesen et al. 2010), on el quocient és baix en aquells nuclis que contenen un objecte jove embegut i alt en nuclis sense formació estel·lar. En canvi, per la regió IRAS 20126+4104 trobem que el quocient

$\text{NH}_3/\text{N}_2\text{H}^+$  en el nucli associat amb el nucli molecular calent, i per tant associat amb formació estel·lar, té un valor de 300, molt més alt que els valors típics del quocient per les regions de baixa massa, però semblant al resultat que obtenim per AFGL 5142. En canvi, en els altres nuclis de la regió, tots ells sense formació estel·lar associada, trobem que el quocient és encara més alt, al voltant de 400–600. Aquest resultat recolza el fet que en regions on la temperatura és molt elevada, com en el dels nuclis moleculars calents, el valor del quocient creix considerablement, assolint valors fins i tot més alts que en nuclis pre-estel·lars.

## **Desaparició del $\text{N}_2\text{H}^+$ en el proto-cúmulo massiu AFGL 5142**

AFGL 5142 és una regió de formació estel·lar situada a una distància de 1.8 kpc en el braç de Perseus. Les primeres observacions amb alta resolució mostren una font de radio continu que coincideix amb el pic de l'emissió de  $\text{NH}_3$  (Torrelles et al. 1992; Estalella et al. 1993) i que està associada també amb emissió de la pols a 3 mm (Hunter et al. 1999). A longituds d'ona de l'infraroig proper Hunter et al. (1995) detecten un cúmulo de 28 fonts agrupades en una regió de 0.3 pc, i posteriors observacions amb el satèl·lit Spitzer permeten identificar 44 objectes, la majoria d'ells agrupats al voltant de l'estrella massiva (Qiu et al. 2008). Recentment, Zhang et al. (2007) troben que la font de radio continu consisteix en tres fonts centimètriques i que l'emissió de la pols està resolta en cinc fonts mil·limètriques. També s'han detectat diversos fluxos moleculars associats amb les condensacions de pols. Tot això indica que la regió AFGL 5142 està formant estrelles en mode cúmulo. L'emissió del gas dens s'ha estudiat principalment utilitzant telescopis d'antena única en  $\text{NH}_3$ , CS, HCN,  $\text{HCO}^+$ ,  $\text{CH}_3\text{OH}$ , and  $\text{CH}_3\text{CN}$  (Verdes-Montenegro et al. 1989; Estalella et al. 1993; Hunter et al. 1995, 1999; Cesaroni et al. 1999b). En concret, l'emissió de la molècula de  $\text{NH}_3$  s'ha observat amb l'interferòmetre VLA i consisteix en un nucli central i compacte associat amb l'emissió de la pols i que conté al menys tres objectes joves de massa intermitja/alta (Zhang et al. 2002, 2007) envoltat per una estructura més extensa sense indicis de formació estel·lar. Per tant, AFGL 5142 és una regió excel·lent per investigar el quocient  $\text{NH}_3/\text{N}_2\text{H}^+$  ja que conté nuclis en diferents estats evolutius, un d'ells associat amb formació estel·lar en mode cúmulo i que conté nuclis moleculars calents.

Vam observar amb CARMA l'emissió a 3 mm, així com l'emissió de la transició  $\text{N}_2\text{H}^+$  (1–0). L'emissió del continu mostra una única font compacta (amb un tamany de 5200 AU) envoltada per una estructura extensa i aplanada. La massa que derivem per aquesta condensació és de  $23 M_\odot$ . Pel que fa a l'emissió de  $\text{N}_2\text{H}^+$  (1–0) hem trobat que el nucli més intens en  $\text{NH}_3$  (nucli central) pràcticament no té emissió de  $\text{N}_2\text{H}^+$  associada. L'emissió més intensa en  $\text{N}_2\text{H}^+$  està associada amb dos nuclis situats a l'oest i a l'est del nucli central. Aquests dos nuclis semblen estar associats amb fonts infraroja, tot i que no tenim evidències de que aquestes fonts estiguin realment associades amb el gas dens així com tampoc podem descartar la possibilitat d'altres objectes embeguts en ells. Per tant, la naturalesa d'aquests dos nuclis no és gens clara.

A partir de treballs de la literatura hem estudiat la química de la regió. En concret, hem analitzat la densitat columnar de diferents espècies moleculars:  $\text{N}_2\text{H}^+$  (1–0),  $\text{NH}_3$  (1,1) i (2,2) (Zhang et al. 2002), i  $\text{HCO}^+$  (1–0) i  $\text{H}^{13}\text{CO}^+$  (1–0) (Hunter et al. 1999). Per poder comparar l'emissió d'aquestes molècules hem convolucionat la seva emissió a un feix circular de  $4''$ . Després hem obtingut els espectres de totes aquestes molècules en una xarxa de  $1'' \times 1''$ , i hem ajustat l'estructura hiperfina per cada espectre pel cas de  $\text{N}_2\text{H}^+$  (1–0) i  $\text{NH}_3$  (1,1) mentre que pel cas de  $\text{NH}_3$  (2,2),  $\text{HCO}^+$  (1–0), i  $\text{H}^{13}\text{CO}^+$  (1–0) hem ajustat una gaussiana. A partir dels ajustos de  $\text{NH}_3$  hem calculat la temperatura rotacional i la densitat columnar de  $\text{NH}_3$  (veure Apèndix). La densitat columnar de  $\text{N}_2\text{H}^+$  i  $\text{HCO}^+$  s'ha calculat utilitzant l'expressió per una molècula lineal suposant que tots els nivells estan poblats amb una única temperatura d'excitació (veure per exemple l'expressió de Caselli et al. 2002b).

El mapa de densitat columnar de  $\text{N}_2\text{H}^+$  mostra diferències significatives entre els 3 nuclis associats amb la regió. Els valors més elevats s'assoleixen en els nuclis est i oest, mentre que la densitat columnar en el nucli central (que és molt intens en  $\text{NH}_3$ ) és un ordre de magnitud més baixa. Per altra banda, el  $\text{NH}_3$  presenta variacions petites, i contràriament al  $\text{N}_2\text{H}^+$  el valor màxim s'assoleix en el nucli central. La distribució de  $\text{HCO}^+$  està correlacionada amb la densitat columnar de  $\text{NH}_3$  i anticorrelacionada amb la densitat columnar de  $\text{N}_2\text{H}^+$ . Finalment hem obtingut el mapa del quocient  $\text{NH}_3/\text{N}_2\text{H}^+$ , on els valors més alts estan associats amb el nucli central que conté el cúmul de fonts mil·limètriques. En canvi, els nuclis oest i east tenen valors del quocient entre 50 i 100, similars als resultats obtinguts en estudis previs per nuclis associats amb objectes estel·lars joves (Caselli et al. 2002a; Hotzel et al. 2004; Palau et al. 2007; Friesen et al. 2010). Tots aquests

estudis mostren que quocients alts ( $\leq 300$ ) estan associats amb nuclis sense formació estel·lar, mentre que el quocient és baix, al voltant de 60–90, en objectes estel·lars joves. Això suggereix una anticorrelació entre el quocient  $\text{NH}_3/\text{N}_2\text{H}^+$  i l'estat evolutiu. Aleshores, els valors tant alts del quocient  $\text{NH}_3/\text{N}_2\text{H}^+$  en el nucli central de AFGL 5142 no segueix la tendència dels estudis citats prèviament, i per tant altres factors a més de l'evolució poden tenir un paper important en la determinació d'aquest quocient.

Per tal d'estudiar el comportament del quocient  $\text{NH}_3/\text{N}_2\text{H}^+$  hem dut a terme el modelatge químic de la regió fent ús del model químic UCL\_CHEM (Viti and Williams 1999; Viti et al. 2004). Els paràmetres inicials del model, com per exemple la temperatura, s'han escollit d'acord amb els valors observats a partir del  $\text{NH}_3$ , 70 K pel cas del nucli central i 25 K pels nuclis oest i est. Llavors, hem explorat un rang de densitats  $n \simeq 10^5 - 10^7 \text{ cm}^{-3}$ , i per cada densitat hem variat el percentatge de molècules que es dipositen sobre els grans de pols al final de l'etapa de col·lapse gravitatòri. A partir d'aquest anàlisi trobem que els valors del quocient  $\text{NH}_3/\text{N}_2\text{H}^+$  poden ser reproduïts pel nostre model quan s'utilitza un percentatge alt de molècules congelades en els grans de pols, i adoptant una densitat de  $10^6 \text{ cm}^{-3}$  pel nucli central i una densitat de  $10^5 \text{ cm}^{-3}$  pel cas dels nuclis oest i est. Els resultats del model ens mostren que les diferències observades en el quocient  $\text{NH}_3/\text{N}_2\text{H}^+$  entre el nucli central i els nuclis oest i est són degudes a efectes de densitat i en particular de temperatura. A mesura que la temperatura augmenta la fracció d'espècies que s'evaporen dels grans de pols augmenta i per tant la química evolucionaria de forma diferent. Pel nucli central la temperatura màxima és de 70 K i això produeix que la molècula de  $\text{N}_2\text{H}^+$  es destrueixi a causa de reaccions amb el CO, el qual és evaporat dels grans de pols degut a les altes temperatures assolides i possiblement als fluxes moleculars presents en la regió. Per tant, a més de l'evolució les propietats físiques del nucli tenen un paper molt important en la determinació del quocient  $\text{NH}_3/\text{N}_2\text{H}^+$ .

Per tant, en aquest estudi del quocient  $\text{NH}_3/\text{N}_2\text{H}^+$  en la regió AFGL 5142 hem trobat que el quocient es comporta de forma diferent que en el cas de baixa massa degut principalment a les altes temperatures que s'assoleixen en els nuclis moleculars calents.

## El quocient $\text{NH}_2\text{D}/\text{NH}_3$ en nuclis pre-protostellar entorn de la regió UCH II IRAS 20293+3952

La regió IRAS 20293+3952 té unes 6300  $L_\odot$  i està situada a una distància de 2 kpc (Beuther et al. 2004b). Aquesta regió està associada amb una regió H II ultra compacta (UCH II) molt a prop d'un núvol de gas dens observat en  $\text{NH}_3$  amb alta resolució angular (Palau et al. 2007), i conté una gran varietat d'objectes estel·lars joves i nuclis densos en diferents estats evolutius. Mentre que la part nord del núvol conté diversos objectes estel·lars joves associats amb fluxes moleculars (Beuther et al. 2004a; Palau et al. 2007), la part del sud està poblada principalment per nuclis sense formació estel·lar, identificats a partir de l'emissió de la pols i del  $\text{NH}_3$  i anomenats BIMA 3 i BIMA 4. La regió també està associada amb un núvol més petit i sense formació estel·lar situat cap al nord-oest (núvol oest). Nosaltres hem observat amb alta resolució angular amb el PdBI l'emissió de l'amoniac deuterat ( $\text{NH}_2\text{D}$ ) per tal d'estimar per primera vegada la fracció de deuteració a partir del quocient  $\text{NH}_2\text{D}/\text{NH}_3$  amb alta resolució angular en una regió de formació estel·lar d'alta massa.

L'emissió del  $\text{NH}_2\text{D}$  està associada principalment amb els nuclis que no contenen formació estel·lar, és a dir amb els nuclis situats al sud del núvol principal i en el núvol oest, mentre que aquells nuclis que contenen un objecte jove embegut pràcticament no presenten emissió de  $\text{NH}_2\text{D}$  (veure Fig. 5.1). Hem obtingut els espectres de  $\text{NH}_2\text{D } 1_{11} - 1_{01}$  en una xarxa de  $2'' \times 2''$  i hem ajustat l'estructura hiperfina per cada espectre. A partir dels resultats de l'ajust hem obtingut l'opacitat de la molècula de  $\text{NH}_2\text{D}$ , la temperatura d'excitació, i l'amplada intrínseca de la línia, que ens ha permès calcular la densitat columnar de  $\text{NH}_2\text{D}$ . El mapa de l'amplada de la línia mostra un cert eixamplament de la línia en el núvol de l'oest i en dos nuclis associats amb el núvol principal (BIMA 3 i BIMA 4), mentre que els altres nuclis semblen ser més quiescents. Tal i com suggereix Palau et al. (2007) un dels fluxos moleculars de la regió està interaccionant amb BIMA 4 i això podria produir l'eixamplament observat. A més, l'eixamplament del núvol de l'oest coincideix espacialment (en projecció) amb emissió d'alta velocitat del flux molecular D. Aleshores, el fet que trobem línies tan amples suggereix que el gas deuterat està fortament perturbat pels fluxos moleculars.

El mapa de densitat columnar de  $\text{NH}_2\text{D}$  presenta diferències importants entre el

núvol de l'oest i el principal. Mentre que la densitat columnar en el núvol de l'oest és  $\sim 25 \times 10^{14} \text{ cm}^{-2}$ , en el núvol principal la densitat columnar de  $\text{NH}_2\text{D}$  és un ordre de magnitud més petita, al voltant de  $1 - 8 \times 10^{14} \text{ cm}^{-2}$ .

Per tal de derivar la fracció de deuteració, definida com  $D_{\text{frac}} = N(\text{NH}_2\text{D})/N(\text{NH}_3)$ , hem utilitzat el mateix rang  $uv$  per les dues molècules i hem convolucionant la seva emissió a un feix circular de  $7''$ . En posicions associades amb objectes estel·lars joves hem derivat límits superiors, amb  $D_{\text{frac}} < 0.1$ . Aquesta diferència en la fracció de deuteració entre els nuclis que contenen objectes embeguts i els que no suggereix que la producció de  $\text{NH}_2\text{D}$  és més eficient en la fase pre-protostel·lar que en la protoestel·lar. El valor de  $D_{\text{frac}}$  en el núvol de l'oest és  $\sim 0.8$ . Per altra banda, la fracció de deuteració en el núvol principal presenta variacions importants entre els diferents nuclis, amb  $D_{\text{frac}}$  disminuint des del nord-oest ( $D_{\text{frac}} \simeq 0.5$ ) cap al sud-est ( $D_{\text{frac}} \simeq 0.1$ ). Aquest resultat indica que hi ha una diferenciació química al llarg del núvol principal. Aquesta diferenciació química també s'ha observat a partir del quocient  $\text{NH}_3/\text{N}_2\text{H}^+$  (Palau et al. 2007). Aleshores, per aquesta regió el comportament de la fracció de deuteració mesurada a partir del quocient  $\text{NH}_2\text{D}/\text{NH}_3$  és similar al comportament del quocient  $\text{NH}_3/\text{N}_2\text{H}^+$ . Per tant aquests dos quocients es poden utilitzar per diferenciar entre nuclis pre-protostel·lars i protoestel·lars.

## Discussió general i conclusions

En aquest treball s'ha fet un estudi del quocient  $\text{NH}_3/\text{N}_2\text{H}^+$  en regions de formació estel·lar d'alta massa mitjançant observacions a gran escala d'un núvol fosc en l'infraroig observacions amb alta resolució angular amb l'objectiu en 4 regions de formació estel·lar d'alta massa amb l'objectiu d'entendre el comportament d'aquest quocient i la seva utilitat com a "reelotge químic". També hem estudiat la fracció de deuteració i la seva relació amb el quocient  $\text{NH}_3/\text{N}_2\text{H}^+$ . Les conclusions principals són les següents:

- En el núvol fosc en l'infraroig G14.2–0.60 hem trobat que tant la pols com l'emissió del gas dens traçat per l'amoníac presenten estructures filamentàries i grumolloses. Aquestes estructures apareixen de forma jeràrquica des d'escala de 1 pc fins a 0.02 pc, de manera que el procés de fragmentació del núvol té lloc a totes les escales. En concret, quan observem amb alta resolució angular una

certa condensació de pols, aquesta es fragmenta en 16 fonts mil·limètriques, amb masses molt més grans que les esperades a partir dels models actuals teòrics, suggerint que la turbulència i/o els camps magnètics poden ser molt importants en aquesta regió.

- A G14.2–0.60 el quocient  $\text{NH}_3/\text{N}_2\text{H}^+$  assoleix valors molt alts, possiblement a causa de la baixa resolució angular assolida amb els telescopis d'una única antena. Al llarg d'un filament trobem una certa tendència del quocient amb l'estat evolutiu, amb valors més alts en els nuclis que no presenten formació estel·lar i valors més baixos en aquells nuclis associats amb formació estel·lar. Tanmateix, és necessari realitzar observacions interferomètriques de la molècula de  $\text{N}_2\text{H}^+$  per tal d'entendre el comportament del quocient  $\text{NH}_3/\text{N}_2\text{H}^+$  en els núvols foscos en l'infraroig a escales dels nuclis densos.
- Hem estudiat amb interferometres el quocient  $\text{NH}_3/\text{N}_2\text{H}^+$  en quatre regions de formació estel·lar d'alta massa. En la regió IRAS 00117+6412 el quocient és alt en el nucli dens associat amb l'objecte més jove i baix en el nucli associat amb un objecte més evolucionat. En la regió IRAS 22134+5834 hem trobat que els efectes de la radiació ultraviolada són importants en la determinació del quocient, ja que aquest és molt més baix en aquells nuclis influenciats per un camp de radiació provinent de l'estrella més massiva. Finalment, en la regió IRAS 20126+4104 hem trobat valors molt alts del quocient degut a l'alta temperatura que s'assoleix en el nucli molecular calent.
- Per el cúmulo massiu protoestel·lar AFGL 5142 hem aplicat el model químic i hem trobat que els alts valors del quocient  $\text{NH}_3/\text{N}_2\text{H}^+$  són degut a les altes temperatures que s'assoleixen en els nuclis moleculars calents. En aquestes condicions la molècula de CO s'evapora dels grans de pols, fet que produeix la destrucció de  $\text{N}_2\text{H}^+$ . Aleshores, a més de l'evolució del nucli, les propietats físiques d'aquest, com la densitat i en concret la temperatura, són paràmetres molt importants que determinen el quocient  $\text{NH}_3/\text{N}_2\text{H}^+$ .
- Hem fet una llista de regions de formació estel·lar tenint en compte tant les regions de baixa massa com d'alta massa que han estat observades en  $\text{NH}_3$  i  $\text{N}_2\text{H}^+$ , i per les quals s'ha pogut estimar el quocient  $\text{NH}_3/\text{N}_2\text{H}^+$ . A partir d'aquesta llista hem trobat que la mediana del quocient  $\text{NH}_3/\text{N}_2\text{H}^+$  es més alta en nuclis pre-protoestel·lars que en nuclis protoestel·lars. Hem trobat una seqüència evolutiva del quocient  $\text{NH}_3/\text{N}_2\text{H}^+$  tant en la fase pre-protoestel·lar

com en la fase protoestel·lar. Inicialment, hi ha un període d'or per la molècula de  $\text{NH}_3$  en el qual el quocient presenta primer valors alts i amb l'evolució del nucli pre-protoestel·lar el quocient va disminuint. Durant la fase protoestel·lar, justament després de la formació de la protoestrella el quocient disminueix, en aquest cas degut al període d'or del  $\text{N}_2\text{H}^+$ . Després, a mesura que el nucli protoestel·lar evoluciona el quocient  $\text{NH}_3/\text{N}_2\text{H}^+$  torna a assolir valors alts degut als efectes de les altes temperatures i dels fluxos moleculars.

- En la regió IRAS 20293+3952 la fracció de deuteració  $D_{\text{frac}} = N(\text{NH}_2\text{D})/N(\text{NH}_3)$  augmenta durant l'etapa pre-protoestel·lar a mesura que l'objecte s'acosta al moment en què té lloc la formació d'una estrella. Tanmateix, tant els fluxos moleculars com la radiació ultraviolada poden jugar també un paper molt important en la determinació de la fracció de deuteració. A més, els dos quocients,  $\text{NH}_3/\text{N}_2\text{H}^+$  i  $\text{NH}_2\text{D}/\text{NH}_3$  estan relacionats amb l'estat evolutiu del gas dens, indicant que els dos quocients es poden utilitzar com a "rellotges químics" abans del procés de col·lapse gravitatòri.
- A partir de l'experiència d'aquest treball i pensant en el treball futur suggerim la utilització d'altres quocients com a complement del quocient  $\text{NH}_3/\text{N}_2\text{H}^+$ . Entre ells, proposem l'estudi d'espècies deuterades així com també molècules primerenques com ara el  $\text{C}^{18}\text{O}$  o el  $\text{CS}$  ja que poden ser una eina complementària a les molècules que contenen nitrogen en els nuclis pre-protoestel·lars més joves. Per altra banda, el quocient d'espècies amb sofre pot ser molt útil durant l'etapa evolutiva dels nuclis moleculars calents.



# Chapter 1

## Introduction

### 1.1 The birth sites of high-mass stars

Stars in the Galaxy are formed in the spiral arms as well as near the center of the Galaxy. Their birth sites are condensations of gas and dust where hydrogen is found primarily in molecular form,  $\text{H}_2$ , called molecular clouds, which are the coldest and densest parts of the interstellar medium. According to their mass, molecular clouds are traditionally classified in two categories: giant molecular clouds (GMC) and dark cloud. Dark clouds have masses  $\sim 10^3 M_\odot$ , sizes of a few parsecs, and very low temperatures ( $\sim 10 - 20$  K). They are very abundant and close enough ( $< 500$  pc) to be seen in silhouette against the background Galactic starlight because their dust absorbs the radiation from stars behind (see Fig. 1.1 Left). Examples of nearby molecular clouds are Taurus, Perseus, and Ophiuchus, which are forming low-mass stars either in isolation or in small groups or clusters. On the other hand, GMC lie at largest distances, typically  $> 1$  kpc except Orion GMC, have masses around  $10^4 - 10^6 M_\odot$ , sizes of few tenths of parsecs, and temperatures of  $\sim 20$  K. They are forming rich stellar clusters and contain embedded massive stars.

Traditionally, the birth places of star formation has been separated in GMC and dark clouds. However, the mid-infrared data provided by the Infrared Space Telescope (ISO; Perault et al. 1996) and the Midcourse Space Experiment (MSX; Egan et al. 1998) satellites identified a new class of interstellar clouds, the Infrared Dark Clouds (IRDCs). IRDCs, seen at infrared wavelengths as absorption features against the bright galactic background (see Fig. 1.1 Right), frequently in filamentary



Figure 1.1: **Left:** Three-color (BVI) composite image of Barnard 68 (B68) dark globule obtained with VLT ANTU and FORS1. **Right:** Three-color composite image (3.6/8/24  $\mu\text{m}$ ) obtained with the Spitzer Space Telescope toward the IRDC G11.11-0.11.

shapes, contain thousands of  $M_{\odot}$  of dense ( $n \gtrsim 10^5 \text{ cm}^{-3}$ ) and cold ( $T \simeq 10 - 15 \text{ K}$ ) gas (see e. g., Carey et al. 1998; Pillai et al. 2006a and the review of Menten et al. 2005 for a complete description of the physical and chemical structure of IRDCs), and appear to preserve the pristine environment, and thus the initial conditions for massive star and cluster formation. Thus, in the traditional picture of molecular clouds outlined above, these new population, the IRDCs, may represent the densest parts of GMC or, alternatively they may be the earliest stage of molecular cloud evolution.

In this context, detailed studies of IRDCs or high-mass starless cores are essential for unveiling the physical and chemical features and for providing the initial conditions that lead to the formation of massive stars. For example, important questions concerning formation of high-mass and cluster are: Will all clumps within IRDCs form high-mass stars? How do the clumps break up? Do they fragment into Jeans mass at early stages (as proposed by Bonnell and Bate 2002; Bonnell et al. 2004), or is the protostellar heating, as suggested by Krumholz and McKee (2008), responsible to stop the fragmentation process? Only a few observational works (Beuther et al. 2005; Pillai et al. 2006b; Rathborne et al. 2007, 2008; Wang et al. 2008; Beuther and Henning 2009; Fallscheer et al. 2009; Zhang et al. 2009) have addressed the study of IRDCs with high angular resolution, and only the work of Wang et al. (2008) focuses on the gas emission of an entire IRDC at high angular resolution. The study of cloud structure and kinematics at core size-scales and the formation of high-mass

protostars within a dense core, cannot be assessed with single dish telescopes, and hence high angular resolution observations of the dust and dense gas are definitely required.

### 1.1.1 Fragmentation

The internal structure of molecular clouds is highly inhomogeneous and contains high density regions ( $n \simeq 10^4 \text{ cm}^{-3}$ ), called clumps, embedded in a larger-scale, lower-density medium. These clumps themselves contain dense cores ( $n \gtrsim 10^5 \text{ cm}^{-3}$ ), which are the birth places of star formation within a cloud, and is the final stage of cloud fragmentation (e. g., Williams et al. 2000). Thus, it is clear that fragmentation is a highly hierarchical process.

There are several mechanism that have been proposed to explain fragmentation of a collapsing cloud core into star clusters: rotation, turbulence and magnetic fields. Simulations of fragmentation of a rotating cloud with different equations of state, density profiles, and shapes show that most cores with some angular momentum can fragment into multiple objects. Turbulent fragmentation simulations show that turbulent cores generally fragment into several stars, and that the number of stars that form raises with increasing turbulence. However, these simulations (rotational fragmentation and turbulent fragmentation), which do not include magnetic fields, are not able to correctly predict the observed properties, such as number of stars, separations, and distributions of the fragments (see Goodwin et al. 2007, and references therein).

Simulations of a collapsing and rotating cloud core including magnetic fields show that magnetic fields tend to suppress fragmentation via the “magnetic-braking” (e. g., Hosking and Whitworth 2004), but still fragmentation occurs when either the rotation is relatively high or magnetic field strength relatively low (Machida et al. 2005). At present, it is not clear which mechanism determines the multiple fragmentation of cloud cores. Recently, Zhang et al. (2009) performed high angular resolution observations ( $\sim 1''.2$  or 6000 AU) of the dust emission at 1.2 mm toward the IRDC G28.34+0.06 and find that magnetic fields and/or turbulence must be important in the cloud fragmentation.

### 1.1.2 Stages of massive star formation

While the evolutionary paradigm for low-mass stars is well established (Lada 1987), the current picture of the different evolutionary stages of high-mass stars is still unclear. The earliest evolutionary stages of massive star formation are represented by high-mass starless cores or pre-protostellar cores (e. g., Evans et al. 2002). Thus, IRDCs are the best places to look for high-mass pre-protostellar core candidates. This phase is followed by the formation of a high-mass protostellar object, which initially is not detectable at centimeter wavelengths, the so-called Hot Molecular Cores (HMC; e. g., Kurtz et al. 2000; Cesaroni 2005). After the hot core is formed, the massive protostar eventually produces free-free emission from ionized gas and forms an hypercompact HII region (HCH II). At some point, the HCH II region begins to expand and forms an ultracompact HII region (UCH II) and later to a more evolved HII region (see e. g., Garay and Lizano 1999; Kurtz et al. 2000). In this thesis we will focus on the very first stages (i. e., IRDCs, hot molecular cores, and HCH II/UCH II regions) when the high-mass protostellar objects are still deeply embedded in the dense gas.

## 1.2 The relevance of chemistry in high-mass star-forming regions

Thanks to the advances in sensitivity and angular resolution of ground-base radio telescopes and infrared satellites our knowledge of the interstellar chemistry has been grown considerably during the last decades. At present, about 137 molecules (205 including isotopomers) have been detected in the interstellar medium. Molecular line observations provide information about the gas component of clouds, and in particular about their velocity structure, density, temperature, and chemical composition. In this section we briefly summarize the chemical composition of the core material based on observational studies performed mainly in low-mass star-forming regions and present some of chemical features found in regions of massive star formation.

Stars form within the densest portions of molecular clouds, the so called dense cores. Before the formation of a protostellar object, dense cores or pre-protostellar cores, are characterized by low temperatures ( $\sim 10$  K) and relatively high densi-

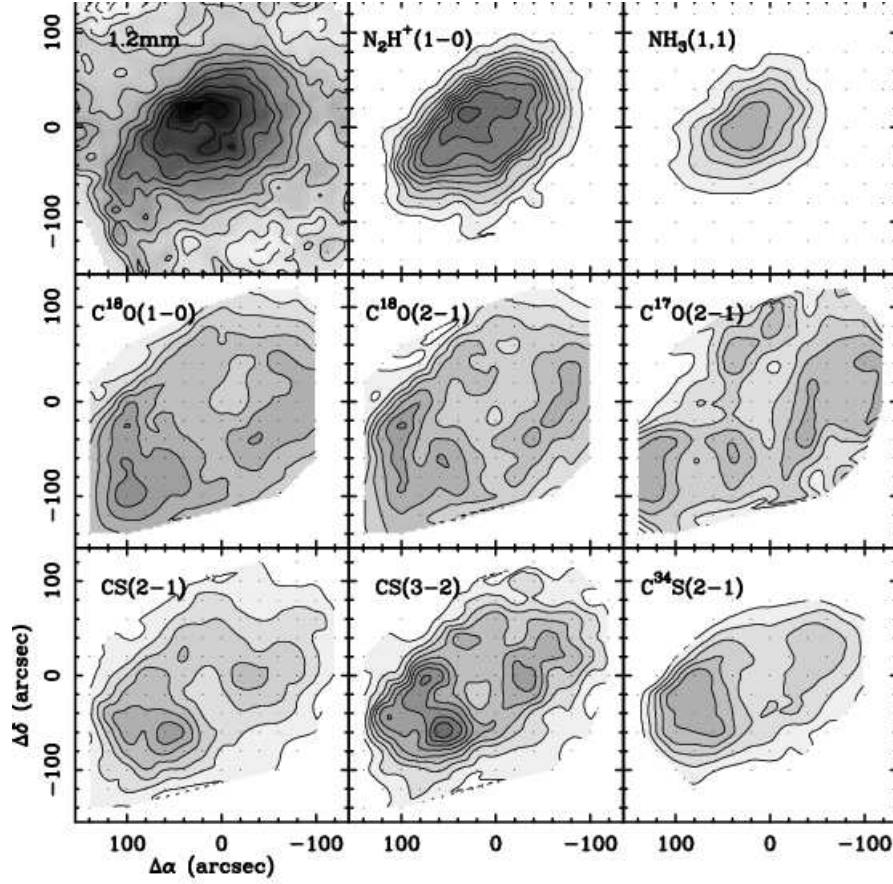


Figure 1.2: Integrated intensity maps for continuum and molecular lines observed by Tafalla et al. (2004) toward L 1498. Note that almost all molecules freeze-out at the core centers while dust,  $\text{NH}_3$ , and  $\text{N}_2\text{H}^+$  present a centrally peaked morphology.

ties ( $\gtrsim 10^5 \text{ cm}^{-3}$ ). These conditions yield to the most prominent feature of core chemistry, which is the disappearance of a number of gas-phase species at the core center. In particular, all C- and O-bearing molecules freeze-out onto dust grains, producing characteristic maps of emission in the form of a ring that surrounds the core density peak (see e. g., Tafalla et al. 2004, 2006). To illustrate the central depletion of molecules we show in Fig. 1.2 the emission of 8 different molecules of L 1498 starless cores (Tafalla et al. 2004). Among all the species mapped in this region only two ( $\text{NH}_3$  and  $\text{N}_2\text{H}^+$ ) survive in the central density peak. A similar behavior is found in the intermediate/high-mass regime (e. g., Pillai et al. 2007; Alonso-Albi et al. 2010). Thus, nitrogen-bearing molecules, like  $\text{NH}_3$  and  $\text{N}_2\text{H}^+$ , together with the dust emission are the most reliable tracers of the densest gas. This behavior,

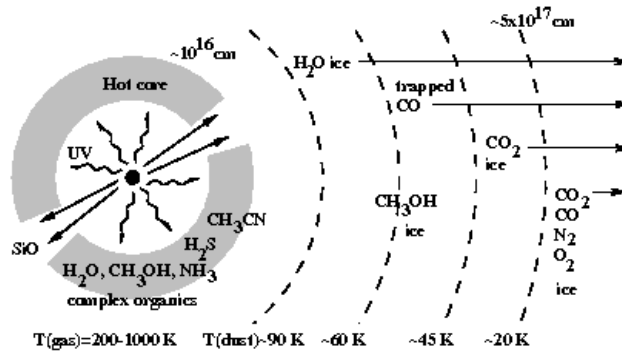


Figure 1.3: schematic illustration of the chemical environment in high-mass YSOs from van Dishoeck and Blake (1998).

i.e., the observed depletion of most molecules except N-bearing species, was initially thought to be a consequence of the different binding energies between CO and  $\text{N}_2$ , the parent molecule of  $\text{NH}_3$  and  $\text{N}_2\text{H}^+$ . However, recent laboratory measurements indicate that the binding energies of these two molecules are almost the same (Öberg et al. 2005; Bisschop et al. 2006), so at present this behavior is not completely understood.

Once the protostar is born eventually it heats up the surrounding material with its radiation, raising the dust temperature and forming a HMC. These objects are regions close to young stars, where ice mantles evaporate off dust grains and high-temperature gas-phase chemistry creates complex organic species. Molecular surveys at (sub-)millimeters wavelengths reveal a rich chemistry of these objects, for instance as observed toward Orion-KL (e.g., Schilke et al. 2001; Comito et al. 2005). HMC are typically associated with high-mass stars but they are also found in low-mass star-forming regions during the earliest protostellar phase (e.g., Bottinelli et al. 2007) and in intermediate-mass Class 0 sources (Fuente et al. 2005a; Sánchez-Monge et al. 2010), the so-called hot corinos. The large abundance of saturated species, such as  $\text{H}_2\text{S}$ ,  $\text{CH}_3\text{OH}$ , and complex organic H-rich molecules, like  $\text{HCOOCH}_3$ ,  $\text{CH}_3\text{COOH}$ , suggests an active surface chemistry because gas phase routes appear to be slow. In Figure 1.3 we show an sketch of the complex chemistry involved in envelopes of high-mass young stellar objects.

Finally, one of the most conspicuous phenomenon during the earliest stages of star formation is the presence of powerful and collimated molecular outflows both

in low- and high-mass star-forming regions. Molecular outflows presents a very rich chemistry. They are detected in several molecular species like CO, SiO, CH<sub>3</sub>OH, SO, SO<sub>2</sub>, HCO<sup>+</sup>, HCN, H<sub>2</sub>CO, and H<sub>2</sub>O. One of the best examples is the chemically active L1157 molecular outflow, where a punch of molecules have been detected in the outflow lobes (e. g., Bachiller et al. 2001; Codella et al. 2010). Outflows shock the material along their passage, raising the gas temperature and partially destroying dust grains, and thus they allow new chemical processes to occur. The chemical manifestation of these shocks depend on whether the shocks are of the J (jump) or C (continuous) type. In C-type shocks (low electron fraction and with velocities below 50 km s<sup>-1</sup>) molecular species, in particular H<sub>2</sub>, do not dissociate. In these conditions, some important endothermic reactions become fast and rapidly convert most of the free oxygen into water and sulphur, mainly into SO and SO<sub>2</sub> (e. g., Pineau des Forêts et al. 1993). On the other hand, in J shocks the temperature is increased to such high values that all molecules are dissociated.

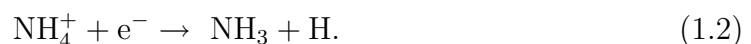
At present, there are still many uncertainties about the chemistry in star-forming regions, specially regarding the surface chemistry and gas phase reactions at high temperatures, which are essential to interpret the observational results toward hot molecular cores and molecular outflows.

### 1.2.1 N-bearing chemistry

A possible entry route to the nitrogen chemistry is through dissociative ionization of N<sub>2</sub> with He<sup>+</sup> ions reactions

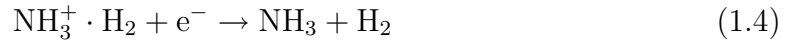
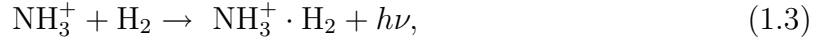


followed by consecutive hydrogenation of N<sup>+</sup> (via reactions with H<sub>2</sub> molecular hydrogen) produces NH<sub>4</sub><sup>+</sup>. Although the reaction pathway to NH<sub>3</sub> is not well understood, the principal formation mechanism generally proposed to form NH<sub>3</sub> is via dissociative recombination of NH<sub>4</sub><sup>+</sup>



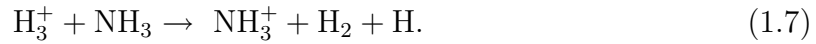
The synthesis of NH<sub>3</sub> may also be enhanced at low temperatures,  $T \simeq 10 - 20$  K,

by radiative association reactions



However, the formation rate of  $\text{NH}_3$  depends critically on the ortho-to-para ratio of  $\text{H}_2$  in molecular clouds, which is not well known.

The main dissociation mechanism of  $\text{NH}_3$  are:



The reactions of nitrogen atoms with  $\text{NH}^+$  and  $\text{NH}_2^+$  ions, as well as the neutral reactions



where  $\text{NO}$  will react again with atomic  $\text{N}$  to form  $\text{N}_2$ , starts the synthesis of  $\text{N-N}$  bonds in molecules and ions.  $\text{N}_2$  is a very stable molecule and models predict that most of the nitrogen in molecular clouds is locked up in  $\text{N}_2$ . Maret et al. (2006) demonstrate that only a small fraction of nitrogen in the gas phase is in molecular form, with most of it being atomic. However, the rotational or vibrational transitions of  $\text{N}_2$  are not observable so its abundance in the interstellar medium remains still poorly known.

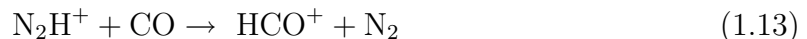
Then, reactions of  $\text{N}_2$  with  $\text{H}_3^+$  form  $\text{N}_2\text{H}^+$ :



and is destroyed by the following reactions:



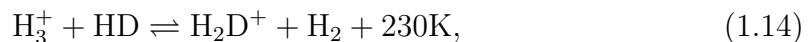
and:



### 1.2.2 Deuterated species

In the last few years our knowledge of the deuterium chemistry has grown considerably due to a large amount of deuterated species detected in the interstellar medium and the advances in chemical models. Both observational results and models strongly suggest that the deuterium fractionation, defined as the ratio of a deuterated species over its counterpart containing H, is enhanced during the earliest phases of star formation (e. g., Roberts and Millar 2000; Bacmann et al. 2003; Roberts et al. 2003; Roueff et al. 2005). Two different mechanisms have been invoked to explain the large deuterium fractionation. The first mechanism is based in gas phase-chemistry starting with the reaction shown below (Eq. 1.14). The second mechanism is based on grain surface chemistry (e. g., Tielens 1983) which forms highly deuterated ices that, eventually, are released in the gas phase during the collapse when the new born star heats and evaporates the ices. However, the role of surface chemistry in enhancing molecular D/H ratios is uncertain since to date no D-bearing species have been observed in the solid state.

In cold ( $T \simeq 10$  K) and dense ( $n \gtrsim 10^5 \text{ cm}^{-3}$ ) regions, where CO is frozen out onto dust grains surfaces, the abundance of [D/H] may exceed the cosmic elemental abundances, of  $\sim 10^{-5}$ , by 2–3 orders of magnitude (Oliveira et al. 2003; Linsky et al. 2006). Under these conditions, the deuterium chemistry is mostly regulated by the following reaction:



where at low temperatures the backward, endothermic reaction occurs slowly while the forward reaction, which is slightly exothermic, favors the production of  $\text{H}_2\text{D}^+$ , and consequently the abundance of the deuterated ions increases. Moreover,  $\text{H}_2\text{D}^+$  and  $\text{H}_3^+$  are mainly destroyed through reactions with CO. Thus, in environments where CO is depleted onto dust grains, they can survive and give rise to a high degree of deuteration. Then other reactions of  $\text{H}_2\text{D}^+$  transfer this enrichment of the deuterium fractionation in to a wide diversity of molecules and molecular ions. Actually, observations of dense cores have provided a rich variety of single, doubly and triply deuterated species. For example,  $\text{NH}_3$  has been detected in all its multiple deuterated forms (Lis et al. 2002; van der Tak et al. 2002; Roueff et al. 2005).

Deuterated species have been detected in several environments, like in cold dense pre-protostellar cores (e. g., Saito et al. 2000; Caselli et al. 2003; Crapsi et al. 2005), in massive cold cores or Infrared Dark Clouds (Pillai et al. 2007; Chen et al. 2010), and even in protostellar envelopes of low-mass protostars (Ceccarelli et al. 1998; Parise et al. 2002, 2006; Hatchell 2003), as well as in hot molecular cores and photo dissociation regions (PDRs; Leurini et al. 2006). While in cold dense cores gas-phase chemistry seems to be the main responsible to produce large amounts of deuterated species, in warm dense cores, such as in low-mass protostellar objects and hot cores, grain chemistry most likely plays an important role in enhancing the fraction of deuterated species detected in these environments.

### 1.2.3 Column density ratios as tracers of chemical evolution

Based on observational studies, most of them carried out in low-mass star-forming regions, there are several column density ratios that have been proposed to be good tracers of the chemical evolution of dense cores, and hence they can be used as “chemical clocks”. Among these, the most extensively studied is the  $\text{NH}_3/\text{N}_2\text{H}^+$  ratio. First, Caselli et al. (2002a) conducted  $\text{N}_2\text{H}^+$  observations using the FCRAO 14 m antenna toward 57 low-mass cloud cores already studied in  $\text{NH}_3$  by Benson and Myers (1989). Their sample contains both pre-protostellar and protostellar cores, and the comparison of  $\text{NH}_3$  and  $\text{N}_2\text{H}^+$  shows a significant correlation between the  $\text{NH}_3$  and  $\text{N}_2\text{H}^+$  column densities for the sample of pre-protostellar cores. On the other hand, in this study the authors pointed out that the lack of correlation between these two molecules in protostellar cores suggests a different chemical evolution of  $\text{NH}_3$  and  $\text{N}_2\text{H}^+$ , and that the  $\text{NH}_3/\text{N}_2\text{H}^+$  ratio is smaller in cores containing young

stellar objects (YSOs) than in pre-protostellar cores. Later, Hotzel et al. (2004) mapped two dense cores in  $\text{NH}_3$  and  $\text{N}_2\text{H}^+$ , Barnard 217 and LDN 1262, which have very similar morphologies: they both contain a Class I source offset from the dense pre-protostellar nucleus. The authors find that the  $\text{NH}_3$  and  $\text{N}_2\text{H}^+$  column densities show the same pattern in both cores: the average  $\text{NH}_3/\text{N}_2\text{H}^+$  abundance ratios are 140–190 in the pre-protostellar cores while they drop to about 60–90 in the regions around the YSOs due to an enhanced fractional abundance in the quiescent part of the core. More recently, other works also confirm the same tendency (Friesen et al. 2010; Miettinen et al. 2010).

In the high-mass regime, Palau et al. (2007) also find the same trend toward the intermediate-mass pre-protostellar and protostellar cores surrounding the UCH II region IRAS 20293+3952. Thus, all these studies strongly suggests that the  $\text{NH}_3/\text{N}_2\text{H}^+$  ratio is consistent with being a “chemical clock”.

Other column density ratios that have been proposed as good “chemical clocks” are the  $\text{SiO}/\text{C}^{34}\text{S}$ ,  $\text{CN}/\text{N}_2\text{H}^+$ , and  $\text{HCN}/\text{N}_2\text{H}^+$  ratios (Fuente et al. 2005b). In this work Fuente et al. (2005b) observe an intermediate-mass Class 0 protostar (NGC 7129–FIRS 2) and a more evolved object, a Herbig Be star (LkH $\alpha$  234), in several molecular transitions, and find significant differences in the column densities ratios between these two objects. For instance, the  $\text{SiO}/\text{C}^{34}\text{S}$  ratio decreases by a factor of twenty between the two objects, being higher in the Class 0 object. They suggest that this ratio is especially useful to determine the evolutionary stage of the youngest objects, which are associated with the most energetic molecular outflows. On the other hand,  $\text{CN}/\text{N}_2\text{H}^+$  and  $\text{HCN}/\text{N}_2\text{H}^+$  ratios increase from the Class 0 object to the Herbig Be star.

Tafalla and Santiago (2004) propose the  $\text{C}^{18}\text{O}/\text{N}_2\text{H}^+$  ratio as a good indicator of the evolutionary stage during the pre-protostellar phase. These two molecules are known to have different depletion behaviors at typical core densities: while  $\text{C}^{18}\text{O}$  depletes at densities of a few  $10^4 \text{ cm}^{-2}$ ,  $\text{N}_2\text{H}^+$  seems to remain in the gas phase up to densities of about  $10^6 \text{ cm}^{-2}$ . Then, differences on the  $\text{C}^{18}\text{O}/\text{N}_2\text{H}^+$  ratio are reflecting different chemical ages of prestellar cores. In young pre-protostellar cores only a small fraction of  $\text{C}^{18}\text{O}$  is found to be depleted, so the  $\text{C}^{18}\text{O}/\text{N}_2\text{H}^+$  ratio is high, while relatively more evolved cores have a low ratio since  $\text{C}^{18}\text{O}$  is strongly depleted. Therefore, if chemical youth is correlated with the lack of depletion, the  $\text{C}^{18}\text{O}/\text{N}_2\text{H}^+$  ratio is enhanced in young pre-protostellar cores because of their low

$\text{N}_2\text{H}^+$  abundance.

In addition, the deuterium fractionation has been found to be also a good tracer of core evolution both in low-mass pre-protostellar and protostellar cores. Crapsi et al. (2005) performed a survey of  $\text{N}_2\text{H}^+$  and  $\text{N}_2\text{D}^+$  toward a sample of 31 low-mass pre-protostellar cores, and identify a set of properties that characterize the most evolved ones. Among these, the most evolved pre-protostellar cores have higher  $\text{N}_2\text{H}^+$  and  $\text{N}_2\text{D}^+$  column densities, higher  $D_{\text{frac}}$ , more pronounced CO depletion, broad lines with infall asymmetry, and higher central  $\text{H}_2$  column densities than the averaged cores. All these properties strongly suggest that the deuterium fractionation increases as the pre-protostellar core approaches the onset of star formation. Nevertheless, as pointed out by Crapsi et al. (2005), when considering the subsample of Taurus cores they behave more homogeneously, indicating that external environments could play an important role in the core evolution.

During the protostellar phase, Emprechtinger et al. (2009) find that protostars in a stage shortly after the beginning of collapse (Class 0 objects) have an  $\text{N}_2\text{H}^+/\text{N}_2\text{D}^+$  ratio higher than 0.15 and later on it decreases at the Class 0/I borderline. Therefore, at least in low-mass star-forming regions,  $D_{\text{frac}}$  is found to increase until the onset of star formation and decrease afterwards.

Finally, it has been suggested that sulfur chemistry can also be used as “chemical clock” (e. g., Charnley 1997; Hatchell et al. 1998) because of the rapid evolution of S-bearing species in warm gas and because their abundance increase significantly with the temperature (by ice evaporation and shock interaction). Thus, the strong time dependence of these species may be a useful tool for tracing the evolution in the hot molecular core phase (e. g., Viti et al. 2004). Recent observations of a set of S-bearing species toward massive cores forming high-mass stars (two mid-infrared quiet and two mid-infrared bright) show that  $\text{SO}/\text{OCS}$  and  $\text{SO}_2/\text{OCS}$  abundance ratios increase with time, while  $\text{OCS}/\text{H}_2\text{S}$ ,  $\text{CS}/\text{H}_2\text{S}$ ,  $\text{CS}/\text{SO}$ , and  $\text{SO}_2/\text{SO}$  abundance ratios decrease, and hence they can be good indicators of evolution (Herpin et al. 2009).

## 1.3 The aim and structure of the thesis

### 1.3.1 Goal of the thesis

This work aims at investigating the evolution of chemical properties of the dense gas at the onset of star formation. We studied mainly the behavior of the  $\text{NH}_3/\text{N}_2\text{H}^+$  abundance ratio in a sample of nearby ( $d \leq 3$  kpc) high-mass star-forming regions, and the deuterium fractionation in a particular region. Previous studies, carried out mainly toward low-mass star-forming regions, have shown that the  $\text{NH}_3/\text{N}_2\text{H}^+$  ratio is low, around 60–90, close to YSOs, while it rises up to 200 in starless cores (e. g., Caselli et al. 2002a; Hotzel et al. 2004; Friesen et al. 2010; Miettinen et al. 2010). Moreover, in the high-mass regime, Palau et al. (2007) find the same trend toward the intermediate-mass cores surrounding an UCH II region. All these studies suggest that the  $\text{NH}_3/\text{N}_2\text{H}^+$  ratio could be used as “chemical clock” to study the history of star formation in molecular clouds.

The main goal of this thesis is to extend the study to high-mass cores with high angular resolution observations of the dense gas emission in order to see whether the differences seen in  $\text{NH}_3$  and  $\text{N}_2\text{H}^+$  arise because cores were formed at different times (and hence related with chemical evolution of the gas) or because the high temperatures and interactions from molecular outflows and/or UV radiation affect the evolution of the dense gas.

### 1.3.2 Strategy: why $\text{NH}_3$ and $\text{N}_2\text{H}^+$ at high angular resolution?

The interstellar dense gas is traced by transitions of molecules with high critical densities ( $n > 10^3 \text{ cm}^{-3}$ ) and in particular  $\text{NH}_3$  and  $\text{N}_2\text{H}^+$  are widely used for several reasons. First, both species have hyperfine structure, which allows us to derive the optical depth by observing one single transition. Second, the two inversion transition of the lower rotational states  $(J, K) = (1, 1)$  and  $(2, 2)$  are very close in frequency (hence can be observed simultaneously) and can be used to obtain a reliable measurement of the temperature. Third, for high densities ( $\gtrsim 10^3 - 10^4 \text{ cm}^{-3}$ ) and low temperatures ( $\sim 10$  K) most molecules are depleted onto dust

grains, while N-bearing molecules, like  $\text{NH}_3$  and  $\text{N}_2\text{H}^+$ , do not freeze out until they reach very high densities, around  $10^6 - 10^7 \text{ cm}^{-2}$ .

All the intermediate/high-mass star-forming regions studied in this work are located at distances  $\leq 3 \text{ kpc}$  and are associated with clusters. Since we are interested in characterizing each individual core, with typical core sizes of  $0.03\text{--}0.2 \text{ pc}$  within a cloud, we need to resolve them at distances of a few kiloparsecs. Therefore, it is necessary to reach angular resolutions between  $3''\text{--}5''$  ( $3''$  at a distance of  $2 \text{ kpc}$  yields to a spatial resolution of  $0.03 \text{ pc}$ ), which can be achieved only with interferometers.

### 1.3.3 Thesis organization and status of the different projects constituting the thesis

In the following we describe the structure of this thesis and explain the status of each work.

To understand the large scale ( $\sim 10 \text{ pc}$ ) context where high-mass star formation occurs we first present in chapter 2 the preliminary results of the Infrared Dark Cloud G14.2-0.60 to study the cloud structure, kinematics, and chemistry at the very first stages of massive star formation. We first used single-dish telescopes to study the main physical and chemical properties of the entire cloud by observing the dust emission with APEX,  $\text{N}_2\text{H}^+$  (1-0) with the FCRAO telescope, and  $\text{NH}_3$  (1,1) and (2,2) using the Effelsberg radio telescope. Moreover, we conducted high angular resolution observations of the  $\text{NH}_3$  (1,1) and (2,2) using the Very Large Array (VLA) and combined them with the Effelsberg data to recover the extended structures filtered out by the interferometer to investigate the cloud structure at core size scales down to  $0.1 \text{ pc}$ . Finally, we zoomed into a selected dust clump and observed it with the Submillimeter Array at an angular resolution of  $\sim 1''.5$  ( $\sim 3400 \text{ AU}$  or  $0.02 \text{ pc}$ ) in order to study the fragmentation in the cloud process and cluster formation.

Next, in the following chapters we focus on the emission of dense gas tracers on scales of single clumps within molecular clouds ( $\sim 0.5 \text{ pc}$ ) observed with interferometers towards five intermediate/high-mass star-forming regions. In the previous chapter we started with one of the clumps of G14.2-0.60, presumably the youngest of our sample, and follow with other slightly more evolved clusters.

To investigate the behavior of the  $\text{NH}_3/\text{N}_2\text{H}^+$  ratio, we present in chapter 3 the

results for three high-mass star-forming regions, which have been observed in  $\text{NH}_3$  and  $\text{N}_2\text{H}^+$  with high angular resolution. All regions contain cores in different evolutionary stages, from pre-protostellar cores, to hot molecular cores, and to UCH II regions. This work will be submitted for publication to Monthly Notices of the Royal Astronomical Society, including all high-mass star forming regions studied in  $\text{NH}_3$  and  $\text{N}_2\text{H}^+$  and analyzed in the same way in order to perform a statistical analysis.

In chapter 4 we analyze the high-mass protostellar cluster AFGL 5142 observed in  $\text{N}_2\text{H}^+$  with CARMA. We study its chemical environment using additional dense gas tracers,  $\text{NH}_3$  and  $\text{HCO}^+$ , from works in the literature. We first constrain the physical parameters of the region and then we performed the chemical modeling using the time-dependent chemical model UCL\_CHEM. This work, entitled  *$\text{N}_2\text{H}^+$  depletion toward the massive protostellar cluster AFGL 5142*, and authored by G. Busquet, R. Estalella, Q. Zhang, S. Viti, A. Palau, P. T. P. Ho, and Á. Sánchez-Monge, has been accepted for publication to Astronomy and Astrophysics.

In chapter 5 we show the results of an intermediate/high-mass star-forming region, observed with the Plateau de Bure Interferometer (PdBI) in deuterated ammonia. Using the  $\text{NH}_3$  data from the literature, we derived the deuterium fractionation,  $D_{\text{frac}}$ , from  $\text{NH}_2\text{D}/\text{NH}_3$ , a good tracer of the evolutionary stage of dense cores. This work, entitled *The  $\text{NH}_2\text{D}/\text{NH}_3$  ratio toward pre-protostellar cores around the UCH II region in IRAS 20293+3952* and authored by G. Busquet, A. Palau, R. Estalella, J. M., Girart, Á., Sánchez-Monge, S. Viti, P. T. P., Ho, and Q. Zhang, appeared in Astronomy and Astrophysics Letters, 2010, volume 517, page L6.

Finally, in chapter 6 we discuss the global results and summarize the main findings derived from this work.

In addition to the work presented in this thesis, between 2006 and 2010 I've been also involved in other projects related to the star formation field that have resulted into several publication. These are:

- López, R., Sánchez, S. F., García-Lorenzo, B., Gómez, G., Estalella, R., Riera, A., & Busquet, G. *The nature of HHL 73 from optical imaging and integral field spectroscopy*, 2008. Monthly Notices of the Royal Astronomical Society, 384, 464-476.
- Busquet, G., Palau, A., Estalella, R., Girart, J. M., Anglada, G., & Sepúlveda,

- I. *Low-mass protostars and dense cores in different evolutionary stages in IRAS 00213+6530*, 2009, *Astronomy & Astrophysics*, 506, 1183-1198.
- Palau, A., Sánchez-Monge, Á., Busquet, G., Estalella, R., Zhang, Q., Ho, P. T. P., Beltrán, M. T., & Beuther, H. *Three intermediate-mass YSOs with different properties emerging from the same natal cloud in IRAS 00117+641*, 2010, *Astronomy & Astrophysics*, 510, A5.
  - Frau, P. Girart, J. M., Beltrán, M. T., Morata, O., Masqué, J. M., Busquet, G., Alves, F. O., Sánchez-Monge, Á., Estalella, R., & Franco, G. A. P. *Young starless cores embedded in the magnetically dominated Pipe Nebula*, 2010, *Astrophysical Journal*, 723, 1665-1677.

## Chapter 2

# G14.2–0.60: an example of a large Infrared Dark Cloud at the onset of star formation

### 2.1 Introduction

The IRDC G14.2–0.60, located at a distance of 2.3 kpc (Jaffe et al. 1981) was selected on basis of the extinction features seen in the MSX images. Most of the studies performed so far toward this region focus on the brightest infrared sources of the region, IRAS 18153–1651 with a luminosity of  $\sim 1.1 \times 10^4 L_{\odot}$  (Jaffe et al. 1981) and IRAS 18152–1658, which is associated with a centimeter source (Jaffe et al. 1982), lies about  $\sim 7'$  to the south, and has a luminosity of  $\sim 3900 L_{\odot}$  (Jaffe et al. 1982). Single-dish observations show that IRAS 18153–1651 is associated with H<sub>2</sub>O maser emission (Jaffe et al. 1981; Comoretto et al. 1990; Palagi et al. 1993), CS and NH<sub>3</sub> emission (Plume et al. 1992; Anglada et al. 1996; Bronfman et al. 1996). A recent study of H<sub>2</sub>O maser emission with the VLA (Wang et al. 2006) reveals H<sub>2</sub>O maser emission in 9 different positions along the cloud, indicating that star formation is already going on in some parts of the cloud.

In this chapter we present a comprehensive study toward the IRDC G14.2–0.60 performed first with single-dish telescopes in dust continuum and dense gas tracers in order to study the physical and chemical properties of the entire cloud on large scales

( $\sim 10$  pc). Furthermore, we conducted interferometric observations of the  $\text{NH}_3$  (1,1) and (2,2) using the VLA and millimeter observations of a particular region of the cloud of  $\sim 1$  pc using the Submillimeter Array in its extended configuration, which will allow us resolve structures down to 3500 AU. The relatively close distance of G14.2-0.60 makes this region a perfect laboratory to investigate the  $\text{NH}_3$  dense gas emission at spatial resolutions of  $\sim 0.05$  pc, two times better than that reached in previous studies.

## 2.2 Observations

### 2.2.1 APEX observations

Continuum observations at  $870 \mu\text{m}$  were carried out using LABOCA bolometer array, installed on the Atacama Pathfinder EXperiment (APEX<sup>1</sup>) telescope. The array consists of 259 channels, which are arranged in 9 concentric hexagons around the central channel. The field of view (FOV) of the array is  $11'.4$ , and the angular resolution of each beam is  $18''.6 \pm 1''$ .

Our data were acquired on 2008 August 24+31 during the ESO program 081.C-0880A, under excellent weather conditions (zenith opacity values ranged from 0.15 to 0.24 at  $870\mu\text{m}$ ). Observations were performed using a spiral raster mapping. This observing mode consists of a set of spirals with radii between  $2'$  and  $3'$  at a combination of 9 and 4 raster positions separated by  $60''$  in azimuth and elevation, with an integration time of 40 seconds per spiral. This mode provides a fully sampled and homogeneously covered map in an area of  $15' \times 15'$ . The final map consisted of a mosaic of two points centered at  $\alpha(J2000) = 18^{\text{h}}18^{\text{m}}17^{\text{s}}.5$ ,  $\delta(J2000) = -16^{\circ}44'00''.0$ , and  $\alpha(J2000) = 18^{\text{h}}18^{\text{m}}17^{\text{s}}.5$ ;  $\delta(J2000) = -16^{\circ}57'00''.0$ , respectively. The total on-source integration time was  $\sim 2$  hours per position. Calibration was performed using observations of Mars as well as secondary calibrators. The absolute flux calibration uncertainty is estimated to be  $\sim 8\%$ . The telescope pointing was checked every hour, finding a rms pointing accuracy of  $2''$ . Focus settings were checked once per night and during the sunset.

---

<sup>1</sup>This work is partially based on observations with the APEX telescope. APEX is a collaboration between the Max-Planck-Institute für Radioastronomie, the European Southern Observatory, and the Onsala Space Observatory

We reduced the data using MiniCRUSH software package (see Kovács 2008). The pre-processing steps consisted of flagging dead or cross-talk channels frames with too high telescope accelerations and with unsuitable mapping speed, as well as temperature drift correction using two blind bolometers. Data reduction process included flat-fielding, opacity correction, calibration, correlated noise removal (atmospheric fluctuations seen by the whole array, as well as electronic noise originated in groups of detector channels), and de-spiking. Every scan was visually inspected to identify and discard corrupted data. The final map was smoothed to a final angular resolution of  $\sim 22''$ , and the rms noise level achieved was  $25 \text{ mJy beam}^{-1}$ .

### 2.2.2 FCRAO observations

The observations were carried out in 2004 May 30 with the 14 m Five College Radio Astronomy Observatory (FCRAO) telescope using the SEQUOIA (Second Quabbin Observatory Imaging Array) 16 beam array receiver. We used a bandwidth of 12 MHz with 60 channels to observe the  $\text{N}_2\text{H}^+$  (1–0) molecular transition centered at a frequency of 93.173 GHz, providing a spectral resolution of  $0.652 \text{ km s}^{-1}$ . The half-power beam width (HPBW) is  $\sim 58''$ . The weather conditions during the observations were good, providing averaged system temperatures of  $\sim 200 \text{ K}$ . The observations were performed using the On-The-Fly (OTF) mapping technique, covering a region of  $10' \times 20'$  at beam spacing. The map center was  $\alpha(J2000) = 18^{\text{h}}18^{\text{m}}17^{\text{s}}.5$ ;  $\delta(J2000) = -16^{\circ}51'00''$ . The CLASS package of IRAM was used to perform the data reduction.

### 2.2.3 Effelsberg observations

The  $\text{NH}_3$  ( $J, K$ ) = (1,1) and (2,2) observations were carried out in 2008 April 4–7 with the Effelsberg 100 m telescope of the Max-Planck-Institut für Radioastronomie. At the observed wavelength of 1.3 cm, the HPBW of the telescope is  $40''$ . We used the 18–26 GHz HEMT receiver with the 16384 channel Fast Fourier Transform Spectrometer (FFTS), allowing the simultaneous observations of  $\text{NH}_3$  (1,1) and (2,2). The total bandwidth used was 100 MHz, which provides a velocity resolution of  $0.075 \text{ km s}^{-1}$ . The observations were conducted in frequency switching mode with a frequency throw of 7.5 MHz. The map covered an area of  $8' \times 13'$  and was made by observing the positions of a grid with half-beam spacing between points ( $20''$ ). The

map center was  $\alpha(J2000) = 18^{\text{h}}18^{\text{m}}14^{\text{s}}05$ ;  $\delta(J2000) = -16^{\circ}56'59''$ . Pointing was checked at roughly hourly intervals by means of continuum drift scans on nearby pointing sources. The pointing accuracy was estimated to be better than  $6 - 8''$ . The data reduction was performed using the CLASS package, which is part of the Gildas software.

### 2.2.4 VLA observations

The observations of the  $(J, K) = (1, 1)$  and  $(J, K) = (2, 2)$  inversion transition lines of the ammonia molecule were conducted using the Very Large Array (VLA) of the NRAO<sup>2</sup> in the D configuration on 2005 November 12. We performed a 34-pointing mosaic covering an  $7' \times 13'$  region. The integration time was about 9 minutes per pointing. The adopted flux density of the absolute calibrator 1331+305 (3C 286) was 2.41 Jy at a wavelength of 1.3 cm. The time variation of the gains was calibrated by quasar 1832-105, with a bootstrapped flux of  $0.97 \pm 0.01$  Jy, and the bandpass calibrator used was 1229+020 (3C 273).

We used the 4IF spectral line mode that splits the 256 channel correlator into four sections to allow simultaneous observations of the  $\text{NH}_3$  (1, 1) and (2, 2) lines with two circular polarizations for each line. The bandwidth used was 3.12 MHz, with 63 channels and a channel separation of 48.8 kHz ( $\sim 0.6 \text{ km s}^{-1}$  at the line frequency), centered at  $\sim 21 \text{ km s}^{-1}$ , plus a continuum channel that contains the average of the central 75 % of the bandwidth. The visibility data sets were calibrated using the AIPS software package of the NRAO. Imaging was performed following the standard procedures of mosaicing in the Multichannel Image Reconstruction Image Analysis and Display (MIRIAD; Sault et al. 1995). The average rms of the final images is  $\sim 6.4 \text{ mJy beam}^{-1}$  per 48.8 KHz wide channel. The synthesized beam of the naturally-weighted map is about  $5''.22 \times 4''.15$ , P.A. =  $-11.9^\circ$ . In order to recover extended structures filtered out by the interferometer, we combined the visibility data from the VLA with the Effelsberg 100 m single-dish data for both  $\text{NH}_3$  (1, 1) and  $\text{NH}_3$  (2, 2) lines following the MIRIAD procedure outlined in Vogel et al. (1984). The resulting synthesized beam was  $5''.44 \times 3''.60$ , with a position angle of  $-29.49^\circ$ , and the rms achieved was  $\sim 5.3 \text{ mJy beam}^{-1}$  per channel.

---

<sup>2</sup>The VLA is operated by the National Radio Astronomy Observatory (NRAO), a facility of the National Science Foundation operated under cooperative agreement by Associated Universities, Inc.

### 2.2.5 SMA observations

The observations were carried out with the SMA<sup>3</sup> (Ho et al. 2004) with 8 antennas in the compact configuration on 2008 June 29, and in the extended configuration in 2008 July 21. We performed a 3–pointing mosaic covering an area of  $2' \times 1'$ , which encompasses the southern NH<sub>3</sub> cores of the cloud.

For the compact configuration the receivers were tuned to an LO frequency of 221.982 GHz to cover rest frequencies from 216 through 218 GHz in the LSB, and 226 through 228 GHz in the USB to observe the SiO (5–4), DCO<sup>+</sup> (3–2), and DCN (3–2) molecular transitions. For the extended configuration, the receivers were tuned to an LO of 225.415 GHz, providing rest frequencies ranging from 219.5 to 221.5 GHz in the LSB, and from 229.4 to 231.4 GHz in the USB to observe the CO (2–1) transition and its isotopologues. For both configurations the correlator was set to a standard mode, providing a uniform channel spacing of 0.406 MHz (or 0.52 km s<sup>−1</sup> per channel) across the full bandwidth of 2 GHz. The primary beam size (half-power beamwidth) of the SMA 6 m diameter antennas at 221 GHz is about 57", and that at 230 GHz is about 54". The zenith opacity ( $\tau_{225 \text{ GHz}}$ ), measured with the National Radio Astronomy Observatory (NRAO) tipping radiometer located at the Caltech Submillimeter Observatory, was very stable, 0.2 during the first run (June 29), and around 0.08–0.09 during the second run (July 21). The projected baselines range from 8 to 100 m in the compact configuration, and 10 to 160 m in the extended configuration.

The visibility data were calibrated using the standard procedures of MIRIAD. We used quasars 1733–130 and 1911–201 to calibrate time-dependent gains, and we used 3C454.3 and 3C273 to remove the gain variations across the band. Observations of Uranus provided the absolute scale for the flux density calibration. The continuum was constructed from the line-free channels in the visibility domain. We combined the continuum data from both configurations yielding a synthesized beam of about  $1''.52 \times 1''.42$ , P.A.= 35°. The rms noise level achieved was  $\sim 1$  mJy beam<sup>−1</sup>. Here we will present only the results obtained from the continuum data.

---

<sup>3</sup>The Submillimeter Array is a joint project between the Smithsonian Astrophysical Observatory and the Academia Sinica Institute of Astronomy and Astrophysics, and is funded by the Smithsonian Institution and the Academia Sinica

## 2.3 Preliminary results and analysis

### 2.3.1 Dust emission

The 870  $\mu\text{m}$  continuum image of IRDC G14.2–0.60 is presented in Fig. 2.1 with the zooms of each part of the cloud shown in Fig. 2.2, Fig 2.3, Fig 2.4, and Fig. 2.5. With the aim of finding possible infrared sources embedded in the cloud, we searched the IRAS Catalog of Point Sources, Version 2.0 (IPAC 1986) and the *Spitzer* GLIMPSE I Spring 07' catalog surveys. In Table 2.1 we list the IRAS source found in the field, giving their position, IRAS flux densities, distance and bolometric luminosity, when available. The bolometric luminosity derived from the IRAS flux densities has been estimated using the recipe of Connelley et al. (2007). Using the photometry of the *Spitzer* GLIMPSE I Spring 07' catalog and following the same criteria used by Qiu et al. (2008) to classify the YSOs in the IRAC color-color diagram we assigned a different color according to the [3.6]–[4.5] vs. [5.8]–[8.0] color-color diagram:

- Blue for  $0.2 < [3.6] - [4.5] < 0.8$  and  $0.4 < [5.8] - [8.0] < 1.1$ , corresponding to Class II objects.
- Yellow for  $[5.8] - [8.0] > 1.1$  and  $0.2 < [3.6] - [4.5] < 0.4$ , corresponding to Class I/II objects.
- Red for protostars (Class 0 and Class I objects), which have  $[3.6] - [4.5] > 0.8$  and  $[5.8] - [8.0] > 0.2$ , or,  $[3.6] - [4.5] \gtrsim 0.4$  and  $[5.8] - [8.0] > 1.1$ .

As can be seen in Fig. 2.1 the dust emission sometimes follows filamentary structures and displays many compact fragments or clumps, following the 8  $\mu\text{m}$  absorption feature very well. The cloud extends over about 21', i. e., about 14 pc at the cloud's distance. We separated the large scale structures in five main regions, labeled as G14.33–0.64, G14.2–0.60 North, G14.2–0.60 East, G14.2–0.60 West, and G14.2–0.60 South. In addition, within each main region, we made a complete census of the 870  $\mu\text{m}$  clumps, where a clump is defined if at least the  $6\sigma$  level is closed. Table 2.2 lists the name, position, peak intensity, flux density, and deconvolved size for each clump labeled in Figs. 2.2, 2.3, Fig 2.4, and 2.5.

We used the  $\text{NH}_3$  data to estimate the temperature of each clump and ultimately derive its mass. To do so, we first convolved the  $\text{NH}_3$  data (taking into account the

Table 2.1: IRAS sources in the LABOCA field of view

| IRAS Source | $\alpha(J2000)$<br>(h:m:s) | $\delta(J2000)$<br>( $^{\circ}$ : $'$ : $''$ ) | $d$<br>(kpc)     | F <sub>12</sub><br>(Jy) | F <sub>25</sub><br>(Jy) | F <sub>60</sub><br>(Jy) | F <sub>100</sub><br>(Jy) | $L_{\text{bol}}$<br>( $L_{\odot}$ ) |
|-------------|----------------------------|--|------------------|-------------------------|-------------------------|-------------------------|--------------------------|-------------------------------------|
| 18148-1659  | 18:17:42.2                 | -16:57:54                                      | ...              | 3.64                    | < 9.72                  | < 29.9                  | < 950                    | 4000 <sup>a</sup>                   |
| 18149-1701  | 18:17:50.7                 | -16:59:55                                      | ...              | 3.11                    | < 9.72                  | <145                    | 923                      | 4600 <sup>a</sup>                   |
| 18150-1656  | 18:17:58.9                 | -16:55:05                                      | ...              | < 3.97                  | 1.64                    | <145                    | < 1230                   | 5600 <sup>a</sup>                   |
| 18151-1645  | 18:18:00.7                 | -16:44:18                                      | ...              | <3.42                   | < 3.30                  | 14.4                    | < 139                    | 750 <sup>a</sup>                    |
| 18152-1658  | 18:18:09.4                 | -16:57:15                                      | 2.3 <sup>c</sup> | < 2.49                  | < 8.15                  | 145                     | 646                      | 3200                                |
| 18153-1651  | 18:18:16.0                 | -16:50:39                                      | 2.3 <sup>c</sup> | 6.71                    | 32.8                    | 399                     | 1230                     | 7000 <sup>b</sup>                   |
| 18154-1655  | 18:18:20.1                 | -16:54:02                                      | ...              | 3.58                    | < 5.99                  | < 36.7                  | <1230                    | 5100 <sup>a</sup>                   |
| 18155-1705  | 18:18:26.1                 | -17:03:59                                      | ...              | <4.18                   | 3.45                    | < 37.9                  | < 458                    | 2100 <sup>a</sup>                   |
| 18155-1657  | 18:18:26.5                 | -16:56:19                                      | ...              | 2.49                    | 5.65                    | <145                    | <1230                    | 5600 <sup>a</sup>                   |
| 18157-1654  | 18:18:38.5                 | -16:53:33                                      | ...              | <3.58                   | 5.99                    | 34.4                    | <2820                    | 11100 <sup>a</sup>                  |
| 18159-1648  | 18:18:53.5                 | -16:47:39                                      | 2.5 <sup>d</sup> | <6.43                   | 56                      | 994                     | 2820                     | 20500                               |

**Notes.** <sup>a</sup> We assumed a distance of 2.4 kpc. <sup>b</sup> Note that Jaffe et al. (1981) report a far-infrared luminosity of  $1.1 \times 10^4 L_{\odot}$ . <sup>c</sup> Jaffe et al. (1981). <sup>d</sup> Molinari et al. (1996)

VLA and Effelsberg observations) to the same angular resolution as the dust emission (i. e., to a circular beam of  $22''$ ) and then we derived the rotational temperature and converted it to kinetic temperature following the same procedure as described in the Appendix. Since  $\text{NH}_3(2,2)$  is only detected in some parts of the cloud (see next section and Fig. 2.8), we were able to obtain the rotational temperature only for a few clumps. For those clumps without an accurate estimation of the rotational temperature we adopted the following criteria: *i*)  $T_{\text{d}} \sim 10\text{--}15$  K for clumps with no signpost of star formation activity (i. e., neither maser emission nor infrared sources embedded within it); *ii*)  $T_{\text{d}} \sim 15\text{--}25$  K for clumps containing *Spitzer* infrared sources and/or associated with maser emission; and *iii*)  $T_{\text{d}} \sim 50$  K for clumps associated with bright IRAS sources. In cold and dense clouds like IRDCs dust grains are supposed to be coagulated and covered of icy mantles (Peretto and Fuller 2009), so we derived the mass by adopting a dust mass opacity coefficient at  $870 \mu\text{m}$  of  $1.7 \text{ g cm}^{-1}$ , which corresponds to agglomerated grains with thick ice mantles in cores of densities  $\sim 10^5 \text{ cm}^{-3}$  (Ossenkopf and Henning 1994), and assuming that the dust emission at  $870 \mu\text{m}$  is optically thin, a gas-to-dust ratio of 100, and the dust temperature given in Col. (8) of Table 2.2. The derived masses are reported in Col. (9) of Table 2.2. Additionally, we list in Cols. (10) and (11) the association with  $\text{H}_2\text{O}$  maser emission or with and infrared source.

We identified 74 clumps, with masses ranging from  $11 M_{\odot}$  to  $1000 M_{\odot}$ , and clump sizes in the range of 0.2–1.2 pc. The mean mass is  $\sim 133 M_{\odot}$ , and the mean radii is  $\sim 0.37$  pc. The total mass of the IRDC G14.2–0.60, excluding the region G14.33–0.69, and assuming a dust temperature  $T_d \sim 35$  K, is estimated to be  $\sim 5480 M_{\odot}$ .

Considering a spherically symmetric structure we derive the molecular hydrogen volume density and the column density traced by dust using equations  $n = M / (\frac{4}{3}\pi R^3 \mu m_H)$  and  $N(\text{H}_2) = M / (A \mu m_H)$ , respectively, where  $\mu = 2.8$  is the mean molecular weight per  $\text{H}_2$  molecule and  $m_H$  is the hydrogen mass. In Table 2.3 we present the main results obtained for each clump, giving the density, column density, and visual extinction  $A_V$ , where the visual extinction has been obtained using the relation  $A_V = 1.258 \times 10^{-21} N(\text{H}_2)$  (Wagenblast and Hartquist 1989). The mean values for the density, column density, and visual extinction are  $1.6 \times 10^4 \text{ cm}^{-3}$ ,  $1.8 \times 10^{22} \text{ cm}^{-2}$ , and 23 magnitudes, respectively.

Moreover, for each clump we have computed the mass surface density  $\Sigma = \frac{M}{\pi R^2}$  (Krumholz and McKee 2008), and the result is shown in Col. (5) of Table 2.3. As can be seen in this table the values of the surface density  $\Sigma$  are in the range  $\sim 0.01 - 0.5 \text{ g cm}^{-2}$ , with a mean value of  $0.1 \text{ g cm}^{-2}$ . We found that none of the clumps in G14.2–0.60 have a surface density above the theoretical value of  $0.7 \text{ g cm}^{-2}$  required for high-mass star formation according to Krumholz and McKee (2008). López-Sepulcre et al. (2010) recently conducted a comparative study of 49 high-mass cluster forming clumps, selected from the survey of Rathborne et al. (2006), Beuther et al. (2002a), Faúndez et al. (2004), and Hill et al. (2005), and also find that the majority of the clumps lie below this threshold. However, as already pointed out by the López-Sepulcre et al. (2010), these results could be a consequence of clumps actually containing smaller and denser cores not resolved by the single-dish telescopes (see section 2.3.3 and 2.4.3 for further discussion). Actually, when observing clump SMM10 with the SMA the surface density of some millimeter condensations lies above the  $0.7 \text{ g cm}^{-2}$  threshold of Krumholz and McKee (2008).

Recently, Kauffmann and Pillai (2010) establish a mass-size threshold for massive star formation,  $m(r) > 870 M_{\odot} (r/\text{pc})^{1.33}$ , a new assessment of the ability of IRDCs to form massive stars and star clusters. IRDCs below this limit might still form stars and clusters of up to intermediate mass. Then, we used this relation to estimate the fraction of clumps in G14.2–0.60 that will form massive stars. For

each cloud fragment (i. e., clump) we derived the mass ratio  $m(r)/m_{\text{lim}}(r)$ , where  $m_{\text{lim}}(r) = 870M_{\odot} (r/pc)^{1.33}$  is the limiting mass, and the result is reported in Col. (6) of Table 2.3. Then, only clumps with masses exceeding the limiting mass are supposed to be candidates to form massive stars. Taking into account only clumps resolved by APEX, we found that in G14.2–0.60 only 10 clumps out of 43 (S7, S8, S10, W6, W10, W11, W12, W24, N1, and G1) follow this relation (i. e., they exceed the limiting mass  $m_{\text{lim}}(r)$ ). This means that only a small fraction of clumps in the IRDC G14.2–0.60, around  $\sim 23$  %, might form high-mass stars.

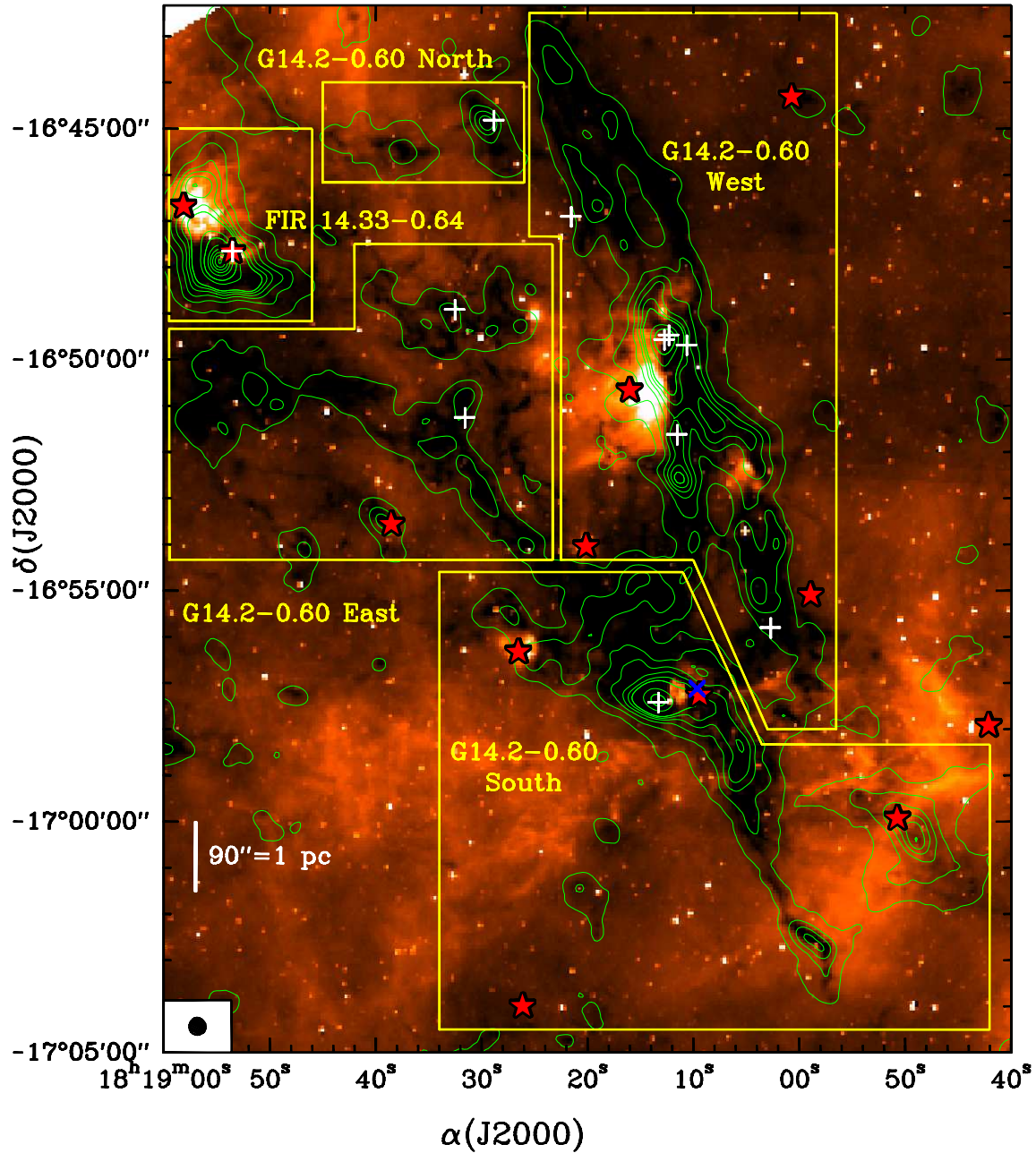


Figure 2.1: 870  $\mu\text{m}$  submillimeter continuum image of the IRDC G14.2-0.60 (contours) obtained with LABOCA bolometer array at the APEX telescope overlaid on the *Spitzer* 8  $\mu\text{m}$  image (color scale). Contour levels range from 3 to  $53\sigma$  in steps of  $10\sigma$ , from 53 to  $153\sigma$  in steps of  $50\sigma$ , and from 153 to  $653\sigma$  in steps of  $100\sigma$ , where  $\sigma$  is the rms of the map,  $25 \text{ mJy beam}^{-1}$ . White crosses mark  $\text{H}_2\text{O}$  maser emission (Wang et al. 2006; Jaffe et al. 1981) and the blue tilted cross indicates the position of a centimeter source associated with IRAS 18152-1658 (Jaffe et al. 1982). IRAS sources in the field are indicated by red stars. The beam size, of  $22''$ , is shown in the bottom left corner of the image.

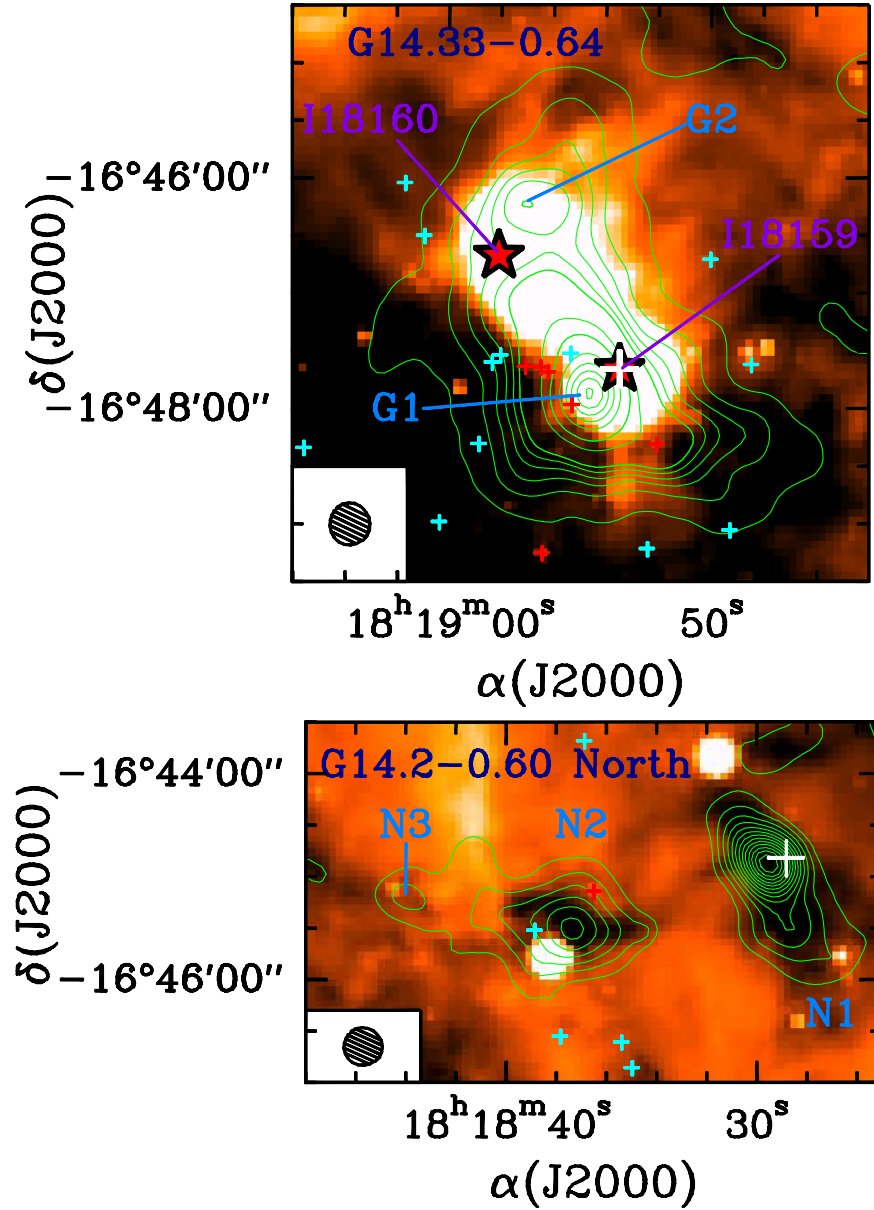


Figure 2.2: 870  $\mu\text{m}$  dust emission maps (contours) of G14.33-0.62 (*Top*) and G14.2-0.60 North (*Bottom*) overlaid on the *Spitzer* GLIMPSE 24  $\mu\text{m}$  image. *Top*: Contour levels range from 3 to  $53\sigma$  in steps of  $10\sigma$ , from 53 to  $153\sigma$  in steps of  $50\sigma$ , and from 153 to  $653\sigma$  in steps of  $100\sigma$ , where  $\sigma$  is the rms of the map,  $25 \text{ mJy beam}^{-1}$ . *Bottom*: Contour levels range from 3 to  $39\sigma$  in steps of  $3\sigma$ , where  $\sigma$  is the rms of the map,  $25 \text{ mJy beam}^{-1}$ . White crosses indicate the position of  $\text{H}_2\text{O}$  maser emission. Red stars mark the position of IRAS 18159-1648 and IRAS 18160-1647. Clumps detected in LABOCA images are labeled and indicated in each plot. Small red and blue crosses represent infrared sources detected by *Spitzer* IRAC bands, with the color corresponding to different infrared excess as explained in the text. In both images, the beam size of  $22''$  is shown in the bottom left corner.

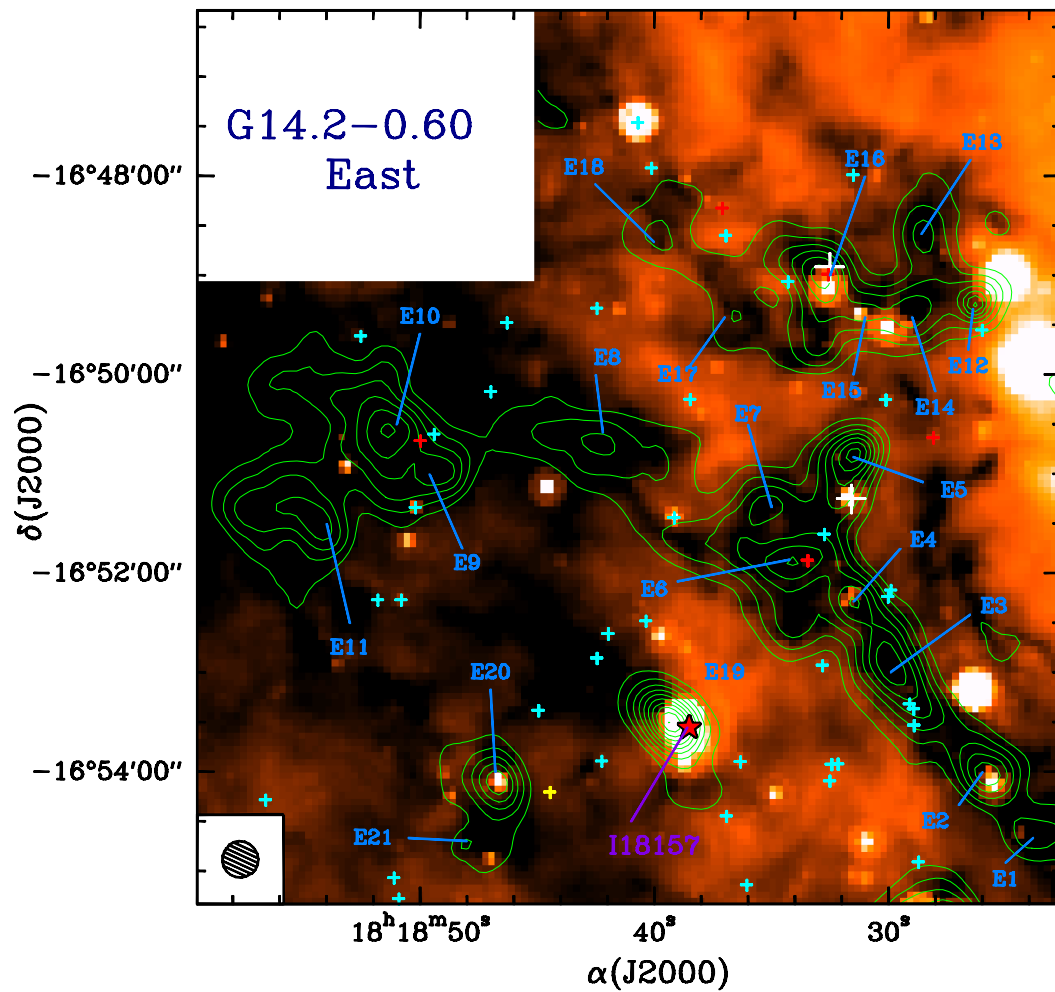


Figure 2.3: Same convention as Fig. 2.2 for LABOCA maps of G14.2-0.60 East. Contour levels range from  $3$  to  $39\sigma$  in steps of  $3\sigma$ , where  $\sigma$  is the rms of the map,  $25 \text{ mJy beam}^{-1}$ .

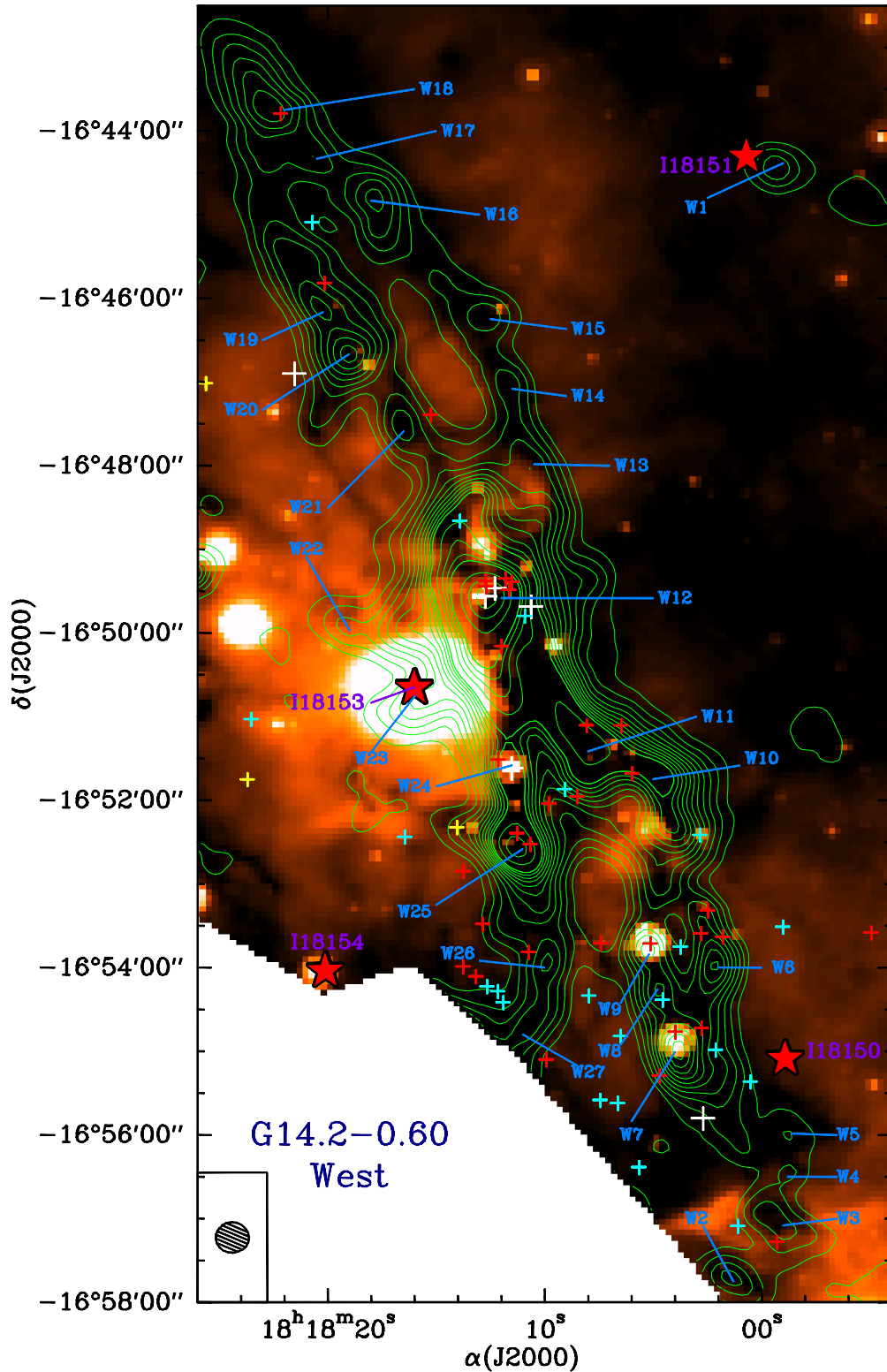


Figure 2.4: Same convention as Fig. 2.2 for LABOCA maps of G14.2-0.60 West. Contour levels range from  $3$  to  $33\sigma$  in steps of  $3\sigma$ , from  $33$  to  $73\sigma$  in steps of  $10\sigma$ , and from  $73$  to  $273\sigma$  in steps of  $50\sigma$ , where  $\sigma$  is the rms of the map,  $25 \text{ mJy beam}^{-1}$ .

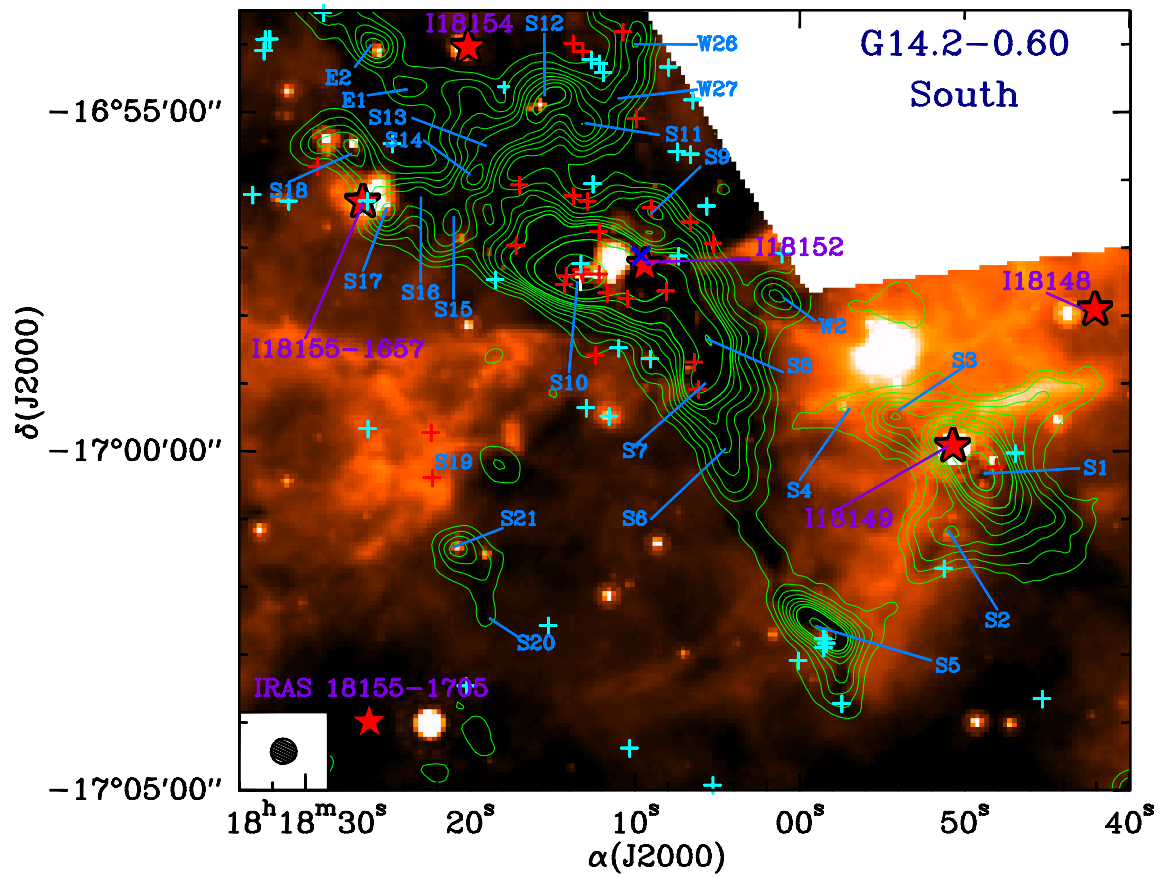


Figure 2.5: Same convention as Fig. 2.2 for LABOCA maps of G14.2-0.60 South. Contour levels range from  $3$  to  $24\sigma$  in steps of  $3\sigma$ , from  $24$  to  $44\sigma$  in steps of  $10\sigma$ , and from  $44$  to  $144\sigma$  in steps of  $50\sigma$ , where  $\sigma$  is the rms of the map,  $25 \text{ mJy beam}^{-1}$ .

Table 2.2: Submillimeter clumps in the IRDC G14.2-0.60

| (1)                | (2)             | (3)             | (4)                      | (5)        | (6)               | (7)       | (8)                       | (9)             | (10)             | (11)         |
|--------------------|-----------------|-----------------|--------------------------|------------|-------------------|-----------|---------------------------|-----------------|------------------|--------------|
| Clump              | $\alpha(J2000)$ | $\delta(J2000)$ | $I_{\nu}^{\text{peak}}$  | $S_{\nu}$  | Size <sup>a</sup> |           | $T_{\text{d}}^{\text{b}}$ | $M$             | H <sub>2</sub> O | IRAS/Spitzer |
| Name               | (h:m:s)         | (°:':")         | (Jy beam <sup>-1</sup> ) | (Jy)       | (arcsec)          | (pc)      | (K)                       | ( $M_{\odot}$ ) | maser            | source       |
| <i>G14.2 South</i> |                 |                 |                          |            |                   |           |                           |                 |                  |              |
| SMMS1              | 18 17 48.9      | -17 00 22       | 1.34±0.28                | 16.42±1.55 | 104×49.6          | 1.16×0.55 | 50                        | 158.8           | N                | Y            |
| SMMS2              | 18 17 50.9      | -17 01 10       | 0.39±0.09                | 1.98±0.22  | ...               | ...       | 15-25                     | 98.3-45.9       | N                | Y            |
| SMMS3              | 18 17 54.2      | -16 59 30       | 0.46±0.10                | 1.94±0.26  | 59.6×33.8         | 0.66×0.38 | 15-25                     | 96.3-48.9       | N                | Y            |
| SMMS4              | 18 17 55.9      | -16 59 26       | 0.17±0.03                | 0.32±0.04  | ...               | ...       | 15-25                     | 15.9-7.4        | N                | Y            |
| SMMS5              | 18 17 58.9      | -17 02 34       | 0.89±0.22                | 5.93±0.87  | 66.8×26.4         | 0.74×0.29 | 15-25                     | 294.4-137.2     | N                | Y            |
| SMMS6              | 18 18 04.5      | -16 59 50       | 0.41±0.09                | 1.72±0.23  | ...               | ...       | 10-15                     | 179.5-85.4      | N                | N            |
| SMMS7              | 18 18 05.9      | -16 58 54       | 1.01±0.15                | 3.52±0.51  | ...               | ...       | 17                        | 142.9           | N                | Y            |
| SMMS8              | 18 18 05.6      | -16 58 18       | 1.11±0.23                | 6.73±0.59  | ...               | ...       | 13                        | 426.7           | N                | N            |
| SMMS9              | 18 18 08.7      | -16 56 30       | 0.49±0.06                | 1.37±0.15  | 64.7×24.7         | 0.72×0.28 | 15-25                     | 68.0-31.7       | N                | Y            |
| SMMS10             | 18 18 13.2      | -16 57 22       | 4.47±0.79                | 36.45±4.11 | 89.7×39.3         | 1.00×0.33 | 21                        | 1077.5          | Y                | Y            |
| SMMS11             | 18 18 13.2      | -16 55 10       | 0.53±0.10                | 1.47±0.23  | 43.1×37.4         | 0.48×0.42 | 10-15                     | 153.4-73.9      | N                | N            |
| SMMS12             | 18 18 14.9      | -16 54 46       | 0.67±0.15                | 3.53±0.32  | 68.7×43.0         | 0.77×0.48 | 12                        | 258.6           | N                | Y            |
| SMMS13             | 18 18 17.9      | -16 55 22       | 0.52±0.09                | 1.30±0.12  | ...               | ...       | 10-15                     | 135.7-64.5      | N                | Y            |
| SMMS14             | 18 18 19.6      | -16 55 58       | 0.58±0.11                | 1.58±0.14  | ...               | ...       | 10-15                     | 164.9-78.4      | N                | N            |
| SMMS15             | 18 18 21.0      | -16 56 38       | 0.49±0.09                | 1.84±0.18  | 58.4×43.0         | 0.65×0.48 | 10-15                     | 192.1-91.4      | N                | N            |
| SMMS16             | 18 18 22.9      | -16 56 14       | 0.43±0.07                | 0.75±0.06  | ...               | ...       | 10-15                     | 78.3-37.2       | N                | N            |
| SMMS17             | 18 18 25.2      | -16 56 30       | 0.49±0.09                | 1.52±0.21  | 41.9×32.6         | 0.47×0.36 | 50                        | 14.7            | N                | Y            |
| SMMS18             | 18 18 27.1      | -16 55 30       | 0.42±0.07                | 1.50±0.15  | 66.0×33.3         | 0.74×0.37 | 10-15                     | 145.6-74.9      | N                | Y            |
| SMMS19             | 18 18 18.2      | -17 00 10       | 0.16±0.04                | 0.30±0.05  | 35.2×15.9         | 0.39×0.18 | 10-15                     | 31.3-15.9       | N                | Y            |
| SMMS20             | 18 18 19.0      | -17 02 22       | 0.11±0.03                | 0.15±0.09  | ...               | ...       | 10-15                     | 15.6-7.4        | N                | N            |
| SMMS21             | 18 18 20.7      | -17 01 38       | 0.36±0.08                | 1.98±0.22  | 49.6×25.4         | 0.55×0.28 | 15-25                     | 98.3-45.8       | N                | Y            |
| <i>G14.2 West</i>  |                 |                 |                          |            |                   |           |                           |                 |                  |              |
| SMMW1              | 18 17 59.3      | -16 44 26       | 0.29±0.06                | 0.47±0.01  | 20.0×15.6         | 0.22×0.17 | 10-15                     | 49.1-23.3       | N                | Y            |
| SMMW2              | 18 18 01.5      | -16 57 42       | 0.33±0.07                | 0.99±0.14  | 38.6×29.5         | 0.43×0.33 | 12                        | 72.5            | N                | N            |
| SMMW3              | 18 17 59.5      | -16 56 58       | 0.28±0.06                | 1.05±0.15  | 57.5×29.1         | 0.64×0.32 | 15-25                     | 52.1-24.3       | N                | Y            |
| SMMW4              | 18 17 58.7      | -16 56 26       | 0.16±0.03                | 0.22±0.03  | ...               | ...       | 10-15                     | 22.9-10.9       | N                | N            |
| SMMW5              | 18 17 58.7      | -16 56 02       | 0.15±0.03                | 0.29±0.05  | ...               | ...       | 10-15                     | 30.3-14.4       | N                | N            |

Continued on Next Page...

Table 2.2 – Continued

| (1)               | (2)        | (3)       | (4)       | (5)        | (6)        | (7)       | (8)   | (9)         | (10) | (11) |
|-------------------|------------|-----------|-----------|------------|------------|-----------|-------|-------------|------|------|
| SMMW6             | 18 18 02.0 | -16 53 58 | 0.61±0.11 | 2.27±0.29  | 53.3×17.9  | 0.59×0.20 | 10    | 236.9       | N    | Y    |
| SMMW7             | 18 18 03.7 | -16 54 58 | 0.79±0.16 | 3.47±0.45  | 58.7×31.9  | 0.65×0.36 | 13    | 220.0       | N    | Y    |
| SMMW8             | 18 18 04.8 | -16 54 14 | 0.29±0.07 | 1.04±0.15  | ...        | ...       | 10    | 108.6       | N    | Y    |
| SMMW9             | 18 18 05.1 | -16 53 46 | 0.57±0.12 | 1.17±0.22  | 41.1×17.3  | 0.46×0.19 | 16    | 52.3        | N    | Y    |
| SMMW10            | 18 18 04.8 | -16 51 42 | 0.95±0.18 | 3.07±0.34  | ...        | ...       | 12    | 224.9       | N    | N    |
| SMMW11            | 18 18 07.9 | -16 51 22 | 1.23±0.23 | 6.82±0.55  | ...        | ...       | 14    | 380.2       | N    | Y    |
| SMMW12            | 18 18 12.6 | -16 49 34 | 6.41±1.33 | 22.73±3.82 | 55.6×32.1  | 0.62×0.36 | 19    | 778.5       | Y    | Y    |
| SMMW13            | 18 18 10.7 | -16 48 02 | 0.38±0.07 | 0.68±0.07  | ...        | ...       | 18    | 25.3        | N    | N    |
| SMMW14            | 18 18 11.8 | -16 47 02 | 0.28±0.06 | 0.63±0.11  | ...        | ...       | 10–15 | 65.8–31.3   | N    | N    |
| SMMW15            | 18 18 12.7 | -16 46 14 | 0.29±0.06 | 0.79±0.09  | 43.2×30.6  | 0.48×0.34 | 10–15 | 82.5–39.3   | N    | N    |
| SMMW16            | 18 18 17.9 | -16 44 50 | 0.40±0.08 | 1.59±0.21  | 61.2×26.5  | 0.68×0.30 | 10–15 | 165.9–78.9  | N    | N    |
| SMMW17            | 18 18 20.7 | -16 44 18 | 0.30±0.04 | 0.59±0.07  | ...        | ...       | 10–15 | 61.6–29.3   | N    | N    |
| SMMW18            | 18 18 22.6 | -16 43 42 | 0.52±0.12 | 2.94±0.31  | 81.3×31.4  | 0.91×0.35 | 15–25 | 146.0–68.0  | N    | Y    |
| SMMW19            | 18 18 20.4 | -16 46 06 | 0.47±0.08 | 1.83±0.18  | ...        | ...       | 15–25 | 90.9–42.3   | N    | Y    |
| SMMW20            | 18 18 19.0 | -16 46 42 | 0.64±0.12 | 2.35±0.28  | 43.9×38.3  | 0.49×0.43 | 15–25 | 116.7–54.4  | N    | Y    |
| SMMW21            | 18 18 16.5 | -16 47 30 | 0.35±0.06 | 1.05±0.13  | 58.2×20.4  | 0.65×0.23 | 10–15 | 109.6–52.1  | N    | N    |
| SMMW22            | 18 18 19.0 | -16 49 54 | 0.25±0.05 | 1.12±0.15  | ...        | ...       | 15–25 | 55.6–25.9   | N    | Y    |
| SMMW23            | 18 18 15.4 | -16 50 46 | 0.42±0.10 | 1.23±0.17  | ...        | ...       | 50    | 11.9        | N    | Y    |
| SMMW24            | 18 18 11.5 | -16 51 42 | 1.01±0.14 | 3.16±0.24  | ...        | ...       | 15    | 156.9       | Y    | Y    |
| SMMW25            | 18 18 11.2 | -16 52 34 | 1.48±0.33 | 4.76±0.63  | 45.8×26.4  | 0.51×0.29 | 16    | 212.8       | N    | Y    |
| SMMW26            | 18 18 09.8 | -16 53 58 | 0.39±0.06 | 0.95±0.15  | ...        | ...       | 14    | 52.9        | N    | Y    |
| SMMW27            | 18 18 10.7 | -16 54 38 | 0.35±0.05 | 0.61±0.09  | ...        | ...       | 12    | 44.7        | N    | N    |
| <i>G14.2 East</i> |            |           |           |            |            |           |       |             |      |      |
| SMME1             | 18 18 23.8 | -16 54 38 | 0.19±0.04 | 0.46±0.06  | ...        | ...       | 15    | 22.8        | N    | N    |
| SMME2             | 18 18 25.7 | -16 54 02 | 0.44±0.10 | 1.18±0.21  | 37.5×18.3  | 0.42×0.20 | 14    | 65.8        | N    | Y    |
| SMME3             | 18 18 29.9 | -16 52 54 | 0.51±0.12 | 2.51±0.31  | 83.5×25.7  | 0.93×0.29 | 10–15 | 262.0–124.6 | N    | N    |
| SMME4             | 18 18 31.6 | -16 52 18 | 0.46±0.20 | 1.21±0.14  | ...        | ...       | 15–25 | 60.1–28.0   | N    | Y    |
| SMME5             | 18 18 31.6 | -16 50 50 | 0.56±0.13 | 1.71±0.24  | 53.1×21.8  | 0.59×0.24 | 10–15 | 178.5–84.9  | Y    | Y    |
| SMME6             | 18 18 34.1 | -16 51 54 | 0.46±0.08 | 2.23±0.18  | 78.2×45.1  | 0.87×0.50 | 15–25 | 110.7–51.6  | N    | Y    |
| SMME7             | 18 18 35.2 | -16 51 18 | 0.34±0.07 | 1.14±0.13  | ...        | ...       | 10–15 | 119.0–56.6  | N    | N    |
| SMME8             | 18 18 42.2 | -16 50 42 | 0.25±0.03 | 1.71±0.12  | 112.6×36.5 | 1.26×0.41 | 10–15 | 178.5–84.9  | N    | N    |

Continued on Next Page...

Table 2.2 – Continued

| (1)                | (2)         | (3)         | (4)        | (5)         | (6)        | (7)       | (8)   | (9)         | (10) | (11) |
|--------------------|-------------|-------------|------------|-------------|------------|-----------|-------|-------------|------|------|
| SMME9              | 18 18 49.4  | −16 50 58   | 0.37±0.09  | 0.91±0.17   | 40.6×25.5  | 0.45×0.28 | 10–15 | 95.0–45.2   | N    | Y    |
| SMME10             | 18 18 51.4  | −16 50 34   | 0.46±0.10  | 3.86±0.37   | 113.2×53.9 | 1.22×0.60 | 10–15 | 402.9–191.7 | N    | N    |
| SMME11             | 18 18 54.4  | −16 51 30   | 0.35±0.08  | 2.58±0.25   | 82.2×46.6  | 0.92×0.52 | 10–15 | 269.3–128.1 | N    | N    |
| SMME12             | 18 18 26.3  | −16 49 18   | 0.55±0.12  | 0.78±0.18   | 18.9×12.5  | 0.21×0.14 | 10–15 | 81.4–38.7   | N    | N    |
| SMME13             | 18 18 28.5  | −16 48 34   | 0.26±0.06  | 0.99±0.17   | 64.6×23.4  | 0.72×0.26 | 10–15 | 103.3–49.2  | N    | N    |
| SMME14             | 18 18 29.1  | −16 49 22   | 0.35±0.07  | 1.01±0.15   | ...        | ...       | 10–15 | 105.4–50.1  | N    | N    |
| SMME15             | 18 18 31.0  | −16 49 22   | 0.33±0.07  | 0.52±0.09   | ...        | ...       | 15–25 | 25.8–12.0   | Y    | Y    |
| SMME16             | 18 18 32.9  | −16 48 58   | 0.49±0.11  | 1.98±0.24   | 71.5×46.7  | 0.79×0.52 | 15–25 | 98.3–45.8   | N    | Y    |
| SMME17             | 18 18 36.6  | −16 49 26   | 0.15±0.03  | 0.25±0.03   | ...        | ...       | 15–25 | 12.4–5.8    | N    | Y    |
| SMME18             | 18 18 39.9  | −16 48 34   | 0.17±0.04  | 0.57±0.06   | ...        | ...       | 10–15 | 59.5–28.3   | N    | N    |
| SMME19             | 18 18 39.4  | −16 53 30   | 0.75±0.18  | 2.31±0.52   | 33.9×15.7  | 0.38×0.18 | 50    | 22.3        | N    | N    |
| SMME20             | 18 18 46.6  | −16 54 06   | 0.44±0.10  | 1.24±0.24   | 31.3×20.4  | 0.35×0.23 | 15–25 | 61.6–28.7   | N    | Y    |
| SMME21             | 18 18 48.0  | −16 54 42   | 0.16±0.04  | 0.18±0.05   | ...        | ...       | 10–15 | 18.8–8.9    | N    | Y    |
| <i>G14.2 North</i> |             |             |            |             |            |           |       |             |      |      |
| SMMN1              | 18 18 29.34 | −16 44 54.0 | 1.04±0.23  | 4.21±0.77   | 47.5×20.9  | 0.53×0.23 | 10–15 | 439.4–209.1 | Y    | N    |
| SMMN2              | 18 18 37.41 | −16 45 30.0 | 0.48±0.11  | 3.39±0.38   | 70.9×41.1  | 0.79×0.46 | 15–25 | 168.3–78.4  | N    | Y    |
| SMMN3              | 18 18 44.10 | −16 45 10.0 | 0.18±0.03  | 0.40±0.06   | 38.4×19.7  | 0.43×0.22 | 15–25 | 19.9–9.3    | N    | Y    |
| <i>G14.33-0.69</i> |             |             |            |             |            |           |       |             |      |      |
| SMMG1              | 18 18 54.69 | −16 47 50.0 | 16.71±2.53 | 83.00±15.21 | 39.1×26.3  | 0.44×0.29 | 50    | 802.6       | Y    | Y    |
| SMMG2              | 18 18 56.91 | −16 46 14.0 | 1.33±0.34  | 8.84±1.11   | 55.7×43.1  | 0.62×0.48 | 50    | 85.5        | N    | Y    |

<sup>a</sup>Deconvolved size obtained from a 2d Gaussian fitting.<sup>b</sup> $T_d$  is estimated by correcting the rotational temperature from  $\text{NH}_3$  (see Sect. 5.3.2) to kinetic temperature following the expression of Tafalla et al. (2004). For clumps with bright IRAS sources we adopted  $T_d \simeq 50$  K; clumps containing *Spitzer* sources  $T_d \simeq 15$ –25 K; and  $T_d \simeq 10$ –15 K for clumps without infrared sources.

Table 2.3: Properties of the 870  $\mu\text{m}$  clumps in the IRDC G14.2-0.60

| (1)                | (2)                                      | (3)   | (4)             | (5)                                  | (6)                        |
|--------------------|--|---|-----------------|--------------------------------------|----------------------------|
| Clump              | $n$<br>( $\times 10^4 \text{ cm}^{-3}$ ) | $N(\text{H}_2)$<br>( $\times 10^{22} \text{ cm}^{-2}$ ) | $A_V$<br>(mag.) | $\Sigma^a$<br>( $\text{g cm}^{-2}$ ) | $m(r)/m_{\text{lim}}(r)^a$ |
| <i>G14.2 South</i> |  |   |                 |                                      |                            |
| SMMS1              | 0.1                                      | 0.02  | 4.4             | 0.017                                | 0.25                       |
| SMMS2              | 23.1–10.7                                | 2.3– 1.1  | 29.2–13.6       | >0.109–0.05                          | >0.73–0.34                 |
| SMMS3              | 0.3– 0.1                                 | 0.5– 0.3  | 6.8– 3.2        | 0.03–0.01                            | 0.28–13                    |
| SMMS4              | 0.4– 0.2                                 | 0.4– 0.2  | 4.7– 2.2        | >0.02–0.01                           | >0.12–0.06                 |
| SMMS5              | 1.0– 0.5                                 | 1.9– 0.9  | 24.5–11.4       | 0.09–0.04                            | 0.94–0.44                  |
| SMMS6              | 4.2– 2.0                                 | 4.2– 2.0  | 53.4–25.4       | >0.20–0.09                           | >1.34–0.64                 |
| SMMS7              | 3.4                                      | 3.4   | 42.5            | >0.158                               | >1.07                      |
| SMMS8              | 10.0                                     | 10.1  | 126.9           | >0.473                               | >3.18                      |
| SMMS9              | 2.6– 1.2                                 | 0.5– 0.2  | 6.0– 2.8        | 0.02–0.01                            | 0.23–0.11                  |
| SMMS10             | 1.9                                      | 4.5   | 58.3            | 0.217                                | 2.59                       |
| SMMS11             | 0.6– 0.3                                 | 1.1– 0.5  | 13.6– 6.5       | 0.05–0.02                            | 0.51–0.24                  |
| SMMS12             | 0.4                                      | 1.0   | 12.5            | 0.05                                 | 0.58                       |
| SMMS13             | 3.2– 1.5                                 | 3.2– 1.5  | 40.4–19.2       | >0.15–0.07                           | >1.01–0.48                 |
| SMMS14             | 3.9– 1.8                                 | 3.9– 1.8  | 49.1–23.3       | >0.18–0.09                           | >1.23–0.58                 |
| SMMS15             | 3.8– 1.8                                 | 0.9– 0.4  | 11.0– 5.2       | 0.04–0.02                            | 0.48–0.23                  |
| SMMS16             | 1.8– 0.9                                 | 1.9– 0.9  | 23.3–11.1       | >0.09–0.04                           | >0.58–0.28                 |
| SMMS17             | 0.07                                     | 0.1   | 1.6             | 0.01                                 | 0.06                       |
| SMMS18             | 0.4– 0.2                                 | 0.8– 0.4  | 10.2– 4.8       | 0.04–0.02                            | 0.43–0.20                  |
| SMMS19             | 0.6– 0.3                                 | 0.6– 0.3  | 7.9– 3.8        | 0.03–0.01                            | 0.21–0.10                  |
| SMMS20             | 0.4– 0.2                                 | 0.4– 0.2  | 4.7– 2.2        | >0.02–0.01                           | >0.12–0.06                 |
| SMMS21             | 0.6– 0.3                                 | 0.9– 0.4  | 11.4– 5.3       | 0.04–0.02                            | 0.39–0.18                  |
| <i>G14.2 West</i>  |  |   |                 |                                      |                            |
| SMMW1              | 2.3– 1.1                                 | 1.9– 0.9  | 23.4–11.1       | 0.09–0.04                            | 0.50–0.24                  |
| SMMW2              | 0.5                                      | 0.7   | 9.1             | 0.03                                 | 0.31                       |
| SMMW3              | 0.2– 0.1                                 | 0.4– 0.2  | 4.5– 2.1        | 0.02–0.01                            | 0.17–0.08                  |
| SMMW4              | 0.5– 0.3                                 | 0.5– 0.3  | 6.8– 3.2        | 0.03–0.01                            | 0.17–0.08                  |
| SMMW5              | 0.7– 0.3                                 | 0.7– 0.3  | 9.0– 4.3        | 0.03–0.02                            | 0.23–0.11                  |
| SMMW6              | 2.0                                      | 2.8   | 35.8            | 0.13                                 | 1.13                       |
| SMMW7              | 0.7                                      | 1.3   | 16.8            | 0.06                                 | 0.66                       |
| SMMW8              | 2.5                                      | 2.6   | 32.3            | >0.12                                | >0.81                      |
| SMMW9              | 0.7                                      | 0.8   | 10.7            | 0.04                                 | 0.30                       |
| SMMW10             | 5.3                                      | 5.3   | 66.7            | >0.25                                | >1.68                      |
| SMMW11             | 8.9                                      | 9.0   | 113.1           | >0.42                                | >2.84                      |
| SMMW12             | 2.6                                      | 4.9   | 62.3            | 0.23                                 | 2.43                       |
| SMMW13             | 0.6                                      | 0.6   | 7.5             | >0.03                                | >0.19                      |
| SMMW14             | 1.5– 0.7                                 | 1.6– 0.7  | 19.6– 9.3       | >0.07–0.03                           | >0.49–0.23                 |
| SMMW15             | 0.4– 0.2                                 | 0.7– 0.3  | 9.0– 4.2        | 0.03–0.02                            | 0.32–0.15                  |
| SMMW16             | 0.6– 0.3                                 | 1.1– 0.5  | 14.5– 6.9       | 0.05–0.03                            | 0.55–0.26                  |
| SMMW17             | 1.4– 0.7                                 | 1.4– 0.7  | 18.3– 8.7       | >0.07–0.03                           | >0.46–0.22                 |
| SMMW18             | 0.3– 0.1                                 | 0.7– 0.3  | 8.2– 3.8        | 0.03–0.01                            | 0.36–0.17                  |
| SMMW19             | 2.1– 1.0                                 | 2.1– 1.0  | 27.0–12.6       | >0.10–0.05                           | >0.69–0.32                 |
| SMMW20             | 0.4– 0.2                                 | 0.8– 0.4  | 9.9– 4.6        | 0.04–0.02                            | 0.38–0.12                  |
| SMMW21             | 0.7– 0.3                                 | 1.0– 0.5  | 13.1– 6.2       | 0.05–0.02                            | 0.45–0.21                  |
| SMMW22             | 1.3– 0.6                                 | 1.3– 0.6  | 16.5– 7.7       | >0.06–0.03                           | >0.42–0.19                 |
| SMMW23             | 0.3                                      | 0.3   | 3.5             | >0.01                                | >0.09                      |
| SMMW24             | 3.7                                      | 3.7   | 46.7            | >0.17                                | >1.17                      |

Continued on Next Page...

Table 2.3 – Continued

| (1)                | (2)                                      | (3)   | (4)             | (5)                                  | (6)                        |
|--------------------|--|---|-----------------|--------------------------------------|----------------------------|
| Clump              | $n$<br>( $\times 10^4 \text{ cm}^{-3}$ ) | $N(\text{H}_2)$<br>( $\times 10^{22} \text{ cm}^{-2}$ ) | $A_V$<br>(mag.) | $\Sigma^a$<br>( $\text{g cm}^{-2}$ ) | $m(r)/m_{\text{lim}}(r)^a$ |
| SMMW25             | 1.3                                      | 2.1   | 25.7            | 0.10                                 | 0.87                       |
| SMMW26             | 1.2                                      | 1.3   | 15.8            | >0.06                                | >0.39                      |
| SMMW27             | 1.0                                      | 1.1   | 13.3            | >0.05                                | >0.33                      |
| <i>G14.2 East</i>  |  |   |                 |                                      |                            |
| SMME1              | 0.5                                      | 0.5   | 6.7             | >0.03                                | >0.17                      |
| SMME2              | 0.9                                      | 1.1   | 13.9            | 0.05                                 | 0.39                       |
| SMME3              | 0.6– 0.3                                 | 1.4– 0.7  | 17.3– 8.3       | 0.06–0.03                            | 0.72–0.34                  |
| SMME4              | 1.4– 0.7                                 | 1.4– 0.7  | 17.9– 8.3       | >0.07–0.03                           | >0.45–0.21                 |
| SMME5              | 1.2– 0.5                                 | 1.8– 0.9  | 22.5–10.7       | 0.08–0.04                            | 0.75–0.36                  |
| SMME6              | 0.1– 0.06                                | 0.4– 0.2  | 4.5– 2.1        | 0.02–0.01                            | 0.22–0.10                  |
| SMME7              | 2.8– 1.3                                 | 2.8– 1.3  | 35.4–16.8       | >0.13–0.06                           | >0.89–0.42                 |
| SMME8              | 0.2– 0.1                                 | 0.5– 0.2  | 6.2– 2.9        | 0.02–0.01                            | 0.32–0.15                  |
| SMME9              | 0.7– 0.3                                 | 1.1– 0.5  | 13.5– 6.4       | 0.05–0.02                            | 0.43–0.21                  |
| SMME10             | 0.2– 0.1                                 | 0.8– 0.4  | 9.8– 4.7        | 0.04–0.02                            | 0.57–0.27                  |
| SMME11             | 0.3– 0.1                                 | 0.8– 0.4  | 10.1– 4.8       | 0.04–0.02                            | 0.51–0.24                  |
| SMME12             | 9.2– 4.4                                 | 5.5– 2.6  | 69.2–32.9       | 0.26–0.12                            | 1.22–0.58                  |
| SMME13             | 0.4– 0.2                                 | 0.8– 0.4  | 9.9– 4.7        | 0.04–0.02                            | 0.36–0.17                  |
| SMME14             | 2.5– 1.2                                 | 2.5– 1.2  | 31.4–14.9       | >0.12–0.06                           | >0.79–0.37                 |
| SMME15             | 0.6– 0.3                                 | 0.6– 0.3  | 7.7– 3.6        | >0.03–0.01                           | >0.19–0.09                 |
| SMME16             | 0.1– 0.06                                | 0.3– 0.2  | 4.3– 2.0        | 0.02–0.01                            | 0.20–0.09                  |
| SMME17             | 0.3– 0.1                                 | 0.3– 0.1  | 3.7– 1.7        | >0.01–0.006                          | >0.09–0.04                 |
| SMME18             | 1.4– 0.7                                 | 1.4– 0.7  | 17.7– 8.4       | >0.07–0.03                           | >0.44–0.21                 |
| SMME19             | 0.4                                      | 0.5   | 5.8             | 0.03                                 | 0.15                       |
| SMME20             | 0.9– 0.4                                 | 1.1 –0.5  | 13.7– 6.4       | 0.05–0.02                            | 0.38–0.18                  |
| SMME21             | 0.4– 0.2                                 | 0.4–0.2   | 13.6– 6.4       | >0.02–0.01                           | >0.14–0.07                 |
| <i>G14.2 North</i> |  |   |                 |                                      |                            |
| SMMN1              | 3.6– 1.7                                 | 5.1–2.4   | 64.4–30.6       | 0.24–0.11                            | 2.05–0.97                  |
| SMMN2              | 0.3– 0.1                                 | 0.7–0.3   | 8.3– 3.9        | 0.03–0.01                            | 0.38–0.18                  |
| SMMN3              | 0.2– 0.1                                 | 0.3–0.1   | 3.7– 1.7        | 0.01–0.007                           | 0.11–0.05                  |
| <i>G14.33-0.69</i> |  |   |                 |                                      |                            |
| SMMG1              | 6.1                                      | 8.9   | 112.3           | 0.42                                 | 3.63                       |
| SMMG2              | 0.2.                                     | 0.4   | 5.1             | 0.02                                 | 0.22                       |

<sup>a</sup>Lower limit because the clump is not resolved. The interval corresponds to the two values adopted for the temperature to compute the mass.

### 2.3.2 Dense gas emission

#### NH<sub>3</sub>

Figure 2.6 presents the integrated intensity map of the NH<sub>3</sub> (1,1) line, integrated for all the hyperfine components, obtained from the combined NH<sub>3</sub> data set (Efstelsberg and VLA) overlaid on the *Spitzer* image at 8  $\mu\text{m}$ . The dense gas traced by NH<sub>3</sub> reveals several compact cores forming extended filamentary structures and mimicking the overall morphology of the dust continuum emission (see Fig. 2.1). As can be seen in Fig. 2.7 these filaments contain chains of dense cores, distributed at somewhat regular spacings of about 40". Note, however, that the NH<sub>3</sub> mosaic does not encompass all the submillimeter clumps covered by the LABOCA field. Clearly, the high angular resolution of the NH<sub>3</sub> data allowed us to resolve the submillimeter clumps into several dense cores. These filaments are highly structured, and in some cases they appear approximately parallel. We labeled in Fig. 2.8 the most prominent filaments using a nomenclature based on its position angle. In Table 2.4 we report on the length and width of each filament. In average, we found that the length-to-width ratio of these filaments is  $\sim 7 : 1$ . It is worth noting that the filamentary structures appear to be hierarchical, from scales of 0.2 pc seen in the dust emission map to scales of 0.06 pc seen in NH<sub>3</sub> at higher angular resolution. Along each filament most of the cores appear to be elongated in the same direction as the filament, which could imply the possibility of further substructures. Similar filamentary structures are also found in well studied regions of low and high-mass star formation, such as Taurus molecular cloud (Goldsmith et al. 2008) and Orion (e. g., Wiseman and Ho 1998), and recently with Herschel towards Aquila Rift and Polaris clouds (André et al. 2010). Another interesting feature seen in Fig. 2.6 and Fig. 2.7 is the presence of NH<sub>3</sub> dense gas emission surrounding the bright infrared source IRAS 18153–1651, which strongly suggest a cavity that has been created by this luminous star in the process of clearing up its surrounding natal material.

The NH<sub>3</sub> (2,2) integrated intensity emission for the main hyperfine component is shown in Fig. 2.8. The NH<sub>3</sub> (2,2) emission is detected mainly in the strongest cores of the integrated intensity map of NH<sub>3</sub> (1,1), which also correspond to the strongest submillimeter clumps detected with the APEX telescope, mainly towards SMMS10, SMMW12, and SMMW25.

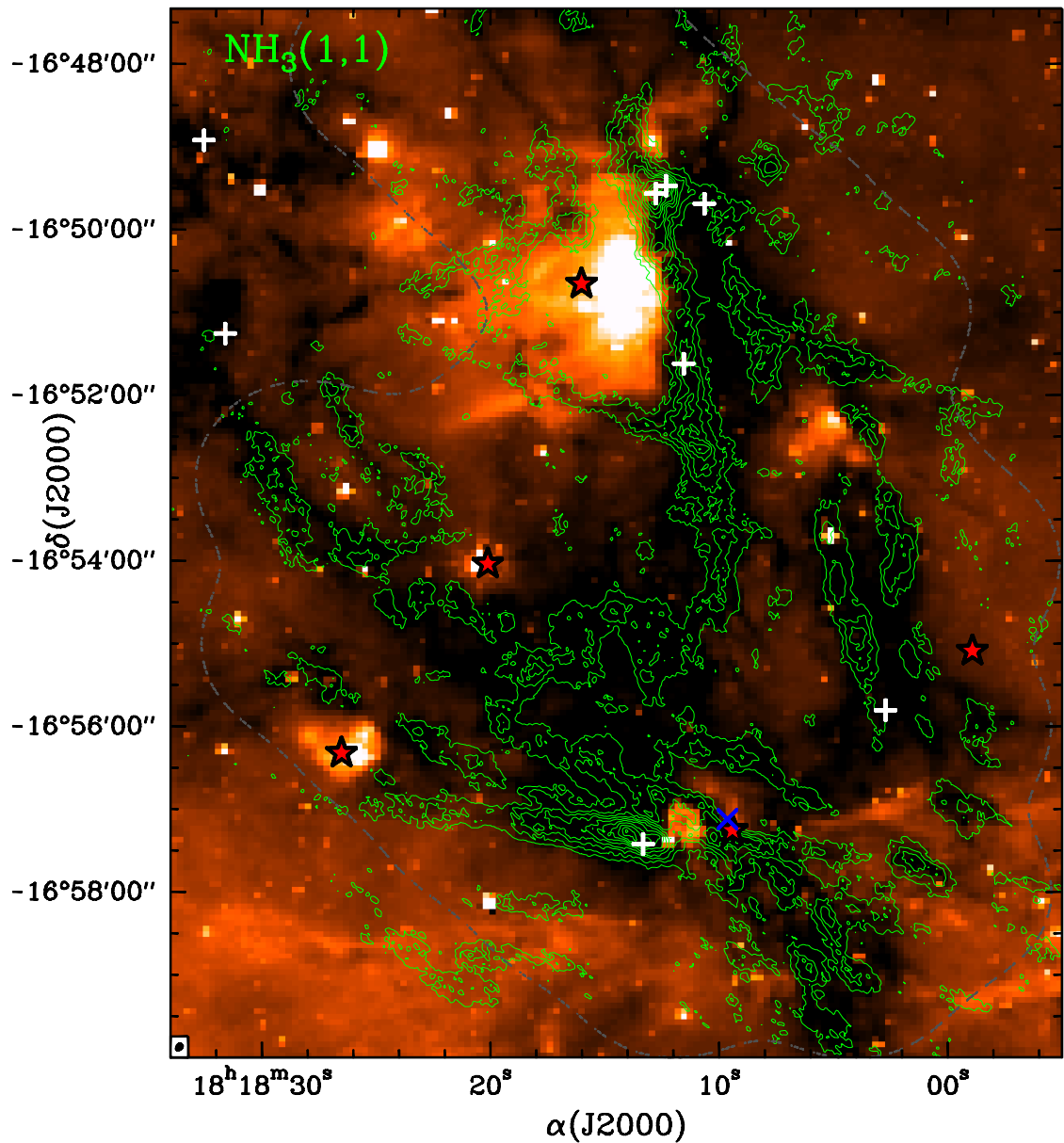


Figure 2.6: Contours: integrated intensity of the combined  $\text{NH}_3(1,1)$  emission. The  $\text{NH}_3(1,1)$  image is contoured at 8 %, increasing in steps of 10 % of the peak intensity,  $\sim 0.4 \text{ Jy beam}^{-1} \text{ km s}^{-1}$ . Color scale: *Spitzer*  $8 \mu\text{m}$  image. Symbols are the same as in previous figures. The grey dashed line indicates 50 % of the sensitivity level of the 34-pointing mosaic performed in  $\text{NH}_3$ . The synthesized beam,  $5''.44 \times 3''.60$ , P.A. =  $-29^\circ.5$ , is shown in the bottom left corner of the image.

Table 2.4: Size of each filament seen in  $\text{NH}_3(1,1)$ 

| Filament  | length<br>(pc) | width<br>(pc) | axis<br>ratio |
|-----------|----------------|---------------|---------------|
| PA12-main | 4.3            | 0.5           | 8.6           |
| PA12-1    | 2.2            | 0.3           | 7.3           |
| PA12-2    | 2.3            | 0.3           | 7.7           |
| PA61      | 3.7            | 0.5           | 7.4           |
| PA70-1    | 1.7            | 0.3           | 5.7           |
| PA70-2    | 2.3            | 0.4           | 5.8           |
| PA70-3    | 2.2            | 0.3           | 7.3           |
| PA85      | 4.0            | 0.5           | 8.0           |
| PA114     | 1.3            | 0.2           | 6.5           |

The map of the first order-moment (intensity weighted mean  $v_{\text{LSR}}$ ) of the  $\text{NH}_3(1,1)$  main line is shown in Fig. 2.9. As can be seen in this figure, all the molecular emission is essentially at the same radial velocity,  $20.5 \pm 1.8 \text{ km s}^{-1}$ , with each filamentary structure showing, in general, small variations in velocity, indicating that each individual filament is possibly a single coherent object. A similar result was found by Jackson et al. (2010) in the ‘Nessie’ Nebula, a filamentary IRDC of 81 pc length, which presents small variations in velocity along the cloud. Among the small variations, it is worth noting a global north-south gradient associated with filament PA12-main, spanning velocities of  $19.2 \text{ km s}^{-1}$  towards the northern part to  $21.5 \text{ km s}^{-1}$  in the southern part of the filament, which seems to be part of the global velocity gradient of the cloud. Another small velocity gradient can be seen in the small region in between filaments PA12-main and PA61, from  $18.6 \text{ km s}^{-1}$  to  $20.4 \text{ km s}^{-1}$ . This velocity gradient is coincident with the position of the submillimeter clump SMMS13. However, the original kinematics of the cloud is difficult to disentangle, mainly because it may be affected by stellar winds from the most luminous IRAS source, as suggested by the presence of a cavity around IRAS 18153–1651, and/or by collisions between filaments.

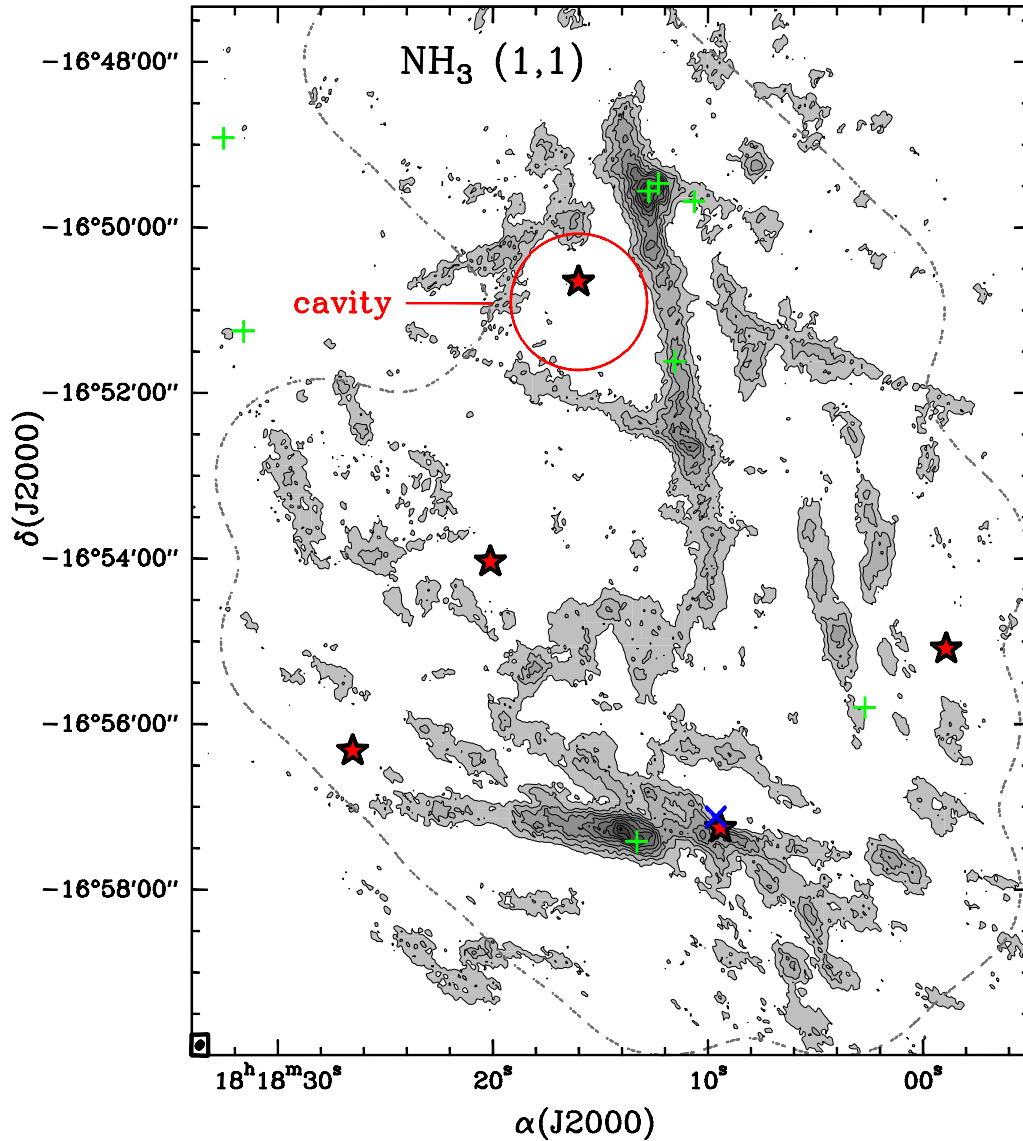


Figure 2.7: Integrated intensity of the combined  $\text{NH}_3$  (1,1) emission. The  $\text{NH}_3$  (1,1) image is contoured at 8 %, increasing in steps of 10 % of the peak intensity,  $\sim 0.4 \text{ Jy beam}^{-1} \text{ km s}^{-1}$ . Contours and symbols are the same as in previous figures, with the green crosses indicating  $\text{H}_2\text{O}$  maser emission (Wang et al. 2006; Palagi et al. 1993). The grey dashed line indicates 50 % of the sensitivity level of the 34-pointing mosaic performed in  $\text{NH}_3$ . The synthesized beam,  $5''.44 \times 3''.60$ , P.A. =  $-29^\circ.5$ , is shown in the bottom left corner of the image.

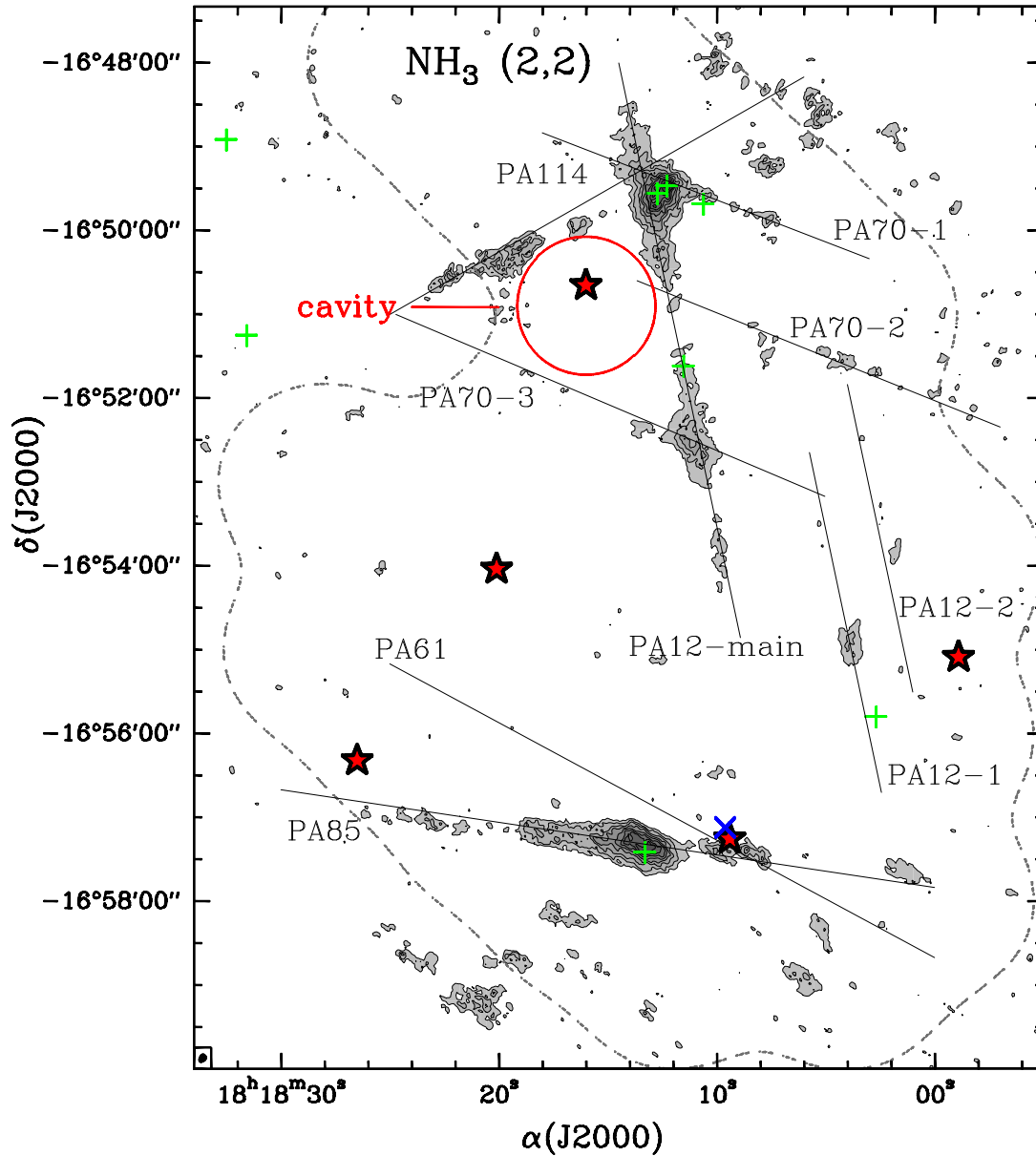


Figure 2.8: Integrated intensity of the combined  $\text{NH}_3$  (2,2) emission. Contours start at 5 %, increasing in steps of 10 % of the peak intensity,  $\sim 0.2 \text{ Jy beam}^{-1} \text{ km s}^{-1}$ . Symbols are the same as in Fig. 2.7. The grey dashed line indicates 50 % of the sensitivity level of the 34-pointing mosaic performed in  $\text{NH}_3$ . The synthesized beam,  $5''.43 \times 3''.60$ , P.A. =  $-29^\circ 8'$ , is shown in the bottom left corner of the image.

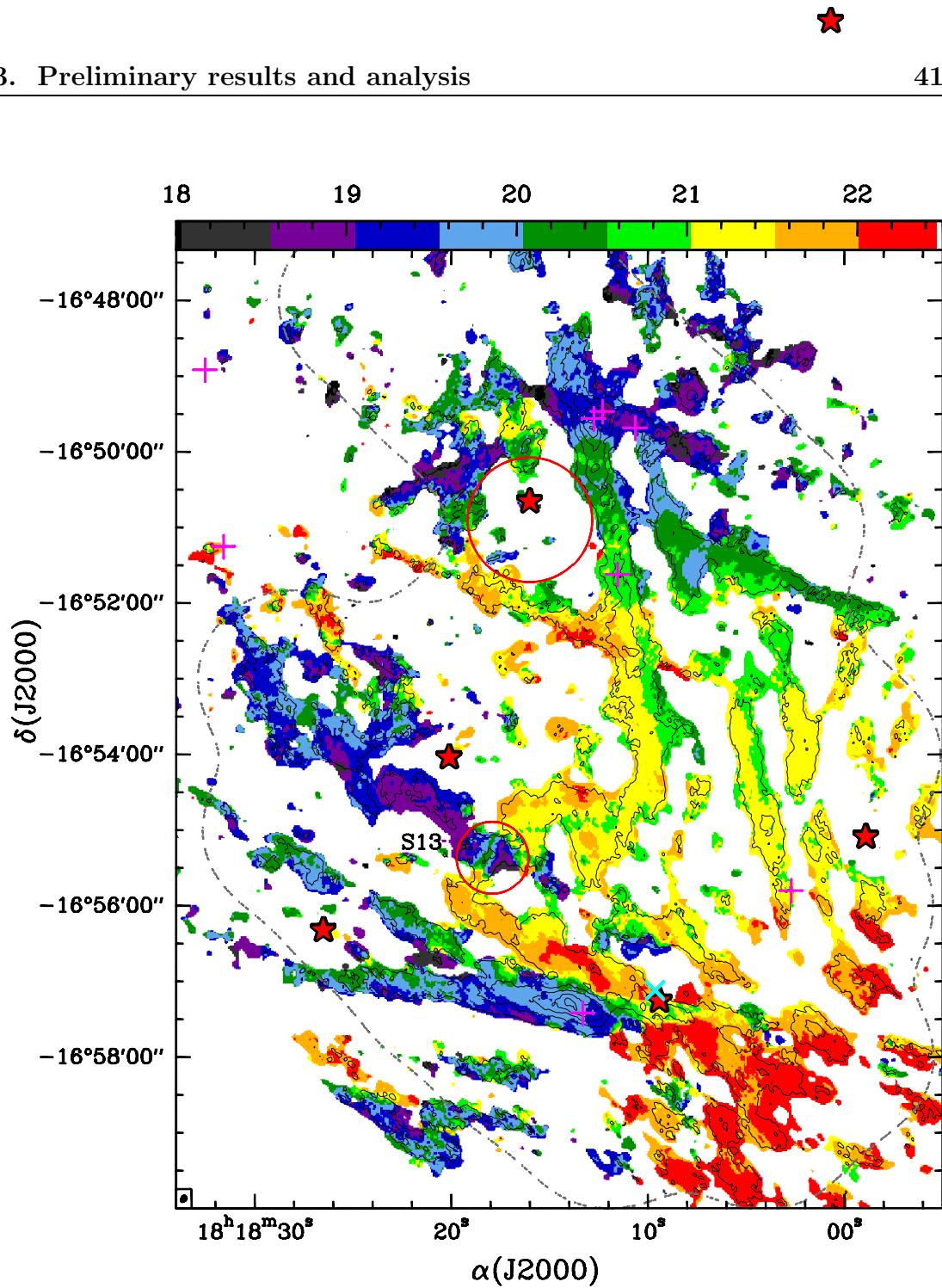


Figure 2.9: Color scale: first-order moment map of the combined  $\text{NH}_3$  (1,1) emission, including only the main line. Contours:  $\text{NH}_3$  (1,1) integrated intensity emission, starting at 8 % and increasing in steps of 20 % of the peak intensity. Color wedge scale are in  $\text{km s}^{-1}$ . Symbols are the same as in Fig. 2.7, with pink crosses indicating  $\text{H}_2\text{O}$  maser emission. The synthesized beam is shown in the bottom left corner of the image.

In Fig. 2.10 we present the second-order moment map (intensity weighted velocity dispersion) of the  $\text{NH}_3$  (1,1) main line emission. We found that the velocity dispersion is enhanced towards filaments PA12-main, PA85, and SMMS13. Typically, the velocity dispersion in cores associated with filaments P12-main and P85 is  $\sim 0.7 - 1.3 \text{ km s}^{-1}$ , which corresponds to a linewidth for a Gaussian line profile to a full width at half maximum (*FWHM*) of  $\sim 0.9 - 2.7 \text{ km s}^{-1}$  (corrected for instrumental resolution). As can be seen in this figure, most of the cores within these two filaments are associated with  $\text{H}_2\text{O}$  maser emission (pink crosses in Fig. 2.10), indicating that star formation is taking place, and that the line broadening could be due to the presence of embedded protostar(s). Interestingly, the higher values of the linewidth, around  $\sim 3.5 \text{ km s}^{-1}$ , are found toward SMMS13 and in a region where filaments PA85 and PA61 seem to merge. The line broadening seen in this merging region is associated with IRAS 18152–1658 and elongated roughly in the east/west direction. This line broadening could be produced either by the IRAS source or by a strong interaction of these two filaments. Additionally, there is evidence of line broadening associated with the cavity around IRAS 18153–1651, suggesting a strong interaction of the star with the dense gas. In contrast, all the other filaments appear as more quiescent, with a typical velocity dispersion of  $0.4\text{--}0.6 \text{ km s}^{-1}$ , corresponding to linewidths of  $\sim 0.7\text{--}1.3 \text{ km s}^{-1}$  (corrected for instrumental resolution). These values are significantly higher than the expected thermal linewidth  $\sim 0.23 \text{ km s}^{-1}$  (estimated for a kinetic temperature of 20 K) found in isolated low-mass starless cores (e.g., Caselli et al. 2002a; Crapsi et al. 2005; Kirk et al. 2007). However, in pre-protostellar cores associated with intermediate/high-mass protoclusters the linewidth is usually much higher than the expected thermal linewidth (Palau et al. 2007; Fontani et al. 2009; Busquet et al. 2010b), indicative of a strong contribution from non-thermal processes such as turbulence or magnetic fields.

Using the  $\text{NH}_3$  data convolved to a circular beam of  $22''$  we made a rough estimation of the ammonia abundance,  $X(\text{NH}_3) = N(\text{NH}_3)/N(\text{H}_2)$ , by computing the ratio of the  $\text{NH}_3$  (1,1) integrated intensity map over the  $870 \mu\text{m}$  dust emission map. The resulting map is presented in Fig. 2.11, which shows significant variations, of a factor of 4, in the  $\text{NH}_3$  abundance along the cloud. In particular, we found that

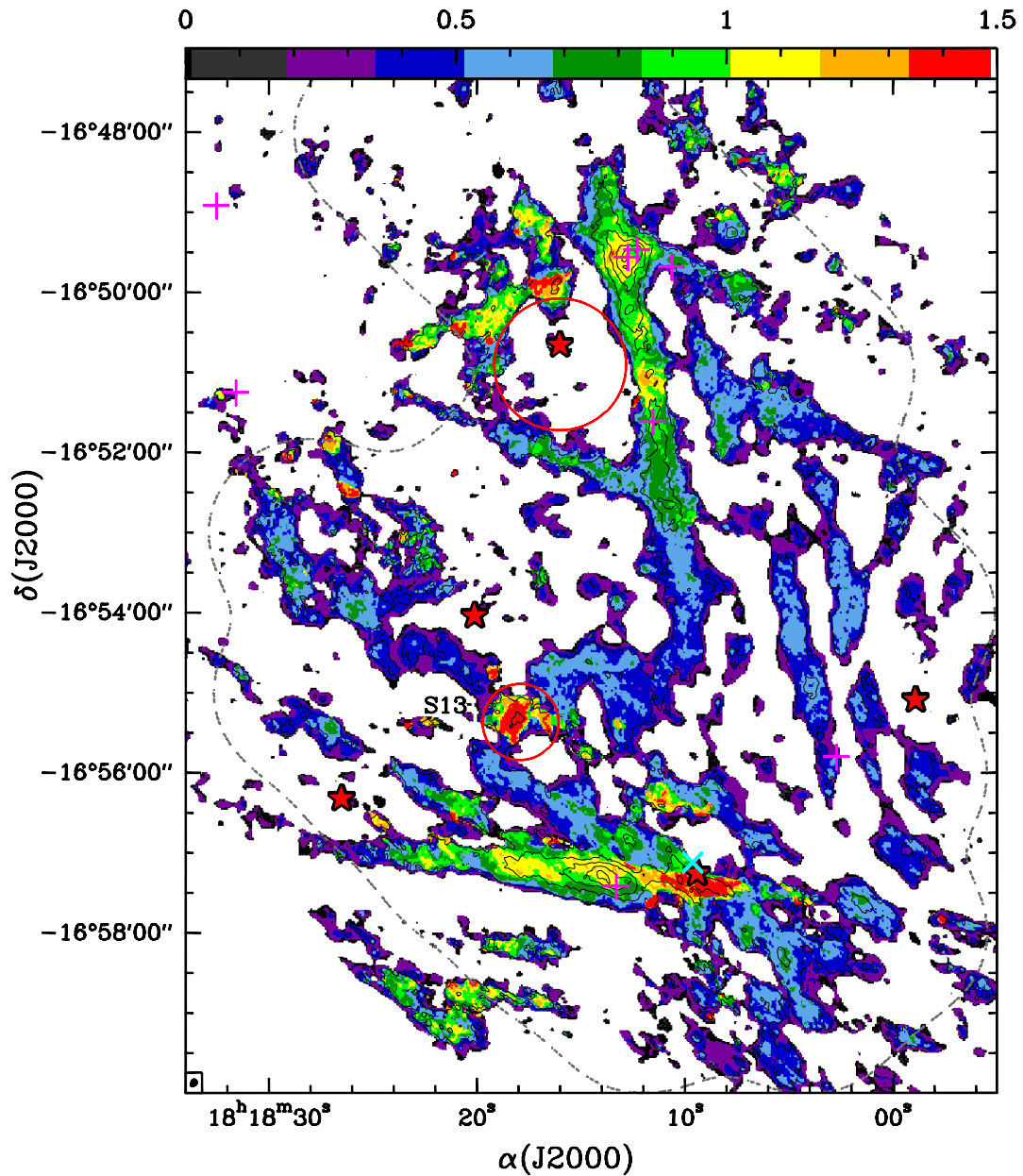


Figure 2.10: Color scale: second-order moment map (velocity dispersion) of the combined  $\text{NH}_3$  (1,1) emission. Contours:  $\text{NH}_3$  (1,1) integrated intensity emission, starting at 8 % and increasing in steps of 20 % of the peak intensity. Color wedge scale are in  $\text{km s}^{-1}$ . Symbols are the same as in Fig. 2.9. The synthesized beam is shown in the bottom left corner of the image. Note that second-order moment gives the velocity dispersion, and must be multiplied by the factor  $\sqrt{2 \ln 2} \simeq 2.35$  to convert to full width at half maximum.

the  $\text{NH}_3$  abundance is lower in the northern part of filament P12-main, increasing when moving toward the south. Similarly, we also found important variations along filament PA85, roughly in the west/east direction. Note that the gas forming the cavity presents also high values of the  $\text{NH}_3$  abundance, specially to the north-east, which might indicate gas being photo-illuminated by the star IRAS 18153–1651. We performed a more accurate estimation of the  $\text{NH}_3$  abundance, taking into account opacity and excitation effects, by deriving first the  $\text{NH}_3$  column density and then the fractional abundance of  $\text{NH}_3$ ,  $X(\text{NH}_3)$ , in some clumps of IRDC G14.2–0.60. In Table 2.5 we report on the rotational temperature,  $T_{\text{rot}}$ , derived for those clumps where both  $\text{NH}_3$  (1,1) and (2,2) are well detected, together with the intrinsic line width, the  $\text{NH}_3$  column density, and the  $\text{NH}_3$  fractional abundance. The values of the  $\text{NH}_3$  abundance listed in this table are consistent with the map shown in Fig. 2.11. The rotational temperature is around  $\sim 10 - 18$  K, similar to the values derived in other IRDCs (e. g., Pillai et al. 2006a; Sakai et al. 2008). As can be seen in this table, we obtained values in the range  $\sim 10^{-7} - 10^{-8}$ , in accordance with the values derived by Pillai et al. (2006a) towards a sample of 9 infrared dark clouds. It is important to note that the lowest values of the  $\text{NH}_3$  abundance are reached in regions of active star formation.

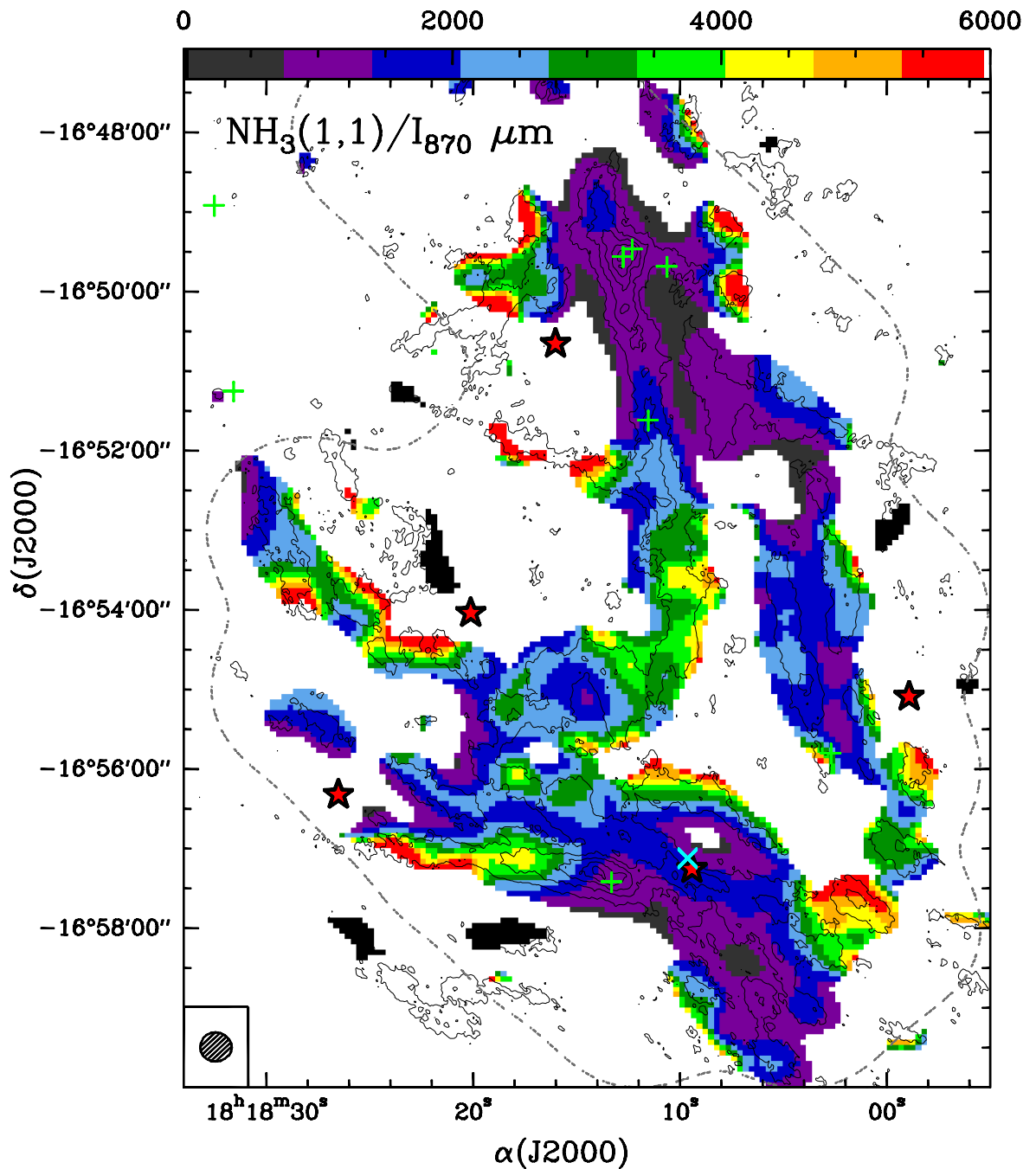


Figure 2.11: Ratio of the  $\text{NH}_3(1,1)$  integrated intensity map over the  $870 \mu\text{m}$  emission map of G14.2-0.60. Contours and symbols are the same as in previous figures. The beam size, of  $22''$ , is shown in the bottom left corner of the image.

Table 2.5: NH<sub>3</sub> column density and abundance in G14.2–0.60

| Clump  | $T_{\text{rot}}$<br>(K) | $\Delta v^{\text{a}}$<br>(km s <sup>-1</sup> ) | $N(\text{NH}_3)$<br>( $\times 10^{15}$ cm <sup>-2</sup> ) | $X(\text{NH}_3)$<br>( $\times 10^{-8}$ ) |
|--------|-------------------------|--|---|--|
| SMMS7  | 15.3                    | 1.15   | 0.74  | 2.2                                      |
| SMMS8  | 11.8                    | 1.16   | 1.70  | 1.7                                      |
| SMMS10 | 17.8                    | 2.04   | 3.31  | 7.4                                      |
| SMMS12 | 10.8                    | 1.15   | 1.54  | 15.4                                     |
| SMMW2  | 11.3                    | 1.23   | 1.76  | 25.1                                     |
| SMMW6  | 9.9                     | 1.03   | 2.22  | 7.9                                      |
| SMMW7  | 12.3                    | 1.03   | 1.45  | 11.2                                     |
| SMMW8  | 9.6                     | 1.15   | 1.10  | 4.2                                      |
| SMMW9  | 14.3                    | 1.31   | 1.87  | 23.4                                     |
| SMMW10 | 11.6                    | 1.01   | 1.15  | 2.2                                      |
| SMMW11 | 12.5                    | 1.02   | 1.44  | 1.6                                      |
| SMMW12 | 16.4                    | 2.22   | 2.38  | 4.9                                      |
| SMMW13 | 15.6                    | 2.09   | 1.59  | 26.5                                     |
| SMMW24 | 13.6                    | 1.75   | 1.58  | 4.3                                      |
| SMMW25 | 14.1                    | 1.41   | 2.07  | 9.8                                      |
| SMMW26 | 13.0                    | 1.04   | 1.17  | 9.0                                      |
| SMMW27 | 11.5                    | 1.03   | 1.16  | 10.5                                     |
| SMME1  | 13.6                    | 1.22   | 0.29  | 5.8                                      |
| SMME2  | 12.8                    | 1.65   | 0.83  | 7.5                                      |

**Notes.** <sup>a</sup> Line width derived from the fits to the hyperfine structure of NH<sub>3</sub> (1,1).

### N<sub>2</sub>H<sup>+</sup> emission and the NH<sub>3</sub>/N<sub>2</sub>H<sup>+</sup> ratio

In Fig. 2.12 we show the zero-order moment map of N<sub>2</sub>H<sup>+</sup> (1–0) transition integrated for all the hyperfine components obtained with the FCRAO. The overall structure of N<sub>2</sub>H<sup>+</sup> (1–0) resembles roughly the emission of the Effelsberg NH<sub>3</sub> (1,1), shown also in Fig. 2.12 in contours. The emission consists of four main N<sub>2</sub>H<sup>+</sup> clumps, labeled as P1, P2, P3, and P4, corresponding to the submillimeter clumps W12, S10, S11, and E15/E16, respectively.

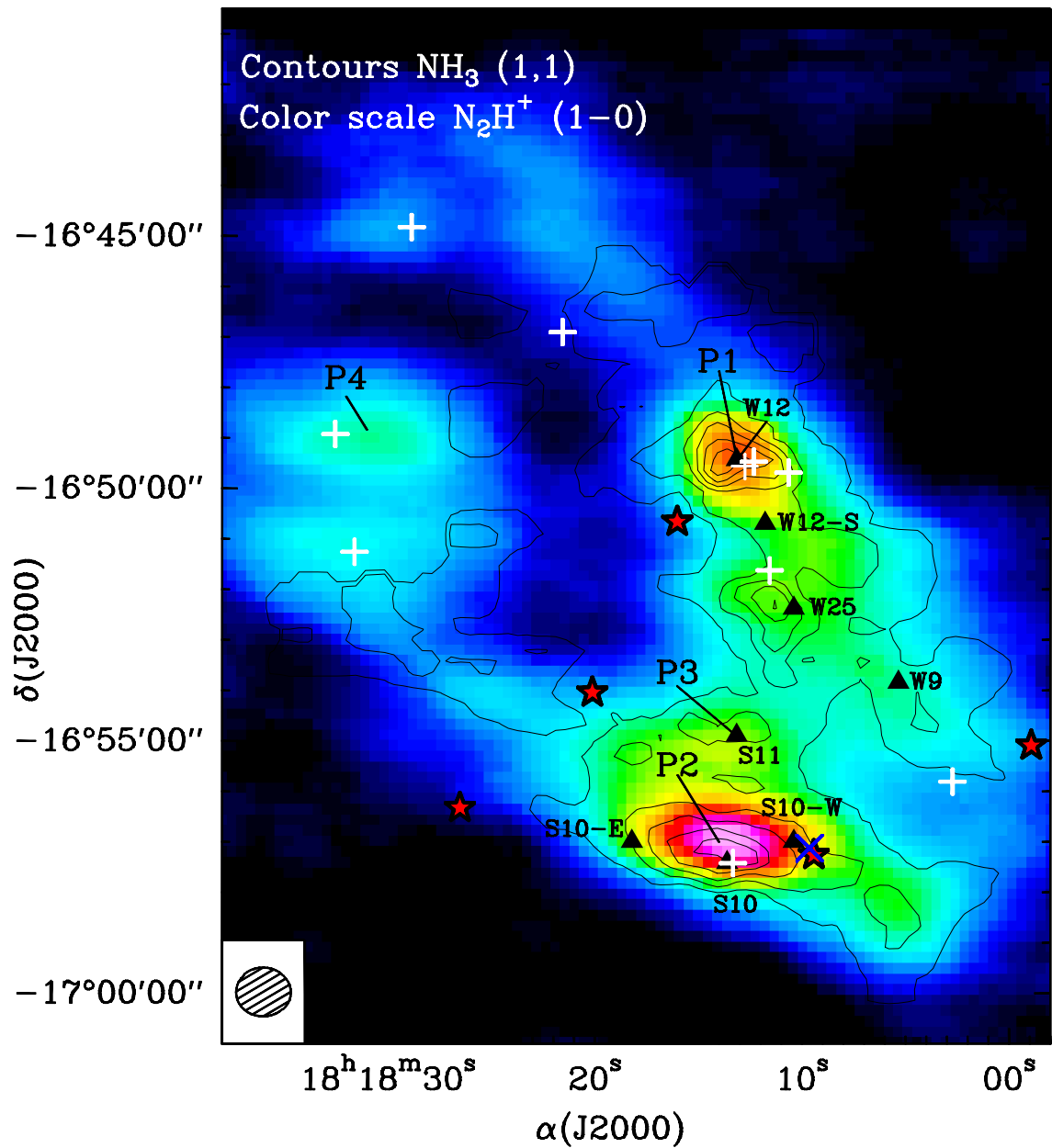


Figure 2.12: Color scale:  $\text{N}_2\text{H}^+$  (1-0) integrated intensity map from the FCRAO. Contours:  $\text{NH}_3$  (1,1) integrated intensity map from Effelsberg. Symbols are the same as in Fig. 2.7. The four main clumps identified in  $\text{N}_2\text{H}^+$  are labeled as P1, P2, P3, and P4. Triangles mark the position where we computed the  $\text{NH}_3/\text{N}_2\text{H}^+$  abundance ratio. The  $\text{N}_2\text{H}^+$  beam size, of  $58''$ , is shown in the bottom left corner of the image.

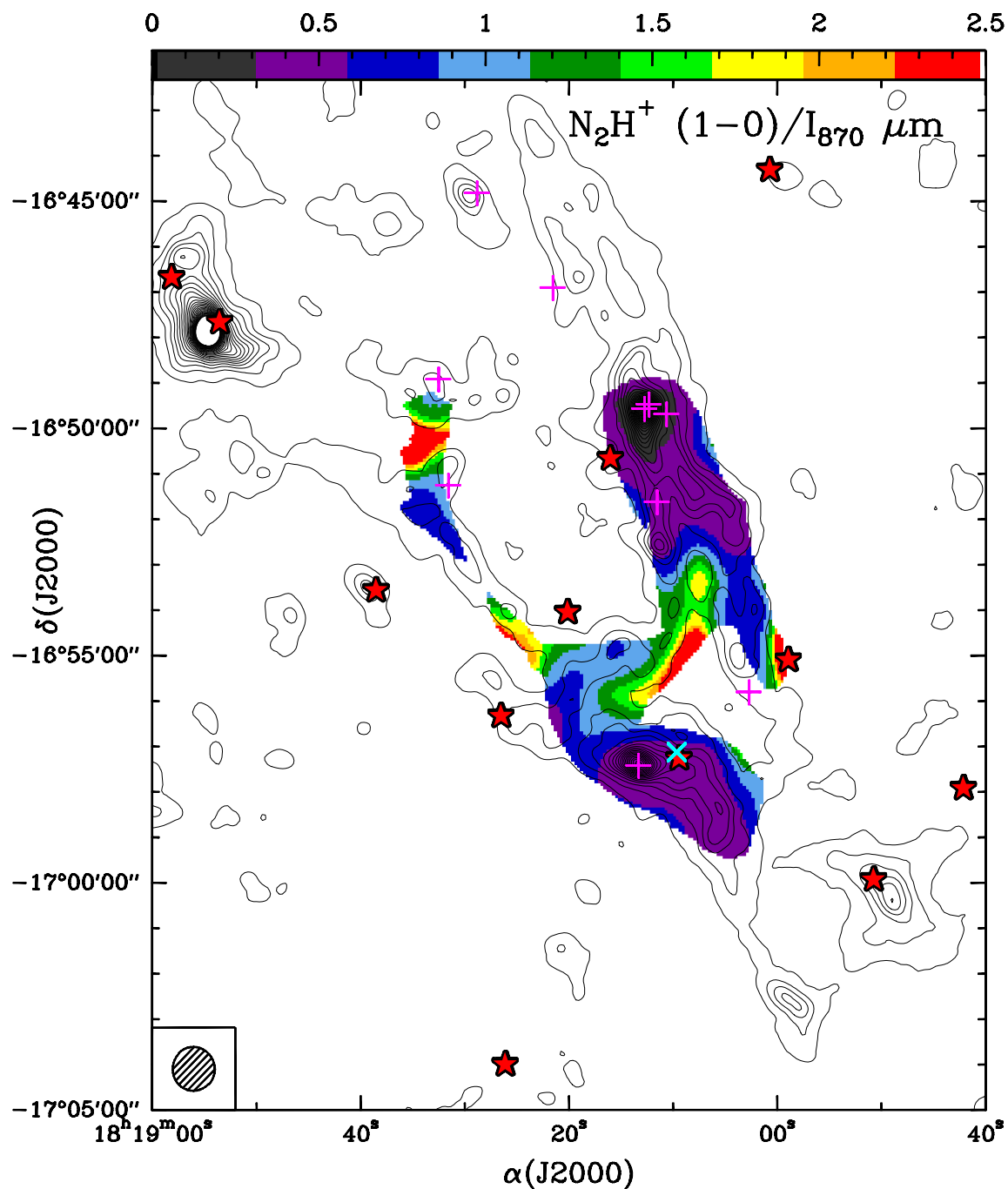


Figure 2.13: Color scale: ratio of the  $N_2H^+$  (1-0) integrated intensity map over the  $870 \mu m$  emission map of G14.2-0.60. Contours and symbols are the same as in Fig. 2.1. The beam size, of  $58''$ , is shown in the bottom left corner of the image.

Table 2.6:  $\text{NH}_3/\text{N}_2\text{H}^+$  ratio at some selected positions of G14.2–0.60

| Position  | $N(\text{NH}_3)$<br>( $\times 10^{14} \text{ cm}^{-2}$ ) | $N(\text{N}_2\text{H}^+)$<br>( $\times 10^{12} \text{ cm}^{-2}$ ) | Ratio <sup>a</sup> | $\text{H}_2\text{O}$<br>maser? | IR<br>source? |
|-----------|--|---|--------------------|--------------------------------|---------------|
| S10       | 14.4   | 2.3   | 616                | Y                              | Y             |
| S10–East  | 10.9   | 1.8   | 617                | N                              | N             |
| S10–West  | 12.9   | 2.2   | 592                | N                              | Y             |
| S11       | 8.9  | 1.3   | 693                | N                              | N             |
| W9        | 6.6  | 1.2   | 531                | N                              | Y             |
| W12       | 8.3  | 1.8   | 455                | Y                              | Y             |
| W12–South | 7.8  | 1.6   | 479                | N                              | N             |
| W25       | 5.2  | 1.2   | 425                | N                              | Y             |

**Notes.** <sup>a</sup> Ratio of  $N(\text{NH}_3)$  over  $N(\text{N}_2\text{H}^+)$ .

In order to estimate the  $\text{NH}_3/\text{N}_2\text{H}^+$  abundance ratio we convolved the  $\text{NH}_3$  Effelsberg data (angular resolution  $\sim 40''$ ) to the angular resolution of the  $\text{N}_2\text{H}^+$  emission ( $\sim 58''$ ). Then, we extracted the spectra toward some selected positions, and using CLASS we fitted the hyperfine structure of  $\text{NH}_3(1,1)$  and  $\text{N}_2\text{H}^+(1-0)$  and a single Gaussian for  $\text{NH}_3(2,2)$ . From the results of the fits, we computed the rotational temperature, and the  $\text{NH}_3$  and  $\text{N}_2\text{H}^+$  column densities following the procedure outlined in Chapter 4 (see also the Appendix). In Table 2.6 we list the resulting column densities and the  $\text{NH}_3/\text{N}_2\text{H}^+$  ratio for these positions. We derived values of the  $\text{NH}_3/\text{N}_2\text{H}^+$  ratio in the range  $\sim 425 - 693$ . We found some hints of a possible evolutionary trend of the  $\text{NH}_3/\text{N}_2\text{H}^+$  ratio along filament P12-main, in which the ratio is low, around  $\sim 455$ , in clump P1 (which corresponds with the submillimeter clump W12, associated with  $\text{H}_2\text{O}$  maser emission, i. e., star formation activity) and it increases, up to 693, in clump P3, where neither maser emission nor infrared sources are detected. It is worth noting that the lowest values of the ratio are found in clumps located in the vicinity of the bright infrared source IRAS 18153-1651 (i. e., W12 and W25), suggesting that UV radiation might produce some effects on the surrounding gas. As can be seen in this table, both clumps containing IR source and/or maser emission (e. g., SMMS10, SMMW12, SMMW25) and clumps with starless properties (e. g., SMMS11) are associated with high values of the  $\text{NH}_3/\text{N}_2\text{H}^+$  ratio, much higher than the values obtained in cores containing YSOs or in starless cores (e. g., Caselli et al. 2002a; Hotzel et al. 2004; Palau et al.

2007; Friesen et al. 2010). In Section 2.4.1 we will discuss possible explanations for the values found in the IRDC G14.2–0.60.

We made a rough estimation of the  $\text{N}_2\text{H}^+$  abundance,  $X(\text{N}_2\text{H}^+) = N(\text{N}_2\text{H}^+)/N(\text{H}_2)$ , by first convolving the dust emission map to a circular beam of  $58''$  and then we computed the ratio of the  $\text{N}_2\text{H}^+$  (1–0) integrated intensity map over the  $870 \mu\text{m}$  dust emission map (see Figure 2.13). What is clear from this figure is that the  $\text{N}_2\text{H}^+$  abundance does not show significant changes (less than a factor of 2) along the cloud (note that the highest values are just the result of border effects). Therefore, the variations found in the  $\text{NH}_3/\text{N}_2\text{H}^+$  ratio are more likely due to variations in the  $\text{NH}_3$  abundance (see Fig. 2.11).

### 2.3.3 SMA dust emission

We performed high angular resolution observations of the dust emission using the SMA toward SMMS10, the most massive clump detected with the APEX telescope. Figure 2.14 presents the 1.3 mm dust continuum emission obtained with the SMA after combining both configurations (compact and extended), overlaid on the  $\text{NH}_3$  (1,1) integrated emission map. We identified 16 millimeter sources above the  $3 \sigma$  level, which corresponds to a mass sensitivity of  $0.3 M_\odot$  (assuming  $T_d=25 \text{ K}$ ). In Table 2.7 we show the main parameters of the detected sources, listing their position (Col. 2 and Col. 3), peak intensity (Col. 4), flux density (Col. 5), and deconvolved size obtained from a 2-d Gaussian fitting (Col. 6). We estimated the mass of each dust condensation using the dust mass opacity coefficient at 1.3 mm of  $0.9 \text{ g cm}^{-1}$  (agglomerated grains with thin ice mantles in cores of densities  $\sim 10^6 \text{ cm}^{-3}$ , Ossenkopf and Henning 1994), and using the  $\text{NH}_3$  data to determine the dust temperature of each millimeter condensation. Due to the uncertainty in the dust mass opacity coefficient, the values of the derived masses are good within a factor of 2. The derived masses, reported in Col. (9) of Table 2.7, range between 0.5 and  $16 M_\odot$  and the average separation between the different members of the cluster is  $\sim 4''$  ( $\sim 10000 \text{ AU}$ ). If we consider only the central cluster (see Fig. 2.14 top panel) the average separation is  $\sim 3''$  ( $7500 \text{ AU}$ ). Additionally, in Table 2.7 we list in Col. (10), Col. (11), and Col. (12) the molecular hydrogen volume density, the column density, and the visual extinction, estimated considering a spherically symmetric structure and using the same equations as in Sec. 2.3.1. The average density is  $\sim 2.2 \times 10^6 \text{ cm}^{-3}$ , and the average column density is  $\sim 1.8 \times 10^{23} \text{ cm}^{-2}$ .

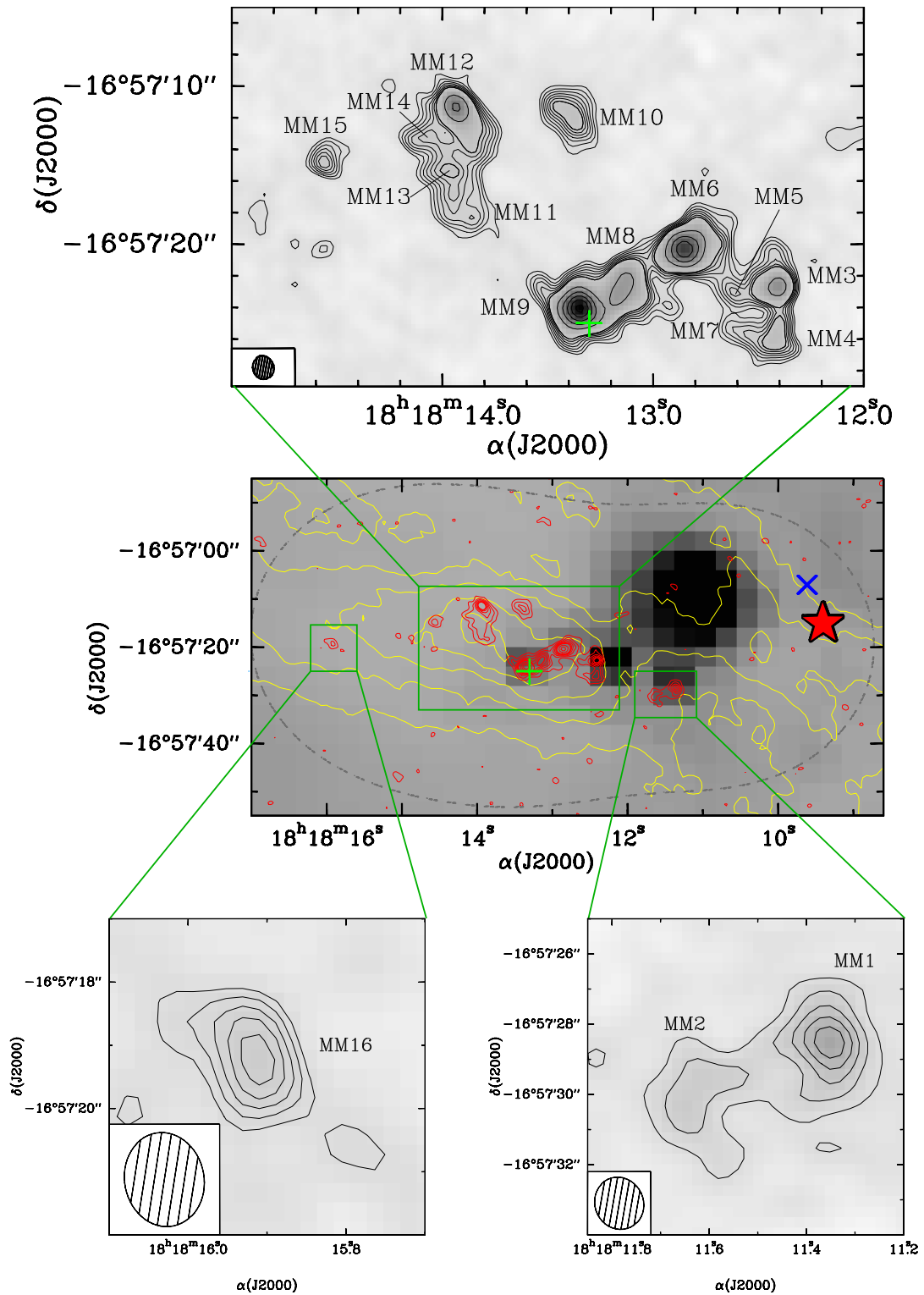


Figure 2.14: (see behind)

Figure 5.12: **Middle panel:** SMA 1.3 mm continuum emission of the combined data sets (red contours) overlaid on the 24  $\mu\text{m}$  *Spitzer* image (grey scale) and the  $\text{NH}_3$  (1,1) integrated intensity map (yellow contours). The green cross marks the position of  $\text{H}_2\text{O}$  maser emission. The star indicates the nominal position of IRAS 18152–1658, and the blue titled cross marks the position of a centimeter source (Jaffe et al. 1982). **Top panel:** Enlarged 1.3 mm continuum emission of the central cluster. Contour levels range from 3 to 9 in steps of  $1\sigma$  and from 9 to 59 in steps of  $10\sigma$ , where  $\sigma$  is the rms of the map,  $1 \text{ mJy beam}^{-1}$ . **Bottom panel:** Enlarged 1.3 mm continuum emission of MM1 and MM2 (right) and MM16 (left). Contour levels are 3 to 15 in steps of 3, times  $1 \text{ mJy beam}^{-1}$ , and 3 to 7 in steps of 1, times  $1 \text{ mJy beam}^{-1}$ , respectively. The synthesized beam of the SMA ( $1''.52 \times 1''.42$ , P.A.=  $35^\circ$ ) is shown in the bottom left corner of the image.

We additionally computed the mass surface density  $\Sigma$  for each condensation and the result is listed in Col. (13) of Table 2.7. The average value is  $\sim 0.87 \text{ g cm}^{-2}$ , above the surface density threshold of  $0.7 \text{ g cm}^{-2}$  needed to form a massive star (Krumholz and McKee 2008). In particular, 6 out of the 16 condensations have values above the  $0.7 \text{ g cm}^{-2}$  threshold value. As shown in Sec. 2.3.1, clumps in G14.2–0.60 fell all below this limit, which could be the result of clumps being inhomogeneous and actually forming small and denser cores. This is the case of SMMS10, in which we derived  $\Sigma = 0.217 \text{ g cm}^{-2}$  from the single-dish data, but when observed at high angular resolution the clump fragments into several small and denser condensations with values closer and even higher to the value reported by Krumholz and McKee (2008).

Using the  $\text{NH}_3$  data we have calculated the virial mass of each millimeter condensation following Estalella et al. (1993). The result is listed in Col. (15) of Table 2.7. As can be seen in this Table, 4 out of the 16 condensations (i. e., MM3, MM6, MM9, and MM12) have  $M > M_{\text{vir}}$ , indicating that these condensations might be unstable and undergoing collapse. On the other hand, for MM4, MM8, and MM13 their masses are  $1/2 M_{\text{vir}} < M < M_{\text{vir}}$ , indicating that the material is stable and near virial equilibrium. Concerning the remaining sources (i. e., MM1, MM2, MM5, MM7, MM10, MM11, MM12, MM14, MM15, and MM16), they do not appear to be collapsing, as they have masses much smaller than the virial mass. However, gas masses have been calculated from the interferometric continuum data, strongly affected by the flux filtered out by the interferometer, while the virial masses are calculated using the combined interferometric and single-dish  $\text{NH}_3$  data, and hence the inclusion of short-spacing corrects the effects introduced by the missing flux. Thus, the fact that most of the sources have masses smaller than the virial mass could be a consequence of the flux filtered out by the interferometer. To confirm this, we should perform 1.3 mm single-dish observations of the region to combine with the interferometric data and properly estimate the masses of each source.

Finally, we estimated the fraction of missing flux resolved out by the SMA by comparing the total flux at 1.3 mm ( $\sim 0.67 \text{ Jy}$ ) with the flux density measured with APEX. We extrapolated the flux measured at  $870 \mu\text{m}$  with the APEX telescope adopting a dust emissivity index of  $\beta = 1.5$  and the resulting flux of SMMS10 clump encompassing the field of view observed with the SMA at 1.3 mm is  $7.8 \text{ Jy}$ , indicating that the fraction of flux filtered out by the SMA is  $\sim 91 \%$ .

Table 2.7: Parameters of the 1.2 mm continuum sources in G14.2–0.60

| (1)    | (2)                        | (3)  | (4)  | (5)                | (6)                                | (7)                    | (8)                              | (9)                               | (10)   | (11)  | (12)                     | (13)                               | (14)  | (15)   |
|--------|----------------------------|--|--|--------------------|------------------------------------|------------------------|----------------------------------|-----------------------------------|--|---|--------------------------|------------------------------------|---|--|
| Source | $\alpha(J2000)$<br>(h:m:s) | $\delta(J2000)$<br>( $^{\circ}$ :': $''$ ) | $I_{\nu}^{\text{peak}}$<br>(mJy beam $^{-1}$ ) | $S_{\nu}$<br>(mJy) | Deconv. size<br>( $'' \times ''$ ) | P.A.<br>( $^{\circ}$ ) | $T_{\text{d}}^{\text{a}}$<br>(K) | $M^{\text{b}}$<br>( $M_{\odot}$ ) | $n(\text{H}_2)$<br>( $\times 10^6 \text{ cm}^{-3}$ ) | $N(\text{H}_2)$<br>( $\times 10^{22} \text{ cm}^{-2}$ ) | $A_{\text{V}}$<br>(mag.) | $\Sigma$<br>( $\text{g cm}^{-2}$ ) | $\Delta v^{\text{c}}$<br>( $\text{km s}^{-1}$ ) | $M_{\text{vir}}^{\text{d}}$<br>( $M_{\odot}$ ) |
| MM1    | 18 18 11.35                | -16 57 28.5                                | 17.9   | 36.5 $\pm$ 2.4     | 2.1 $\times$ 1.8                   | 177                    | 35                               | 2.6                               | 0.9  | 8.0   | 100.5                    | 0.38                               | 2.71  | 16.7   |
| MM2    | 18 18 11.64                | -16 57 30.3                                | 8.1  | 21.2 $\pm$ 2.2     | 2.9 $\times$ 2.7                   | 133                    | 35                               | 1.5                               | 0.2  | 2.2   | 28.2                     | 0.11                               | 1.41  | 6.5  |
| MM3    | 18 18 12.40                | -16 57 22.5                                | 24.2   | 48.7 $\pm$ 2.2     | 2.0 $\times$ 1.6                   | 106                    | 26                               | 5.0                               | 2.2  | 17.9  | 225.5                    | 0.99                               | 0.84  | 4.9  |
| MM4    | 18 18 12.42                | -16 57 25.8                                | 11.8   | 28.5 $\pm$ 1.9     | 2.7 $\times$ 2.4                   | 133                    | 22                               | 3.6                               | 0.5  | 6.4   | 80.2                     | 0.30                               | 1.53  | 7.0  |
| MM5    | 18 18 12.61                | -16 57 23.1                                | 8.5  | 8.2 $\pm$ 1.1      | ...                                | ...                    | 24                               | 0.9                               | 0.7  | 4.9   | 62.1                     | >0.23                              | 1.53  | 4.0  |
| MM6    | 18 18 12.86                | -16 57 20.4                                | 46.8   | 119.0 $\pm$ 2.9    | 3.0 $\times$ 2.1                   | 110                    | 25                               | 12.9                              | 2.1  | 23.3  | 293.7                    | 1.29                               | 1.10  | 9.1  |
| MM7    | 18 18 12.92                | -16 57 24.0                                | 5.2  | 4.3 $\pm$ 1.0      | ...                                | ...                    | 25                               | 0.5                               | 0.4  | 2.5   | 31.0                     | >0.12                              | 2.76  | 13.1   |
| MM8    | 18 18 11.64                | -16 57 23.1                                | 22.1   | 79.0 $\pm$ 2.6     | 4.2 $\times$ 1.8                   | 137                    | 21                               | 10.6                              | 1.3  | 16.1  | 202.1                    | 0.76                               | 2.11  | 14.3   |
| MM9    | 18 18 13.15                | -16 57 24.0                                | 62.4   | 136.8 $\pm$ 2.8    | 2.1 $\times$ 1.7                   | 94                     | 24                               | 15.6                              | 5.8  | 49.8  | 626.6                    | 2.34                               | 2.35  | 12.2   |
| MM10   | 18 18 13.34                | -16 57 12.0                                | 11.1   | 32.0 $\pm$ 2.3     | 3.2 $\times$ 1.9                   | 41                     | 28                               | 3.0                               | 0.5  | 5.7   | 71.3                     | 0.27                               | 2.59  | 19.4   |
| MM11   | 18 18 13.34                | -16 57 18.3                                | 7.2  | 15.0 $\pm$ 1.9     | ...                                | ...                    | 17                               | 2.7                               | 2.1  | 14.1  | 177.4                    | >0.66                              | 2.82  | 13.7   |
| MM12   | 18 18 13.86                | -16 57 11.4                                | 30.5   | 77.3 $\pm$ 2.8     | 2.4 $\times$ 1.5                   | 40                     | 20                               | 11.1                              | 4.0  | 35.2  | 442.2                    | 1.65                               | 2.11  | 9.9  |
| MM13   | 18 18 13.97                | -16 57 15.3                                | 9.8  | 29.3 $\pm$ 2.1     | ...                                | ...                    | 17                               | 5.2                               | 4.1  | 27.5  | 346.4                    | >1.29                              | 2.59  | 11.5   |
| MM14   | 18 18 14.07                | -16 57 13.2                                | 8.6  | 14.8 $\pm$ 1.5     | ...                                | ...                    | 17                               | 2.6                               | 2.1  | 13.9  | 175.0                    | >0.65                              | 2.11  | 7.7  |
| MM15   | 18 18 14.55                | -16 57 14.7                                | 8.9  | 13.6 $\pm$ 1.8     | 1.7 $\times$ 1.4                   | 110                    | 17                               | 2.4                               | 1.6  | 11.6  | 145.8                    | 0.54                               | 2.35  | 9.9  |
| MM16   | 18 18 15.91                | -16 57 19.2                                | 7.8  | 10.2 $\pm$ 1.6     | 2.5 $\times$ 0.9                   | 57                     | 15                               | 2.1                               | 1.6  | 10.9  | 137.4                    | 0.51                               | 2.11  | 7.8  |

**Notes.** <sup>a</sup> Estimated from the  $\text{NH}_3$  observations and converted to kinetic temperature following the expression of Tafalla et al. (2004). <sup>b</sup> Masses of gas and dust derived assuming a dust-to-mass ratio  $g = 100$  and a dust mass opacity of  $\kappa_{250 \text{ GHz}} = 0.9 \text{ g cm}^{-1}$  (Ossenkopf and Henning 1994). <sup>c</sup> Linewidth derived from the  $\text{NH}_3$  second-order moment map. <sup>d</sup> Virial mass obtained from  $[\frac{M_{\text{vir}}}{M_{\odot}}] = 210 [\frac{R}{\text{pc}}] [\frac{\Delta v}{\text{km s}^{-1}}]$ , where  $R$  is the radius of the millimeter condensation, taken as half the geometrical mean of the major and minor axes, and  $\Delta v$  is the intrinsic linewidth given in Col. (14).

### 2.3.4 The mass spectrum of the clumps

If the clump mass distribution can be fitted by a single power-law of the form

$$\frac{\Delta N}{\Delta M} \propto M^\beta \quad (2.1)$$

with  $\Delta N$  the number of clumps per mass bin  $\Delta M$ , then the cumulative mass spectrum can be written as

$$N(> M) \propto -\frac{1}{1+\beta} M^{1+\beta} \quad (2.2)$$

for  $\beta < -1$ . As a result of a finite sampling one should take into account the upper mass cutoff  $M_{\max}$  (Reid and Wilson 2006), and the cumulative mass spectrum is expressed as

$$N(> M) \propto \begin{cases} \frac{1}{1+\beta}(M_{\max}^{1+\beta} - M^{1+\beta}) & M < M_{\max} \\ 0 & M \geq M_{\max} \end{cases} \quad (2.3)$$

for  $\beta < -1$ .

Figure 2.15 (left panel) shows the normalized cumulative mass spectrum for masses above  $\sim 10 M_\odot$  of the 870  $\mu\text{m}$  clumps detected with APEX in G14.2–0.60. We fitted both expressions given in Eqs. (2.2) and (2.3), and the results are  $\beta = -1.1$  and  $\beta = -1.5$ , respectively. The inclusion of  $M_{\max}$  in the fit produces a more accurate fit, so we adopted  $\beta = -1.5$ . The result from the APEX observations shows us a clump mass distribution with a relatively flat slope compared with other regions (e.g., Beltrán et al. 2006 and references therein), but comparable to the value of  $\beta \simeq -1.7$  obtained for the clump mass function of molecular clouds derived from CO molecular gas observations (e.g., Kramer et al. 1998). In a sample of 11 IRDCs, Ragan et al. (2009) also find a shallower clump mass distribution than the Salpeter-like core mass function reported in other regions.

In Fig. 2.15 (right panel) we present the normalized cumulative mass spectrum for masses above  $\sim 0.5 M_\odot$  of the 1.3 mm cores detected with the SMA. In this case, the resulting fit of Eqs. (2.2) and (2.3) gives a power law index  $\beta = -1.0$  and  $\beta = -1.4$ , respectively, in accordance with the value of  $\beta$  obtained with the APEX data. It is worth noting the bump seen in the distribution starting at  $\sim 1.5 M_\odot$ .

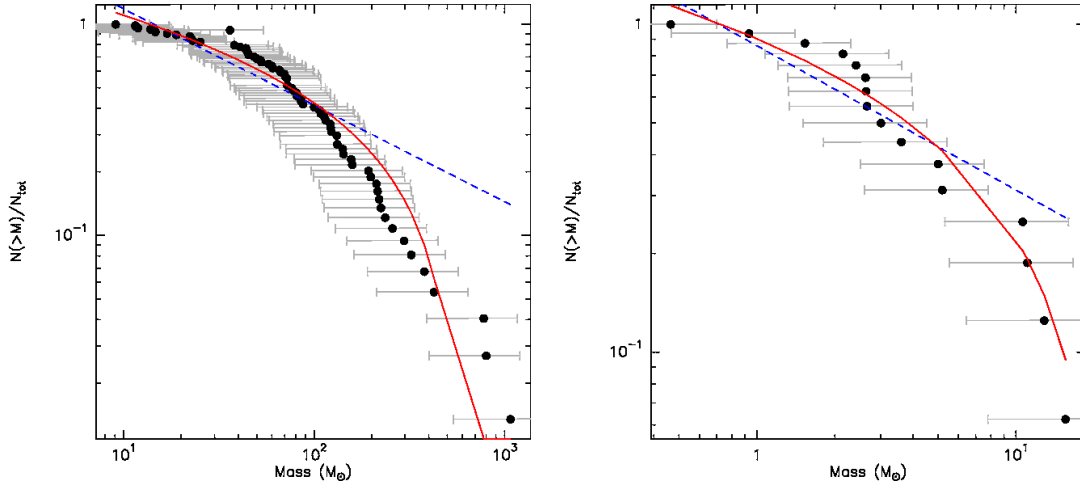


Figure 2.15: Normalized cumulative mass spectrum of G14.2–0.60 using APEX data (left) and of SMA data toward the submillimeter clump S10 (right). The solid red line and dashed blue line represent the best fit of Eq. (2.3) and Eq. (2.2) with a power-law index  $\beta = -1.5 \pm 0.2$  and  $\beta = -1.1 \pm 0.2$ , respectively for the APEX data and  $\beta = -1.4 \pm 0.2$  and  $\beta = -1.0 \pm 0.2$  for SMA data.

However, it is not clear if it reflects a real feature in the distribution or if it is a consequence of the uncertainties in mass.

We found, thus, a relatively flat slope ( $\beta \simeq -1.4$ ) if we compare with the result found in the high-mass protocluster IRAS 19410+2336 (Beuther and Schilke 2004; Rodón 2009), where the high angular resolution observations show a slope of  $\beta \simeq -2.3$ , similar to the Salpeter value of  $\sim -2.35$  for the stellar initial mass function (IIMF; Salpeter 1955). On the other hand, Rodón (2009) observed two high-mass protoclusters with the SMA and obtain a flat slope, with  $\beta \simeq -1.5$ , similar to the result found in G14.2–0.60. Numerical models of the evolution of molecular clouds show that if pure gravitational contraction dominates the dynamical evolution, the clump mass distribution exhibits shallower slope, with  $\beta \simeq -1.5$ , whereas when the cloud is supported by turbulence the result is a steeper clump mass distribution (Klessen 2001). Based on these simulations, Rodón (2009) suggest that the differences of the slope in his sample of high-mass protoclusters could indicate the relative age of the cloud, being more flattened as the cluster is in a earlier evolutionary stage, with gravity dominating the dynamics of the molecular cloud.

While observations of low-mass star-forming regions strongly suggest that the IMF is determined at very early evolutionary stages (e. g., Testi and Sargent 1998; Motte et al. 1998), the current picture in the high-mass regime is not so clear. Different cloud properties, star formation processes, ages, and dynamical processes, might result in a different slope of the mass function, and hence more studies are needed to establish the slope of the mass function in high-mass star-forming regions.

## 2.4 Discussion

### 2.4.1 On the behavior of the $\text{NH}_3/\text{N}_2\text{H}^+$ ratio in IRDCs

Our study of the  $\text{NH}_3/\text{N}_2\text{H}^+$  ratio toward the IRDC G14.2–0.60 reveals very high values of the ratio, ranging from 425 and up to 700, much higher than the values found in other high-mass star-forming regions (Palau et al. 2007; Busquet et al. 2010a). The  $\text{NH}_3/\text{N}_2\text{H}^+$  ratio has been computed in clumps with different properties, including clumps with no signpost of star formation activity and clumps containing embedded infrared sources and/or  $\text{H}_2\text{O}$  maser emission. While previous studies have shown that the  $\text{NH}_3/\text{N}_2\text{H}^+$  ratio seems to be anticorrelated with the evolutionary stage of the dense cores in the cloud (e. g., Caselli et al. 2002a; Hotzel et al. 2004; Palau et al. 2007; Friesen et al. 2010), with low values of the  $\text{NH}_3/\text{N}_2\text{H}^+$  ratio, around 60–90, associated with cores harboring YSOs, and high values, up to 300, toward pre-protostellar cores, in G14.2–0.60 we only found some hints of a possible trend of the  $\text{NH}_3/\text{N}_2\text{H}^+$  with the evolutionary stage of the clump along filament P12-main.

A possible interpretation of the high values of the  $\text{NH}_3/\text{N}_2\text{H}^+$  ratio could be that G14.2–0.60 is chemically younger than the regions of the studies mentioned above. The production of  $\text{NH}_3$  and  $\text{N}_2\text{H}^+$  differs during evolution in collapsing pre-protostellar cores. While there is a golden period of the formation of  $\text{NH}_3$ ,  $\text{N}_2\text{H}^+$  keeps roughly a constant abundance (Aikawa et al. 2001, 2003), and hence this could be an explanation for the high values of the  $\text{NH}_3/\text{N}_2\text{H}^+$  seen in this region.

Another possibility to explain the high values found in G14.2–0.60 could be given in terms of the huge differences in linear scales between this study and previous ones. With single-dish telescopes, like our observations of  $\text{NH}_3$  and  $\text{N}_2\text{H}^+$  in G14.2–0.60,

we are resolving linear scales of  $\sim 0.6$  pc. The typical size of a dense core for most high-mass star-forming regions is  $\sim 0.1$  pc or even smaller, and this can be reached only with interferometers. Thus, dense cores in G14.2–0.60 are not resolved with our single-dish observations, so the  $\text{NH}_3/\text{N}_2\text{H}^+$  ratio may be the contribution of several cores, making difficult to elucidate the truly nature of each individual core and see any possible trend of the  $\text{NH}_3/\text{N}_2\text{H}^+$  ratio with the evolutionary stage. However, at high angular resolution  $\text{N}_2\text{H}^+(1-0)$  is not (or marginally) detected in some IRDCs, such as G14.2–0.60, G28.53–00.25, and G30.88+00.13 (G. Busquet, K. Wang, private communication), even though they contain several  $\text{NH}_3$  dense cores observed with the VLA. We used the rms noise level to estimate a lower limit of the  $\text{N}_2\text{H}^+$  column density to compute the ratio in these three IRDCs at the  $\text{NH}_3$  peak. The resulting values of the  $\text{NH}_3/\text{N}_2\text{H}^+$  ratio are  $> 1000$ ,  $> 9800$ , and  $> 3400$ , for G14.2–0.60, G28.53–00.25, and G30.88+00.13, respectively, significantly higher than the values found in other regions. The fact that  $\text{N}_2\text{H}^+$  is not detected may indicate that its emission arises from cold and diffuse regions, only seen with single-dish observations, and not from small compact dense cores. Further studies at high angular resolution and in several molecular species of IRDCs should be conducted to draw any definitive conclusion to explain the lack of  $\text{N}_2\text{H}^+$  emission at core scales.

### 2.4.2 Filamentary structures

As seen in section 2.3.2 the  $\text{NH}_3$  emission reveals extended clumpy filaments, sometimes appearing rather parallel, and which appear to be fragmented into chains of dense clumps elongated in the same direction as the filament. The velocity field along the filaments does not suffer significant variations, and they have, instead, approximately uniform velocity, suggesting that their presence is intrinsic to the cloud structure and not the result of evolutionary factors like star-formation activity. Moreover, these filamentary structures appear to be hierarchical. An intriguing feature is the enhancements of the linewidth along the strongest filaments. This could be due to the presence of a high-mass young stellar object deeply embedded in the  $\text{NH}_3$  dense gas, although we can not discard other interpretations like a superposition/merging of two filaments.

We compare the main properties of the filamentary structures seen in IRDC G14.2–0.60 with filaments seen in Taurus molecular cloud and in the Orion ridge. In G14.2–0.60, dense cores within a filament are uniformly distributed, with a typical

separation of  $\sim 40''$  or 0.45 pc. This value is one order of magnitude higher than the characteristic separation found in Orion, which is  $\sim 30''$  or 0.065 pc (Wiseman and Ho 1998). Concerning the dimensions of these filaments, in G14.2–0.60 we found lengths ranging from 1.3 pc up to 4.3 pc, with a typical length-to-diameter aspect ratio of 7:1. These values are slightly different than the dimension of the filaments seen in Taurus or Orion. The filaments in Taurus molecular cloud have lengths of 0.1–3 pc, and a length-to-diameter ratio of 15:1 (Goldsmith et al. 2008) whereas Orion filaments have typically  $\sim 0.5$  pc of length and a length-to-diameter aspect ratio of 10:1 (Wiseman and Ho 1998). It is worth noting that the studies performed in Taurus and Orion ridge reach spatial resolutions of  $\sim 6300$  AU and  $\sim 3800$  AU, respectively, a factor of 2–3 times better than our spatial resolution ( $\sim 12000$  AU), suggesting that filaments in G14.2–0.60 could be constituted of further filamentary substructures.

There are many questions regarding the origin and nature of these filamentary structures. Are they filaments or sheets? How did they form? Which is the agent responsible to make them nearly parallel? These filamentary nearly parallel structures could be the “limb-brightened” edges of tubes or cylinders, or maybe we are seeing two bundles of filaments which are formed by magnetic field lines. Cylindrical and sheetlike structures are thought to be gravitationally unstable and will collapse by fragmentation. This fragmentation process seems to be hierarchical, with chains of dense cores along the filament observed at different spatial scales, which can also be fragmented themselves, and so on. Another possibility is that these filamentary structures with different velocities can also come from bent filaments which have different projected velocities along the line of sight, and hence along the filament. Unfortunately, with the current data we cannot elucidate the nature and evolution of these structures. A key ingredient for understanding the relation of filamentary structures with the fragmentation process of a cloud are the direction and strength of the magnetic field. Future observations of the magnetic field at large and small scales would allow us to contrast observations with the current theories of fragmentation and star formation.

### 2.4.3 High-mass star formation in IRDC G14.2–0.60

In this chapter we have used two different tools as a diagnostic to evaluate whether or not clumps within the Infrared Dark Cloud G14.2–0.60 will eventually form massive

stars. On one hand, we applied the criterium of Krumholz and McKee (2008), for which surface density thresholds of  $0.7\text{--}1.5 \text{ g cm}^{-2}$  are required to form stars of  $10\text{--}200 M_{\odot}$ , respectively. In this theoretical work the authors show that only clouds with densities of at least  $\sim 1 \text{ g cm}^{-2}$  can avoid fragmentation and form massive stars. Using the dust emission from APEX we estimated the surface density of each clump (listed in Col. (5) of Table 2.3). In Fig. 2.16 we show a plot of the surface density against clump mass. The average surface density is  $\Sigma \simeq 0.1 \text{ g cm}^{-2}$ , and none of the clumps observed with APEX have a value above the theoretical  $\Sigma = 0.7 \text{ g cm}^{-2}$  for massive star formation according to Krumholz and McKee (2008). As already explained in Sec. 2.3.1 clumps in G14.2–0.60 may not be homogeneous but containing small and denser cores not resolved by our single-dish observations. Follow up observations with the SMA toward a particular clump show that these clumps actually fragment into several dust millimeter condensations. In this case the surface density exceeds the threshold value of  $0.7 \text{ g cm}^{-2}$  in 6 out of the 16 millimeter condensations detected with the SMA (see Fig. 2.16 and Table 2.7). Krumholz and McKee (2008) predict that clusters formed with  $\Sigma \ll 1 \text{ g cm}^{-2}$  should be deficient in massive stars. In SMMS10, the derived masses are in the range  $\sim 0.5\text{--}16 M_{\odot}$ , although they are not distributed equally, being more dominant the population of low-mass objects, with only 4 out of 16 detections having masses above  $10 M_{\odot}$ . Thus, in SMMS10 we could expect that at least 4 high-mass stars will be formed. However, these objects are supposed to be in the main accretion phase and thus they may grow in mass and eventually form a cluster of intermediate/high-mass stars, even when we found  $\Sigma = 0.127 \text{ g cm}^{-2}$  at clump size scales. Thus, we need to know not only the mass at cloud or clump scales ( $\sim 10 \text{ pc}$ ) from single-dish observation, but also look at core scales ( $\sim 0.1 \text{ pc}$ ) to really know whether or not a clump and/or core will form massive stars and star clusters.

On the other hand, we used the empirical mass-size threshold for massive star formation reported recently by Kauffmann and Pillai (2010). Based on clouds with and without massive star formation, the authors establish  $m(r) > 870 M_{\odot} (r/\text{pc})^{1.33}$  as a limit to form massive stars. IRDCs below this limit will form stars and clusters of low/intermediate mass, like in the Ophiuchus and Perseus molecular clouds (Kauffmann et al. 2010a,b). Using this relation we found that only 10 APEX clumps are potential sites for massive star formation (see Fig. 2.17 and Table 2.3), being SMMS10 one of them. Therefore, the two methods used here, one theoretical and the other one empirical (i. e., the surface density and mass-size thresholds for massive star formation), applied to G14.2–0.60 yield to the same conclusion that clump

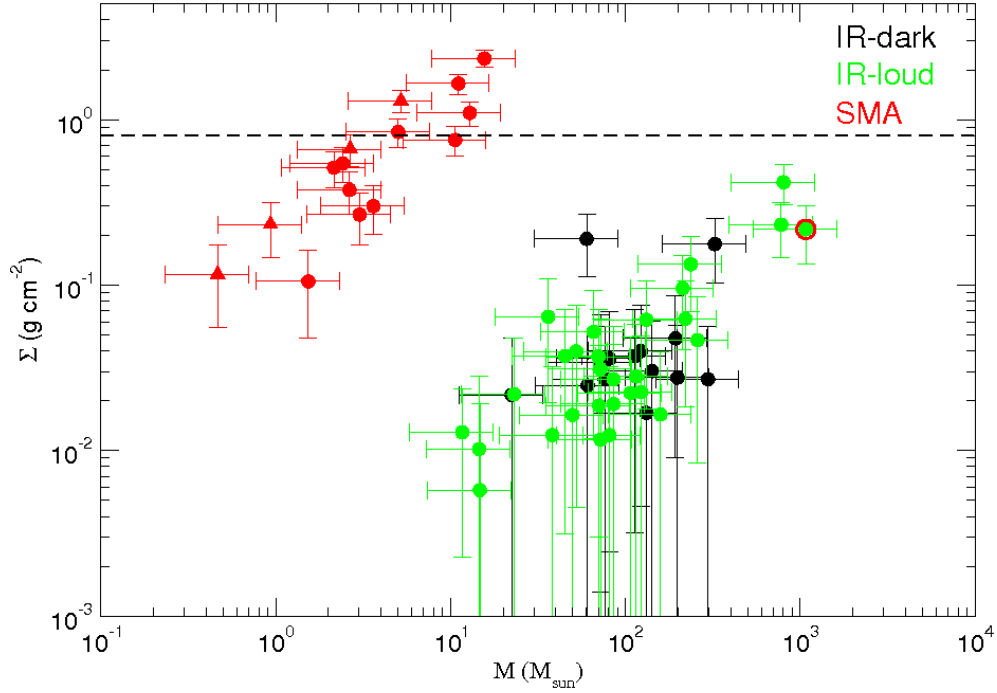


Figure 2.16: Surface density,  $\Sigma$ , against clump mass,  $M$ , of G14.2–0.60 for clumps devoid of an IR source (black dots), clumps containing IR emission (green dots). Clump SMMS10, observed with the SMA at high angular resolution, is highlighted by a red circle. The SMA millimeter condensations embedded in SMMS10 are denoted in red, with triangles representing a lower limit. The dot-dashed horizontal line marks the  $\Sigma$  threshold of  $0.7 \text{ g cm}^{-2}$  given by Krumholz and McKee (2008).

SMMS10 will form high-mass stars if they are applied to the appropriate spatial scale. We suggest that the empirical mass-size relation of Kauffmann and Pillai (2010) is more suitable to distinguish between clumps/cores that will form high-mass stars from those forming low- and intermediate-mass stars at large scales, while Krumholz and McKee (2008) criterion is better suited for small scales (i. e., cores).

#### 2.4.4 Fragmentation and cluster formation

In this section we discuss the fragmentation of SMMS10 using the 1.3 mm continuum data from the SMA. We detected 16 sources, with masses from 0.5 to  $16 M_{\odot}$ , and with an average separation of 0.05 pc. Based on our APEX observations at  $870 \mu\text{m}$ ,

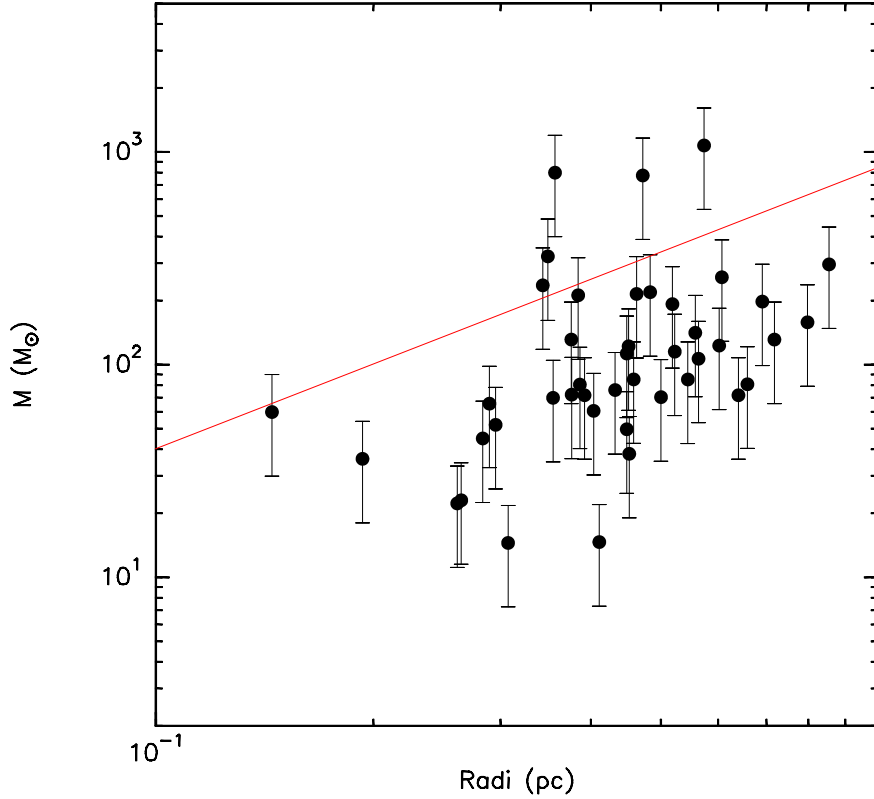


Figure 2.17: Mass against radii of clumps in G14.2-00.60. The red line represents the mass-size limit for massive star formation (Eq. 1 of Kauffmann and Pillai 2010).

the average density in the more densely packed region is  $\sim 4 \times 10^5 \text{ cm}^{-3}$ . The Jeans mass can be expressed as

$$M_J = 5M_\odot \left( \frac{T_k}{\text{K}} \right)^{3/2} \left( \frac{n}{\text{cm}^{-3}} \right)^{-1/2} \quad (2.4)$$

and the corresponding Jeans length is

$$\lambda_J = 0.19 \text{ pc} \left( \frac{T}{10 \text{ K}} \right)^{1/2} \left( \frac{n}{10^4 \text{ cm}^{-3}} \right)^{-1/2}. \quad (2.5)$$

For SMMS10 the Jeans mass is  $\sim 1 M_\odot$  and the Jeans length is 0.02 pc. Here we used an average kinetic temperature of  $\sim 23 \text{ K}$  derived from the  $\text{NH}_3$  data. The derived Jeans length is slightly smaller than the mean distance between the 16 sources. Even though our SMA observations spatially resolve the Jeans length (the angular resolution is  $\sim 1''.5$  or  $3450 \text{ AU} \sim 0.017 \text{ pc}$ ) we have measured separations

larger than the Jeans length, and masses larger than the thermal Jeans mass. Thus, it is not clear if the fragmentation of SMMS10 was purely thermal. Thus, other agents like turbulence and/or magnetic fields, in addition to thermal pressure and gravity may control the cloud fragmentation. In fact, from the  $\text{NH}_3$  data we obtained linewidths in the range of  $\sim 1.4 - 3.3 \text{ km s}^{-1}$ , much larger than the thermal line width of  $\sim 0.2 \text{ km s}^{-1}$ .

Zhang et al. (2009) investigate the initial fragmentation in the IRDC G28.34+0.60 comparing the observational results with the current theoretical models. The authors conclude that neither the competitive accretion model (Bonnell and Bate 2002) nor the turbulent accretion model (McKee and Tan 2002, 2003) can not explain the observational results even if one includes stellar feedback in both models. We performed a similar analysis to that done in Zhang et al. (2009). In the competitive accretion model of Bonnell and Bate (2002), clouds initially fragment into cores of Jeans mass  $\sim 0.5 M_\odot$ . Our  $3\sigma$  mass sensitivity is  $\sim 0.3 M_\odot$ , enough to allow us to detect low-mass objects of  $0.5 M_\odot$ . Despite our high sensitivity we only detected one object of  $0.5 M_\odot$ , and only 2 out of the 16 sources have a mass below  $1 M_\odot$ . Then, the masses in G14.2–0.60 SMMS10 are significantly larger than those assumed in the competitive accretion model. On the other hand, as proposed by Krumholz (2006) and Krumholz et al. (2007) heating from the embedded protostars produces an enhancement of the gas temperature and thus the Jeans mass increases. However, to reach a mass of  $16 M_\odot$ , we would need a gas temperature of 160 K, which is much larger (a factor of 6) than the gas temperature estimated from  $\text{NH}_3$ , and hence this mechanism of increasing Jeans mass is not sufficient to explain the observed masses. Another processes which could increase the Jeans mass is the inclusion of turbulence (Mac Low and Klessen 2004) and magnetic fields, which should suppress fragmentation, and these cloud play an important role in G14.2–0.60.

## 2.5 Conclusions

We observed with the APEX, FCRAO, and Effelsberg single-dish telescopes the continuum emission at  $870 \mu\text{m}$ , and the  $\text{N}_2\text{H}^+$  (1–0), and  $\text{NH}_3$  (1,1) and (2,2) emission toward the Infrared Dark Cloud G14.2–0.60. We additionally conducted interferometric observations of the  $\text{NH}_3$  molecule using the VLA to map the cloud and SMA 1.3 mm continuum observations of a selected clump. Our main conclusions can be

summarized as follows:

1. The dust emission at 870  $\mu\text{m}$  from APEX reveals 74 clumps forming filamentary structures and following the 8  $\mu\text{m}$  absorption feature remarkably well. The clump masses range from 11 to 1000  $M_{\odot}$ , and the clump sizes are  $\sim 0.2 - 1.2$  pc. The total mass of G14.2-0.60 is estimated to be  $\sim 5500 M_{\odot}$ , with an average density of  $n \simeq 1.6 \times 10^4 \text{ cm}^{-3}$ . The mean value of the hydrogen column density is  $\sim 2 \times 10^{22} \text{ cm}^{-2}$  and the visual extinction averaged for all clumps in the cloud is  $\sim 23$  magnitudes.
2. We built the cumulative mass spectrum for the clumps detected with APEX using a single power-law. The best fit was obtained for  $\beta = -1.5$ , a relatively flat slope if we compare with other regions but in agreement with the clump mass function derived from CO molecular gas observations by Kramer et al. (1998).
3. The combined single-dish and interferometric image of  $\text{NH}_3(1,1)$  shows the presence of highly structured filaments, which appear to be fragmented into chains of dense cores. The length-to-diameter aspect ratio is on average 7:1. What is more, the filamentary structures seem to be hierarchical, as they are seen at different scales. Further observations, in particular of magnetic fields at large and small scales, should be conducted in order to understand the origin, nature and evolution of these filaments.
4. We performed the  $\text{NH}_3/\text{N}_2\text{H}^+$  ratio toward some selected positions of the IRDC G14.2-0.60, both in clumps with signpost of star formation activity and in pre-protostellar cores candidates. The resulting values are in the range 400–700, higher than typical values found in other star-forming regions, probably because of our poor spatial resolution. We found hints of a possible trend of the  $\text{NH}_3/\text{N}_2\text{H}^+$  ratio with the evolutionary stage along filament P12-main. The preliminary results on the high angular resolution  $\text{N}_2\text{H}^+$  data show that this molecule is not or marginally detected in IRDCs. Thus, further observations toward other IRDCs are required to find out the behavior of  $\text{N}_2\text{H}^+$  in these clouds.
5. The high angular resolution 1.3 mm continuum observations performed with the SMA reveal a cluster of 16 millimeter sources, with masses from 0.5 to

16  $M_{\odot}$ , all of them embedded in SMMS10 clump. A comparison of our observational results with the current theoretical models for massive stars and cluster formation seems to indicate that neither the competitive accretion model of Bonnell and Bate (2002) nor the turbulent accretion model of McKee and Tan (2002) can explain the observed properties of the observed cluster. Future high sensitivity observations at millimeters/submillimeter wavelengths with high angular resolution of the IRDC G14.2—0.60 would provide some insights into the process of fragmentation during the earliest stages of massive star formation, and for this ALMA will be the most suitable instrument.

6. We applied two different methods to study the capability of each clump to form massive stars. First, we estimated the surface density for each clump detected with APEX and found that none of the clumps have a surface density above the theoretical values of  $\Sigma = 0.7 \text{ g cm}^{-2}$  required to form massive stars according to Krumholz and McKee (2008). On the other hand, we used the new empirical mass-size threshold for massive star formation (Kauffmann and Pillai 2010), and the results show that only 10 out of the 43 clumps (i. e., a 23 %) resolved with APEX are potential sites to form massive stars. Since the high angular resolution observations actually reveals the presence of an embedded cluster within one of the clumps exceeding the threshold limit, we suggest that the mass-size relation is more suitable to distinguish between clumps that will form high-mass stars from those forming low/intermediate-mass stars at clump scales (observed with single-dish telescopes) while the theoretical threshold of Krumholz and McKee (2008) is better suited for small scales.



## Chapter 3

# The $\text{NH}_3/\text{N}_2\text{H}^+$ abundance ratio in a sample of high-mass star-forming regions

### 3.1 Introduction

As we have seen in the previous chapter, to study dense cores in high-mass star-forming regions, typically at distance  $\geq 1$  kpc, we need to observe them with high angular resolution in order to resolve the emission of each individual core. Then, in this chapter and the following ones, we will zoom in five high-mass star-forming regions observed with interferometers.

In this chapter we report on high angular resolution observations of dense gas tracers molecules,  $\text{NH}_3$  and  $\text{N}_2\text{H}^+$ , toward a sample of nearby ( $d \lesssim 2.5$  kpc) massive star-forming regions, selected from the lists of high-mass protostellar candidates from Sridharan et al. (2002) and Molinari et al. (1996). Our sample consists of three massive star-forming regions: IRAS 00117+6412, IRAS 20126+4104, and IRAS 22134+5834. The sample sources, their IRAS coordinates, distance, luminosity, and the evolutionary stage of the most massive object are listed in Table 3.1. All regions contain dense cores in different evolutionary stages, while IRAS 20126+4104 contains a hot molecular core, IRAS 00117+6412 and IRAS 22134+5834 are tracing an UCHII region that is in the process of clearing up its molecular material. Fur-

Table 3.1: Observed sample

| Source          | $\alpha(J2000)$<br>(h:m:s) | $\delta(J2000)$<br>(°:':") | $d$<br>(kpc) | $L_{\text{bol}}$<br>( $L_{\odot}$ ) | Evolutionary<br>stage | Survey <sup>a</sup> |
|-----------------|----------------------------|----------------------------|--------------|-------------------------------------|-----------------------|---------------------|
| IRAS 00117+6412 | 00:14:27.7                 | 64:28:46                   | 1.8          | 1400                                | UCHII region          | M96                 |
| IRAS 20126+4104 | 20:14:26.0                 | 41:13:31                   | 1.7          | 13000                               | Hot Core              | M96, S02            |
| IRAS 22134+5834 | 22:15:09.1                 | 58:49:09                   | 2.6          | 12500                               | UCHII region          | S02                 |

**Notes.** <sup>a</sup> M96: Molinari et al. (1996); S02: Sridharan et al. (2002)

thermore, all of them are associated with molecular outflow emission, and contain both pre-protostellar and protostellar cores, being thus excellent targets to study the effects of temperature, UV radiation and molecular outflows on the chemistry of the dense gas and to further investigate the behavior of the  $\text{NH}_3/\text{N}_2\text{H}^+$  abundance ratio in the high-mass regime.

## 3.2 Observations

### 3.2.1 Very Large Array observations

The observations of  $(J, K) = (1, 1)$  and  $(J, K) = (2, 2)$  inversion lines of the ammonia molecule towards I00117 were carried out using the Very Large Array (VLA)<sup>a</sup> on 2007 May 12 with the array in its D configuration with 9 EVLA antennas. The phase center of these observations was  $\alpha(J2000) = 00^{\text{h}}14^{\text{m}}27^{\text{s}}.725$ ,  $\delta(J2000) = +64^{\circ}28'46''.171$ . Absolute flux calibration was achieved by observing 1331+305 and 0137+331, with an adopted flux density of 2.41 Jy and 1.05 Jy, respectively. The bandpass calibrator was 0319+415 (3C84), and phase calibration was performed by observing 0102+584, with a bootstrapped flux of  $3.85 \pm 0.06$  Jy. We used the 4IF spectral line mode, which allows simultaneous observations of the  $\text{NH}_3$  (1,1) and (2,2) lines with two polarizations for each line. The bandwidth was 3.12 MHz, and the channel separation was 48.8 kHz, corresponding to  $0.6 \text{ km s}^{-1}$ .

<sup>a</sup>The National Radio Astronomy Observatory is a facility of the National Science Foundation operated under cooperative agreement by the Associated Universities, Inc

Table 3.2: Observational parameters

| Observation                         | Frequency<br>(GHz) | Telescope | Config. | Beam<br>(arcsec)   | PA<br>( $^{\circ}$ ) | Spec. resol.<br>( $\text{km s}^{-1}$ ) | rms<br>( $\text{mJy beam}^{-1}$ ) |
|-------------------------------------|--------------------|-----------|---------|--------------------|----------------------|--|-----------------------------------|
| <b>IRAS 00117+6412</b>              |                    |           |         |                    |                      |  |                                   |
| NH <sub>3</sub> (1, 1)              | 23.694             | VLA       | D       | $3.91 \times 3.52$ | 46                   | 0.6                                    | 2.2 <sup>a</sup>                  |
| NH <sub>3</sub> (2, 2)              | 23.722             | VLA       | D       | $4.90 \times 4.30$ | 49                   | 0.6                                    | 2.2 <sup>a</sup>                  |
| <b>IRAS 22134+5834</b>              |                    |           |         |                    |                      |  |                                   |
| N <sub>2</sub> H <sup>+</sup> (1–0) | 93.176             | CARMA     | D       | $5.49 \times 4.09$ | –82                  | 0.4                                    | 45 <sup>a</sup>                   |
| NH <sub>3</sub> (1, 1)              | 23.694             | VLA       | D       | $3.77 \times 3.10$ | 88                   | 0.3                                    | 1.7 <sup>a</sup>                  |
| NH <sub>3</sub> (2, 2)              | 23.722             | VLA       | D       | $3.69 \times 3.00$ | 84                   | 0.3                                    | 1.7 <sup>a</sup>                  |
| <b>IRAS 20126+4104</b>              |                    |           |         |                    |                      |  |                                   |
| N <sub>2</sub> H <sup>+</sup> (1–0) | 93.173             | BIMA      | C+D     | $7.58 \times 6.92$ | 76                   | 0.3                                    | 70 <sup>a</sup>                   |
| NH <sub>3</sub> (1, 1)              | 23.694             | VLA       | D       | $3.57 \times 3.20$ | 10                   | 0.3                                    | 3.5 <sup>a</sup>                  |
| NH <sub>3</sub> (2, 2)              | 23.722             | VLA       | D       | $3.68 \times 3.05$ | 29                   | 0.3                                    | 3.5 <sup>a</sup>                  |
| Continuum                           | 346.510            | SMA       | Sub.    | $4.42 \times 4.04$ | 31                   | ...                                    | 10                                |

**Notes.** <sup>a</sup> per channel

Data reduction was conducted following the VLA high-frequency guidelines for calibration and imaging using the Astronomical Imaging Processing System (AIPS) of the NRAO. Images were obtained using the robust parameter of Briggs (1995) set equal to 5. In addition, for the NH<sub>3</sub> (2, 2) transition we applied a  $uv$ -taper function of  $40 k\lambda$  in order to improve the sensitivity and recover the extended emission.

Searching the VLA archive, we found NH<sub>3</sub> observations in IRAS 22134+5834 (project AK558). The observations of NH<sub>3</sub> (1,1) and (2,2) were carried out on 2003 May 1st with the array in its D configuration. The phase center of these observations was  $\alpha(\text{J2000}) = 22^{\text{h}}15^{\text{m}}08^{\text{s}}.10$ ,  $\delta(\text{J2000}) = +58^{\circ}49'10''.0$ . Absolute flux calibration was achieved by observing 1331+305 (3C286) and 0137+331 (3C48), with an adopted flux density of 2.41 Jy and 1.05 Jy, respectively. The bandpass calibrator was 0319+415 (3C84) and 1221+020 (3C273), and phase calibration was performed by observing 2148+611, with a bootstrapped flux of  $0.595 \pm 0.004$  Jy. Simultaneous observations of the NH<sub>3</sub> (1,1) and NH<sub>3</sub> (2,2) lines were conducted using the 2IF spectral line mode. The bandwidth was 3.125 MHz, and the channel separation was 24.4 kHz, corresponding to  $0.31 \text{ km s}^{-1}$  at 1.3 cm. Data reduction was conducted following the VLA high-frequency guidelines for calibration and imaging using AIPS of the NRAO. Images were obtained using the robust parameter of Briggs (1995) set equal to 5.

We performed observations of the  $(J, K) = (1, 1)$  and  $(J, K) = (2, 2)$  inversion

transition line of the ammonia molecule towards the massive star-forming region IRAS 20126+4104 (hereafter I20126) using the VLA on 1999 May 30 in its D configuration. The phase center of the observations was  $\alpha(\text{J2000}) = 20^{\text{h}}14^{\text{m}}26^{\text{s}}05$ ,  $\delta(\text{J2000}) = +41^{\circ}13'31''5$ . Quasars 3C48 and 3C286 were used for flux calibration, with an adopted flux density of 2.41 Jy and 1.05 Jy, respectively. Bandpass calibration was performed by observing 3C273 and 3C84, and phase calibration was performed by observing 2013+370. We used the 2IF spectral line mode, which allows simultaneous observations of the  $\text{NH}_3$  (1,1) and  $\text{NH}_3$  (2,2) lines. The bandwidth was 3.125 MHz with 128 channels with a channel spacing of 24.4 kHz, corresponding to  $0.31 \text{ km s}^{-1}$  at 1.3 cm, centered at  $v_{\text{LSR}} = -3.9 \text{ km s}^{-1}$ , plus a continuum channel that contains the average of the central 75 % of the bandwidth. Data reduction was conducted following the standard procedures of AIPS of the NRAO, and images were constructed using the robust parameter of Briggs (1995) set equal to 5.

In Table 3.2 we summarize the observational parameters, the resulting synthesized beams and the final rms noise.

### 3.2.2 CARMA observations

The 3.2 mm continuum and  $\text{N}_2\text{H}^+$  (1–0) emission were observed towards I22134 with the Combined Array for Research in Millimeter-wave Astronomy (CARMA)<sup>b</sup> on 2008 June 23 using the array in the D configuration with 14 antennas (five 10.4 m antennas and nine 6 m antennas). The phase center was  $\alpha(\text{J2000}) = 22^{\text{h}}15^{\text{m}}09^{\text{s}}23$ ,  $\delta(\text{J2000}) = +58^{\circ}49'08''9$ , and the projected baselines ranged from 9.6 m to 137.6 m. The FWHM of the primary beam at the frequency of the observations was  $132''$  for the 6 m antennas and  $77''$  for the 10 m antennas. System temperatures were around 200 K.

The digital correlator was configured to observe simultaneously the continuum emission and the  $\text{N}_2\text{H}^+$  (1–0) group of the hyperfine transitions (93.176331 GHz, in the lower side band). The continuum data were recorded in two  $\sim 500$  MHz

---

<sup>b</sup>Supports for CARMA construction was derived from the Gordon and Betty Moore Foundation, the Kenneth t. and Eileen L. Norris Foundation, the Associates of the California Institute of Technology, the states of California, Illinois, and Maryland, and the National Science Foundation. Ongoing CARMA development and operations are supported by the National Science Foundation under a cooperative agreement, and by the CARMA partner universities.

bands covering the frequency ranges 93.47–93.91 GHz and 96.06–97.50 GHz from the receivers lower and upper sidebands, respectively. We used two consecutive and overlapping bands of 8 MHz of bandwidth with 63 channels in each band, providing a spectral resolution of  $0.42 \text{ km s}^{-1}$  to observe the  $\text{N}_2\text{H}^+$  (1–0) emission.

Phase calibration was performed with BLLAC, and flux and bandpass calibration was set by using MWC 349 and 3C454.3, respectively. Data were calibrated and imaged using the standard procedures in MIRIAD (Sault et al. 1995). The rms noise level was  $\sim 45 \text{ mJy beam}^{-1}$  per  $0.42 \text{ km s}^{-1}$  channel in the line data. The resulting synthesized beam is  $5''.5 \times 4''.1$ , P. A. =  $-82^\circ$ . The  $\text{N}_2\text{H}^+$  emission was cleaned using a box around the emitting region. In Table 3.2 we summarized the observational parameters.

### 3.2.3 BIMA observations

The  $\text{N}_2\text{H}^+$  (1–0) line at 93.173 GHz was observed towards I20126 with the Berkeley-Illinois-Maryland Array (BIMA)<sup>c</sup> at Hat Creek. The observations were carried out on 1999 March 28 in the D configuration, and on 1999 April 13 in the C configuration, with 10 antennas in the array. The phase center of the observations was  $\alpha(J2000) = 20^{\text{h}}14^{\text{m}}25^{\text{s}}35$ ,  $\delta(J2000) = +41^\circ13'12''.9$ . The FWHM of the primary beam at the frequency of the observations was  $\sim 120''$ .

The digital correlator was configured to observe the  $\text{N}_2\text{H}^+$  (1–0) group of the hyperfine transitions (93.176331 GHz, in the lower side band). We used a bandwidth of 25 MHz with 256 channels of 100 kHz width, providing a spectral resolution of  $0.32 \text{ km s}^{-1}$ . Phase calibration was performed with 2013+370. Data were calibrated and imaged using the standard procedures in MIRIAD (Sault et al. 1995). The main observational parameters are listed in Table 3.2.

---

<sup>c</sup>The BIMA array was operated by the Berkeley-Illinois-Maryland Association with the support from the National Science Foundation.

### 3.2.4 SMA observations

The Submillimeter Array (SMA<sup>d</sup>; Ho et al. 2004) was used to observe the 0.85 mm continuum emission (centered at 346.51 GHz in the upper sideband) towards I20126 on 2007 April 27 with 6 antennas in the subcompact configuration. The phase center of the observations was  $\alpha(J2000) = 20^{\text{h}}14^{\text{m}}26^{\text{s}}.04$ ,  $\delta(J2000) = +41^{\circ}13'32''.6$  and the projected baselines ranged from  $7 k\lambda$  to  $28 k\lambda$ . The half-power width of the SMA primary beam was  $\sim 35''$ .

The digital spectral correlator, which has a bandwidth of 2 GHz in each sideband, was set to the standard mode, which provides a spectral resolution of 0.8125 MHz (or  $0.7 \text{ km s}^{-1}$  per channel) across the full band-width. The raw data were calibrated with the MIR-IDL<sup>e</sup> package, originally developed for the Owens Valley Radio Observatory (OVRO; Scoville et al. 1993) and adopted for the SMA. The passband response was obtained from observations of 3 C273. The baseline-based calibration of the amplitudes and phases was performed using mwc349a, and flux calibration was set by using 3 C273. Imaging and data analysis were conducted using the standard procedures of MIRIAD (Sault et al. 1995) and AIPS. The continuum was obtained by averaging all the line-free channels of the upper sideband and the lower sideband. Cleaned images were made with a robust parameter of  $-2$ , which is close to uniform weighting. The resulting synthesized beam size was  $4''.42 \times 4''.04$  with a position angle of  $31^\circ$ , and the achieved rms noise level was  $10 \text{ mJy beam}^{-1}$ . The observational parameters are summarized in Table 3.2.

## 3.3 IRAS 00117+6412

### 3.3.1 Description

IRAS 00117+6412 (hereafter I00117) has a bolometric luminosity of  $1400 L_\odot$  and is located at a distance of 1.8 kpc (Molinari et al. 1996). The brightest infrared

---

<sup>d</sup>The SMA is a joint project between the Smithsonian Astrophysical Observatory and the Academia Sinica Institute of Astronomy and Astrophysics, and is funded by the Smithsonian Institution and the Academia Sinica.

<sup>e</sup>The MIR cookbook by Charlie Qi can be found at <http://cfa-www.harvard.edu/~cqi/mircook.html>

source in the Two Micron All Sky Survey Catalog of Point Sources (2MASS PSC, Skrutskie et al. 2006) is associated with compact centimeter emission tracing an UCHII region produced by a B2 star at the border of a dusty cloud (Sánchez-Monge et al. 2008). The dusty cloud, located  $\sim 15''$  to the west of the UCHII region, is associated with an embedded cluster reported by Kumar et al. (2006), two H<sub>2</sub>O maser spots (Cesaroni et al. 1988; Wouterloot et al. 1993), and CO (2–1) bipolar molecular outflow emission (Zhang et al. 2005; Kim and Kurtz 2006; Palau et al. 2010). Interferometric millimeter observations carried out recently with the PdBI and the SMA (Palau et al. 2010) show two main millimeter sources, MM1 and MM2, separated  $\sim 15''$ , and deeply embedded in the dusty cloud. Subsequent centimeter observations with higher angular resolution at 3.6 cm reveal that the UCHII region is actually resolved into two components, one of them associated with MM1 whose spectral index is compatible with an ionized wind (Palau et al. 2010). Furthermore, MM1, associated with a 2MASS infrared source and driving a CO (2–1) powerful and collimated high-velocity outflow elongated in the northeast-southwest direction, is an intermediate-mass YSO in the Class 0/Class I phase. On the other hand, the intermediate-mass source MM2, associated with H<sub>2</sub>O maser emission, is undergoing rotation and infall motions but no hints of CO (2–1) molecular outflow neither infrared emission are found associated with it, indicating that MM2 is most likely in an extremely early evolutionary stage. Regarding the dense gas emission of the region, I00117 harbors three main clumps traced by the N<sub>2</sub>H<sup>+</sup> molecule, one associated with MM1, another clump associated with MM2, and a third clump falling at the southwestern edge of the field (Palau et al. 2010). Thus, while the UCHII region has already cleared up the natal cloud, active star formation is taking place in the surrounding dense gas.

### 3.3.2 Results

The zero-order moment map of the NH<sub>3</sub> (1,1) integrated for the main line and inner satellite lines is shown in Fig. 3.1a overlaid on the  $K_s$ -band image of 2MASS. The NH<sub>3</sub> (1,1) integrated emission consists of two main clumps, named MM1 ridge and MM2. The MM1 ridge, with a size of  $\sim 20''$  ( $\sim 0.2$  pc), is elongated in the northeast-southwest direction, in the same direction as the CO (2–1) molecular outflow and

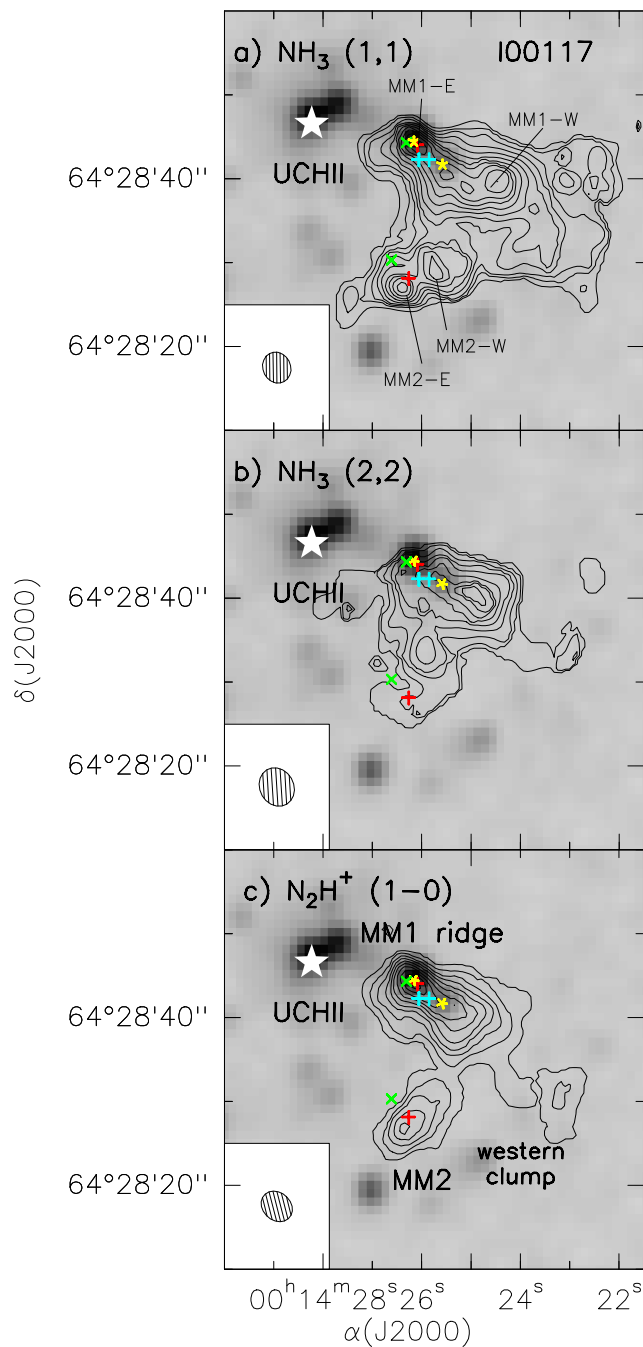


Figure 3.1: **a)** Zero-order moment for the  $\text{NH}_3$  (1,1) line. Contours start at 10 %, increasing in steps of 10 % of the peak intensity,  $0.07 \text{ Jy beam}^{-1} \text{ km s}^{-1}$ . **b)**  $\text{NH}_3$  (2,2) zero-order moment. Contours start at 20 %, increasing in steps of 8 % of the peak intensity  $0.02 \text{ Jy beam}^{-1} \text{ km s}^{-1}$ . **c)**  $\text{N}_2\text{H}^+$  zero-order moment integrated for all the hyperfine components of the (1–0) transition from Palau et al. (2010). Contours start at 5 %, increasing in steps of 10 % of the peak intensity,  $0.36 \text{ Jy beam}^{-1} \text{ km s}^{-1}$ . In all panels Grey scale is the 2MASS  $K_s$ -band infrared emission. The white star marks the position of the UCHII region IRAS 00117+6412. Red crosses indicate the position of MM1 and MM2 and blue crosses mark the position of MM1-south and MM1-southwest (see Palau et al. 2010). The green titled crosses indicate the  $\text{H}_2\text{O}$  maser spots (Cesaroni et al. 1988), and the yellow five-point stars indicate the position of 2MASS sources associated with the millimeter sources. The synthesized beams for each transition are shown in the bottom left corner, and are listed in Table 3.2.

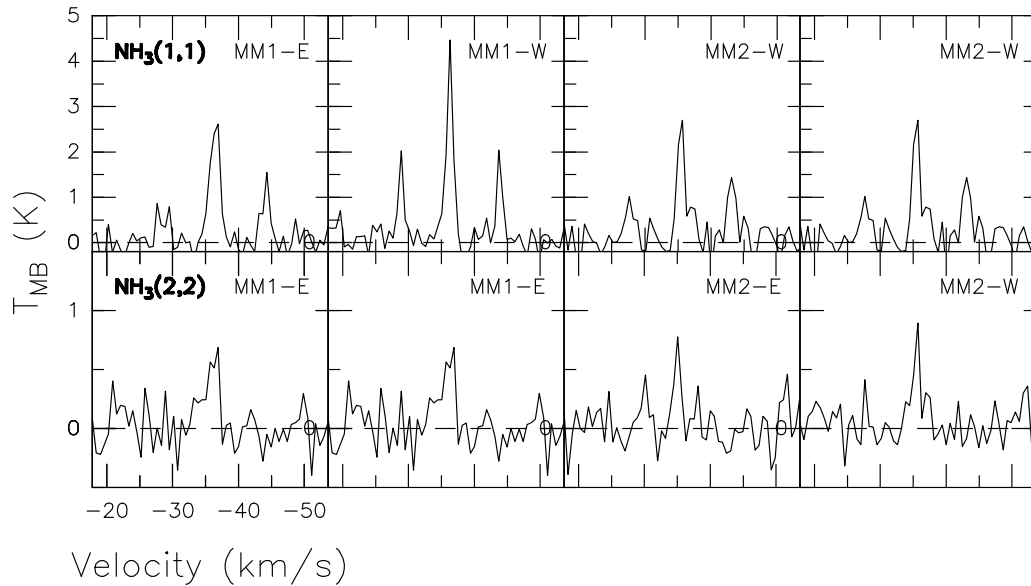


Figure 3.2: Spectra toward 4 positions of the IRAS 00117+6412  $\text{NH}_3$  (1,1) (*top*) and  $\text{NH}_3$  (2,2) (*bottom*). The 4 positions, which are labeled in the top right corner of each panel, are, from left to right MM1-E, MM1-W, MM2-E, and MM2-W.

the  $\text{N}_2\text{H}^+$  emission axis (Palau et al. 2010). Actually, this clump is resolved into two main components, one of them, MM1-E core is associated with the millimeter condensation MM1 and the other one MM1-W core, located  $\sim 10''$  to the southwest, has no signpost of stellar activity associated with it. Furthermore, two additional cores are detected along the ridge structure connecting MM1-E and MM1-W. The MM2 clump, located  $\sim 20''$  to the south of MM1, is elongated in the southeast-northwest direction with a length of  $\sim 10''$ , or 0.09 pc at the distance of the source. MM2 also consists of two  $\text{NH}_3$  cores, MM2-E, associated with the millimeter source MM2, and MM2-W located  $\sim 5''$  to the north-west. In addition, we found faint and extended  $\text{NH}_3$  emission toward the western edge of the field, partially coinciding with the western clump, where there is no millimeter neither centimeter continuum emission associated.

In Fig. 3.1b we present the zero-order moment map of the  $\text{NH}_3$  (2,2) main line.  $\text{NH}_3$  (2,2) emission resembles closely that of  $\text{NH}_3$  (1,1) but being more compact. However, we did not detect  $\text{NH}_3$  (2,2) associated with the western clump, and MM2 is marginally detected in  $\text{NH}_3$  (2,2). The  $\text{NH}_3$  (2,2) emission in the eastern edge of the MM1 clump shows emission reaching the southern side of the UCH II region. It

is worth noting that we did not detect dense gas emission associated with the UCH II region, indicating that the UCH II region has already cleared up its natal material. Finally, we show in Fig. 3.1c the integrated  $\text{N}_2\text{H}^+$  (1–0) emission from Palau et al. (2010) to compare the emission of both dense gas tracers. The emission of  $\text{NH}_3$  roughly mimics the  $\text{N}_2\text{H}^+$  emission, but being the  $\text{NH}_3$  emission more extended. This is a consequence of VLA being more sensitive to larger angular scales than the PdBI. However, there are significant differences between both molecules. For instance, in the MM1 clump the  $\text{N}_2\text{H}^+$  emission peaks at the position of the millimeter condensation (i. e., in MM1-E), whereas the strongest core in  $\text{NH}_3$  is found associated with MM1-W.

Spectra, not corrected for the primary beam response, for  $\text{NH}_3$  (1,1) and  $\text{NH}_3$  (2,2) are shown in Fig. 3.2.

## 3.4 IRAS 22134+5834

### 3.4.1 Description

IRAS 22134+5834 (hereafter I22134) has a bolometric luminosity of  $\sim 12400 L_\odot$  and is located at a distance of 2.6 kpc. The source is found in a compact molecular cloud detected in  $^{12}\text{CO}$  (1–0) and  $^{13}\text{CO}$  (1–0) by Dobashi et al. (1994). The emission at millimeter wavelengths shows an extended and elliptical distribution with a single resolved peak centered on the IRAS source (Chini et al. 2001; Beuther et al. 2002a). In addition, the IRAS source is associated with a compact centimeter continuum source with a flat spectral index in all the centimeter range ( $\alpha \simeq -0.1$ ), tracing a cometary UCHII region (Sánchez-Monge 2011). The dusty cloud is associated with an embedded cluster reported by Kumar et al. (2006),  $\text{H}_2\text{O}$  maser emission (Cesaroni et al. 1988; Wouterloot et al. 1993), and a massive molecular outflow (Dobashi and Uehara 2001; Beuther et al. 2002b; López-Sepulcre et al. 2010). Regarding the near-infrared emission in the region, Kumar et al. (2003) find a rich centrally symmetric and flattened embedded cluster and a central dark region, probably an empty cavity, surrounded by a ring of bright and massive stars associated with the FIR/(sub)millimeter emission. All the bright stars in the ring are found to have intrinsic infrared excess emission and are likely to be early-to late-B type stars (Kumar et al. 2003). The dense gas emission has been studied with single-dish

telescopes in CS, HCO<sup>+</sup>, H<sup>13</sup>CO<sup>+</sup>, N<sub>2</sub>H<sup>+</sup>, H<sub>2</sub>CO, NH<sub>3</sub> (1,1) and (2,2), HCN, and C<sup>18</sup>O (Beuther et al. 2002a; Richards et al. 1987; Fuller et al. 2005; Sridharan et al. 2002; López-Sepulcre et al. 2010), with all molecules peaking close to the position of the IRAS source, marked in Fig. 3.3 with a red star.

### 3.4.2 Results

The zero-order moment map of the NH<sub>3</sub> (1,1) emission (integrated for the main and inner satellite lines) is shown in Fig 3.3a, where we also show the 2MASS  $K_s$ -band image. Using the photometry of the 2MASS catalog, we estimated the infrared excess for each 2MASS source from the  $(J - H)$  vs.  $(H - K)$  diagram, measured as the difference between the  $(H - K)$  color and the  $(H - K)$  color corresponding to a reddened main-sequence star following the reddening law of Rieke and Lebofsky (1985). We assigned a different color to each infrared excess interval: blue for infrared excesses  $< -0.4$ ; green for the interval  $(-0.4-0)$ , corresponding to main-sequence stars, giants, and Class III and II sources with small infrared excess; yellow for  $(0-0.4)$ , corresponding to Class II sources; and red for infrared excesses  $> 0.4$ , corresponding to Class 0/I protostars (Matsuyanagi et al. 2006). The NH<sub>3</sub> emission in IRAS 22134+5834 consists of 10 main cores, with sizes ranging from 0.02 pc to 0.06 pc, forming an extended and irregular structure of  $\sim 70''$  in size ( $\sim 0.9$  pc) and elongated in the east-west direction. Most of the dense NH<sub>3</sub> cores are located to the south of the UCHII region, which has already cleared up part of its molecular material. As can be seen in Fig. 3.3a, core A and core B seem to contain an infrared source embedded in the dense gas, located close to the position of the NH<sub>3</sub> peak, with typical colors of Class 0/I and Class II sources, respectively, whereas the other cores appear to be starless. Figure 3.3b shows the zero-order moment map of the NH<sub>3</sub> (2,2) emission, which is more compact than that of the NH<sub>3</sub> (1,1).

The zero-order moment map of N<sub>2</sub>H<sup>+</sup> (1-0), integrated for all the hyperfine transitions, is presented in Fig. 3.3c. The morphology of the N<sub>2</sub>H<sup>+</sup> emission resembles that of the NH<sub>3</sub> (1,1) emission. All cores seen in NH<sub>3</sub> are detected in N<sub>2</sub>H<sup>+</sup>. However, the angular resolution achieved in the N<sub>2</sub>H<sup>+</sup> observations is not enough to resolve some substructures seen in NH<sub>3</sub>.

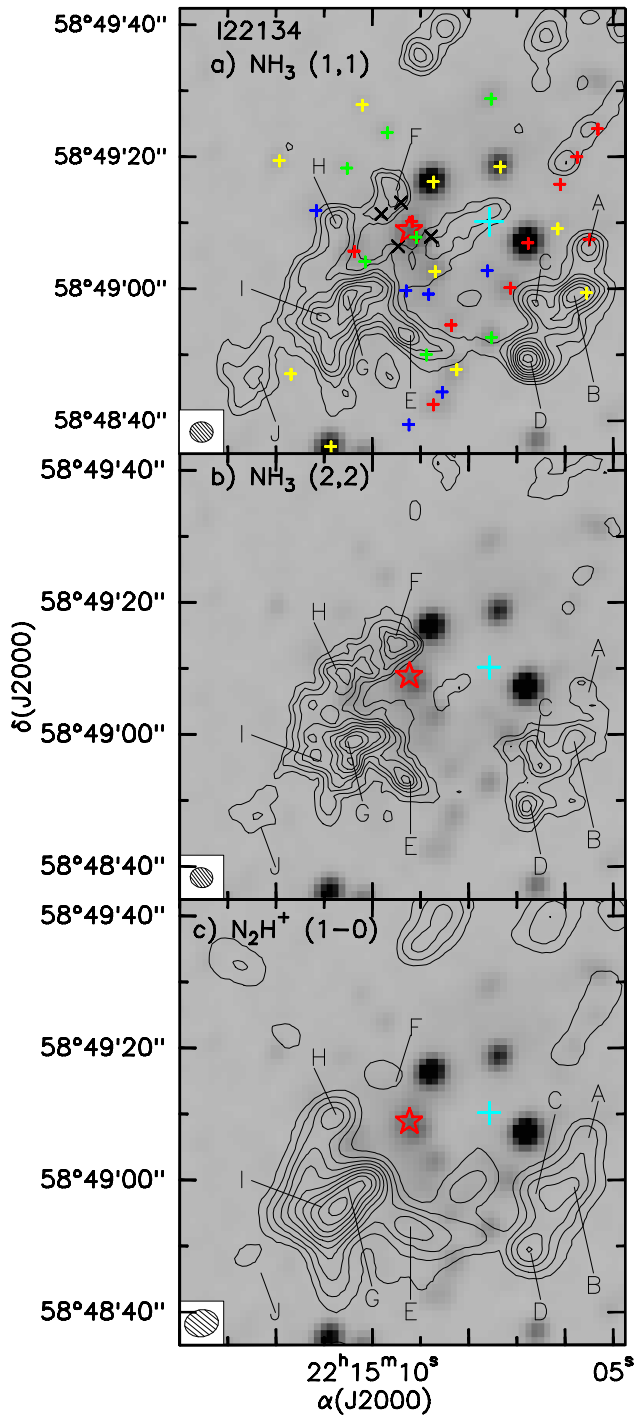


Figure 3.3: **a)**  $\text{NH}_3(1,1)$  zero-order moment. Contours start at 15 %, increasing in steps 10 % of of the peak intensity  $0.032 \text{ Jy beam}^{-1}\text{km s}^{-1}$ . **b)**  $\text{NH}_3(2,2)$  zero-order moment. Contours start at 10 %, increasing in steps of 10 % of the peak intensity  $0.018 \text{ Jy beam}^{-1}\text{km s}^{-1}$ . **c)**  $\text{N}_2\text{H}^+$  zero-order moment integrated for all the hyperfine components of the (1–0) transition. Contours start at 5 %, increasing in steps of 10 % of the peak intensity  $3.78 \text{ Jy beam}^{-1}\text{km s}^{-1}$ . Grey scale is the 2MASS  $K_s$ -band infrared emission. The red star marks the position of the UCHII region, IRAS 22134+5834. The blue cross indicates the position of  $\text{H}_2\text{O}$  maser emission (Cesaroni et al. 1988), and black titled crosses show the 4 millimeter condensations detected by Palau et al. in prep. Color crosses indicate 2MASS sources with the color corresponding to different infrared excess as described in the text. The synthesized beams for each transition are shown in the bottom right corner, and are listed in Table 3.2. Dense cores are labeled in each panel.

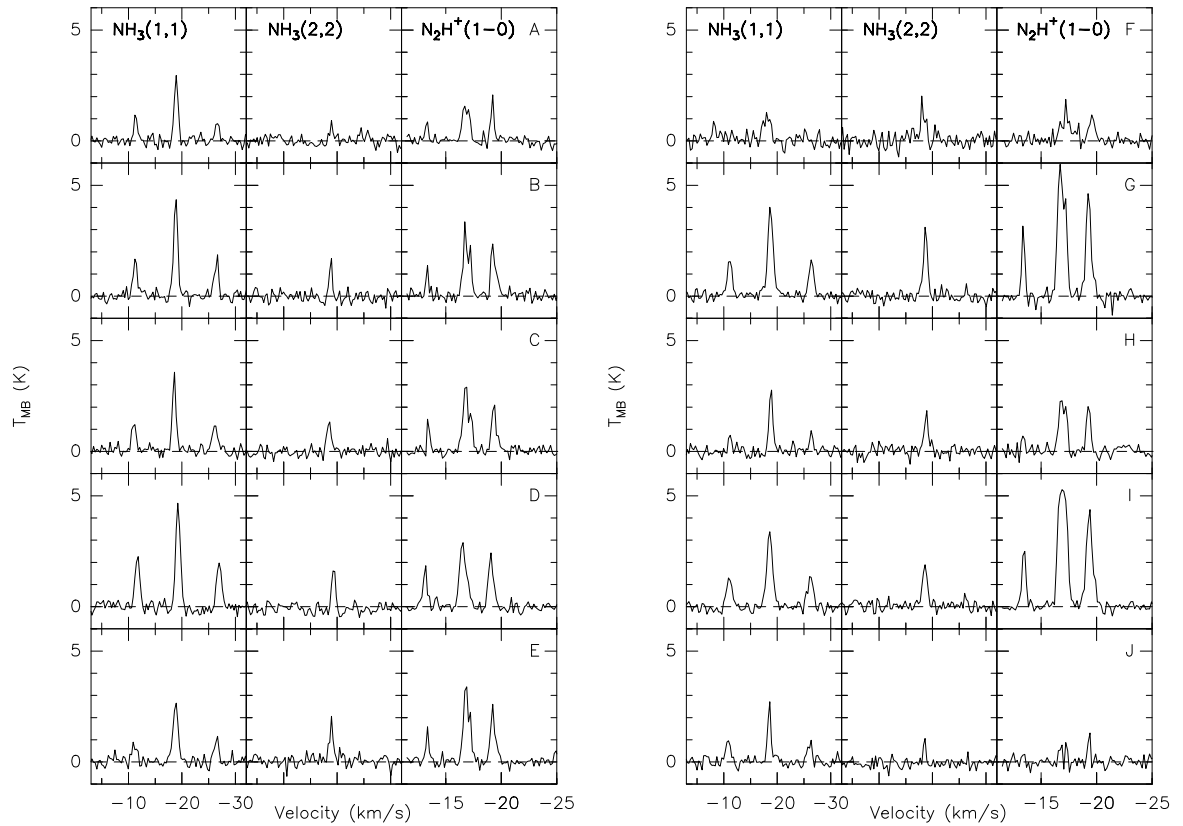


Figure 3.4: Spectra toward 10 positions of the IRAS 22134+5834 region for the three transitions studied, from left to right,  $\text{NH}_3(1,1)$ ,  $\text{NH}_3(2,2)$ , and  $\text{N}_2\text{H}^+(1-0)$ . The ten positions are labeled on the right panel of each row, and correspond to the ten cores labeled in Fig. 3.3.

In Fig. 3.4 we show the spectra, not corrected for the primary beam response, of  $\text{NH}_3(1,1)$ ,  $\text{NH}_3(2,2)$ , and  $\text{N}_2\text{H}^+(1-0)$  toward each core. As can be seen in this figure, while the  $\text{NH}_3$  emission is stronger in cores B and D, the  $\text{N}_2\text{H}^+$  emission reaches the maximum value in cores G and I.

## 3.5 IRAS 20126+4104

### 3.5.1 Description

IRAS 20126+4104, located at a distance of 1.7 kpc in the Cygnus X complex (Wilk-  
ing et al. 1989), is a nearby high-mass star-forming region with a bolometric luminos-  
ity of  $1.3 \times 10^4 L_\odot$ , corresponding to a zero-age main-sequence star of spectral type  
B0.2 (Cesaroni et al. 1997), and colors typical of UCHII regions (Wood and Church-  
well 1989). The region has been studied by several authors and in a wide range of  
wavelengths, from the near-infrared to the centimeter range, due to its relatively  
small distance and unconfused structure. The IRAS source is deeply embedded in  
a compact dusty cloud with some extended structure (Cesaroni et al. 1999a). The  
dense gas emission traced by the  $\text{NH}_3$  molecule consists of a compact core, sug-  
gested to be a flattered disk-like structure, associated with IRAS 20126+4104 and  
surrounded by a more extended structure (Zhang et al. 1998; Keto and Zhang 2010).  
High angular resolution observations in the centimeter range reveal the presence of  
3 components associated with the IRAS 20126+4101 core region (Hofner et al. 1999,  
2007), which has been interpreted as emission coming from an ionized jet. Fur-  
thermore, interferometric observations at millimeter and submillimeter wavelengths  
reveal the presence of a hot molecular core, with a mass of  $\sim 7 M_\odot$ , and the ex-  
istence of a disk-outflow system associated with IRAS 20126+4104 (Cesaroni et al.  
1997; Zhang et al. 1998; Cesaroni et al. 1999a, 2005). The outflow/jet system is  
clearly identified in a wide variety of tracers. A well-collimated outflow/jet was re-  
vealed in SiO,  $\text{HCO}^+$  (1–0),  $\text{CH}_3\text{OH}$  (2–1), CO,  $\text{NH}_3$  (3,3), and near-IR  $\text{H}_2$  emission  
(Cesaroni et al. 1997, 1999a, 2005; Kawamura et al. 1999; Zhang et al. 1999; Su  
et al. 2007; Shepherd et al. 2000). This jet is traced at linear scales of a few hundred  
AU through water maser emission (Moscadelli et al. 2000), with the maser spots  
expanding at speeds of  $\sim 35\text{--}110 \text{ km s}^{-1}$  from the high-mass YSO (Moscadelli et al.  
2005). In addition,  $\text{NH}_3$  (3,3) maser emission was detected along the SiO jet (Zhang  
et al. 1999) and 29  $\text{H}_2\text{O}$  maser spots were identified by Trinidad et al. (2005) through  
VLA-A configuration observations (angular resolution  $\sim 0''.1$ ), 21 of them grouped  
in a cluster of  $0''.1$  with motions showing a component of rotation.

Table 3.3: Parameters of the 0.85 mm condensations associated with IRAS 20126+4104 region.

| Source <sup>a</sup> | $\alpha(J2000)$<br>(h:m:s) | $\delta(J2000)$<br>(°:':") | $I_{\mu}^{\text{peak}}$<br>(Jy beam <sup>-1</sup> ) | $S_{\mu}$<br>(Jy) | Deconv. size <sup>b</sup><br>("×") | PA<br>(°) |
|---------------------|----------------------------|----------------------------|---|-------------------|------------------------------------|-----------|
| I20126–C            | 20:14:25.99                | 41:13:32.6                 | 2.7 ±0.1  | 3.5 ±0.2          | 3.8×3.1                            | 114       |
| I20126–E            | –                          | –                          | ...   | 2.0 ±0.3          | ...                                | ...       |
| I20126–T            | –                          | –                          | ...   | 5.2 ±0.2          | 8.3×6.6                            | 116       |
| I20126–S            | 20:14:25.59                | 41:13:20.1                 | 0.20±0.03   | 0.19±0.04         | 3.1×0.0                            | 14        |

**Notes.** <sup>a</sup> Sources are labeled as follows: I20126–C (compact component), I20126–E (extended emission surrounding the compact component), I20126–T (total emission; i. e., compact+extended), and I20126–S (source I20126–South). <sup>b</sup> Two-dimensional Gaussian fitting was applied.

### 3.5.2 Results

#### Continuum emission

Figure 3.5 shows the 0.85 mm SMA continuum emission of I20126 region. There are two compact components: the strongest source coincides with the massive young stellar object IRAS 20126+410, reported previously at millimeter wavelengths by Cesaroni et al. (1997, 1999a, 2005); and the other source I20126–South, lying  $\sim 13''$  to the south of I20126, is a new detection. The emission of I20126 consists of a compact component with a deconvolved size of  $3''8 \times 3''1$  (or  $\sim 6500 \times 5300$  AU at the distance of the source) surrounded by an extended envelope elongated in the southeast-northwest direction. In Table 3.3 we list the position, peak intensity, flux density, and deconvolved size measured by applying a two-dimensional Gaussian fit for each source.

On the assumption that the dust emission is optically thin at 0.85 mm and the temperature distribution of the dust continuum emission is uniform, the mass of the dusty condensations is estimated to be  $28 M_{\odot}$  and  $11\text{--}3.6 M_{\odot}$  for I20126 and I20126–South, respectively (see Table 3.4). Here, we assumed a temperature of 45 K (for I20126) and 10–20 K (for I20126–South), a gas-to-dust ratio of 100, and a dust

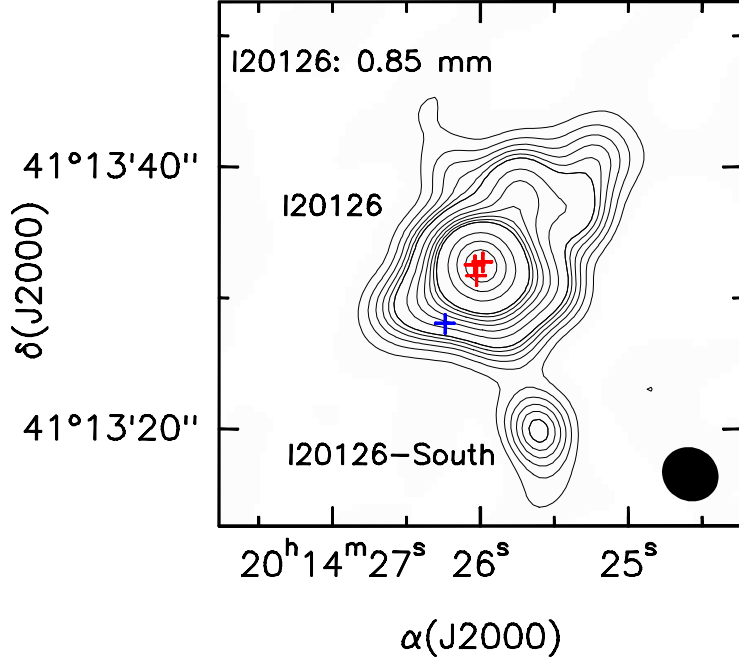


Figure 3.5: SMA 0.85 mm continuum image. Levels range from 3 to 18 in steps of  $3\sigma$ , from 18 to 72 in steps of  $9\sigma$ , and from 72 to 272 in steps of  $50\sigma$ , where  $\sigma$  is the rms of the map, of  $10 \text{ mJy beam}^{-1}$ . Red crosses indicate the position of centimeter sources associated with free-free emission from ionized gas and the blue cross marks the position of a highly variable centimeter source, which is most likely gyrosynchrotron emission from a low-mass pre-main sequence star (see Hofner et al. 2007). The synthesized beam is shown in the bottom right corner of the image.

mass opacity coefficient at 0.85 mm of  $1.9 \text{ g cm}^{-1}$  and  $1.5 \text{ g cm}^{-1}$ , corresponding to agglomerated grains with thin ice mantles in cores of densities  $\sim 10^7 \text{ cm}^{-3}$  and  $\sim 10^6 \text{ cm}^{-3}$  (Ossenkopf and Henning 1994) for I20126 and I20126-South, respectively. If we consider only the emission of the compact component, with a flux density of 3.46 Jy, we found that the estimated mass is  $18 M_{\odot}$ , so more than 60 % of the total mass is associated with the compact component.

In order to compare the physical properties of these dust condensations we made an estimation of the average molecular hydrogen volume density using the equation of  $n = M_{\text{H}_2} / (\frac{4}{3}\pi R^3 \mu m_{\text{H}})$  with the assumption of a spherically symmetric structure. Here,  $M_{\text{H}_2}$  is the mass derived from the dust continuum emission,  $\mu = 2.8$  is the mean molecular weight per molecule of  $\text{H}_2$ , which corresponds to a helium abundance of 10 %, and  $m_{\text{H}}$  is the hydrogen mass. We additionally estimated the average

Table 3.4: Masses and column densities of the 0.85 mm condensations in IRAS 20126+4104

| Source   | $M_{\text{env}}^{\text{a}}$<br>( $M_{\odot}$ ) | $R$<br>(AU) | $n$<br>( $10^7 \text{ cm}^{-3}$ ) | $N(\text{H}_2)$<br>( $10^{24} \text{ cm}^{-2}$ ) |
|----------|--|-------------|-----------------------------------|--|
| I20126-C | 18   | 2900        | 2.2                               | 1.3  |
| I20126-E | 11   | ...         | ...                               | ...  |
| I20126-T | 28   | 6300        | 0.3                               | 0.4  |
| I20126-S | 12-3.6   | 2600        | 2.0-0.6                           | 1.1-0.3  |

**Notes.** <sup>a</sup> Masses derived assuming a dust mass opacity coefficient at 0.85 mm of  $1.9 \text{ g cm}^{-1}$  (agglomerated grains with thin ice mantles in cores of densities  $\sim 10^7 \text{ cm}^{-3}$  Ossenkopf and Henning 1994) and a dust temperature of 45 K (Zhang et al. 1998) for I20126, and a dust mass opacity coefficient of  $1.5 \text{ g cm}^{-1}$  (agglomerated grains with thin ice mantles in cores of densities  $\sim 10^6 \text{ cm}^{-3}$  Ossenkopf and Henning 1994) and a dust temperature in the range 10–20 K for I20126-South. The uncertainty in the mass due to the opacity law is estimated to be of a factor of 2.

column density traced by dust using the equation  $N(\text{H}_2) = M/(A\mu m_{\text{H}})$ , where  $A$  is the area of the dust emission. In Table 3.4 we show the main results obtained for each source, listing the considered radius, and the derived volume and column densities. As can be seen in Table 3.4, the values derived for the compact component, associated with the massive protostellar object I20126, and for I20126-South, are very similar. These values are slightly lower than the values estimated by Cesaroni et al. (1999a), who find  $n = 7 \times 10^8 \text{ cm}^{-3}$  and  $N(\text{H}_2) = 2 \times 10^{25} \text{ cm}^{-2}$ . However, these differences arise due to the fact that we are tracing different linear scales: while Cesaroni et al. (1999a) are able to trace structures down to 1700 AU (i.e., disk like structures) our SMA angular resolution is somewhat lower and hence we are sensitive to larger structures, of  $\sim 7500$  AU, tracing the emission from the envelope. Finally, we estimated the fraction of flux filtered out by the interferometric SMA observations. The flux density measured with the  $14''$  beam of the JCMT/SCUBA  $850 \mu\text{m}$  observations is  $\sim 19$  Jy (Cesaroni et al. 1999a), while the total flux density of I20126 region measured with the SMA 0.85 mm continuum observations is 5.48 Jy, indicating that  $\sim 70\%$  of the flux is filtered out by the SMA.

### Molecular line emission

The zero-order moment map of the  $\text{NH}_3$  (1,1) emission (integrated intensity including the main and two inner satellite lines) is presented in Fig. 3.6a, and we show in Fig. 3.6b the average integrated intensity of the two inner satellites components. The overall structure of the  $\text{NH}_3$  (1,1) main line consists of a strong and compact core, with a deconvolved size of  $5''.6 \times 4''.0$  (or  $0.046 \times 0.032$  pc),  $\text{PA} = 54^\circ$ , associated with the massive YSO I20126 surrounded by an extended structure of  $\sim 45''$  size (or  $\sim 0.37$  pc) with some fainter cores. However, since the emission of the  $\text{NH}_3$  (1,1) main line is usually optically thick, a more realistic picture of the  $\text{NH}_3$  emission can be obtained by integrating the emission of the  $\text{NH}_3$  (1,1) satellite lines. As can be seen in Fig. 3.6 b), apart from the compact core, named I20126-core, the emission of the  $\text{NH}_3$  (1,1) actually consists of three additional cores (labeled as core A, B, and C). Core C is associated with the southern 0.85 mm dust condensation I20126-South. A two-dimensional Gaussian fit to core C yields a deconvolved size of  $\sim 12''.9 \times 7''.2$  ( $\sim 0.11 \times 0.06$  pc). Figure 3.6c shows the zero-order moment map of the  $\text{NH}_3$  (2,2), which resembles closely that of the  $\text{NH}_3$  (1,1).

The zero-order moment map integrated for all the hyperfine transitions of the  $\text{N}_2\text{H}^+$  (1-0) is presented in Fig. 3.6d. The overall emission of the  $\text{N}_2\text{H}^+$  molecule is somewhat more extended than the  $\text{NH}_3$  emission (note that the VLA and BIMA interferometers are sensitive to similar spatial scales), and it consists of four main cores. Cores A and B are also detected in  $\text{N}_2\text{H}^+$  (1-0) and core C is resolved into two components, C-N and C-S, separated  $\sim 7''$ . Furthermore, the strongest and compact core detected in  $\text{NH}_3$  and associated with the massive YSO I20126 is not seen in  $\text{N}_2\text{H}^+$ , similarly to the case of AFGL 5142 (see chapter 4).

In Fig. 3.7 we show the  $\text{NH}_3$  (1,1),  $\text{NH}_3$  (2,2), and  $\text{N}_2\text{H}^+$  (1-0) spectra, not corrected for the primary beam response, at some selected positions of the I20126 region.

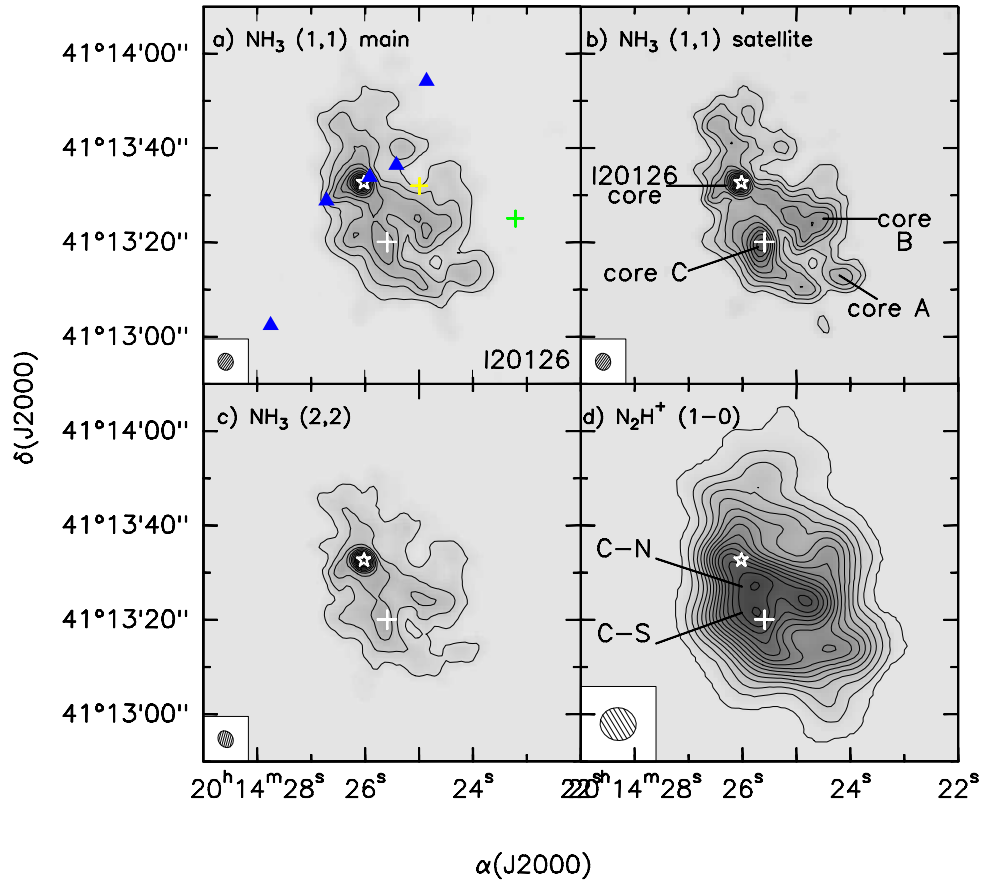


Figure 3.6: **a)** Zero-order moment (integrated intensity) for the  $\text{NH}_3$  (1,1) main and inner satellite lines. Contours start at 8 %, increasing in steps of 8 % of the peak intensity,  $0.43 \text{ Jy beam}^{-1} \text{ km s}^{-1}$ . **b)**  $\text{NH}_3$  (1,1) zero-order moment averaged over the two inner satellite components. Contours start at 8 %, increasing in stapes of 8 % of the peak intensity,  $0.32 \text{ Jy beam}^{-1} \text{ km s}^{-1}$ . **c)**  $\text{NH}_3$  (2,2) zer-order moment. Contours start at 5 %, increasing in steps of 5 % of the peak intensity  $0.40 \text{ Jy beam}^{-1} \text{ km s}^{-1}$ . **d)**  $\text{N}_2\text{H}^+$  zero-order moment integrated for all the hyperfine components of the (1-0) transition. Contours start at 1 %, increasing in steps of 7 % of the peak intensity,  $6.27 \text{ Jy beam}^{-1} \text{ km s}^{-1}$ . In all panels the white star indicates the position of the 1.3 mm continuum from Cesaroni et al. (1999a) and the white cross marks the position of I20126-South. Triangles mark the position of the  $\text{H}_2$  knots from Shepherd et al. (2000). The yellow and green cross marks the position of class I/II and class II objects, respectively (Qiu et al. 2008). The synthesized beams for each transition are shown in the bottom left corner, and are listed in Table 3.2.

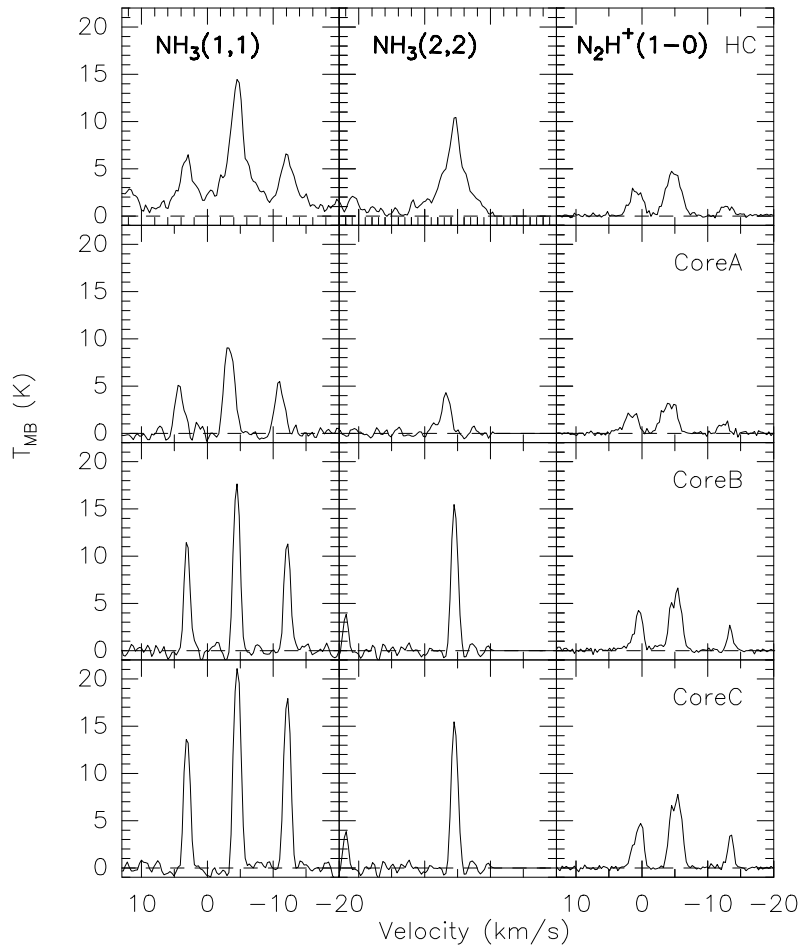


Figure 3.7: Spectra toward 4 positions of the IRAS 20126+4104 region for the three transitions studied, from left to right,  $\text{NH}_3$  (1,1),  $\text{NH}_3$  (2,2), and  $\text{N}_2\text{H}^+$  (1-0). The four positions are labeled on the right panel of each row, and are, from top to bottom, HC (I20126 hot core), Core A, Core B, and Core C.

## 3.6 Analysis

### 3.6.1 Physical parameters of dense gas

Applying the same technique used for AFGL 5142 (see chapter 4) we studied the chemical environment of these three high-mass star-forming regions. In order to compare the emission of both molecules we convolved the  $\text{NH}_3$  and  $\text{N}_2\text{H}^+$  channel maps to obtain a circular beam of  $4''9$ ,  $5''5$ , and  $7''6$ , and we obtained  $\text{NH}_3$  and  $\text{N}_2\text{H}^+$

spectra for positions in a grid of  $1''.5$ ,  $1''.4$ , and  $1''.6$ , for I00117, I22134, and I20126, respectively. Using CLASS we fitted the hyperfine structure of each spectrum for  $\text{NH}_3$  (1,1) and  $\text{N}_2\text{H}^+$  (1-0), and a single Gaussian for  $\text{NH}_3$  (2,2). We performed only the fits for those spectra with an intensity greater than  $5\sigma$  for  $\text{NH}_3$  (1,1) and  $\text{N}_2\text{H}^+$  (1-0) in order to ensure we are detecting all the hyperfine components, whereas for  $\text{NH}_3$  (2,2) we fitted the spectra with an intensity greater than  $4\sigma$ .

The hyperfine structure fitting method in CLASS has been used to determine the LSR velocities ( $v_{\text{LSR}}$ ), the intrinsic linewidths ( $\Delta v$ ), and the optical depths of the main hyperfine component ( $\tau_{\text{m}}$ ). The total optical depth can then be obtained using the relations  $\tau_{(1,1)} = 2\tau_{\text{m}}$  and  $\tau_{(1-0)} = \frac{27}{7}\tau_{\text{m}}$  for  $\text{NH}_3$  (1,1) and  $\text{N}_2\text{H}^+$  (1-0) molecular transitions, respectively. From the results of the fits of the  $\text{NH}_3$  (1,1) and  $\text{NH}_3$  (2,2) spectra we computed the excitation temperature ( $T_{\text{ex}}$ ), opacity, linewidth, rotational temperature ( $T_{\text{rot}}$ ) and column density maps following the procedures described in Ho and Townes (1983) and Harju et al. (1993) (see also the appendix for a description of the method used). We derived the  $\text{N}_2\text{H}^+$  column density by adopting the hyperfine frequencies given in Caselli et al. (1995) and following the expression of Caselli et al. (2002b) with the partition function  $Q_{\text{rot}} \simeq kT_{\text{ex}}/hB \sim 0.4473 T_{\text{ex}}$ , where  $k$  is the Boltzmann constant,  $T_{\text{ex}}$  the excitation temperature,  $h$  is the Planck constant, and  $B$  is the rotational constant of  $\text{N}_2\text{H}^+$ . For both molecules we assumed a filling factor of 1. In the following sections we present the main results obtained for each region.

### IRAS 00117+6412

In Fig. 3.8a and Fig. 3.8c we present the total optical depth maps of the  $\text{NH}_3$  (1,1) and  $\text{N}_2\text{H}^+$  (1-0). The emission of  $\text{NH}_3$  (1,1) is essentially optically thick ( $\tau_{(1,1)} \leq 8$ ), with the highest value reached at the eastern border of the cloud facing the UCH II region, about  $8''$  to the south of MM1. We found important variations of  $\tau_{(1,1)}$  among the several cores identified in the region. For instance, the lowest values, of  $\sim 1$ , are associated with MM1-E, whereas there is a local maxima of  $\sim 4$  located at the peak position of MM1-W. Toward MM2-E the total optical depth is around 2–3, while we found another peak of  $\tau_{(1,1)}$  associated with MM2-W. Regarding the  $\text{N}_2\text{H}^+$  molecule, both MM1 and MM2 clumps have similar values of the optical depth, around  $\tau_{(1-0)} \simeq 0.4$ . As can be seen in Fig. 3.8c, there is an abrupt increase of the optical depth, in a region connecting the MM1 ridge with the western clump, reaching values of  $\sim 1.6$ . Toward the peak position of the western clump the optical

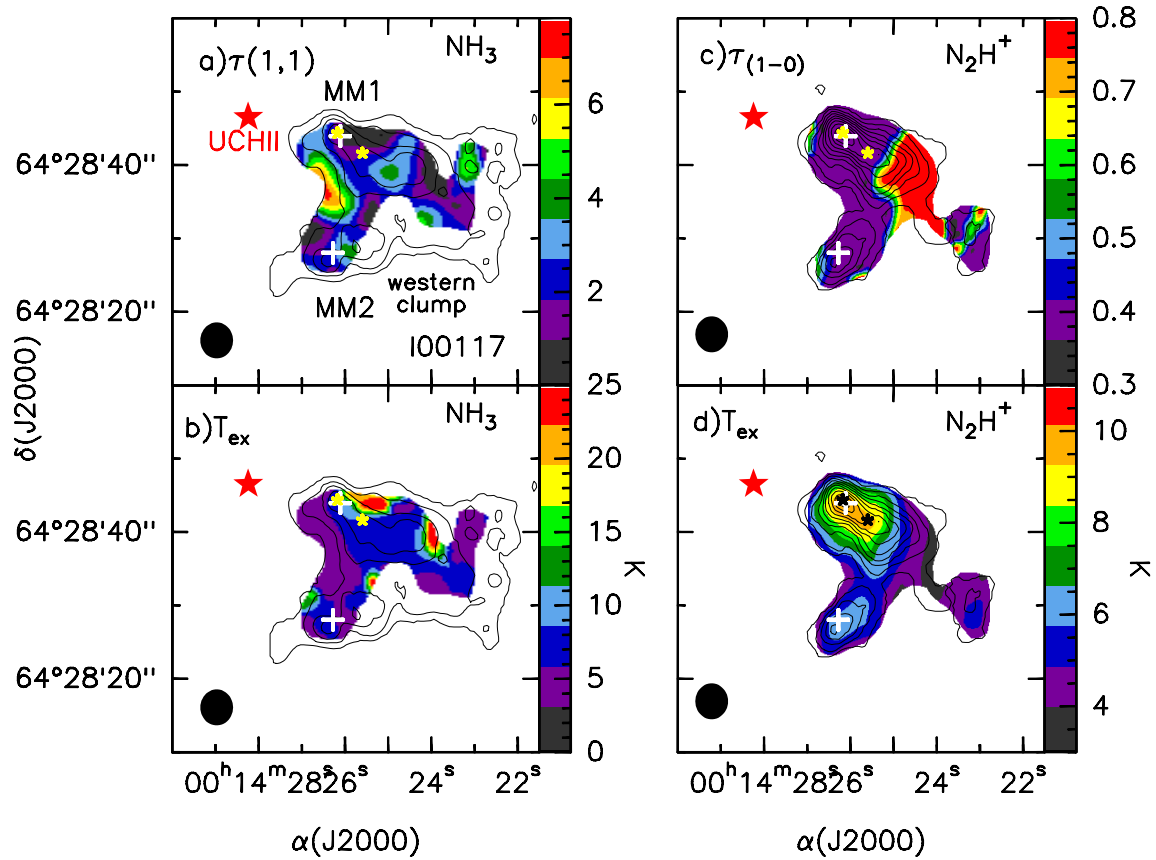


Figure 3.8: **a)** Map of the optical depth of the  $\text{NH}_3$  (1,1) line. **b)** Excitation temperature map from  $\text{NH}_3$  (1,1). **c)** Map of the optical depth of the  $\text{N}_2\text{H}^+$  (1-0) line. **d)** Excitation temperature map derived from  $\text{N}_2\text{H}^+$  (1-0). The contour levels are the same as in Fig. 3.1. The star marks the position of the UCH II region IRAS 00117+6412, white crosses indicate the position of the millimeter condensations MM1 and MM2 detected by Palau et al. (2010), and five-point stars indicate the position of 2MASS point sources. In all panels the synthesized beam, of  $4''.9$ , is drawn in the bottom left corner.

depth is  $\sim 0.6$ .

The excitation temperature maps of  $\text{NH}_3$  and  $\text{N}_2\text{H}^+$  (1-0) are shown in Fig. 3.8b and Fig. 3.8d, respectively. The values derived for  $T_{\text{ex}}$  from  $\text{NH}_3$  are slightly higher than the excitation temperature estimated from the  $\text{N}_2\text{H}^+$  molecule. The lowest values of  $T_{\text{ex}}$ , around  $\sim 3$ – $4$  K are reached in the filamentary structure that connects the MM1 ridge with the western clump. In the MM1 ridge,  $T_{\text{ex}}$  is in the range  $T_{\text{ex}} \simeq 7$ – $10$  K, while MM2 clump has an excitation temperature of  $\sim 5$ – $6$  K

Table 3.5: Summary of the main physical properties of IRAS 00117+6412 cores

| Core  | $\alpha(J2000)$<br>(h:m:s) | $\delta(J2000)$<br>( $^{\circ}$ : $'$ : $''$ ) | $T_{\text{rot}}$<br>(K) | $\Delta v$<br>(km s $^{-1}$ ) | $N(\text{NH}_3)$<br>( $\times 10^{15}$ cm $^{-2}$ ) | $N(\text{N}_2\text{H}^+)$<br>( $\times 10^{12}$ cm $^{-2}$ ) | $N(\text{NH}_3)/N(\text{N}_2\text{H}^+)$ |
|-------|----------------------------|--|-------------------------|-------------------------------|---|--|--|
| MM1-W | 00:14:24.47                | 64:28:39.7                                     | 16                      | 1.0                           | 1   | 3.5  | 150–200                                  |
| MM1-E | 00:14:26.02                | 64:28:43.7                                     | 15                      | 1.5                           | 0.5   | 5  | 50–100                                   |
| MM2-W | 00:14:26.41                | 64:28:27.2                                     | 12                      | 1.4                           | 1.5   | 2.5  | 350–450                                  |
| MM2-E | 00:14:25.71                | 64:28:28.7                                     | 14                      | 1.3                           | 0.7   | 3  | 200–300                                  |

Figure 3.9b shows the rotational temperature map derived toward I00117 region. Interestingly, at the northern and southeastern edges of the MM1 ridge and encompassing the intermediate-mass YSOs deeply embedded in the MM1 ridge, there is a temperature enhancement, reaching a maximum value of  $20 \pm 2$  K. We specifically checked that the fits to the  $\text{NH}_3$  (1,1) and  $\text{NH}_3$  (2,2) at these positions are good, so this heating must be real. These temperature enhancements could be associated with the passage of the a CO (2–1) molecular outflow (Palau et al. 2010) that heats and perturbs the dense gas. In particular, as can be seen in Fig. 9 of Palau et al. (2010), the blueshifted CO (2–1) emission at moderate velocities is spatially coincident with the heating produced at the northern border of MM1 ridge. On the other hand, the heating found toward the southeastern edge of MM1 ridge, with rotational temperatures progressively increasing when approaching the UCH II region, could be produced by the UV radiation field from the B2 star associated with the UCH II region. Finally, since no clear heating is found associated with MM2, where a  $\text{H}_2\text{O}$  maser is present, again suggests that MM2 could harbors an extremely young protostar.

The  $\text{NH}_3$  column density map, corrected for the primary beam response, is presented in Fig. 3.9a. The  $\text{NH}_3$  column density reaches the maximum value, around  $1.5 \times 10^{15}$  cm $^{-2}$ , toward MM2-W, whereas the values estimated for MM2-E, MM1-E, and MM1-W are  $\sim 0.7 \times 10^{15}$  cm $^{-2}$ ,  $0.5 \times 10^{15}$  cm $^{-2}$ , and  $1 \times 10^{15}$  cm $^{-2}$ , respectively. Note that we found the lowest values of  $N(\text{NH}_3)$  just north of MM1, towards the positions with high rotational temperature, suggesting that the molecular outflow is excavating a cavity in the dense gas. Figure. 3.9c shows the  $\text{N}_2\text{H}^+$  column density map of the region. Contrary to  $\text{NH}_3$ , the map of the  $\text{N}_2\text{H}^+$  column density has the maximum value, of  $\sim 8 \times 10^{12}$  cm $^{-2}$ , close to the position of MM1-E. For MM2 and the western clumps we estimated a  $\text{N}_2\text{H}^+$  column density of  $3 - 4 \times 10^{12}$  cm $^{-2}$ .

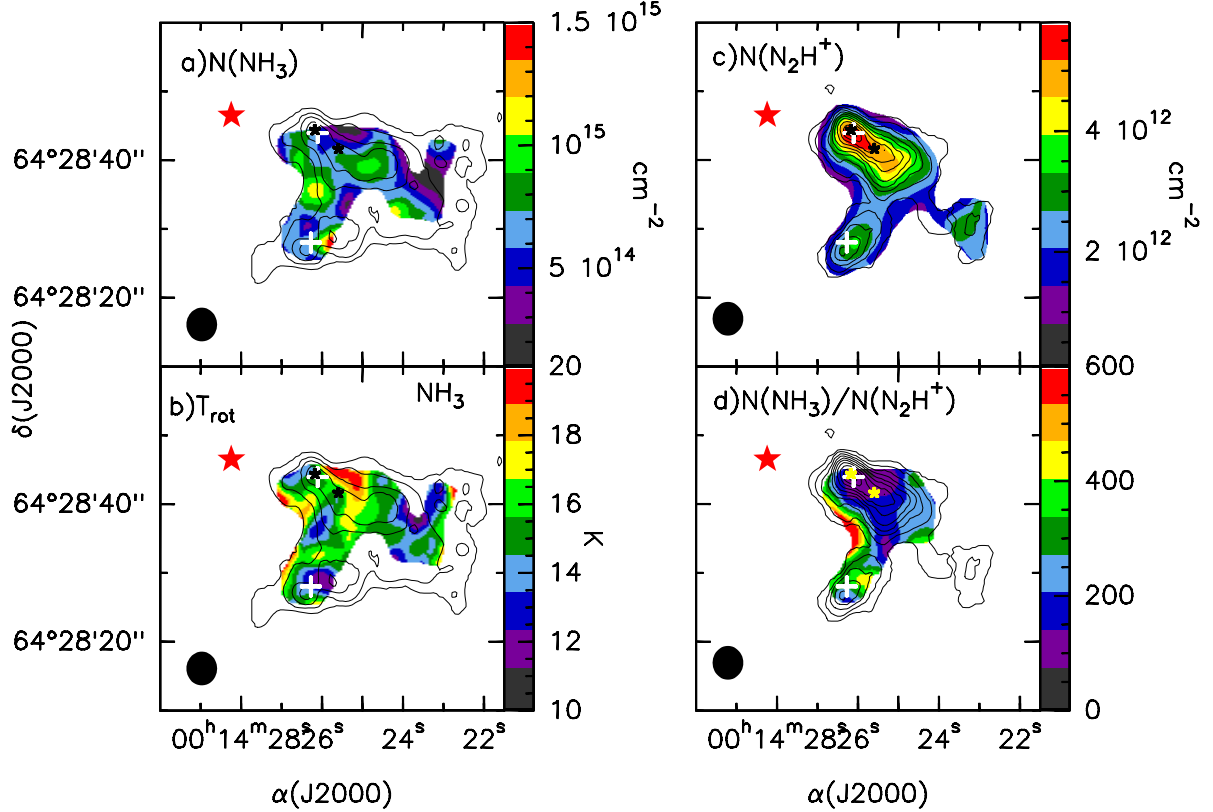


Figure 3.9: **a)**  $\text{NH}_3$  column density map. **b)** Rotational temperature map from  $\text{NH}_3(1,1)$  and  $\text{NH}_3(2,2)$ . **c)**  $\text{N}_2\text{H}^+$  column density map **d)**  $\text{NH}_3/\text{N}_2\text{H}^+$  abundance ratio map. Symbols are the same as in Fig. 3.8. In all panels the synthesized beam, of  $4''.9$ , is drawn in the bottom left corner.

Figure 3.9d presents the  $\text{NH}_3/\text{N}_2\text{H}^+$  abundance ratio map toward I00117. Clearly, there are significant variations in the  $\text{NH}_3/\text{N}_2\text{H}^+$  abundance ratio: while in MM1-E, which contains a Class 0/I intermediate-mass YSO, we determined low values of the  $\text{NH}_3/\text{N}_2\text{H}^+$  ratio,  $\sim 100$ , we found high values, up to 450, toward MM1-W, MM2-E, and MM2-W. For these three cores the  $\text{NH}_3$  column density is high, the rotational temperature is low, around 12–15 K, there are no signs of molecular outflow emission emanating from the cores, and no infrared emission in the  $J$ ,  $H$ , and  $K$  band of 2MASS neither Spitzer bands is seen associated with these cores, suggesting that they could be starless. However, (Palau et al. 2010) studied the kinematics of the region and find that the millimeter source MM2, which is associated with MM2-E, seems to be undergoing rotation and infall motions. In addition, the detection of  $\text{H}_2\text{O}$  maser emission close to MM2-E indicates that star formation activity is taking

place in MM2-E core. The fact we found high values of the  $\text{NH}_3/\text{N}_2\text{H}^+$  abundance ratio would suggest that this object is in a very early evolutionary stage, possibly in the transition of the starless phase to the Class 0 phase, maybe in the first hydrostatic core phase, as found by Enoch et al. (2010) in the dense core Per-Bolo 58 in Perseus molecular cloud. Nevertheless, further observations should be conducted to draw any definitive conclusion about the nature of this object. The values of the  $\text{NH}_3/\text{N}_2\text{H}^+$  ratio in the entire region are consistent with those derived in low-mass star-forming regions (Caselli et al. 2002a; Hotzel et al. 2004; Friesen et al. 2010) and with the values derived by Palau et al. (2007) towards the intermediate-mass cores surrounding the UCH II region IRAS 20293+3952. All these studies find that the low values of the  $\text{NH}_3/\text{N}_2\text{H}^+$  ratio are associated with YSOs, and the high values (up to 300) are found associated with starless cores. It is important to remark that the highest values, of  $\sim 600$ , reached toward the eastern edge of the structure connecting MM1 and MM2 are not real but border effects. In Table 3.5 we summarize the main properties of the dense gas for each core detected in IRAS 00117+6412 region.

### IRAS 22134+5834

Similarly to the previous region, the IRAS 22134+5834 cloud is essentially optically thin for  $\text{N}_2\text{H}^+$  ( $\tau_{(1-0)} \simeq 0.4-0.6$ ), but optically thick for  $\text{NH}_3$  (1,1), with  $\tau_{(1,1)} \leq 6$ . In general, the properties of cores A, B, C, and D (hereafter referred as western cloud) are somewhat different from the other cores (i. e., cores E, F, G, H, I, and J; hereafter referred as main cloud). As can be seen in Fig. 3.10a, the optical depth of  $\text{NH}_3$  (1,1) is higher in the western cloud than in the main cloud, reaching a maximum value of  $\sim 6$  towards core D. The excitation temperature maps of  $\text{NH}_3$  (1,1) and  $\text{N}_2\text{H}^+$  (1-0) are shown in Fig. 3.10b and Fig. 3.10d, respectively. The values of  $T_{\text{ex}}$  for the main cloud are in the range  $\sim 4 - 25$  K, whereas the western cloud has lower values of  $T_{\text{ex}}$ , of  $\sim 4 - 8$  K.  $T_{\text{ex}}$  reaches the highest values of  $\sim 25$  K toward the apparent dense gas cavity west of cores H. In addition, a secondary peak, with  $T_{\text{ex}} \sim 14$  K, is found towards core F.

Concerning the linewidths derived from the fits to the hyperfine structure of  $\text{NH}_3$  (1,1) we found that, in general, they are higher in the main cloud, with values around  $0.9-2 \text{ km s}^{-1}$ , than in the western cloud, where the  $\Delta v \sim 0.5-0.9 \text{ km s}^{-1}$  (see Fig. 3.10c). The map of the rotational temperature is presented in Fig. 3.11b. A

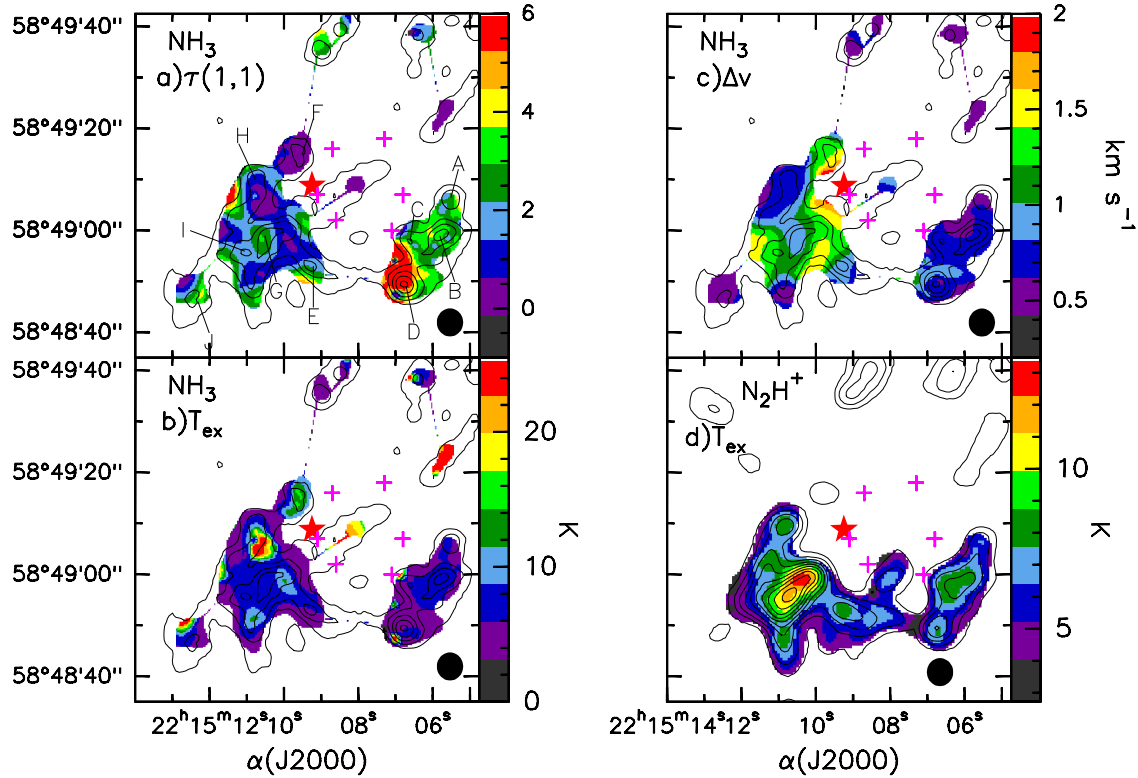


Figure 3.10: **a)** Map of the optical depth of the  $\text{NH}_3(1,1)$  line. **b)** Excitation temperature map from  $\text{NH}_3(1,1)$ . **c)**  $\text{NH}_3(1,1)$  linewidth map. **d)** Excitation temperature map derived from  $\text{N}_2\text{H}^+(1-0)$ . The star marks the position of the UCHII region IRAS 22134+5834 and the pink crosses indicate the position of the early B-type stars constituting the ring detected by Kumar et al. (2003). In all panels the synthesized beam, of  $5''.5$ , is drawn in the bottom right corner.

clear feature seen in the rotational temperature map is the temperature gradient progressively increasing when approaching the UCHII region, with the maximum values,  $30 \pm 7$  K, reached around the cavity seen in the  $\text{NH}_3$  dense gas emission. We also found a temperature enhancement associated with core J, with  $T_{\text{rot}} \sim 21$  K. On the other hand, the western cloud has lower temperatures, of  $14 \pm 2$  K. Therefore, these two features, line broadening and the temperature enhancement seen around the apparent cavity suggest that the UCHII region is radiatively interacting with the surrounding dense gas, being heated by the external UV field from the early B-type star.

Figure 3.11a shows the  $\text{NH}_3$  column density map obtained towards the I22134

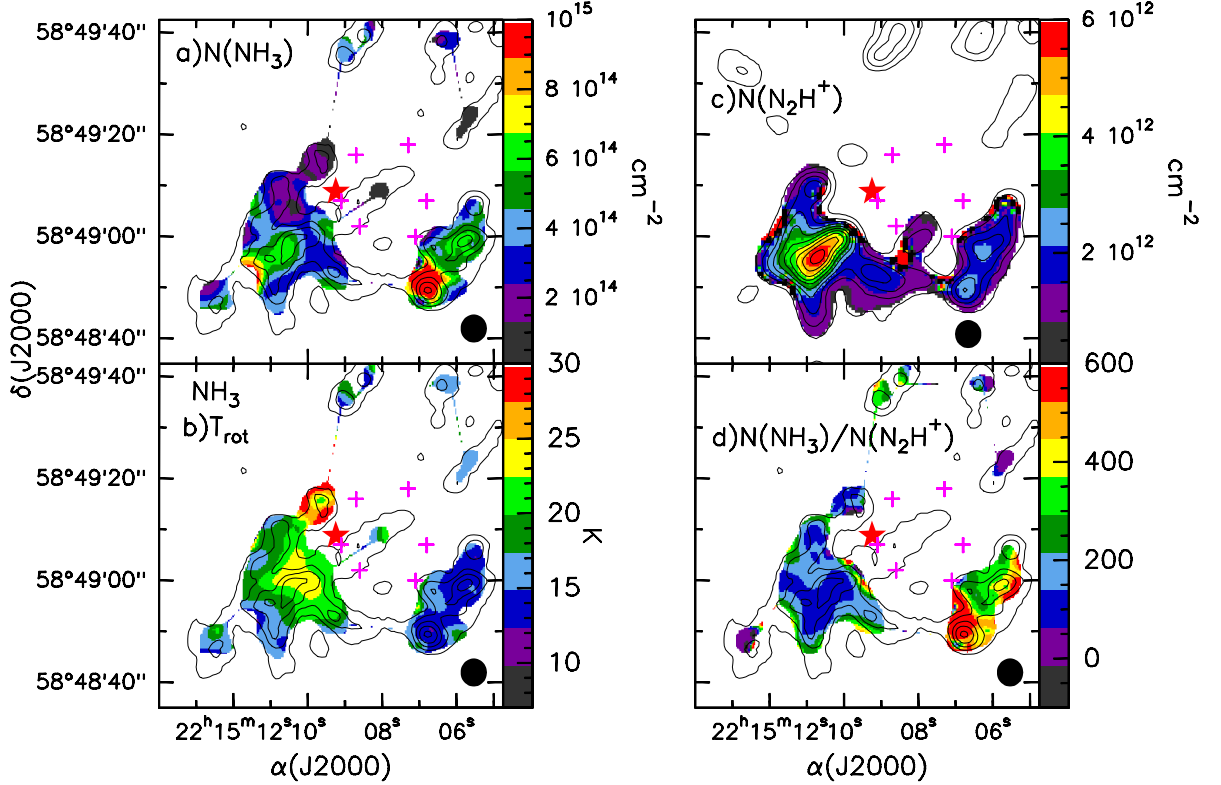


Figure 3.11: **a)**  $\text{NH}_3$  column density map. **b)** Rotational temperature map from  $\text{NH}_3(1,1)$  and  $\text{NH}_3(2,2)$ . **c)**  $\text{N}_2\text{H}^+$  column density map **d)**  $\text{NH}_3/\text{N}_2\text{H}^+$  abundance ratio map. Symbols are the same as in Fig. 3.10. In all panels the synthesized beam, of  $5'' \times 5''$ , is drawn in the bottom right corner.

region. The maximum value,  $1 \times 10^{15} \text{ cm}^{-2}$ , is reached at the position of core D, and a secondary maximum is reached toward cores B, G, and I. A clear feature seen in the  $\text{NH}_3$  column density map is that the lower values are found around the apparent cavity, where we found the highest values of  $T_{\text{rot}}$ . This result suggests that the UCHII region is clearing up the surrounding material. In Fig. 3.11c we present the  $\text{N}_2\text{H}^+$  column density map. Contrary to  $\text{NH}_3$ , the  $\text{N}_2\text{H}^+$  column density reaches the maximum value, around  $6 \times 10^{12} \text{ cm}^{-2}$ , toward the position of core G, and core I, while the values found in the western cloud are  $\sim 2.5 \times 10^{12} \text{ cm}^{-2}$  at the peak position of cores B and D. Finally, in Fig. 3.11d we present the resulting  $\text{NH}_3/\text{N}_2\text{H}^+$  abundance ratio map. The  $\text{NH}_3/\text{N}_2\text{H}^+$  ratio reaches the highest values, around 250–600, toward the cores forming the western cloud, whereas the main cloud is associated with slightly lower values, in the range of 50–200.

Table 3.6: Summary of the main physical properties of IRAS 22134+5834 cores

| Core | $\alpha(J2000)$<br>(h:m:s) | $\delta(J2000)$<br>(°:':") | $T_{\text{ex}}^{\text{b}}$<br>(K) | $\Delta v^{\text{b}}$<br>(km s <sup>-1</sup> ) | $T_{\text{rot}}$<br>(K) | $N(\text{NH}_3)$<br>( $\times 10^{15}$ cm <sup>-2</sup> ) | $N(\text{N}_2\text{H}^+)$<br>( $\times 10^{12}$ cm <sup>-2</sup> ) | $N(\text{NH}_3)/N(\text{N}_2\text{H}^+)$ |
|------|----------------------------|----------------------------|-----------------------------------|--|-------------------------|---|--|--|
| A    | 22:15:05.52                | 58:49:06.5                 | 7                                 | 0.5  | 14                      | 0.4   | 1.0  | 300                                      |
| B    | 22:15:05.79                | 58:49:02.4                 | 7                                 | 0.7  | 14                      | 0.6   | 2.5  | 400                                      |
| C    | 22:15:06.59                | 58:48:57.6                 | 6                                 | 0.7  | 16                      | 0.5   | 1.0  | 250                                      |
| D    | 22:15:06.77                | 58:48:49.3                 | 5                                 | 0.7  | 14                      | 1.0   | 2.5  | 600                                      |
| E    | 22:15:09.25                | 58:48:52.7                 | 6                                 | 0.9  | 20                      | 0.4   | 2.0  | 180                                      |
| F    | 22:15:09.61                | 58:49:14.8                 | 15                                | 1.4  | 25                      | 0.2   | 2.5  | 180                                      |
| G    | 22:15:10.50                | 58:48:58.9                 | 7                                 | 1.0  | 22                      | 0.7   | 6.0  | 100                                      |
| H    | 22:15:10.77                | 58:49:10.7                 | 10                                | 0.7  | 19                      | 0.2   | 1.5  | 100                                      |
| I    | 22:15:11.03                | 58:48:58.9                 | 7                                 | 1.3  | 18                      | 0.7   | 3.5  | 100                                      |
| J    | 22:15:12.45                | 58:48:45.8                 | 7                                 | 0.5  | 16                      | 0.4   | 8.0  | 50                                       |

**Notes.** <sup>a</sup> Position are taken from the  $\text{NH}_3$  integrated intensity map. <sup>b</sup> Excitation temperature derived from the output parameters of the  $\text{NH}_3$  (1,1) hyperfine fit. <sup>c</sup> Line width derived the fits to the hyperfine structure of  $\text{NH}_3$  (1,1).

In Table 3.6 we summarized the main results of the  $\text{NH}_3$  (1,1) and  $\text{N}_2\text{H}^+$  (1–0) emission, listing the position, excitation temperature, linewidth, rotational temperature,  $\text{NH}_3$  and  $\text{N}_2\text{H}^+$  column densities, and the  $\text{NH}_3/\text{N}_2\text{H}^+$  abundance ratio for each core of the IRAS 22134+5834 region.

As shown in Sect. 3.4.2, cores A and B seem to be associated with near-infrared sources displaying typical colors of Class 0/I and Class II YSOs. However, the analysis of the dense gas performed in this section revealed that these cores seem to be actually quiescent because we did not find any hint of perturbation such as local heating and/or line broadening. In fact, these cores have very low temperature ( $T_{\text{rot}} \simeq 14$  K) and linewidths ( $\Delta v \simeq 0.5\text{--}0.7$  km s<sup>-1</sup>), suggesting that the infrared sources are background sources and not associated with the dense gas.

In addition, it is worth noting that the physical properties derived from  $\text{NH}_3$  and  $\text{N}_2\text{H}^+$  (i. e., opacity, temperature, linewidth, and the  $\text{NH}_3/\text{N}_2\text{H}^+$  ratio) of the main cloud and the western cloud are somewhat different, possibly as a result of the strong interaction of the UV photons from the UCH II region. For instance, both the rotational temperature and linewidths are higher in the main cloud. Moreover, the  $\text{NH}_3$  column density is lower in the main cloud than in the western cloud, whereas the  $\text{N}_2\text{H}^+$  column density reaches the highest values toward cores constituting the main cloud (i. e., the  $\text{NH}_3/\text{N}_2\text{H}^+$  ratio is significantly higher in the western cloud

than in the main cloud). The differences found in the  $\text{NH}_3$  column density could be explained in terms of  $\text{NH}_3$  being more affected than  $\text{N}_2\text{H}^+$  under a strong UV radiation field, specially in those cores close to the UCH II region, like cores F, G, and H. In fact,  $\text{NH}_3$  is among the most fragile molecules against UV field (Fuente et al. 1993). When increasing the UV field the  $\text{NH}_3$  formation rate decreases and additionally it is destroyed rapidly by the reaction  $\text{H}^+ + \text{NH}_3 \rightarrow \text{NH}_3^+ + \text{H}$  due to the photodissociation of  $\text{H}_2^+$  that yields to an increase of the  $\text{H}^+$  abundance and consequently the rate of destruction of  $\text{NH}_3$  increases too.

Thus, both the main cloud and the western cloud seem to contain pre-protostellar cores, and the small values of the  $\text{NH}_3/\text{N}_2\text{H}^+$  ratio toward the main cloud could be UV-radiation effects from the UCH II region.

### IRAS 20126+4104

Toward I20126, the results obtained from the fits to the hyperfine structure of  $\text{NH}_3$  indicate that the emission is, in general, optically thick ( $\tau(1,1) \leq 10$ ), with significant differences between the I20126 hot core and the rest of the cloud (see Fig. 3.12a). The optical depth of  $\text{NH}_3(1,1)$  peaks at a value of  $\sim 10$  towards core C, while in the I20126 hot core the maximum is  $\sim 1.5$ . There is a secondary maximum of  $\sim 8$  toward the position of core B. On the other hand, as can be seen in Fig. 3.12d the emission is essentially optically thin for  $\text{N}_2\text{H}^+$  ( $\tau_{1-0} \leq 0.5$ ), with two local maxima of  $\sim 1$  and  $\sim 1.5$  found  $\sim 5''$  south of core C and in the northern side of the cloud. As shown in Fig. 3.12b the values of the excitation temperature,  $T_{\text{ex}}$ , derived from  $\text{NH}_3$  are in the range  $\sim 8$ –22 K, with the maximum values reached toward the position of I20126. The other cores have lower values: core A has a value of  $T_{\text{ex}} \simeq 10$  K,  $T_{\text{ex}} \simeq 16$  K in core B, and core C has a peak value of  $\sim 18$  K. The values of  $T_{\text{ex}}$  derived from  $\text{NH}_3$  are slightly higher than those obtained from  $\text{N}_2\text{H}^+$  (see Fig. 3.12e), which are in the range of  $\sim 4$ –15 K. In this case, the maximum values are reached toward core B, core C-N, and core C-S, whereas toward the position of the IRAS source we found  $T_{\text{ex}} \simeq 8$ –10 K.

Regarding the linewidth obtained from the hyperfine fits we found similar values for both  $\text{NH}_3$  and  $\text{N}_2\text{H}^+$  (see Fig. 3.12c and Fig. 3.12f). The highest values, of  $\sim 2.5 \text{ km s}^{-1}$ , are found to be associated with I20126. Toward core A we obtained also relatively high values, of  $\sim 1.5 \text{ km s}^{-1}$ , whereas core B and core C appear as

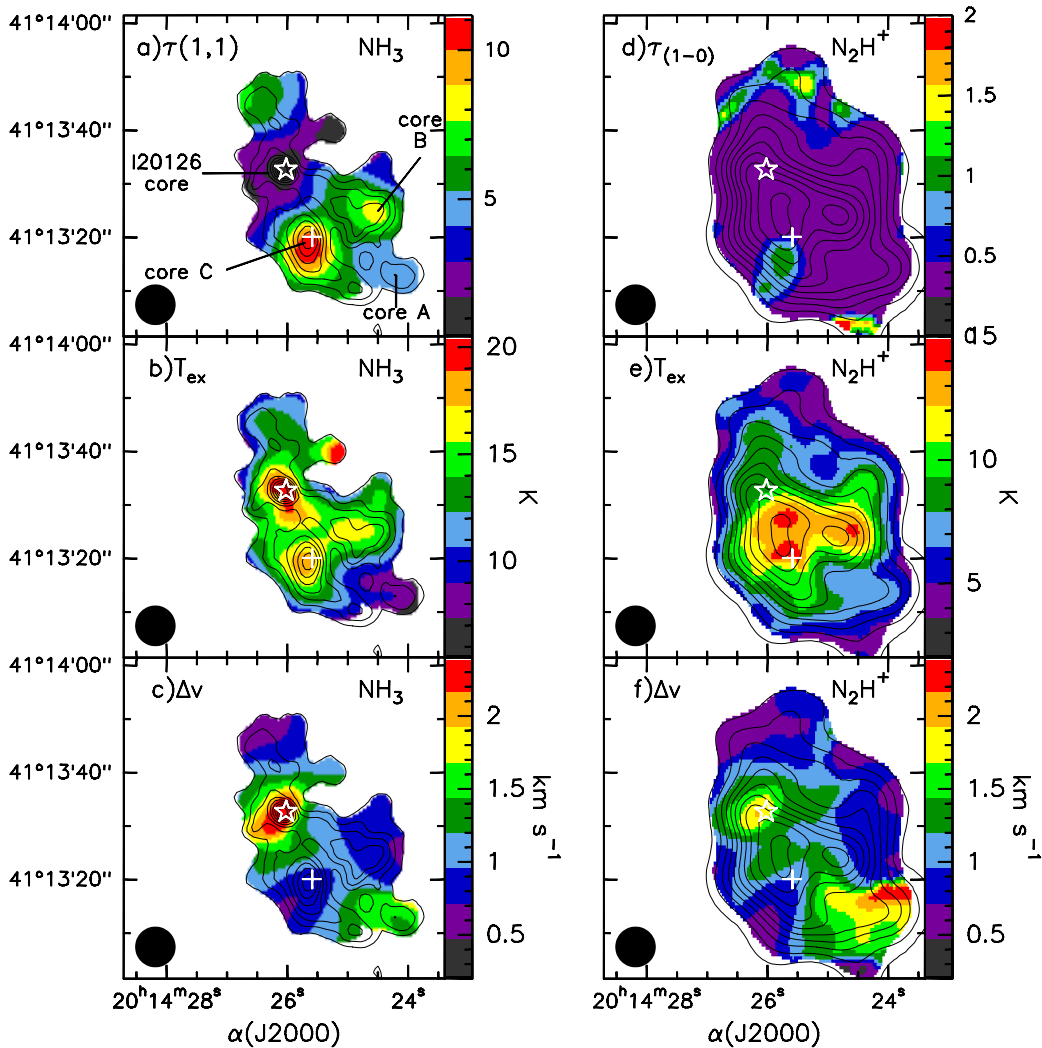


Figure 3.12: **a)** Map of the optical depth of the  $\text{NH}_3$  (1,1) line. **b)** Excitation temperature map from  $\text{NH}_3$  (1,1). **c)**  $\text{NH}_3$  (1,1) linewidth map. **d)** Map of the optical depth of the  $\text{N}_2\text{H}^+$  (1-0) line. **e)** Excitation temperature map derived from  $\text{N}_2\text{H}^+$  (1-0). **f)**  $\text{N}_2\text{H}^+$  (1-0) linewidth map. The star marks the position of IRAS 20126+4104 hot core and the white cross indicates the position of the 0.85 mm condensation I20126-South. In all panels the synthesized beam, of  $7''6$ , is drawn in the bottom left corner.

more quiescent, with values of  $\sim 1 \text{ km s}^{-1}$  and  $\sim 0.8 \text{ km s}^{-1}$ , respectively. All these values are significantly higher than the thermal linewidth  $\sim 0.2\text{--}0.3 \text{ km s}^{-1}$  (estimated for a kinetic temperature of 20 K and 45 K, respectively), indicating that the dense gas have a significant contribution from non-thermal processes.

Table 3.7: Summary of the main physical properties of IRAS 20126+4104 cores

| Core        | $\alpha(J2000)$<br>(h:m:s) | $\delta(J2000)$<br>( $^{\circ}$ : $'$ : $''$ ) | $T_{\text{rot}}$<br>(K) | $\Delta v^a$<br>(km s $^{-1}$ ) | $N(\text{NH}_3)$<br>( $\times 10^{15}$ cm $^{-2}$ ) | $N(\text{N}_2\text{H}^+)$<br>( $\times 10^{13}$ cm $^{-2}$ ) | $N(\text{NH}_3)/N(\text{N}_2\text{H}^+)$ |
|-------------|----------------------------|--|-------------------------|---------------------------------|---|--|--|
| core A      | 20:14:24.21                | 41:13:13.1                                     | 17                      | 1.5                             | 3.0   | 0.6  | 500                                      |
| core B      | 20:14:24.71                | 41:13:24.3                                     | 15                      | 0.9                             | 3.6   | 0.8  | 450                                      |
| core C      | 20:14:25.63                | 41:13:19.5                                     | 15                      | 0.8                             | 5.0   | 1.0  | 500                                      |
| I20126 core | 20:14:26.05                | 41:13:32.3                                     | 22                      | 2.5                             | 2.0   | 0.6  | 300                                      |

**Notes.** <sup>a</sup> Line width derived the fits to the hyperfine structure of  $\text{NH}_3$  (1,1).

The map of the rotational temperature is presented in Fig. 3.13b. The maximum value,  $22 \pm 2$  K, is reached at the position of I20126, and it decreases when moving outwards. This temperature enhancement could be due to the passage of the molecular outflow (extended heating) and to the hot core (more localized and compact). Toward the other cores the derived  $T_{\text{rot}}$  is around 14–16 K. The  $\text{NH}_3$  column density map, corrected for the primary beam attenuation, is shown in Fig. 3.13a. An obvious feature from the  $\text{NH}_3$  column density map is that the highest values are found at the southern part of the cloud, where we found the lowest values in the rotational temperature map (Fig. 3.13b). The highest value, of  $\sim 5 \times 10^{15}$  cm $^{-2}$ , is reached toward core C, and the value obtained for I20126 is around  $2 \times 10^{15}$  cm $^{-2}$ . Note that we did not find a clear peak associated with I20126-core. Figure 3.13c shows the  $\text{N}_2\text{H}^+$  column density map of I20126 region. The maximum value of  $\sim 10^{13}$  cm $^{-2}$  is found associated with cores C-N and C-S, whereas towards the hot core I20126 the column density is around  $\sim 0.5 \times 10^{13}$  cm $^{-2}$ .

Finally, in Fig. 3.13d we present the  $\text{NH}_3/\text{N}_2\text{H}^+$  abundance ratio map derived toward I20126 region. We found important variations in the  $\text{NH}_3/\text{N}_2\text{H}^+$  ratio, with values around  $\sim 300$  associated with the I20126 source, similar to the case of AFGL 5142 (see next chapter), where the  $\text{NH}_3/\text{N}_2\text{H}^+$  ratio is around 400 toward the embedded high-mass protostars. Even higher values, from 400 and up to 600, are found toward cores A, B, and C. Moreover, toward the northern part of the cloud, at  $\sim 12''$  to the north of I20126, we found that the  $\text{NH}_3/\text{N}_2\text{H}^+$  ratio increases up to values of  $\sim 1000$ . The main physical properties estimated for IRAS 20126+4104 region are listed in Table 3.7.

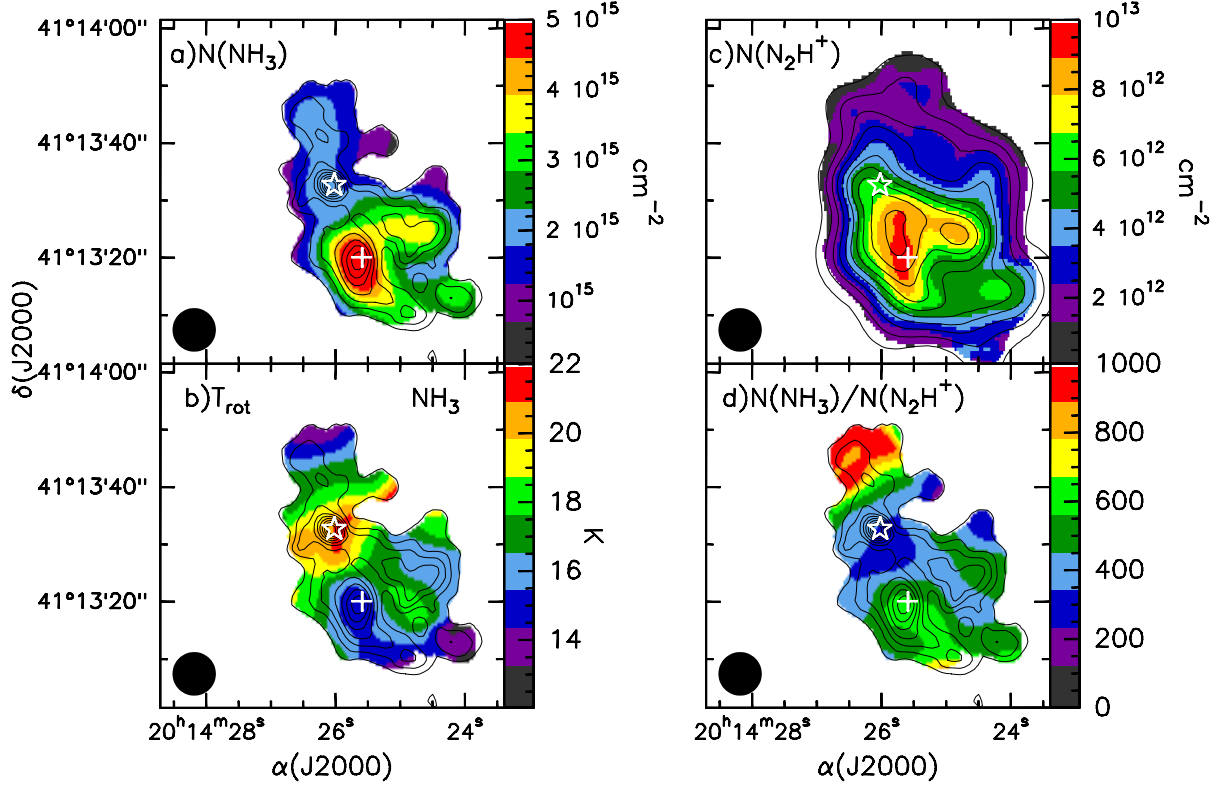


Figure 3.13: **a)**  $\text{NH}_3$  column density map. **b)** Rotational temperature map from  $\text{NH}_3(1,1)$  and  $\text{NH}_3(2,2)$ . **c)**  $\text{N}_2\text{H}^+$  column density map **d)**  $\text{NH}_3/\text{N}_2\text{H}^+$  abundance ratio map. Symbols are the same as in Fig. 3.12. In all panels the synthesized beam, of  $7''.6$ , is drawn in the bottom left corner.

### 3.6.2 $\text{NH}_3$ and $\text{N}_2\text{H}^+$ fractional abundances

Using  $N(\text{H}_2)$  and the column density of  $\text{NH}_3$  and  $\text{N}_2\text{H}^+$  estimated in previous sections, we next calculate the fractional abundance of  $\text{NH}_3$  and  $\text{N}_2\text{H}^+$  relative to  $\text{H}_2$ ,  $X(\text{NH}_3)$  and  $X(\text{N}_2\text{H}^+)$ , for I00117 and I20126. To do so, we first estimated the column density traced by dust,  $N(\text{H}_2)$ , in I00117 using the dust emission from Palau et al. (2010) and following the procedure described in Sect. 3.5.2 for I20126 region. In Table 3.8 we show the mass and radius considered, the volume density, and the derived column density for the two main millimeter condensation, MM1 and MM2, detected by Palau et al. (2010). Note that the fractional abundances of I22134 can not be estimated because dust emission is only detected towards the position of the UCHII region (Sánchez-Monge 2011), not in the dense cores seen in  $\text{NH}_3$  and  $\text{N}_2\text{H}^+$ .

Table 3.8: Parameters of the 1.3 mm condensations in IRAS 00117+6412

| Source | $M_{\text{env}}^{\text{a}}$<br>( $M_{\odot}$ ) | Deconv. size <sup>a</sup><br>("×") | $R^{\text{b}}$<br>(AU) | $n$<br>( $10^7 \text{ cm}^{-3}$ ) | $N(\text{H}_2)$<br>( $10^{23} \text{ cm}^{-2}$ ) |
|--------|--|------------------------------------|------------------------|-----------------------------------|--|
| MM1    | 3.0  | 2.4×1.0                            | 1394                   | 3.3                               | 9.3  |
| MM2    | 1.7  | 2.0 × 0.0                          | 2160                   | 0.5                               | 2.2  |

**Notes.** <sup>a</sup> From Palau et al. (2010). <sup>b</sup> Radius of the millimeter condensation taken as half the geometrical mean of the two linear sizes,  $R = \frac{1}{2}(l_a \times l_b)^{1/2}$ .

Table 3.9: Fractional abundance

| Core         | $X(\text{NH}_3)$<br>( $\times 10^{-9}$ ) | $X(\text{N}_2\text{H}^+)$<br>( $\times 10^{-11}$ ) |
|--------------|--|--|
| I00117-MM1   | 0.6                                      | 0.5  |
| I00117-MM2   | 3.2                                      | 1.4  |
| I20126-core  | 1.6                                      | 0.5  |
| I20126-South | 4.8–16 <sup>a</sup>                      | 1.0–3.2 <sup>a</sup>                               |

**Notes.** <sup>a</sup> Range of values according to the results derived in Sect. 3.5.2 and listed in Table 3.4 for a kinetic temperature of 10 K and 20 K.

Table 3.9 lists the fractional abundances for I00117 and I20126 regions. As can be seen in this table, there are important variations of the fractional abundance in I00117. While in MM1  $X(\text{NH}_3) \sim 6 \times 10^{-10}$ , in MM2 we found values one order of magnitude higher, of  $\sim 3 \times 10^{-9}$ . Moreover, the  $\text{N}_2\text{H}^+$  fractional abundance,  $X(\text{N}_2\text{H}^+)$  appears to be higher in MM2 than in MM1, also with a difference of one order of magnitude. These differences indicate a strong chemical differentiation in the region. On the other hand, in I20126 the fractional abundance of  $\text{NH}_3$  in I20126-South is higher by a factor of 3 than towards I20126-core (i. e., towards the position of the hot molecular core), whereas the fractional abundance of  $\text{N}_2\text{H}^+$  is higher by a factor of 2 in I20126-South than in I20126 core. The values of  $\text{NH}_3$  and  $\text{N}_2\text{H}^+$  fractional abundance,  $X(\text{NH}_3)$  and  $X(\text{N}_2\text{H}^+)$ , obtained for these regions are similar to the values obtained by Johnstone et al. (2010) in a sample of pre-protostellar and protostellar cores in Perseus. Also they are comparable to the values derived by Friesen et al. (2009, 2010) in Ophiuchus molecular cloud, and are in good agreement

with the  $\text{N}_2\text{H}^+$  fractional abundance reported by Fontani et al. (2006) for a sample of high-mass candidates.

## 3.7 Brief discussion

In this chapter we have obtained the rotational temperature, column densities of  $\text{NH}_3$  and  $\text{N}_2\text{H}^+$ , and the  $\text{NH}_3/\text{N}_2\text{H}^+$  ratio in three high-mass star-forming regions harboring several dense cores in different evolutionary stages. In the following section we will briefly discuss the general properties of the dense gas. A more detailed and general discussion of the behavior of the  $\text{NH}_3/\text{N}_2\text{H}^+$  abundance ratio is done in chapter 6.

### 3.7.1 General properties of the dense gas

#### Rotational temperature

The average rotational temperature estimated for the pre-protostellar cores in the three regions studied in this chapter is  $\sim 16$  K, higher than the typical temperature found in low-mass starless cores ( $\sim 10$  K, e. g., Tafalla et al. 2002, 2004; Crapsi et al. 2007). Such high values were also found by Palau et al. (2007) in the pre-protostellar cores surrounding the UCH II region IRAS 20293+3952. This results could indicate either heating produced by a low-mass non-detected YSOs and/or external heating. Actually, in IRAS 22134+5834 and IRAS 00117+6412 we found evidence of external heating toward the immediate surroundings of the UCH II region, with a clear temperature gradient with increasing temperatures when approaching the UCH II region. In addition, in IRAS 00117+6412 the molecular outflow may be interacting with the dense gas, producing the temperature enhancement to the north of the intermediate-mass Class 0/I YSO MM1, similarly to what has been observed in other high-mass star-forming regions (e. g., AFGL 5142: Zhang et al. 2002, IRAS 20293+3952: Palau et al. 2007), where the high temperatures and line broadening arise from shock interaction produced by molecular outflows.

### Column densities

The average  $\text{NH}_3$  column density found in the dense cores is  $\sim 10^{15} \text{ cm}^{-2}$ , similar to the values obtained by Palau et al. (2007). The derived average  $\text{N}_2\text{H}^+$  column density is  $\sim 5 \times 10^{12} \text{ cm}^{-2}$ , which is slightly lower than the values derived by Palau et al. (2007) and Pirogov et al. (2003).

Toward massive cores in Orion, Li et al. (2003) find a general trend for the gas to be colder where the  $\text{NH}_3$  column density is higher. Our estimation of the  $\text{NH}_3$  column density agrees with the result of Li et al. (2003), with the column density being higher in cores with starless properties than in protostellar cores (see for example the case of I00117 and I20126). Another important feature seen in the  $\text{NH}_3$  column density maps is that the lowest values are reached where we found the highest values of the rotational temperature (see for example the case of I22134). This result could be naturally explained if the gas is being perturbed by the passage of a molecular outflow and/or a UV ionization front, either destroying the cavity pushing out the dense material and/or creating a cavity. A good tool to trace enhanced UV fields is the  $\text{CN}/\text{HCN}$  ratio (Fuente et al. 1993; Boger and Sternberg 2005). In fact, CN is detected with the IRAM 30 m Telescope toward IRAS 00117+6412 and IRAS 22134+5834 (Sánchez-Monge, private communication), and hence high angular resolution observations of CN and HCN would allow us to gain insight into the effects of UV fields on the dense gas. This would allow us to distinguish whether the high temperatures and low column densities are due to outflow interaction or UV-radiation field. While in I22134 we find clear evidences of UV field interaction, this is not the case of the I00117 region, where the UCHII region is much less luminous (one order of magnitude) than I22134.

### The $\text{NH}_3/\text{N}_2\text{H}^+$ ratio

Finally, we found important variations in the  $\text{NH}_3/\text{N}_2\text{H}^+$  abundance ratio. Overall, the  $\text{NH}_3/\text{N}_2\text{H}^+$  ratio is higher in pre-protostellar cores than in cores harboring YSOs, in agreement with previous studies performed toward low-mass star-forming regions (Caselli et al. 2002a; Hotzel et al. 2004; Friesen et al. 2010), as well as for the dense cores in the vicinity of the UCHII region IRAS 20293+3952 (Palau et al. 2007). However, while in protostellar cores the  $\text{NH}_3/\text{N}_2\text{H}^+$  ratio is usually  $\sim 50 - 90$ , toward the protostellar core I20126-core we derived values of  $\sim 300$  associated with

the hot molecular core. Similarly to case of AFGL 5142, in such environments where the temperature in the hot core reaches values of  $\sim 200$ , CO desorption produces the destruction of  $\text{N}_2\text{H}^+$ , and consequently the  $\text{NH}_3/\text{N}_2\text{H}^+$  rises significantly with respect to protostellar cores with moderate temperatures ( $T_d \simeq 15\text{--}25$  K).

## Chapter 4

# $N_2H^+$ depletion in the massive protostellar cluster AFGL 5142

*We aim at investigating the  $NH_3/N_2H^+$  abundance ratio toward the high-mass star-forming region AFGL 5142 with high angular resolution in order to study whether the  $NH_3/N_2H^+$  ratio behaves similarly to the low-mass case, for which the ratio decreases from starless cores to cores associated with young stellar objects (YSOs). CARMA was used to observe the 3.2 mm continuum and  $N_2H^+$  (1-0) emission toward AFGL 5142. We used  $NH_3$  (1,1) and (2,2), as well as  $HCO^+$  (1-0) and  $H^{13}CO^+$  (1-0) data available from the literature, to study the chemical environment. Additionally, we performed a time-dependent chemical modeling of the region. The 3.2 mm continuum emission reveals a dust condensation of  $\sim 23 M_\odot$  associated with the massive YSOs, deeply embedded in the strongest  $NH_3$  core (hereafter central core). The dense gas emission traced by  $N_2H^+$  reveals two main cores, the western core of  $\sim 0.08$  pc in size and the eastern core of  $\sim 0.09$  pc, surrounded by a more extended and complex structure of  $\sim 0.5$  pc, mimicking the morphology of the  $NH_3$  emission. The two cores are located to the west and to the east of the 3.2 mm dust condensation. Toward the central core the  $N_2H^+$  emission drops significantly, indicating a clear chemical differentiation in the region. The  $N_2H^+$  column density in the central core is one order of magnitude lower than in the western and eastern cores. Furthermore, we found low values of the  $NH_3/N_2H^+$  abundance ratio  $\sim 50$ – $100$  toward the western and eastern cores and high values up to 1000 associated with the central core. The chemical model used to explain the differences seen in the  $NH_3/N_2H^+$  ratio indicates that density along with temperature is a key pa-*

parameter in determining the abundances of both NH<sub>3</sub> and N<sub>2</sub>H<sup>+</sup>. The high density ( $n \simeq 10^6 \text{ cm}^{-3}$ ) and temperature ( $T \simeq 70 \text{ K}$ ) reached in the central core allow molecules such as CO to evaporate from grain mantles. The CO desorption causes a significant destruction of N<sub>2</sub>H<sup>+</sup>, which favors the formation of HCO<sup>+</sup>. This result is supported by our observations, which show that N<sub>2</sub>H<sup>+</sup> and HCO<sup>+</sup> are anticorrelated in the central core. The observed values of the NH<sub>3</sub>/N<sub>2</sub>H<sup>+</sup> ratio in the central core can be reproduced by our model for times of  $t \simeq 4.5 - 5.3 \times 10^5 \text{ yr}$ , while in the western and eastern cores the NH<sub>3</sub>/N<sub>2</sub>H<sup>+</sup> ratio can be reproduced by our model for times in the range  $10^4 - 3 \times 10^6 \text{ yr}$ . The NH<sub>3</sub>/N<sub>2</sub>H<sup>+</sup> abundance ratio in AFGL 5142 does not follow the same trend as in regions of low-mass star formation mainly because of the high temperature reached in hot cores.

## 4.1 Introduction

It is well known that N-bearing molecules, such as NH<sub>3</sub> and N<sub>2</sub>H<sup>+</sup>, are excellent tracers of the interstellar dense gas because none of these molecules deplete onto dust grains until densities reach  $\sim 10^6 \text{ cm}^{-3}$  (Bergin and Langer 1997; Tafalla et al. 2004; Flower et al. 2006). Thus observations of these dense gas tracers have become a powerful tool when studying the sites of star formation. However, only a few observational studies have focused on comparing NH<sub>3</sub> and N<sub>2</sub>H<sup>+</sup> cores, and these studies, which were carried out toward low-mass star-forming regions, find that the NH<sub>3</sub>/N<sub>2</sub>H<sup>+</sup> abundance ratio is around 60–90 close to the young stellar objects (YSOs), while it rises to 140–190 in starless cores (Caselli et al. 2002a; Hotzel et al. 2004; Friesen et al. 2010). In the intermediate-mass cores surrounding the high-mass star IRAS 20293+3952, Palau et al. (2007) find the same trend, with a high NH<sub>3</sub>/N<sub>2</sub>H<sup>+</sup> ratio, up to 300, in the cores with starless properties, and around 50 for the cores associated with YSOs, clearly showing that chemical differentiation is important in the region. All these studies show that the NH<sub>3</sub>/N<sub>2</sub>H<sup>+</sup> abundance ratio is consistent with being a “chemical clock”.

To investigate the behavior of the NH<sub>3</sub>/N<sub>2</sub>H<sup>+</sup> abundance ratio in high-mass star-forming regions and see if the NH<sub>3</sub>/N<sub>2</sub>H<sup>+</sup> ratio in massive YSOs shows the same trend as in the low-mass regime, we carried out observations and chemical modeling of the high-mass star-forming region AFGL 5142, located at a distance of 1.8 kpc (Snell et al. 1988) in the Perseus arm. The region was selected as a good candidate

for studying the  $\text{NH}_3/\text{N}_2\text{H}^+$  ratio because the high angular resolution  $\text{NH}_3$  emission reveals several dense cores, which have very different temperatures, and one of them is associated with star formation in clustered mode with the presence of hot cores.

The region consists of two main centers of high-mass star formation in different evolutionary stages. The brightest near-infrared source (Hunter et al. 1995) IRAS 05274+3345, with a bolometric luminosity of  $3.8 \times 10^3 L_\odot$  (Carpenter et al. 1990), lies near the western edge of the  $\text{NH}_3$  gas (Estalella et al. 1993) and a lack of dense gas emission associated with it suggests that the IRAS source is a more evolved region, which is consistent with detection of optical nebulosity (Eiroa et al. 1994). Based on its position in the  $J$  vs.  $J - H$  diagram, Chen et al. (2005) classify the IRAS source as a B2 star of 3 Myrs. Torrelles et al. (1992) detect a faint radio continuum source, IRAS 05274+3345 East (hereafter referred as AFGL 5142), about  $30''$  to the east of the IRAS source, which coincides with the peak position of the dust emission at 3.4 mm (Hunter et al. 1999) and the  $\text{NH}_3$  emission peak (Estalella et al. 1993). Assuming that the centimeter emission arises from an optically thin HII region, the flux density is equivalent to a zero-age main sequence (ZAMS) star of spectral type B2 or earlier (Torrelles et al. 1992; Hunter et al. 1995) with a luminosity of  $4 \times 10^3 L_\odot$ .

In the near-infrared, Hunter et al. (1995) report a cluster of 28 embedded sources in a region of  $1'$  ( $\sim 0.3$  pc in radius) near the position of the radio continuum source. Recently, Qiu et al. (2008) carried out Spitzer Space Telescope IRAC and MIPS observations toward AFGL 5142. The authors identify 44 YSOs, 20 of them clustered around the central massive star and surrounded by a more extended and sparse distribution of young stars and protostars. In addition, high angular resolution observations of maser emission reveal a cluster of  $\text{H}_2\text{O}$  and  $\text{CH}_3\text{OH}$  masers in an area of  $\sim 5''$  (Hunter et al. 1995; Goddi and Moscadelli 2006; Goddi et al. 2007). Subsequent observations with the Very Large Array (VLA) in the A configuration at 8.4 GHz and with the Submillimeter Array (SMA) at 1.2 mm with  $\sim 1''$  of angular resolution were carried out by Zhang et al. (2007), who find that the centimeter source is resolved into three peaks, and that the 3.4 mm source detected by Hunter et al. (1999) actually consists of five millimeter sources. Regarding the molecular outflow emission in this region, Zhang et al. (2007) identify three molecular outflows in CO (2–1) and SO  $6_5-5_4$ , one of them coinciding with an  $\text{HCO}^+$  outflow and the well-collimated SiO jet detected by Hunter et al. (1999). All three outflows appear to originate from the dust condensation in a region of about  $3''$ . All this information

indicates that active star formation in clustered mode is taking place in AFGL 5142.

The dense gas emission in this region has been studied with single-dish telescopes in  $\text{NH}_3$ , CS, HCN,  $\text{HCO}^+$ ,  $\text{CH}_3\text{OH}$ , and  $\text{CH}_3\text{CN}$  (Verdes-Montenegro et al. 1989; Estalella et al. 1993; Hunter et al. 1995, 1999; Cesaroni et al. 1999b). In particular, the dense gas emission traced by the  $\text{NH}_3$  molecule has been observed with high angular resolution using the VLA (Zhang et al. 2002). The high angular resolution  $\text{NH}_3$  emission consists of a central and compact core associated with the dust condensation, harboring at least three intermediate/high-mass young stars, surrounded by fainter  $\text{NH}_3$  cores located in a more extended structure with no signs of stellar activity (either maser nor molecular outflow emission associated with it) indicating that the region may harbor cores in different evolutionary stages. The presence of cores containing massive star(s), together with cores with no star-formation activity, makes this region a good choice for studying how the  $\text{NH}_3/\text{N}_2\text{H}^+$  ratio behaves in high-mass star-forming regions.

In this chapter we report CARMA observations of the continuum emission at 3.2 mm and the dense gas traced by  $\text{N}_2\text{H}^+$  (1–0) toward AFGL 5142. The chapter layout is as follows. In § 2 we summarize our observations and the data reduction process. In § 3 we present the main results for the continuum and  $\text{N}_2\text{H}^+$  molecular line emission. In § 4 we analyze the molecular emission of several species by computing their column density maps. In § 5 we show the main results of the chemical model to qualitatively reproduce the abundances of the region. Finally, in § 6 we discuss our findings, and we list the main conclusions in § 7.

## 4.2 Observations

The Combined Array for Research in Millimeter-wave Astronomy<sup>a</sup> (CARMA) was used to observe the 3.2 mm continuum and the  $\text{N}_2\text{H}^+$  (1–0) emission toward AFGL 5142. CARMA consists of six 10 m and nine 6 m antennas located at 2200 meters elevation at Cedar Flat in the Inyo Mountains of California. The observations were carried

---

<sup>a</sup>Support for CARMA construction was derived from the Gordon and Betty Moore Foundation, the Kenneth T. and Eileen L. Norris Foundation, the Associates of the California Institute of Technology, the states of California, Illinois, and Maryland, and the National Science Foundation. Ongoing CARMA development and operations are supported by the National Science Foundation under a cooperative agreement and by the CARMA partner universities.

out on 2007 February 4 and March 11 using the array in the C configuration with 14 antennas in the array. The projected baselines ranged from 26 to 370 m. The phase center was set at  $\alpha = 05^{\text{h}}30^{\text{m}}48^{\text{s}}.02$ ,  $\delta = +33^{\circ}47'54''.47$ . The FWHM of the primary beam at the frequency of the observations was  $132''$  for the 6 m antennas and  $77''$  for the 10 m antennas. System temperatures were around 250 K during both days.

The digital correlator was configured to observe simultaneously the continuum emission and the  $\text{N}_2\text{H}^+$  (1–0) group of the hyperfine transitions (93.176331 GHz, in the lower sideband). The continuum data were recorded in two  $\sim 500$  MHz bands covering the frequency ranges 93.44–93.88 GHz and 96.74–97.18 GHz from the receiver lower and upper sidebands, respectively. We used two consecutive bands of 8 MHz of bandwidth with 63 channels in each band, providing a spectral resolution of  $0.42 \text{ km s}^{-1}$  to observe the  $\text{N}_2\text{H}^+$  (1–0) emission.

Phase calibration was performed with the quasars 0530+135 and 0555+398, with typical rms in the phases of  $12^\circ$  and  $8^\circ$ , respectively. The absolute position accuracy was estimated to be around  $0''.1$ . Flux and bandpass calibration was set by using 3C84. Data were calibrated and imaged using the standard procedures in MIRIAD (Sault et al. 1995). We combined the data from both days of observations. The rms in the naturally weighted maps is  $\sim 0.7 \text{ mJy beam}^{-1}$  in the continuum, and  $\sim 55 \text{ mJy beam}^{-1}$  per  $0.42 \text{ km s}^{-1}$  channel in the line data. The synthesized beam of the continuum image is  $2''.53 \times 1''.71$ , P.A.=  $68.8^\circ$ . For the line emission, which is more extended than the continuum, we applied a  $uv$ -taper function of  $52 \text{ k}\lambda$  ( $3''.5$  in the image plane) to improve the signal-to-noise ratio and to recover the extended emission. The resulting synthesized beam is  $4''.04 \times 3''.53$ , with P.A.=  $79.1^\circ$ . The continuum and  $\text{N}_2\text{H}^+$  emissions were cleaned using a box around the emitting region.

## 4.3 Results

### 4.3.1 Continuum emission

Figure 4.1 presents the continuum map at 3.2 mm. We detected a single millimeter peak associated with IRAS05274+3345 East (we could not resolve the

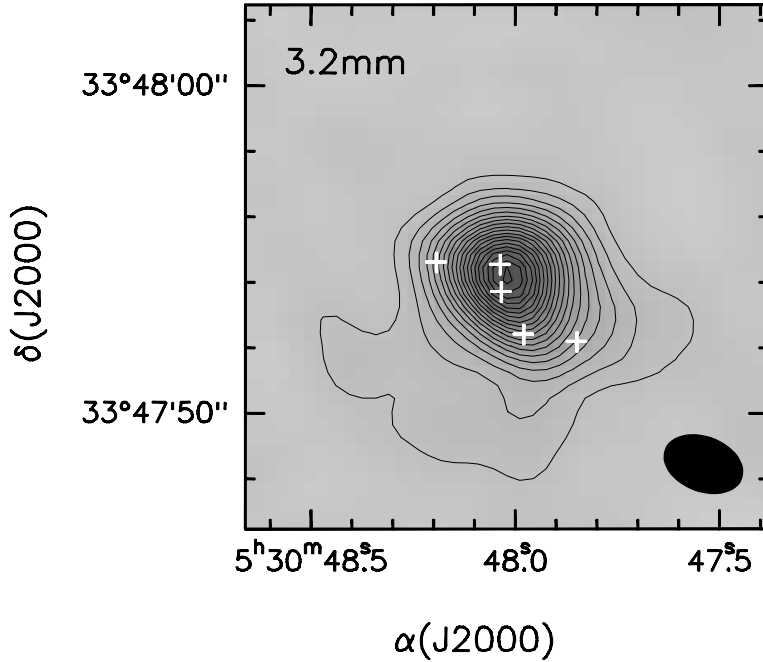


Figure 4.1: 3.2 mm continuum emission toward AFGL 5142. Contour levels range from 3 to  $60\sigma$  in steps of  $3\sigma$ , where  $\sigma$  is the rms of the map,  $0.7 \text{ mJy beam}^{-1}$ . The synthesized beam, shown in the bottom right corner, is  $2''.53 \times 1''.71$ , P.A. =  $68.8^\circ$ . White crosses indicate the millimeter sources detected by Zhang et al. (2007) at 1.2 mm with the SMA.

two main 1.2 mm peaks MM-1 and MM-2, separated by about  $1''$ , detected with the SMA by Zhang et al. 2007). The millimeter continuum emission has a single compact peak component with a flux density of  $107.1 \pm 1.6 \text{ mJy}$ , surrounded by a more extended and flattened emission elongated in the west and southeast directions. A 2D Gaussian fit to the compact component yields a deconvolved size of  $2''.9 \times 2''.3$ , P.A. =  $16.5^\circ$  (5200 AU at the distance of the source). The peak position is  $\alpha(J2000) = 05^{\text{h}}30^{\text{m}}48^{\text{s}}01$ ;  $\delta(J2000) = +33^\circ47'54''.1$ . The total flux density when taking into account the extended emission is  $126.4 \pm 3.1 \text{ mJy}$ , in very good agreement with the flux density at 88 GHz reported by Hunter et al. (1999), which is  $\sim 125 \text{ mJy}$ . Assuming that the dust emission is optically thin, and using the dust opacity law of Hildebrand (1983), with a dust emissivity index of  $\beta = 1$  (see Zhang et al. 2007 for a description of its derivation), and for a dust temperature of 45 K (based on the estimation of Hunter et al. 1999) the total mass of dust and gas from thermal continuum emission is  $23 M_\odot$  (after correcting for the expected contribution,  $\sim 4\%$ ,

from the ionized gas; see Hunter et al. 1999). This mass is consistent with the mass estimated from the 1 mm SMA observations ( $\sim 21 M_{\odot}$ ). Although Zhang et al. (2007) report a mass of  $50 M_{\odot}$ , the difference arises from the value adopted for the dust emissivity index,  $\beta = 1.5$  instead of 1. There is a factor of 4 in the uncertainty of the mass, mainly due to uncertainties in the dust opacity and the dust emissivity index.

### 4.3.2 Molecular line emission: $\text{N}_2\text{H}^+$

In Fig. 4.2 we show the  $\text{N}_2\text{H}^+$  (1–0) spectra not corrected for the primary beam response at some selected positions of AFGL 5142, and in Table 4.1 we present the line parameters obtained from the fit of the hyperfine spectra toward these positions. Figure 4.3 presents the velocity channel maps for the  $\text{N}_2\text{H}^+$  (1–0) emission toward AFGL 5142. The channel with maximum intensity for the hyperfine component  $F_1 F_2 = 01 \rightarrow 12$  was found at the velocity  $v = -3.5 \text{ km s}^{-1}$ . The systemic velocity of the cloud is  $v_{\text{LSR}} = -3 \text{ km s}^{-1}$ .

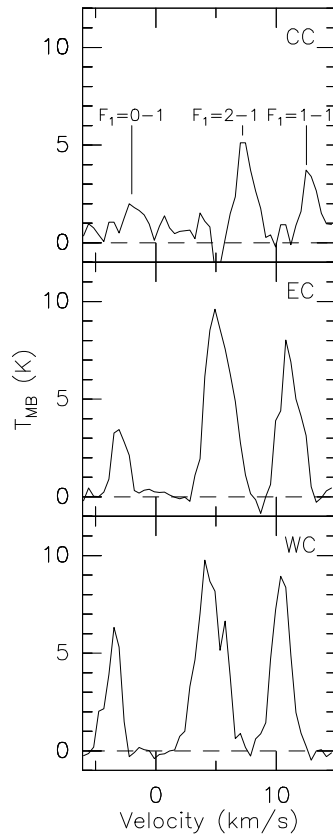


Figure 4.2:  $\text{N}_2\text{H}^+$  (1–0) spectra toward three positions of AFGL 5142. The three positions labeled on each panel are, from top to bottom, CC ( $\text{NH}_3$  peak or central core), EC (peak of the eastern core), and WC (peak of the western core, see Fig. 4.4).

Table 4.1: Parameters of the hyperfine fits to the  $\text{N}_2\text{H}^+$  (1–0) line for the central position of each core

| Core                 | Position <sup>a</sup>  |                        | $A\tau_m^b$<br>(K km s <sup>-1</sup> ) | $v_{\text{LSR}}^c$<br>(km s <sup>-1</sup> ) | $\Delta v$<br>(km s <sup>-1</sup> ) | $\tau_m^d$ | $T_{\text{ex}}$<br>(K) | $N(\text{N}_2\text{H}^+)$<br>( $\times 10^{12}$ cm <sup>-2</sup> ) |
|----------------------|------------------------|------------------------|--|---|-------------------------------------|------------|------------------------|--|
|                      | $\alpha(\text{J2000})$ | $\delta(\text{J2000})$ |  |   |                                     |            |                        |  |
| central <sup>e</sup> | 05:30:48.02            | 33:47:53.4             | 0.51±0.04                              | -0.97±0.06                                  | 1.11±0.10                           | 0.10±0.03  | 8.2±1.6                | 2.8±0.9  |
| eastern              | 05:30:48.73            | 33:47:52.9             | 1.35±0.02                              | -2.92±0.01                                  | 1.60±0.02                           | 0.10±0.02  | 16.7±1.1               | 18.5±1.2   |
| western              | 05:30:47.47            | 33:47:51.7             | 2.45±0.01                              | -3.57±0.01                                  | 1.31±0.03                           | 0.27±0.02  | 12.4±0.8               | 14.4±1.2   |

**Notes.** <sup>a</sup> Positions, given in (h m s) and ( $^{\circ}$  ' "). <sup>b</sup>  $A = f(J_{\nu}(T_{\text{ex}}) - J_{\nu}(T_{\text{bg}}))$ , where  $f$  is the filling factor (assumed to be 1),  $T_{\text{ex}}$  is the excitation temperature of the transition,  $T_{\text{bg}}$  is the background radiation temperature, and  $J_{\nu}(T)$  is the intensity in units of temperature,  $J_{\nu}(T) = (h\nu/k)/(\exp(h\nu/kT) - 1)$ . <sup>c</sup>  $v_{\text{LSR}}$  corresponding to the  $F_1F = 01 \rightarrow 12$  hyperfine component. <sup>d</sup> Optical depth of the main line,  $F_1F = 23 \rightarrow 12$ , obtained from the fit. <sup>e</sup> Position of the central core taken from the  $\text{NH}_3$  emission peak.

The zero-order moment map integrated for all the hyperfine transitions is presented in Fig. 4.4a. For comparison, we also show (in Fig. 4.4b) the  $\text{NH}_3$  (1,1) integrated intensity map from Zhang et al. (2002) overlaid with the cluster of infrared sources reported in recent studies (Hunter et al. 1995; Chen et al. 2005; Qiu et al. 2008) in order to have a complete view of the stellar content in AFGL 5142. The overall structure of the integrated  $\text{N}_2\text{H}^+$  (1–0) emission consists of two main cores, located to the west and to the east of the dust condensation (hereafter western and eastern cores), surrounded by a more extended structure with an X-shape morphology, roughly following the same morphology as the  $\text{NH}_3$  emission. As can be seen in Fig. 4.4, the western core seems to contain at least one infrared source embedded in the dense gas, located close to the position of the  $\text{NH}_3$  peak, and it displays typical characteristics of protostars (Chen et al. 2005), whereas the infrared source lying close to the peak position of the eastern core has no associated infrared excess and has been classified as a Herbig Ae/Be or T Tauri star (Chen et al. 2005). However, there is no clear evidence that these infrared sources are really associated with the dense gas. Additionally, since the sensitivity of Spitzer observations is  $\sim 1 M_{\odot}$  (Qiu et al. 2008) and that of near-infrared studies is  $\sim 0.2\text{--}0.4 M_{\odot}$  (Chen et al. 2005), we cannot discard the possibility of more infrared sources embedded in the dense gas. A 2D Gaussian fit to the western and eastern cores yields deconvolved sizes of

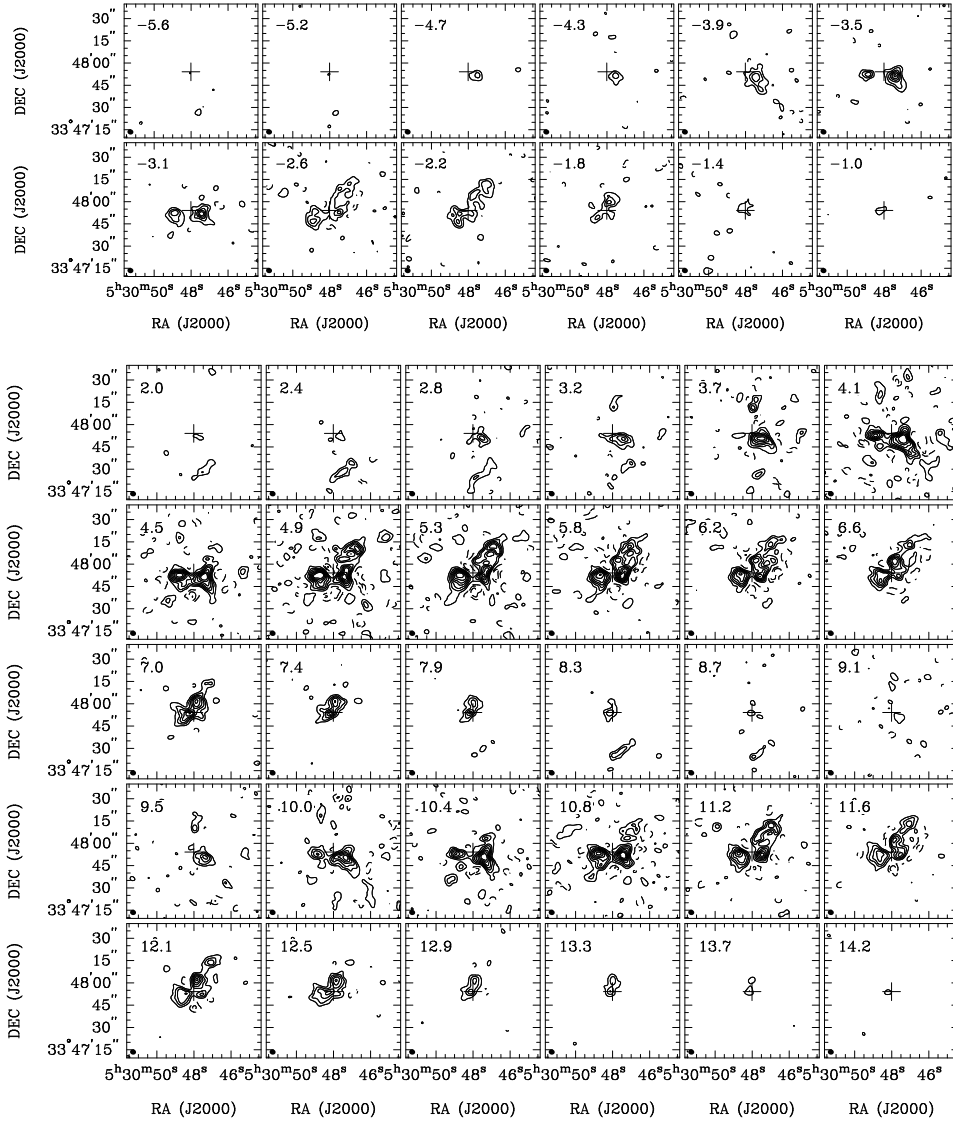


Figure 4.3: *Top panel:*  $N_2H^+$  ( $1-0$ ) channel maps for the hyperfine  $F_1F = 01 \rightarrow 12$  (isolated line) toward AFGL 5142. Contour levels are  $-2, 2, 4, 6, 8, 10,$  and  $12$  times the rms noise of the maps,  $0.055 \text{ Jy beam}^{-1}$ . *Bottom panel:*  $N_2H^+$  ( $1-0$ ) channel maps for the hyperfine  $F_1F = 21 \rightarrow 11, 23 \rightarrow 12, 22 \rightarrow 11,$  and  $F_1F = 11 \rightarrow 10, 12 \rightarrow 12,$  and  $10 \rightarrow 11$ . Contour levels are  $-4, -2, 2, 4, 6, 8, 10, 12,$  and  $14$  times the rms of the map,  $0.055 \text{ Jy beam}^{-1}$ . In all panels the cross marks the position of the 3.2 mm continuum source. The synthesized beam is shown in the bottom left corner. Velocities refer to the  $F_1F = 01 \rightarrow 12$  hyperfine with the systemic velocity  $v_{\text{LSR}} = -3 \text{ km s}^{-1}$ .

$\sim 9''.3 \times 7''.6$  ( $\sim 0.08 \times 0.07$  pc) and  $\sim 10''.4 \times 8''.3$  ( $\sim 0.09 \times 0.07$  pc), respectively. Interestingly, toward the dust condensation where the intermediate/high-mass stars are deeply embedded in the strongest and compact  $\text{NH}_3$  core (hereafter central core), the  $\text{N}_2\text{H}^+$  emission decreases drastically. However, the central core is detected in  $\text{N}_2\text{H}^+$  in some velocity channels from  $7 \text{ km s}^{-1}$  to  $8.7 \text{ km s}^{-1}$ , and its peak positions is slightly shifted to the east ( $\sim 2''$ ) from the dust and  $\text{NH}_3$  peaks.

We used the hyperfine component  $F_1F = 01 \rightarrow 12$  to study the kinematics of the  $\text{N}_2\text{H}^+$  emission seen from Fig. 4.3 since this hyperfine component is strong and not blended with the other hyperfine components. In Fig. 4.5a we show the first-order moment map (intensity weighted mean  $v_{\text{LSR}}$ ), and in Fig. 4.5b the second-order map (intensity weighted velocity dispersion) for this hyperfine component.

The first-order moment map shows that the eastern and western cores appear at different velocities (see also the channel maps shown in Fig. 4.3). Toward the eastern core there is a small velocity gradient in the east-west direction from  $\sim -3.5 \text{ km s}^{-1}$  to  $\sim -1.8 \text{ km s}^{-1}$ . On the other hand, the western core shows a velocity gradient from  $\sim -4.7 \text{ km s}^{-1}$  to  $\sim -2.6 \text{ km s}^{-1}$  with increasing velocities from the southwest to the northeast. In fact, as can be seen in Fig. 4.5b, the emission from the western core has very broad lines, with a velocity dispersion of  $\sim 0.8\text{--}1 \text{ km s}^{-1}$ , which corresponds for a Gaussian line profile, to a  $FWHM$  of  $2\sqrt{2\ln 2} \times \sigma_v$ , where  $\sigma_v$  is the velocity dispersion of  $\sim 1.8\text{--}2.3 \text{ km s}^{-1}$  (corrected for instrumental resolution) at the eastern side of the western core. This region of broad emission coincides with the passage of outflow B of Zhang et al. (2007). The values around  $\sim 2 \text{ km s}^{-1}$  are significantly higher than the thermal line width  $\sim 0.2\text{--}0.3 \text{ km s}^{-1}$  (estimated for a kinetic temperature of 25 K and 45 K, respectively), indicative of  $\text{N}_2\text{H}^+$  having a significant contribution from nonthermal processes, such as turbulence injected by the molecular outflows, and/or global systematic motions. Regarding the eastern core, the typical value found for the velocity dispersion is in the range  $\sim 0.3\text{--}0.5 \text{ km s}^{-1}$ , corresponding to line widths of  $\sim 0.2\text{--}1.1 \text{ km s}^{-1}$  (corrected for instrumental resolution). In addition, there is a clumpy cavity structure toward the northwest clearly visible in the  $-2.6$  and  $-2.2 \text{ km s}^{-1}$  channel maps of Fig. 4.3, which appear redshifted by  $\sim 1 \text{ km s}^{-1}$  with respect to the systemic velocity.

In Fig. 4.6a we present the position-velocity (PV) plot made across the east-west direction (P.A. =  $90^\circ$ ), encompassing the  $\text{N}_2\text{H}^+$  peaks of the western and eastern cores, which clearly shows a ring-like structure with the western core having very

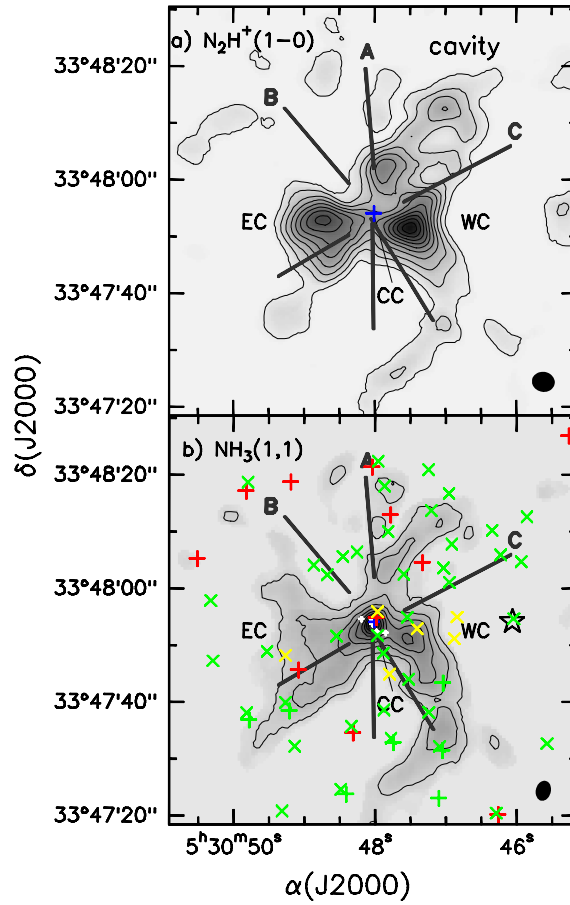


Figure 4.4: a)  $N_2H^+$  zero-order moment integrated for all the hyperfine components of the (1–0) transition. Contours start at 3 %, increasing in steps of 10 % of the peak intensity,  $6.01 \text{ Jy beam}^{-1} \text{ km s}^{-1}$ . b)  $NH_3$  (1,1) zero-order moment (Zhang et al. 2002). Contours start at 10 %, increasing in steps of 10 % of the peak intensity,  $0.202 \text{ Jy beam}^{-1} \text{ km s}^{-1}$ . The synthesized beams,  $4''.04 \times 3''.53$  for  $N_2H^+$  and  $3''.58 \times 2''.64$  for  $NH_3$ , are shown in the bottom right corner. In both panels the blue cross marks the position of the millimeter source reported in this work. Red crosses: type I (protostars); green crosses: type II (class II objects) from Qiu et al. (2008). Yellow and green tilted crosses are from Chen et al. (2005) and represent Class I luminous protostars with  $M < 5 M_\odot$  and Herbig Ae/Be stars or T Tauri stars, respectively. White crosses are the 5 millimeter peaks detected with the SMA by Zhang et al. (2007), and the star marks the position of the IRAS 05274+3345. The western, eastern, and central cores are also labeled as WC, EC, and CC, respectively. The thick straight black lines represent the direction of outflows A, B, and C (Zhang et al. 2007).

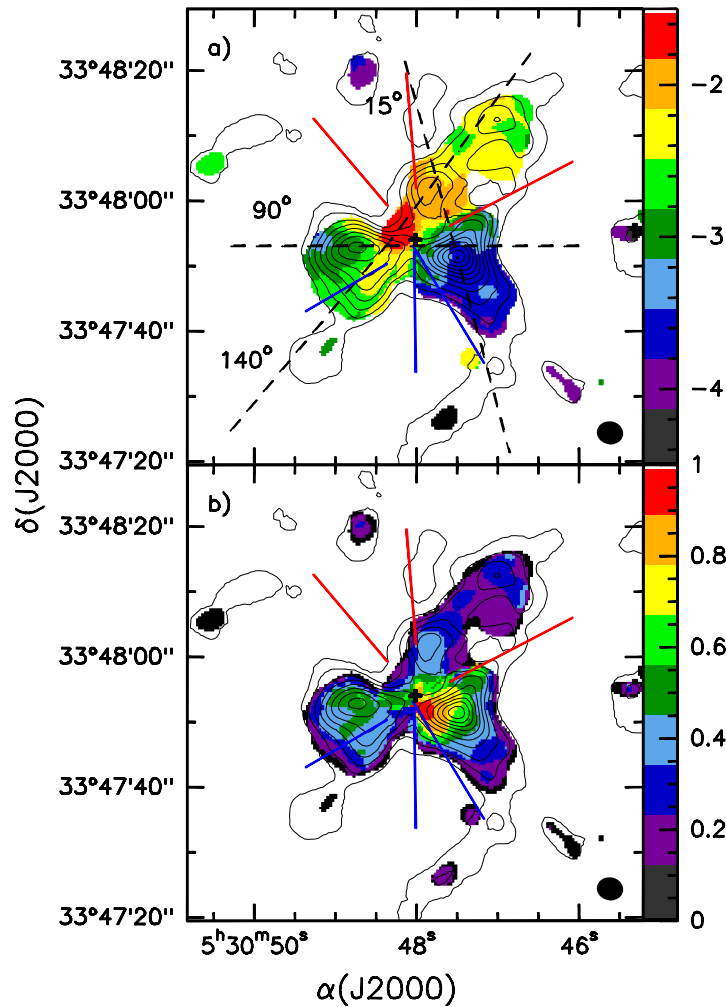


Figure 4.5: a) First-order moment map (velocity) for the hyperfine  $F_1F = 01 \rightarrow 12$  line of  $N_2H^+$  (1-0) toward AFGL 5142 (color scale). b) Second-order moment map (velocity dispersion) for the hyperfine  $F_1F = 01 \rightarrow 12$  line of  $N_2H^+$  (1-0) (color scale). In both figures, black contours are the same as in Fig 4.4 (a), showing the  $N_2H^+$  (1-0) emission, with contours starting at 3 %, and increasing in steps of 10 % of the peak intensity. Color scales are in  $\text{km s}^{-1}$ . The synthesized beam is shown in the bottom right corner of the image. The black cross marks the position of the 3.2 mm source reported in this work. Blue and red lines represent the direction of outflows A, B, and C (Zhang et al. 2007), and the black dashed line in the top panel indicates the position-velocity cuts (see Fig 4.6). The second-order moment gives the velocity dispersion and must be multiplied by the factor  $2\sqrt{2\ln 2} \simeq 2.35$  to convert to  $FWHM$ .

broad line widths. The line broadening of  $\sim 3.5 \text{ km s}^{-1}$  is also seen in the PV-plot made across the western core at P.A.=  $15^\circ$  (Fig. 4.6b). Additionally, we performed a third cut at P.A.=  $140^\circ$  (Fig. 4.6c), picking up the eastern side of the cavity and the eastern core. From this plot, it seems that there are two structures, a velocity gradient associated with the eastern core of  $\sim 1.5 \text{ km s}^{-1}$  in a region of  $7''$  and a curve structure associated with the cavity. The curve structure seen in the PV-plot of Fig. 4.6c suggests that the cavity is expanding. Overall it seems that both cuts, at P.A.=  $90^\circ$  and P.A.=  $140^\circ$ , reveal expanding motions, suggesting that these motions could be produced by a combination of stellar winds, radiation, and/or molecular outflows from the central cluster. As a result, the AFGL 5142 cluster seems to be in process of disrupting the natal cloud. However, we will not discuss the kinematics of the region further since it is not the aim of this study.

## 4.4 Analysis

### 4.4.1 Column density maps

We studied the chemical environment of AFGL 5142 by analyzing the column density of several molecular species. We used the  $\text{N}_2\text{H}^+$  (1–0) (this work),  $\text{NH}_3$  (1,1) and  $\text{NH}_3$  (2,2) from Zhang et al. (2002), and  $\text{HCO}^+$  (1–0) and  $\text{H}^{13}\text{CO}^+$  (1–0) from Hunter et al. (1999) data. To properly compare the emission of all the molecules, we convolved the  $\text{N}_2\text{H}^+$ ,  $\text{NH}_3$ ,  $\text{HCO}^+$ , and  $\text{H}^{13}\text{CO}^+$  channel maps to obtain a final circular beam of  $\sim 4''$ . We computed the column density maps by extracting the spectra for positions in a grid of  $1'' \times 1''$ . Using CLASS we fitted the hyperfine structure of each spectrum for  $\text{N}_2\text{H}^+$  (1–0) and  $\text{NH}_3$  (1,1), and a single Gaussian for the  $\text{NH}_3$  (2,2),  $\text{HCO}^+$  (1–0) and  $\text{H}^{13}\text{CO}^+$  (1–0). We fitted only those positions with an intensity greater than  $5\sigma$  for  $\text{N}_2\text{H}^+$  (1–0) and  $\text{NH}_3$  (1,1) in order to ensure we are detecting all the hyperfine components, whereas for the other molecular species we fitted the spectra with an intensity greater than  $4\sigma$ . In the following sections we show the method used to compute the column density for each molecule. The main results are summarized in Table 4.2.

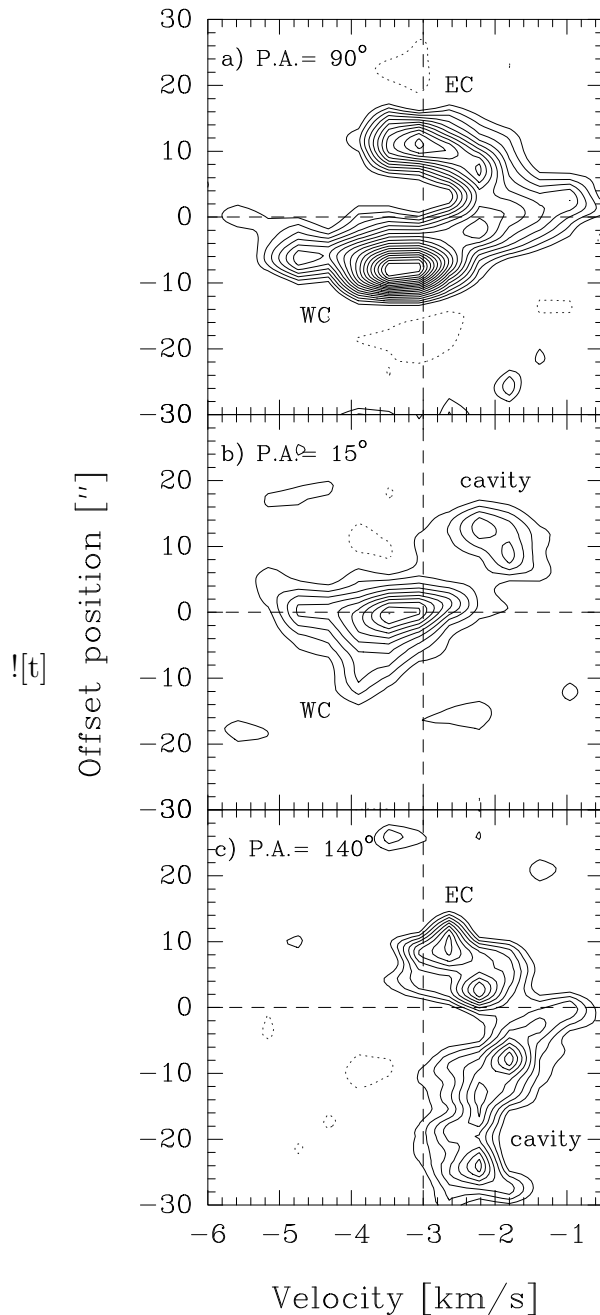


Figure 4.6:  $\text{N}_2\text{H}^+$  p-v plot for the  $F_1F = 01 \rightarrow 12$  hyperfine at a) PA= $90^\circ$  (along the eastern and western cores). Channel maps have been convolved with a beam  $6'' \times 2''$  with P. A. perpendicular to the direction of the cut. Contours start at 10 %, increasing in steps of 5 % of the peak emission,  $0.408 \text{ Jy beam}^{-1}$ . The central position corresponds to the 3.2 mm source. Positive offsets are toward the east. b) PA= $15^\circ$ . Channel maps have been convolved with a beam  $2'' \times 2''$ . Contours start at 10 %, increasing in steps of 10 % of the peak emission,  $0.601 \text{ Jy beam}^{-1}$ . The central position is taken at the peak position of the western core, which is  $\Delta x = -6.5''$ ,  $\Delta y = -3''$  offset from the phase center. Positive offsets are toward the northeast. c) PA= $140^\circ$ . Contours start at 20 %, and increase in steps of 10 % of the peak emission,  $0.376 \text{ Jy beam}^{-1}$ . Positive offsets are toward the southeast. The central position corresponds to  $\Delta x = 3.9''$ ,  $\Delta y = -0.59''$  offset from the phase center. In all panels, the vertical dashed line indicates the systemic velocity,  $v_{\text{LSR}} = -3 \text{ km s}^{-1}$ .

**N<sub>2</sub>H<sup>+</sup>**

We used the hyperfine structure fitting program in CLASS adopting the hyperfine frequencies given in Caselli et al. (1995) to determine the  $v_{\text{LSR}}$ , the intrinsic line widths, total optical depths, and excitation temperatures ( $T_{\text{ex}}$ ) in each position of the grid. The value of  $T_{\text{ex}}$  was derived assuming a filling factor of 1. As shown in Table 4.1, the excitation temperature,  $T_{\text{ex}}$ , derived from the hyperfine fits in the eastern core is in the range  $\sim 14\text{--}16$  K, while  $T_{\text{ex}}$  has lower values around  $\sim 10\text{--}12$  K and  $\sim 8\text{--}9$  K for the western and central cores, respectively.

The results obtained from the fits indicate that the N<sub>2</sub>H<sup>+</sup> emission is essentially optically thin for most of the region ( $\tau_{\text{TOT}} \simeq 0.3\text{--}0.6$ ); however, the optical depth in the western core reaches higher values, around  $\tau_{\text{TOT}} \simeq 1.5\text{--}2$ . We calculated the N<sub>2</sub>H<sup>+</sup> column density, corrected for the primary beam response, following the expression given in Caselli et al. (2002b), and approximating the partition function to  $Q_{\text{rot}} \simeq (kT_{\text{ex}}/hB) \sim 0.4473 T_{\text{ex}}$ , where  $k$  is the Boltzmann constant,  $T_{\text{ex}}$  the excitation temperature,  $h$  the Planck constant, and  $B$  the rotational constant of N<sub>2</sub>H<sup>+</sup>.

Figure 4.7a shows the resulting N<sub>2</sub>H<sup>+</sup> column density map. Clearly, we found important variation in the N<sub>2</sub>H<sup>+</sup> column density in AFGL 5142. The highest value of the N<sub>2</sub>H<sup>+</sup> column density,  $3 \times 10^{13} \text{ cm}^{-2}$ , is reached in the western core. Toward the eastern core we found values of the N<sub>2</sub>H<sup>+</sup> column density around  $\sim 1 \times 10^{13} \text{ cm}^{-2}$ , while the N<sub>2</sub>H<sup>+</sup> column density has the lowest values, around  $\sim 1\text{--}5 \times 10^{12} \text{ cm}^{-2}$ , toward the millimeter condensation, i. e., toward the central core (see Table 4.2). The values found in the western and eastern cores are in good agreement with the N<sub>2</sub>H<sup>+</sup> column densities reported by Pirogov et al. (2003, 2007) for dense molecular cloud cores with massive stars and star clusters and Fontani et al. (2006) for a sample of high-mass protostellar candidates. In addition, the values of the N<sub>2</sub>H<sup>+</sup> column density found in the western and eastern cores of AFGL 5142 are also consistent with those reported in recent studies conducted toward massive star-forming regions observed with interferometers (e. g., Palau et al. 2007; Beuther and Henning 2009), but those obtained in the central core are clearly below. It is important to emphasize the difference of 1 order of magnitude in the N<sub>2</sub>H<sup>+</sup> column density in the central core compared to the western and eastern cores. The uncertainty in the N<sub>2</sub>H<sup>+</sup> column density lies between 25 and 50 %, and it has been estimated taking into account the uncertainty in the output parameters of CLASS and the uncertainty in

the calibration.

### NH<sub>3</sub>

The optical depth of the main line derived from the NH<sub>3</sub> emission is in the range  $\tau_{\text{TOT}} \simeq 1.5\text{--}2.5$  toward the central and compact NH<sub>3</sub> core containing the intermediate/high-mass stars, while the emission in the extended structure is optically thin.

From the results of the fits of the NH<sub>3</sub> (1,1) and NH<sub>3</sub> (2,2) spectra, we derived the rotational temperature ( $T_{\text{rot}}$ ) and computed the NH<sub>3</sub> column density map following the procedures described in Ho and Townes (1983) and Harju et al. (1993) (see also the appendix of Busquet et al. 2009 for a description of the method). It is worth noting that the rotational temperature map obtained from this analysis is similar to the NH<sub>3</sub> (2,2)/NH<sub>3</sub> (1,1) intensity map presented in Zhang et al. (2002).

The NH<sub>3</sub> column density map, corrected for the primary beam attenuation, is shown in Fig. 4.7b. The map shows small variations along the entire cloud. In contrast to N<sub>2</sub>H<sup>+</sup>, the NH<sub>3</sub> column density reaches the maximum value, around  $3 \times 10^{15} \text{ cm}^{-2}$ , toward the central core at the position of the millimeter condensation, and where we found the minimum N<sub>2</sub>H<sup>+</sup> column density (see Table 4.2). The values found for the NH<sub>3</sub> column density toward AFGL 5142 are similar to those obtained by Palau et al. (2007) in the massive star-forming region IRAS 20293+3952. The uncertainty in the NH<sub>3</sub> column density is  $\sim 15\text{--}25\%$ , estimated from the uncertainty in the rotational temperature (see Busquet et al. 2009), the output parameters of CLASS, and the uncertainty in the calibration.

### H<sup>13</sup>CO<sup>+</sup>

To derive the H<sup>13</sup>CO<sup>+</sup> column density, we assumed that H<sup>13</sup>CO<sup>+</sup> (1–0) emission is optically thin while HCO<sup>+</sup> (1–0) is optically thick. The H<sup>13</sup>CO<sup>+</sup> (1–0) optical depth has been estimated from the ratio of the H<sup>13</sup>CO<sup>+</sup> and HCO<sup>+</sup> integrated intensity emission obtained from Gaussian fits and excluding the high-velocity components of HCO<sup>+</sup> (1–0) coming from molecular outflow emission.

Assuming that all levels are populated according to the same excitation temperature  $T_{\text{ex}}$  and approximating the partition function to  $kT_{\text{ex}}/hB$ , with B the rotational

constant of the molecule, the column density of a linear molecule obtained from the transition  $J \rightarrow J - 1$  is

$$N = \frac{3k}{4\pi^3} \frac{1}{\mu^2 \nu_{10} J} T_{\text{ex}} \frac{\exp\left(\frac{J(J+1) h\nu_{10}}{2 kT_{\text{ex}}}\right)}{\exp\left(\frac{J h\nu_{10}}{kT_{\text{ex}}}\right) - 1} \tau_0 \Delta v, \quad (4.1)$$

where  $\mu$  is the electric dipole momentum of the molecule,  $\nu_{10}$  the frequency of the transition  $J = 1 \rightarrow 0$ , and  $\tau_0$  the opacity at the line center.

For the particular case of  $\text{H}^{13}\text{CO}^+$  (1-0) molecular transition,  $\mu = 3.88$  Debye =  $3.88 \times 10^{-18}$  (cgs),  $\nu_{10} = 86.754$  GHz, the column density can be written, in practical units, as

$$\left[ \frac{N(\text{H}^{13}\text{CO}^+)}{\text{cm}^{-2}} \right] = 2.56 \times 10^{11} \frac{1}{1 - e^{-4.16/T_{\text{ex}}}} \left[ \frac{T_{\text{ex}}}{\text{K}} \right] \tau_0 \left[ \frac{\Delta v}{\text{km/s}} \right]. \quad (4.2)$$

In Fig. 4.7c we present the  $\text{H}^{13}\text{CO}^+$  column density map toward the central core of AFGL 5142. An obvious feature is that the  $\text{H}^{13}\text{CO}^+$  column density map is correlated with the  $\text{NH}_3$  column density map, reaching the maximum value, around  $5 \times 10^{12} \text{ cm}^{-2}$  toward the millimeter condensation, but is anticorrelated with the  $\text{N}_2\text{H}^+$  column density. The values obtained for the  $\text{H}^{13}\text{CO}^+$  column density are similar to those found toward regions of high-mass star formation (e. g., Zinchenko et al. 2009). Taking the uncertainty in the output parameters of CLASS and the uncertainty in the calibration into account, we estimated an uncertainty in the  $\text{H}^{13}\text{CO}^+$  column density around  $\sim 30\text{--}45$  %.

#### 4.4.2 The $\text{NH}_3/\text{N}_2\text{H}^+$ abundance ratio map

Figure 4.8 shows the  $\text{NH}_3/\text{N}_2\text{H}^+$  abundance ratio map toward AFGL 5142. First of all, it is important to point out that the  $\text{N}_2\text{H}^+$  spectra toward some positions of the central core have low signal-to-noise, so only a few positions with high enough signal-to-noise ratio were fitted properly, so hence the values obtained toward the central core, especially those toward the southwestern side of the millimeter condensation, are overestimated due to the interpolation process. A clear feature seen from the  $\text{NH}_3/\text{N}_2\text{H}^+$  ratio map is that the highest values, ranging from  $\sim 400$  up to 1000, are reached close to the position of the central core (i. e., harboring a cluster of millimeter

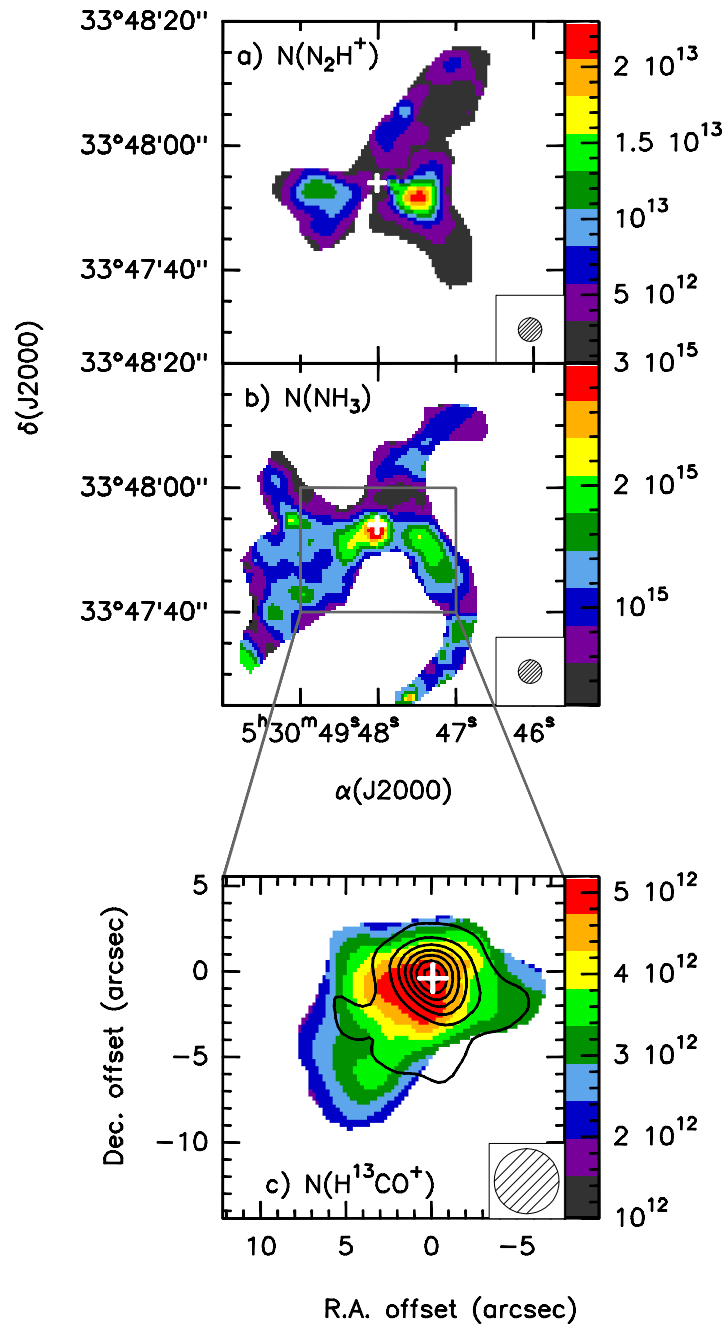


Figure 4.7: a) N<sub>2</sub>H<sup>+</sup> column density map. b) NH<sub>3</sub> column density map. c) H<sup>13</sup>CO<sup>+</sup> column density map overlaid with the 3.2 mm continuum emission (contours). In all panels scale units are cm<sup>-2</sup>. The synthesized beam,  $\sim 4''$ , is shown in the bottom right corner of each panel. The white cross marks the position of the 3.2 mm peak.

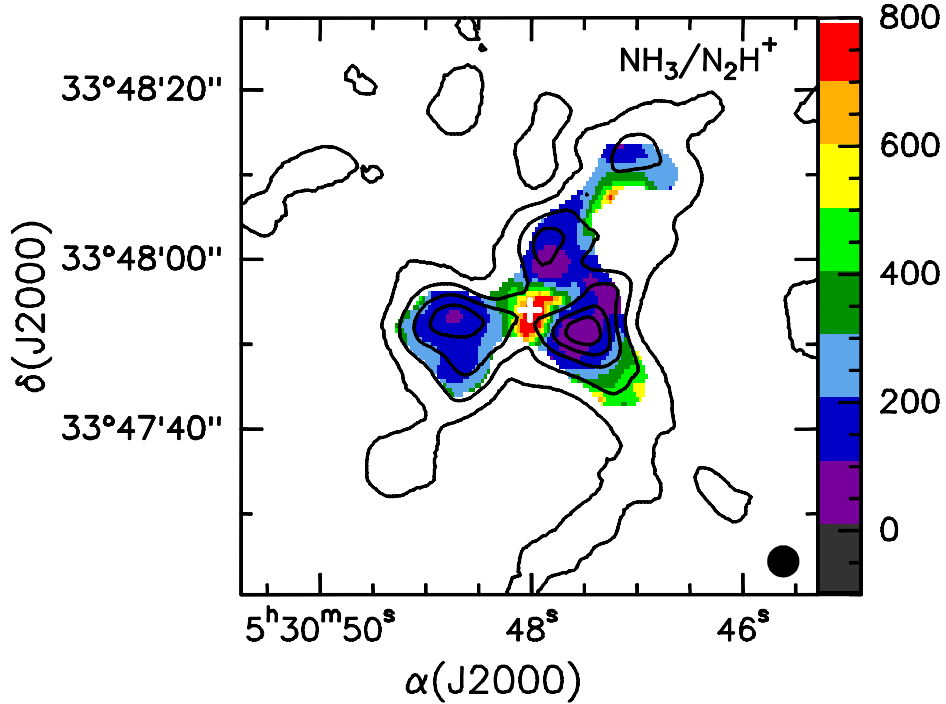


Figure 4.8: Color scale:  $N(\text{NH}_3)/N(\text{N}_2\text{H}^+)$  abundance ratio map overlaid with the  $\text{N}_2\text{H}^+$  emission (black contour), with contours starting at 3 %, and increasing in steps of 20 % of the peak intensity. The synthesized beam,  $\sim 4''$ , is shown in the bottom right corner. The white cross marks the position of the 3.2 mm peak.

sources). We explicitly checked that such high values are real so not produced by the interpolation process. Toward the western core, which could contain a low-mass YSO, we found values of the  $\text{NH}_3/\text{N}_2\text{H}^+$  ratio around 50–100, whereas in the eastern core, maybe containing a more evolved object, the  $\text{NH}_3/\text{N}_2\text{H}^+$  ratio is around 50–100 toward the center of the core and increases up to 200 at the edges. In Table 4.2 we give the average value of the  $\text{NH}_3/\text{N}_2\text{H}^+$  ratio for these three cores. The uncertainty estimated for the  $\text{NH}_3/\text{N}_2\text{H}^+$  abundance ratio is around  $\sim 30\text{--}60\%$ . As already pointed out by Zhang et al. (2002), the VLA  $\text{NH}_3$  data recover 65 % of the flux observed by the Effelsberg 100 m telescope (Estalella et al. 1993), and the missing flux arises mainly from smooth structures with scales larger than  $50''$ . Unfortunately, we cannot estimate the amount of flux filtered out by CARMA in  $\text{N}_2\text{H}^+$  due to the lack of short-spacing information. However, since the CARMA  $\text{N}_2\text{H}^+$  and VLA  $\text{NH}_3$  images are sensitive to similar angular scales, the  $\text{NH}_3/\text{N}_2\text{H}^+$  ratio is not seriously affected by differences in the missing flux.

Table 4.2: Average column density for each dense core

| Core    | $N(\text{NH}_3)$<br>( $\text{cm}^{-2}$ ) | $N(\text{N}_2\text{H}^+)$<br>( $\text{cm}^{-2}$ ) | $N(\text{H}^{13}\text{CO}^+)$<br>( $\text{cm}^{-2}$ ) | $N(\text{NH}_3)/N(\text{N}_2\text{H}^+)$ |
|---------|--|---|---|--|
| central | $2.6 \times 10^{15}$                     | $2.5 \times 10^{12}$                              | $4.5 \times 10^{12}$                                  | 1000                                     |
| eastern | $1.4 \times 10^{15}$                     | $1.1 \times 10^{13}$                              | ...   | 130                                      |
| western | $1.8 \times 10^{15}$                     | $1.8 \times 10^{13}$                              | ...   | 100                                      |

## 4.5 Chemical modeling

### 4.5.1 The UCL\_CHEM model

We employed UCL\_CHEM, a time- and depth- dependent chemical model similar to the one used in Viti and Williams (1999) and Viti et al. (2001, 2004) to study the behavior of the  $\text{NH}_3/\text{N}_2\text{H}^+$  abundance ratio. For simplicity, in this study we performed time-dependent single-point calculations. The model consists of a two-phase calculation. In phase I we follow the chemical and dynamical evolution of a collapsing core. This phase starts from a fairly diffuse medium ( $n \simeq 400 \text{ cm}^{-3}$ ) in neutral atomic form (apart from a fraction of hydrogen in  $\text{H}_2$ ) that undergoes a collapse following the free-fall collapse law described in Rawlings et al. (1992) until densities typical of massive dense cores ( $n \simeq 10^5 - 10^7 \text{ cm}^{-3}$ ) are reached. During this time, atoms and molecules from the gas freeze on to the dust grains and hydrogenate where possible, as in Viti and Williams (1999). The degree of

Table 4.3: Initial gas-phase elemental abundances relative to hydrogen nuclei.

| Atom | Abundance             |
|------|-----------------------|
| H    | 1.0                   |
| He   | 0.075                 |
| O    | $4.45 \times 10^{-4}$ |
| C    | $1.79 \times 10^{-4}$ |
| N    | $8.52 \times 10^{-5}$ |
| S    | $1.43 \times 10^{-6}$ |
| Mg   | $5.12 \times 10^{-6}$ |

freeze out or depletion, defined in terms of the depletion of the CO molecule, is a free parameter (although linked with density, see Rawlings et al. 1992), which we explore in this study. During phase I we adopted a constant temperature of 12 K and assumed a standard value for the cosmic ionization rate,  $\zeta = 3 \times 10^{-17} \text{ s}^{-1}$ . The initial gas-phase elemental abundances relative to hydrogen nuclei adopted in this work, based on the findings of Sofia and Meyer (2001), are listed in Table 4.3. We included 127 gas-phase species and 42 surface species interacting in 1869 chemical reactions adapted from the UMIST 2006 database (Woodall et al. 2007). During the collapse phase (phase I), we let the chemistry develop for 3 Myrs, regardless of when the final density is reached.

In phase II we explored the chemical evolution of the core that harbors a newly born massive star by simulating the presence of an infrared source at the center of the core and by subjecting the core to a time-dependent increase of the gas and dust temperature (assumed to be the same because of the high densities considered), which was performed differently depending on the core we were modeling. For the central core we adopted a maximum temperature of  $\sim 70$  K, whereas the temperature toward the western and eastern cores is around  $\sim 25$  K (both derived from  $\text{NH}_3$  data, see Zhang et al. 2002). During phase II we performed the same treatment for the increasing temperature and evaporation from grains as in Viti et al. (2004), which includes the experimental results on desorption from grains and the evaporation of icy mantles formed in star-forming regions (Collings et al. 2003b,a, 2004). In this case, the evaporation of a fraction of mantle species occur when the temperature for a particular desorption event is reached (see Viti et al. 2004 for a complete description). In phase II we followed the evolution of each core for 3 Myr.

### 4.5.2 Results

We computed a grid of models to investigate the differences observed in the  $\text{N}_2\text{H}^+$  column density and the  $\text{NH}_3/\text{N}_2\text{H}^+$  abundance ratio. For the central core we followed the chemical evolution of a core of 0.02 pc in diameter, whereas we adopted a size of 0.04 pc for the eastern and western cores. We explored a range of densities,  $n \simeq 10^5\text{--}10^7 \text{ cm}^{-3}$ , and for a particular density we used different percentages of freeze-out at the end of phase I. From this analysis we found that the observed values of the  $\text{NH}_3/\text{N}_2\text{H}^+$  ratio can be reproduced by our model using a high degree of depletion at the end of the collapse phase (phase I) and by adopting a density

Table 4.4: Parameters of the UCL\_CHEM model

| Parameter                                    | CC <sup>a</sup> | WC and EC <sup>b</sup> |
|--|-----------------|------------------------|
| Depletion <sup>c</sup> (%)                   | 99              | 99                     |
| Gas Density <sup>c</sup> (cm <sup>-3</sup> ) | 10 <sup>6</sup> | 10 <sup>5</sup>        |
| $A_v^c$                                      | 41              | 10                     |
| $T_{\max}^d$                                 | 70              | 25                     |

**Notes.** <sup>a</sup> CC: central core. <sup>b</sup> WC and EC: western and eastern cores. <sup>c</sup> At the end of phase I. <sup>d</sup> Maximum value reached during phase II.

$n \simeq 10^6 \text{ cm}^{-3}$  for the central core and  $n \simeq 10^5 \text{ cm}^{-3}$  for the western/eastern cores. It is worth noting that the model for the central core is supported by our estimate of the density from the dust continuum emission. Adopting the mass derived in this work (see Sect. 3.1) and a size of  $6''$ , we obtained a density of  $\sim 5 \times 10^6 \text{ cm}^{-3}$ , consistent with the density adopted in the chemical model. In Table 4.4 we list the parameter choices for the two selected models (CC and WC/EC models), which can reproduce both the observed NH<sub>3</sub> and N<sub>2</sub>H<sup>+</sup> column densities and the NH<sub>3</sub>/N<sub>2</sub>H<sup>+</sup> abundance ratio. In the following sections, we discuss the main results obtained by our chemical model for phases I and II.

### Fractional abundances and the NH<sub>3</sub>/N<sub>2</sub>H<sup>+</sup> abundance ratio during phase I

In Fig. 4.9 (left panels) we present the fractional abundances (with respect to hydrogen nuclei) of some molecular species of interest (i. e., CO, N<sub>2</sub>, H<sub>3</sub><sup>+</sup>, NH<sub>3</sub>, N<sub>2</sub>H<sup>+</sup>, and HCO<sup>+</sup>), together with the NH<sub>3</sub>/N<sub>2</sub>H<sup>+</sup> abundance ratio as a function of time for the central core (CC model) and the western/eastern cores (WC/EC model) during phase I. First of all, the fractional abundances obtained for the central core (top panel) and the western/eastern cores (middle panel) do not show significant differences because they only differ in the core size and the final density reached at the end of this phase. As can be seen in Fig. 4.9, the fractional abundance of CO, N<sub>2</sub>, NH<sub>3</sub>, N<sub>2</sub>H<sup>+</sup>, and HCO<sup>+</sup> increases with time (with a more pronounced increase for the case of CO, N<sub>2</sub>, and NH<sub>3</sub>), reaching its maximum value at times  $t \simeq 2.5 \times 10^6 \text{ yr}$ . After this time, the fractional abundances start to decrease because molecules freeze out onto dust grains due to the low temperature ( $T \simeq 12 \text{ K}$ ) and high density ( $n \simeq 10^5 - 10^6 \text{ cm}^{-3}$ ) achieved in these cores. On the other hand, the

ion  $\text{H}_3^+$  keeps more or less a constant abundance until  $t \simeq 2.5 \times 10^6$  yr, and then its abundance rises moderately.

The primary formation route for  $\text{N}_2\text{H}^+$  is through the reaction between H and  $\text{N}_2$ , which also produces  $\text{H}_2$ .  $\text{N}_2\text{H}^+$  can then react with many atoms and molecules such as C, O,  $\text{H}_2\text{O}$ , or CO to form  $\text{N}_2$ . It is therefore clear that the abundance in the gas phase of these removal agents will be critical in determining the abundance of  $\text{N}_2\text{H}^+$  present. At high densities, but before the effects of freeze-out dominate, all the molecular species that are important in the removal of  $\text{N}_2\text{H}^+$  and  $\text{NH}_3$  will be high. In particular, for both models the main formation route for  $\text{N}_2\text{H}^+$  is initially  $\text{H}_2 + \text{N}_2^+ \rightarrow \text{N}_2\text{H}^+ + \text{H}$ , and then the chemical reaction  $\text{H}_3^+ + \text{N}_2 \rightarrow \text{N}_2\text{H}^+ + \text{H}$  becomes important, while  $\text{NH}_3$  is mainly formed via dissociative recombination of  $\text{NH}_4^+$ . The latter is formed via consecutive hydrogenation of  $\text{N}^+$  (via reactions with molecular hydrogen).

During phase I the  $\text{NH}_3/\text{N}_2\text{H}^+$  abundance ratio behaves in the same way for both the central core and the western/eastern cores models, and only during the latest time steps does it depend on the adopted density ( $n \simeq 10^5 \text{ cm}^{-3}$  for the western/eastern cores and  $n \simeq 10^6 \text{ cm}^{-3}$  for the central core). In both cases, the  $\text{NH}_3/\text{N}_2\text{H}^+$  ratio starts from low values and reaches values around 1000 and even higher for  $t > 2.5 \times 10^6$  yr because CO depletion favors the formation of  $\text{NH}_3$  against  $\text{N}_2\text{H}^+$  in core centers at high densities. This suggests that long-lived starless cores are associated with high values of the  $\text{NH}_3/\text{N}_2\text{H}^+$  abundance ratio.

### Fractional abundances and the $\text{NH}_3/\text{N}_2\text{H}^+$ abundance ratio during phase II

Figure 4.9 (right panels) shows the fractional abundances (with respect to hydrogen nuclei) as a function of time of CO,  $\text{N}_2$ ,  $\text{H}_3^+$ ,  $\text{NH}_3$ ,  $\text{N}_2\text{H}^+$ , and  $\text{HCO}^+$  derived from our chemical model during phase II for the central core (top panel) and the western/eastern cores (middle panel). The fractional abundances in the central core clearly have a different behavior compared to that of the western and eastern cores as a consequence of the different density, and especially the different temperature reached at the end of phase II. In the central core, the fractional abundance of CO,  $\text{N}_2$ ,  $\text{N}_2\text{H}^+$ , and  $\text{HCO}^+$  is constant during the initial stages, and once the temperature increases, their fractional abundances rise significantly. On the other hand, the fractional abundance of the molecular ion  $\text{H}_3^+$  decreases with time. This is of course

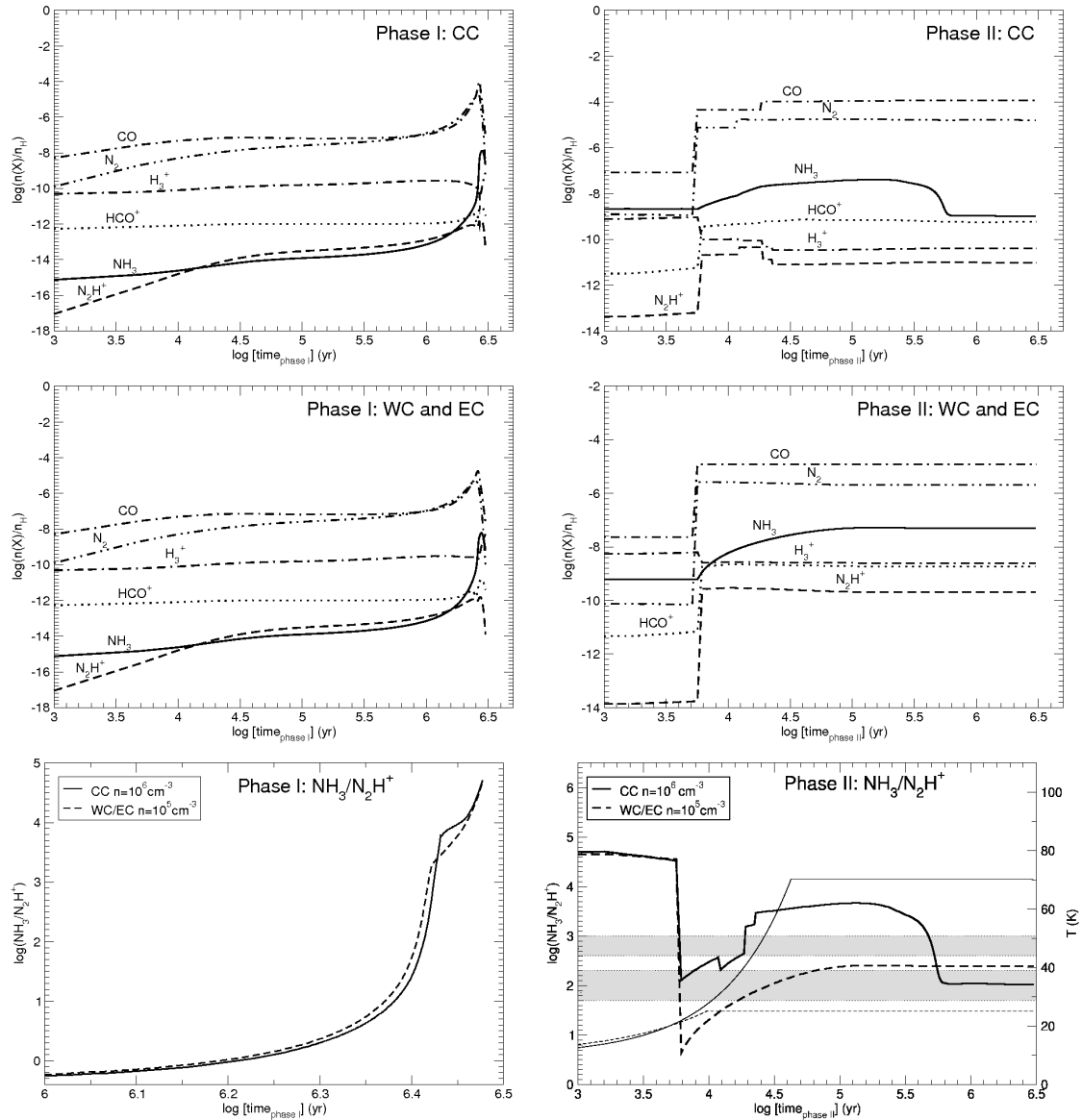


Figure 4.9: *Left:* Fractional abundances with respect to hydrogen as a function of time during phase I for the central core (top panel) and the western/eastern cores (middle panel). The  $NH_3/N_2H^+$  abundance ratio for both the central core and the western/eastern core are also shown in the bottom panel. *Right:* Same as left panels but for phase II calculation. The y-axis ranges according to the model. In the bottom right panel we also show the temperature as a function of time, indicated by the thin lines. The two shaded areas mark the range of values (400–1000 for the central core and 50–200 for the western/eastern cores) of the  $NH_3/N_2H^+$  abundance ratio estimated from the observational data.

because  $\text{H}_3^+$  is highly reactive at high densities. The abrupt increase in the fractional abundance takes place at the same time for all molecules, around  $t \simeq 6.1 \times 10^3$  yr (corresponding to a temperature of  $T \simeq 21$  K). This time corresponds to the time when a fraction of weakly bound species evaporates from the grain mantle (see Table 1 in Viti et al. 2004). The fractional abundance of  $\text{N}_2\text{H}^+$  reaches its maximum value  $4.6 \times 10^{-11}$  (corresponding to a  $\text{N}_2\text{H}^+$  column density of  $\sim 1.8 \times 10^{12} \text{ cm}^{-2}$ ) at  $t \simeq 1.7 \times 10^4$  yr. The rapid destruction of  $\text{N}_2\text{H}^+$  (by the chemical reaction  $\text{N}_2\text{H}^+ + \text{CO} \rightarrow \text{HCO}^+ + \text{N}_2$ ) occurs at  $t \simeq 2.3 \times 10^4$  yr, with a variation in the fractional abundance of one order of magnitude, with the  $\text{N}_2\text{H}^+$  column density around  $\sim 8 \times 10^{11} \text{ cm}^{-2}$ , consistent with the value estimated from the observations. On the other hand,  $\text{HCO}^+$  fractional abundance is constant at  $\sim 6 \times 10^{-10}$ . Assuming  $[\text{HCO}^+/\text{H}^{13}\text{CO}^+]=40$ , we estimated an  $\text{H}^{13}\text{CO}^+$  column density of  $\sim 1.3 \times 10^{12} \text{ cm}^{-2}$ , in good agreement with the estimation from the observational data (see Table 4.2). This chemical behavior could be explained in terms of CO desorption from grain mantles, which causes a substantial destruction of  $\text{N}_2\text{H}^+$  favoring the formation of  $\text{HCO}^+$ , where this reaction is the main removal mechanism of  $\text{N}_2\text{H}^+$  for ‘standard’ CO abundances of  $[\text{CO}/\text{H}_2] \simeq 10^{-4}$  (Jørgensen et al. 2004; Lee et al. 2004). In fact, as can be seen in Fig. 4.9 (top panel), the CO fractional abundance is  $\sim 10^{-4}$ , high enough to lead to significant destruction of  $\text{N}_2\text{H}^+$ .

In contrast to the case of  $\text{N}_2\text{H}^+$  and  $\text{HCO}^+$ , the increase in the  $\text{NH}_3$  fractional abundance is slow, which indicates that gas phase chemistry dominates pure evaporation. This is simply a consequence of most of the ammonia being still locked in water ice; in fact, as shown by the experiments by Collings et al. (2004), ammonia is released back into the gas phase only if temperatures of  $\sim 100$ -120 K are reached (Viti et al. 2004). The maximum value, of  $4.1 \times 10^{-8}$  (or  $\text{N}(\text{NH}_3) \simeq 3.2 \times 10^{15} \text{ cm}^{-2}$ ), is reached at  $t \simeq 1.3 \times 10^5$  yr, and then it drops until it reaches a constant abundance of  $1 \times 10^{-9}$  (or a column density of  $\sim 8.2 \times 10^{13} \text{ cm}^{-2}$ ). This behavior, i. e., the decrease in the  $\text{NH}_3$  fractional abundance, takes place through reactions of the  $\text{NH}_3$  molecule with the ions  $\text{C}^+$  and  $\text{HCO}^+$ . In this situation, the  $\text{C}^+$  fractional abundance increases at late stages, while the fractional abundance of  $\text{HCO}^+$  is more or less constant, which is consistent with  $\text{HCO}^+$  being produced from the destruction of  $\text{N}_2\text{H}^+$  (see above) and destroyed through reactions with  $\text{NH}_3$ .

Regarding the western and eastern cores, which were modeled assuming the same core size ( $\sim 0.04$  pc) and same temperature (the maximum temperature is 25 K), we found that the fractional abundance of  $\text{NH}_3$  increases moderately with time, while

Table 4.5: Results obtained from the chemical model

| Model   | time<br>(yr)                          | $N(NH_3)$<br>( $\times 10^{14} \text{ cm}^{-2}$ ) | $N(N_2H^+)$<br>( $\times 10^{11} \text{ cm}^{-2}$ ) | $NH_3/N_2H^+$ |
|---------|---------------------------------------|---|---|---------------|
| CC      | $1.9 \times 10^4$                     | 17  | 38  | 450           |
| CC      | $4.5 \times 10^5$ – $5.3 \times 10^5$ | 11–3.20   | 0.80  | 1400–400      |
| WC & EC | $1 \times 10^4$ – $3 \times 10^6$     | 2.80–10   | 56–41   | 50–240        |

the fractional abundances of CO,  $N_2$ ,  $N_2H^+$ , and  $HCO^+$  rise considerably during the initial stages due to desorption effects, similar to the case of the the central core model. At  $t \simeq 4 \times 10^3$  yr,  $N_2H^+$  and  $HCO^+$  have constant abundance, around  $\sim 2 \times 10^{-10}$  ( $N(N_2H^+) \simeq 4 \times 10^{12} \text{ cm}^{-2}$ ) and  $\sim 1.8 \times 10^{-9}$  ( $N(HCO^+) \simeq 3.6 \times 10^{13} \text{ cm}^{-2}$  or  $N(H^{13}CO^+) = 9 \times 10^{11} \text{ cm}^{-2}$ , assuming  $[HCO^+/H^{13}CO^+] = 40$ ) for  $N_2H^+$  and  $HCO^+$ , respectively, while the  $NH_3$  fractional abundance increases, up to  $\sim 5.2 \times 10^{-8}$  ( $N(NH_3) \simeq 1 \times 10^{15} \text{ cm}^{-2}$ ) at  $t \simeq 1.3 \times 10^5$  yr, and then remains roughly constant, too. For these cores, the values obtained from the chemical modeling agree (within a factor of 2 in the case of  $N_2H^+$ , and a factor of 4 in the case of  $NH_3$ ) with the column densities reported from the observational data. Finally, the CO fractional abundance in the western/eastern cores is  $\sim 10^{-5}$ , significantly lower than the CO fractional abundance of the central core, indicating that the relatively low CO abundance in the western/eastern cores does not lead to a substantial destruction of  $N_2H^+$ . Therefore, the fraction of CO that will evaporate from grain mantles plays an important role in determining the fractional abundance of  $N_2H^+$ , hence the  $NH_3/N_2H^+$  abundance ratio.

In Table 4.5 we show the values of the  $NH_3$  and  $N_2H^+$  column densities, together with the  $NH_3/N_2H^+$  abundance ratio for the two models that agree with the observed values. In Fig. 4.9 (bottom right panel) we present the  $NH_3/N_2H^+$  abundance ratio as a function of time for the central core and the western/eastern core obtained during phase II. The  $NH_3/N_2H^+$  abundance ratio observed toward the central core, around  $\sim 400$ – $1000$ , can be reproduced by our chemical model for times  $t \simeq 10^4$  yr and  $t = (4.5\text{--}5.3) \times 10^5$  yr. For the time range  $t \simeq 10^4$ – $4.5 \times 10^5$  yr, the model produces a higher  $NH_3/N_2H^+$  abundance ratio,  $\sim 4000$ , slightly above the observed values for the central core. However, we adopted the longer age as it is more realistic. For the western/eastern cores, the  $NH_3/N_2H^+$  abundance ratio initially shows high values,

then it decreases due to desorption effects and finally reaches a constant value  $\sim 200$  for typical ages of low-mass YSOs, at around  $t \simeq 10^5 - 10^6$  yr. In addition, in Fig. 4.9 (bottom panel) we also show the temperature as a function of time. For the central core, when the temperature is low, the  $\text{NH}_3/\text{N}_2\text{H}^+$  ratio is high ( $> 10^4$ ). Around  $T \simeq 21$  K there is a clear drop in the  $\text{NH}_3/\text{N}_2\text{H}^+$  ratio due to desorption effects. As temperature increases, the  $\text{NH}_3/\text{N}_2\text{H}^+$  rises until it reaches a constant value,  $\sim 10^3$ , at around  $T \simeq 45$  K. For the western and eastern cores the temperature varies from 12 to 25 K, producing small variations in the  $\text{NH}_3/\text{N}_2\text{H}^+$  ratio, and only for times in the range  $10^3 - 10^4$  yr does the  $\text{NH}_3/\text{N}_2\text{H}^+$  ratio change significantly, similar to the case of the central core. It is worth noting that in the model for the central core, the visual extinction is  $A_V \simeq 40$ , but typically the visual extinction in hot cores (i. e., embedded in the central core) is around  $\sim 100$  or even higher. To evaluate the error in the  $\text{NH}_3/\text{N}_2\text{H}^+$  abundance introduced by this difference, we performed an additional model with a higher density, which gives a visual extinction of  $A_V \simeq 100$ . In this situation, the  $\text{NH}_3/\text{N}_2\text{H}^+$  ratio is affected by a difference of  $\sim 3 - 25$  %. The abrupt drop in the  $\text{NH}_3/\text{N}_2\text{H}^+$  ratio produced at early ages ( $t \simeq 5 \times 10^3$  yr) in both the central core and western/eastern cores stems from to desorption effects of some molecules.

Finally, we explored the fractional abundances of other molecular species and compared them with observations when available or made some predictions for future observations. We found that the fractional abundance of  $\text{CH}_3\text{CN}$  obtained from the chemical model is in the range  $\sim 8 \times 10^{-8} - 10^{-7}$  at  $t = (4.5 - 5.5) \times 10^5$  yr, in agreement with the value reported by Zhang et al. (2007), which is in the range  $(1 - 4) \times 10^{-8}$ . Additionally, our model predicts a CO abundance of  $10^{-4}$  indicating that CO is desorbed from grain mantles due to the relatively high temperature (around  $\sim 70$  K) and the powerful molecular outflows detected in CO (Zhang et al. 2007). We found that molecules like  $\text{HC}_3\text{N}$ ,  $\text{H}_2\text{CO}$ ,  $\text{C}_2\text{H}$ , and CS should be detectable toward the central core, since their fractional abundances are even higher than the  $\text{NH}_3$  ones. Concerning the western and eastern cores, the CO fractional abundance, of  $10^{-5}$ , is one order of magnitude lower than that of the central core. For these cores, molecules such as CS,  $\text{C}_2\text{H}$ , and  $\text{CH}_3\text{CN}$  are quite abundant and would be detectable, but we would not expect to detect any  $\text{H}_2\text{CO}$  and  $\text{HC}_3\text{N}$ .

In summary, the models that can reproduce the observed values of the  $\text{NH}_3/\text{N}_2\text{H}^+$  abundance ratio toward the central core, as well as in the western and eastern cores, were obtained with a high depletion at the end of phase I. The differences between

the central and the western/eastern cores seen in the NH<sub>3</sub>/N<sub>2</sub>H<sup>+</sup> abundance ratio therefore seem to mainly come from density and temperature effects. In particular, as shown by the chemical modeling of the region, the temperature is a key parameter in determining the NH<sub>3</sub>/N<sub>2</sub>H<sup>+</sup> abundance ratio, hence the abundance of each molecule. As temperature rises, the fraction of species that will evaporate increases, and consequently the chemistry evolves differently.

## 4.6 Discussion

The results obtained from the N<sub>2</sub>H<sup>+</sup> observations, together with NH<sub>3</sub> data from the literature (Zhang et al. 2002) show that there are three dense cores associated with the high-mass star-forming region AFGL 5142. The central core, strong in NH<sub>3</sub> but almost devoid of N<sub>2</sub>H<sup>+</sup>, harbors a cluster of massive stars in their making. On the other hand, the western and eastern cores are stronger in N<sub>2</sub>H<sup>+</sup> than in NH<sub>3</sub> emission. In the following section, we discuss the possible reasons for the observed variation in the NH<sub>3</sub>/N<sub>2</sub>H<sup>+</sup> abundance ratio among the cores found in AFGL 5142.

The central dense core in AFGL 5142 is actively forming a cluster of massive stars, still in the accretion phase, which displays the typical signposts of star formation (molecular outflow and maser emission). Concerning the western and eastern cores, the relatively high temperature, around 20 K, could be due to the presence of an embedded YSO and/or heating produced by the three molecular outflows associated with the central core, which strongly affects the surrounding dense gas (Zhang et al. 2002, 2007). Thus, the association of the western and eastern cores with an infrared source is not obvious.

The NH<sub>3</sub>/N<sub>2</sub>H<sup>+</sup> abundance ratio map presented in Fig. 4.8 shows significant variations with a ratio around  $\sim 50$ – $100$  toward the western and eastern cores and a ratio up to 1000 toward the central core, due to a significant drop in the N<sub>2</sub>H<sup>+</sup> abundance. The values found for the NH<sub>3</sub>/N<sub>2</sub>H<sup>+</sup> abundance ratio in the western and eastern cores are similar to those found in previous studies for cores harboring YSOs, for both low- and high-mass star-forming regions (Caselli et al. 2002a; Hotzel et al. 2004; Palau et al. 2007; Friesen et al. 2010). These studies are all consistent with a high ratio ( $\leq 300$ ) that seems to be associated with starless cores, and a low ratio around 60–90 is found toward the YSOs, suggesting an anticorrelation between the the NH<sub>3</sub>/N<sub>2</sub>H<sup>+</sup> abundance ratio and the evolutionary stage. Thus, the

high  $\text{NH}_3/\text{N}_2\text{H}^+$  ratio toward the central core does not follow the anticorrelation between the  $\text{NH}_3/\text{N}_2\text{H}^+$  ratio and the evolutionary stage of the core as in the studies mentioned above. The noticeable increase in the  $\text{NH}_3/\text{N}_2\text{H}^+$  ratio in the central core suggests a strong differentiation of the  $\text{N}_2\text{H}^+$  abundance between the central core and the western/eastern cores. Below we briefly investigate the origin of such a differentiation.

### UV radiation effects:

As suggested by Qiu et al. (2008), UV photons from IRAS 05274+334 are not likely to affect the dense gas, and the effects of the UV field from the embedded protostar(s) do not seem to be a major concern in determining the  $\text{NH}_3$  and  $\text{N}_2\text{H}^+$  abundance of the central core, since the high visual extinction,  $A_V \simeq 40$  mag or higher, prevents UV photons from penetrating the central core.

### Excitation effects:

Even though we considered the effects of opacity and different  $T_{\text{ex}}$  in the calculation of the column densities, we consider whether the different excitation conditions among the dense cores may be the cause of the lower abundance of  $\text{N}_2\text{H}^+$ , i. e., the high  $\text{NH}_3/\text{N}_2\text{H}^+$  ratio. The critical density of  $\text{N}_2\text{H}^+$  is  $\sim 10^5 \text{ cm}^{-3}$  (Jørgensen 2004), while the critical density of  $\text{NH}_3$  is  $\sim 10^4 \text{ cm}^{-3}$  (Ho 1977). From the dust continuum emission, we estimated a density of  $\sim 10^6 \text{ cm}^{-3}$  in the central core. In addition, the density obtained from single-dish observations at  $850 \mu\text{m}$  (Jenness et al. 1995), adopting a core size of  $\sim 26''$ , is  $\sim 4 \times 10^5 \text{ cm}^{-3}$ . For these densities the transitions of both  $\text{NH}_3$  and  $\text{N}_2\text{H}^+$  are thermalized, and thus excitation effects do not seem appropriate to explain the  $\text{N}_2\text{H}^+$  emission drop in the central core.

On the other hand, the hyperfine structure method in CLASS assumes equal excitation temperature for all the hyperfine components. Daniel et al. (2006) show that this assumption does not hold for the case of high opacities due to radiative processes. Since in AFGL 5142 we derived an opacity of  $\tau_{\text{TOT}} \simeq 0.3\text{--}0.6$  for the  $\text{N}_2\text{H}^+$  molecule, the problem reported by Daniel et al. (2006) is not likely to affect our result.

## Physical and chemical effects:

The high values up to 1000 of the NH<sub>3</sub>/N<sub>2</sub>H<sup>+</sup> abundance ratio found in the central core of AFGL 5142 can be reproduced by our chemical model for high densities ( $n \simeq 10^6 \text{ cm}^{-3}$ ) and high temperatures ( $T \simeq 70 \text{ K}$ ). The chemical modeling performed in Sect. 5 indicates that both density and temperature play an important role in determining the molecular abundance of NH<sub>3</sub> and N<sub>2</sub>H<sup>+</sup>, hence their ratio. The central core has a higher temperature and density than the western and eastern cores. Thus, a different chemistry can develop due to CO evaporation from the grain mantles. The CO desorption in the central core of AFGL 5142 leads to the destruction of N<sub>2</sub>H<sup>+</sup>, so that the NH<sub>3</sub>/N<sub>2</sub>H<sup>+</sup> abundance ratio increases considerably relative to the value found in the western and eastern cores. This is supported by the fact that <sup>13</sup>CO is not frozen out in the central core, whereas it is faintly detected in the western and eastern cores (Zhang et al. 2007). As pointed out in Sect 5.2.2, Collings et al. (2004) find experimental evidence that the desorption of NH<sub>3</sub> from grain mantles takes place at a temperature of  $\sim 120 \text{ K}$ . Therefore, since in our model we assumed a maximum temperature of 70 K, the high NH<sub>3</sub>/N<sub>2</sub>H<sup>+</sup> abundance ratio in the central core is mainly a consequence of the destruction of N<sub>2</sub>H<sup>+</sup> by CO rather than an enhancement of NH<sub>3</sub> in the gas phase. The disappearance of N<sub>2</sub>H<sup>+</sup> from the gas phase has been reported by several authors, both in low- and high-mass star-forming regions. In the low-mass regime, there are several reports of central N<sub>2</sub>H<sup>+</sup> depletion in Class 0/Class I protostars (e. g., IRAM 04191+1522: Belloche and André 2004; VLA 1623: Di Francesco et al. 2004; L483 mm: Jørgensen 2004; Barnard 1c: Matthews et al. 2006; BHR 71 IRS1: Chen et al. 2008). Regarding the high-mass regime, Pirogov et al. (2003, 2007) used a single-dish telescope to observe a sample of dense cores associated with massive stars and star clusters containing IRAS point sources, and find that, for most of the sources, there is a decrease in the N<sub>2</sub>H<sup>+</sup> abundance toward the dust column density peak. Furthermore, interferometric observations of N<sub>2</sub>H<sup>+</sup> toward the high-mass star-forming regions IRAS 23033+5951 (Reid and Matthews 2008) also reveal a significant destruction of N<sub>2</sub>H<sup>+</sup>. Therefore, the high ratio measured toward the central core of AFGL 5142 seems to come from the rapid destruction of N<sub>2</sub>H<sup>+</sup> when CO is released from grain mantles as seems to be the case for the other regions cited above.

### Evolutionary effects:

Although in our chemical model we did not include molecular outflows, they may strongly affect the surrounding dense gas, hence the  $\text{NH}_3/\text{N}_2\text{H}^+$  abundance ratio. As already discussed by Chen et al. (2008), who propose three stages in the interaction between the  $\text{N}_2\text{H}^+$  emission and molecular outflows, based on the morphology of the  $\text{N}_2\text{H}^+$  dense gas and the jet/outflow emission. Here we suggest a qualitative picture of the evolution of the  $\text{NH}_3/\text{N}_2\text{H}^+$  abundance ratio. First, in starless cores with high densities, most molecules are highly depleted, which favors the formation of  $\text{NH}_3$  and  $\text{N}_2\text{H}^+$ . It seems that the CO depletion favors the formation of  $\text{NH}_3$  against  $\text{N}_2\text{H}^+$  in core centers at high densities. Thus, the  $\text{NH}_3/\text{N}_2\text{H}^+$  ratio reaches high values, consistent with the results found in low-mass starless cores (Caselli et al. 2002a; Hotzel et al. 2004; Friesen et al. 2010) as well as for starless cores nearby massive stars, like in the high-mass star-forming regions IRAS 20293+3952 (Palau et al. 2007). The high  $\text{NH}_3/\text{N}_2\text{H}^+$  ratio in starless cores has been reproduced by our chemical model shown in Fig.4.9 (left panels). After this phase, once the star has formed, the  $\text{NH}_3/\text{N}_2\text{H}^+$  ratio decreases, as found in the low-mass regime (Caselli et al. 2002a; Hotzel et al. 2004; Friesen et al. 2010), and in YSOs close to the massive star (e. g., IRAS 20293+3952: Palau et al. 2007; IRAS 00117+612: Busquet et al. in prep.). In this situation, CO is less depleted, and  $\text{N}_2\text{H}^+$  molecules in the envelope are entrained by the molecular outflow, with the  $\text{N}_2\text{H}^+$  emission elongated in the direction of the molecular outflow, as found in IRAS 20293+3952 (Palau et al. 2007) and IRAS 00117+6412 (Palau et al. 2010). Finally, the next evolutionary stage involves the release of CO by powerful molecular outflows, which leads to the destruction of  $\text{N}_2\text{H}^+$  and forms large holes in the envelope. Then, the  $\text{NH}_3/\text{N}_2\text{H}^+$  abundance ratio raises considerably, like in the central core of AFGL 5142.

Therefore, either molecular outflows and density/temperature effects seem to be key pieces in the determination of the  $\text{NH}_3/\text{N}_2\text{H}^+$  abundance ratio. To quantify the importance of the temperature in the  $\text{NH}_3/\text{N}_2\text{H}^+$  ratio, we compared the results obtained in AFGL5142 with the low-mass star-forming region L483. This region seems to be in the same stage of disruption of the envelope as AFGL5142, as the  $\text{N}_2\text{H}^+$  shows two clumps on both sides of the YSO (see Jørgensen 2004; Fuller and Wootten 2000), being then in the later evolutionary stage of the scenario proposed above. However, the  $\text{NH}_3$  emission in L483 also shows a hole close to the position of the YSO, suggesting that possibly the  $\text{NH}_3/\text{N}_2\text{H}^+$  abundance ratio is much lower

than the values found in AFGL 5142, around 400–1000. This seems to indicate that the effects of molecular outflows alone cannot explain the high values derived in AFGL 5142, although this should be modeled to draw a firm conclusion. Thus, the high temperature reached in the central core due to the presence of hot cores seems to affect significantly the NH<sub>3</sub>/N<sub>2</sub>H<sup>+</sup> abundance ratio, indicating that the NH<sub>3</sub>/N<sub>2</sub>H<sup>+</sup> ratio behaves differently than in low-mass star-forming regions.

## 4.7 Conclusions

We used CARMA to observe the 3.2 mm continuum emission and the N<sub>2</sub>H<sup>+</sup> molecular line emission toward the massive protostellar cluster AFGL 5142. The N<sub>2</sub>H<sup>+</sup> dense gas emission, which mimics the morphology of NH<sub>3</sub>, shows two main cores, one to the west (the western core) of the dust condensation of  $\sim 0.08$  pc of size and another core to the east (the eastern core), of  $\sim 0.09$  pc. Interestingly, toward the dust condensation, of  $M \simeq 23 M_{\odot}$ , the N<sub>2</sub>H<sup>+</sup> emission drops significantly, whereas the compact NH<sub>3</sub> core (i. e., the central core) peaks at this position. The analysis of the N<sub>2</sub>H<sup>+</sup> column density and the NH<sub>3</sub>/N<sub>2</sub>H<sup>+</sup> abundance ratio indicates a strong differentiation in the N<sub>2</sub>H<sup>+</sup> abundance. While we found low values around  $\sim 50$ – $100$  of the NH<sub>3</sub>/N<sub>2</sub>H<sup>+</sup> abundance ratio associated with the western and eastern cores, the NH<sub>3</sub>/N<sub>2</sub>H<sup>+</sup> ratio rises significantly up to 1000 toward the central core, in which the formation of several massive stars is taking place. We performed a chemical modeling of the region using the time-dependent chemical model UCL\_CHEM. The chemical model shows that a high NH<sub>3</sub>/N<sub>2</sub>H<sup>+</sup> abundance ratio can be reproduced in three different situations: *i*) in long-lived starless cores; *ii*) in high density cores with low temperature,  $\sim 20$ – $25$  K, and containing YSOs; and *iii*) in high density cores with YSOs and high temperature.

For the central core we found that such a high value of the NH<sub>3</sub>/N<sub>2</sub>H<sup>+</sup> abundance ratio could be explained with a density of  $\sim 10^6$  cm<sup>-3</sup> and a maximum temperature of 70 K, producing a substantial destruction of the N<sub>2</sub>H<sup>+</sup> molecule by CO, which is desorbed from the grains mantles due to the high temperature and possibly the molecular outflows associated with the massive YSOs embedded in the central core. On the other hand, to reproduce the observed NH<sub>3</sub>/N<sub>2</sub>H<sup>+</sup> abundance ratio toward the western and eastern cores, we used a lower density of  $\sim 10^5$  cm<sup>-3</sup> and temperature (maximum temperature reached is 25 K). These results suggests that, in

---

addition to the core evolution, the physical properties of the core, such as density and temperature, play an important role in determining the  $\text{NH}_3/\text{N}_2\text{H}^+$  abundance ratio. In conclusion, in AFG15142 we found that the  $\text{NH}_3/\text{N}_2\text{H}^+$  abundance ratio behaves differently to the low-mass case mainly because of the high temperature reached in hot cores.



## Chapter 5

# The $\text{NH}_2\text{D}/\text{NH}_3$ ratio toward pre-protostellar cores around the UCHII region in IRAS 20293+3952

*The deuterium fractionation,  $D_{\text{frac}}$ , has been proposed as an evolutionary indicator in pre-protostellar and protostellar cores of low-mass star-forming regions. We investigate  $D_{\text{frac}}$ , with high angular resolution, in the cluster environment surrounding the UCHII region IRAS 20293+3952. We performed high angular resolution observations with the IRAM Plateau de Bure Interferometer (PdBI) of the ortho- $\text{NH}_2\text{D } 1_{11}-1_{01}$  line at 85.926 GHz and compared them with previously reported VLA  $\text{NH}_3$  data. We detected strong  $\text{NH}_2\text{D}$  emission toward the pre-protostellar cores identified in  $\text{NH}_3$  and dust emission, all located in the vicinity of the UCHII region IRAS 20293+3952. We found high values of  $D_{\text{frac}} \simeq 0.1-0.8$  in all the pre-protostellar cores and low values,  $D_{\text{frac}} < 0.1$ , associated with young stellar objects. The high values of  $D_{\text{frac}}$  in pre-protostellar cores could be indicative of evolution, although outflow interactions and UV radiation could also play a role.*

## 5.1 Introduction

Characterizing the different evolutionary stages before and after the formation of a star is crucial for understanding the process of star formation itself. Dense cores, where stars are born, are mainly studied through molecular emission of dense gas tracers, and N-bearing molecules are widely used because they do not freeze out onto dust grains until very high densities are reached ( $\sim 10^6 \text{ cm}^{-3}$ ; Flower et al. 2006). Several column density ratios of molecules tracing dense cores have been proposed as good “chemical clocks”, such as  $\text{NH}_3/\text{N}_2\text{H}^+$  or  $\text{CN}/\text{N}_2\text{H}^+$  (Hotzel et al. 2004; Fuente et al. 2005b). Among these, the ratio of a deuterated species over its counterpart containing H, i. e., the deuterium fractionation  $D_{\text{frac}}$ , has been found to be a good tracer of the evolutionary stage of dense cores. Both observations and models strongly suggest that in cold ( $T < 20 \text{ K}$ ) and dense cores ( $n \simeq 10^6 \text{ cm}^{-3}$ ) C-bearing molecules are expected to deplete onto dust grains, leading to an enhancement of the deuterium fractionation (e. g., Roberts and Millar 2000; Bacmann et al. 2003; Pillai et al. 2007) because the  $\text{H}_2\text{D}^+$  ion, the progenitor of most of the deuterated species, including  $\text{NH}_2\text{D}$ , is not destroyed by CO.

In particular, in low-mass star-forming regions,  $D_{\text{frac}}$  is found to increase until the onset of star formation and to decrease afterwards (Crapsi et al. 2005; Emprechtinger et al. 2009). In the high-mass regime, Chen et al. (2010) performed single-dish observations toward massive dense cores and find a decreasing trend of  $D_{\text{frac}}$  with the evolutionary stage during the protostellar phase. However, since massive star formation takes place in cluster environments, to study  $D_{\text{frac}}$  one needs to carry out observations with high angular resolution in order to separate the emission from each individual core. So far, interferometric observations of deuterated species in massive star-forming regions have only been reported by Fontani et al. (2008) and Sandell and Wright (2010), but only the work of Fontani et al. (2008) evaluates  $D_{\text{frac}}$  in the region, where they find two dense cores with  $D_{\text{frac}} \simeq 0.1$ .

In this chapter we present high angular resolution observations of the ortho- $\text{NH}_2\text{D}$   $1_{11}-1_{01}$  line at 85.926 GHz carried out with the Plateau de Bure Interferometer toward the high-mass star-forming region IRAS 20293+3952, located at 2 kpc of distance (Beuther et al. 2004b) and with a luminosity of  $6300 L_{\odot}$ . The region is associated with an UCH II region at the border of a cloud of dense gas mapped in  $\text{NH}_3$  with high angular resolution (Palau et al. 2007), and it harbors a rich variety of young

stellar objects (YSOs) and dense cores at different evolutionary stages, being thus an excellent target to study  $D_{\text{frac}}$ . While the northern side of the main cloud of the region contains several YSOs driving at least four molecular outflows (Beuther et al. 2004a; Palau et al. 2007), the southern side is mainly populated with starless core candidates (BIMA 3 and BIMA 4, two faint millimeter condensations). In addition, there is a small cloud to the northwest, the western cloud, which seems to harbor a very compact starless core (see Fig. 5.1 for an overview of the region). The current  $\text{NH}_2\text{D}$  observations allowed us to estimate for the first time  $D_{\text{frac}}$  from  $\text{NH}_2\text{D}/\text{NH}_3$  with high angular resolution toward a massive star-forming region containing dense cores and YSOs at different evolutionary stages.

## 5.2 Observations

The IRAM Plateau de Bure Interferometer (PdBI)<sup>a</sup> was used to observe the  $\text{NH}_2\text{D}$   $1_{11}-1_{01}$  molecular transition at 85.926 GHz toward IRAS 20293+3952. The observations were carried out during 2008 June 16 and December 4, with the array in the D (4 antennas) and C (6 antennas) configurations, respectively, providing projected baselines ranging from 17.5 m to 175 m. The phase center was  $\alpha(\text{J2000}) = 20^{\text{h}}31^{\text{m}}12^{\text{s}}.7$ ,  $\delta(\text{J2000}) = +40^{\circ}03'13''.4$ . The typical system temperatures for the receivers at 3 mm were  $\sim 150$ – $300$  K during June 16, and  $\sim 100$ – $150$  K during December 4. Atmospheric phase correction was applied.

The 3 mm receiver was tuned at 86.75433 GHz in the lower sideband. The spectral setup included other molecular transitions, which will be presented in a subsequent paper (Busquet et al., in prep). For the ortho- $\text{NH}_2\text{D}$ , we used a correlator unit of 20 MHz of bandwidth and 512 spectral channels, which provides a spectral resolution of  $\sim 0.039$  MHz ( $\sim 0.14$  km s<sup>-1</sup>). The FWHM of the primary beam at 3 mm was  $\sim 56''$ . Bandpass calibration was performed by observing the quasars 3C454.3 on June 16 and 3C273 on December 4. Amplitude and phase calibrations were achieved by monitoring MWC 349 and 2005+403 for both days. The phase rms was  $\sim 20^{\circ}$ . The absolute flux density scale was determined from MWC 349, with an estimated uncertainty  $\sim 10\%$ . The data were calibrated with the program CLIC and imaged with MAPPING, and both are part of the GILDAS software package. Imaging was performed with natural weighting, obtaining a synthesized beam of

<sup>a</sup>IRAM is supported by INSU/CNRS (France), MPG (Germany), and IGN (Spain).

$4''.32 \times 3''.05$  with P. A.=  $111^\circ$ , and rms of  $20.7 \text{ mJy beam}^{-1}$  per channel.

### 5.3 Results

In Fig.5.1 we present the  $\text{NH}_2\text{D } 1_{11}\text{-}1_{01}$  zero-order map integrated for the 6 hyperfine transitions (see Olberg et al. 1985 for a description of the transition) overlaid onto the  $\text{NH}_3(1,1)$  emission from Palau et al. (2007). The integrated  $\text{NH}_2\text{D}$  emission toward the western cloud presents a compact morphology with a deconvolved size of  $6''.5 \times 3''.6$  ( $\sim 0.06 \text{ pc}$ ). We also found  $\text{NH}_2\text{D}$  emission associated with the southern side of the main cloud, covering a spatial extension in the east-west direction of  $\sim 33''$  ( $0.33 \text{ pc}$ ). The emission consists of three main cores, one clearly associated with BIMA 4, another  $\text{NH}_2\text{D}$  core coincident with the dust ridge, and a third core located  $\sim 7''$  south of BIMA 2 (hereafter BIMA 2-S). In addition, we detected faint  $\text{NH}_2\text{D}$  emission associated with BIMA 3. It is worth noting that  $\text{NH}_2\text{D}$  is not (or marginally) detected on the northern side of the main cloud. In this chapter we follow the nomenclature for the YSOs and starless core candidates of Palau et al. (2007).

We studied the deuterium fractionation of the region by first computing the column density map of  $\text{NH}_2\text{D}$  and then the  $N(\text{NH}_2\text{D})/N(\text{NH}_3)$  column density ratio. For this, we extracted the spectra for positions on a grid of  $2'' \times 2''$ , and adopted the hyperfine frequencies listed in Tiné et al. (2000). The column densities are only reported for spectra with a peak intensity greater than  $5 \sigma$ , and with all the hyperfine components detected.

Assuming that all levels are populated according to the same excitation temperature,  $T_{\text{ex}}$ , the column density of the asymmetric top molecule  $\text{NH}_2\text{D}$  is given by

$$\begin{aligned} \left[ \frac{N(\text{NH}_2\text{D})}{\text{cm}^{-2}} \right] &= 1.94 \times 10^3 \left[ \frac{\nu}{\text{GHz}} \right]^2 \left[ \frac{A_{ul}}{\text{s}^{-1}} \right]^{-1} \frac{Q(T_{\text{ex}})}{g_u} \exp \left( \left( \left[ \frac{E_u}{\text{K}} \right] \left[ \frac{T_{\text{ex}}}{\text{K}} \right]^{-1} \right) \right) \\ &\times J_\nu(T_{\text{ex}}) \tau_m \left[ \frac{\Delta v}{\text{km s}^{-1}} \right], \end{aligned} \quad (5.1)$$

where  $\Delta v$  is the linewidth,  $\tau_m$  the optical depth of the main line ( $1_{11}\text{-}1_{01}$ ,  $F=2\text{-}2$ ),  $\nu$  the frequency of the transition ( $\nu = 85.926 \text{ GHz}$ ),  $E_u$  the energy of the upper

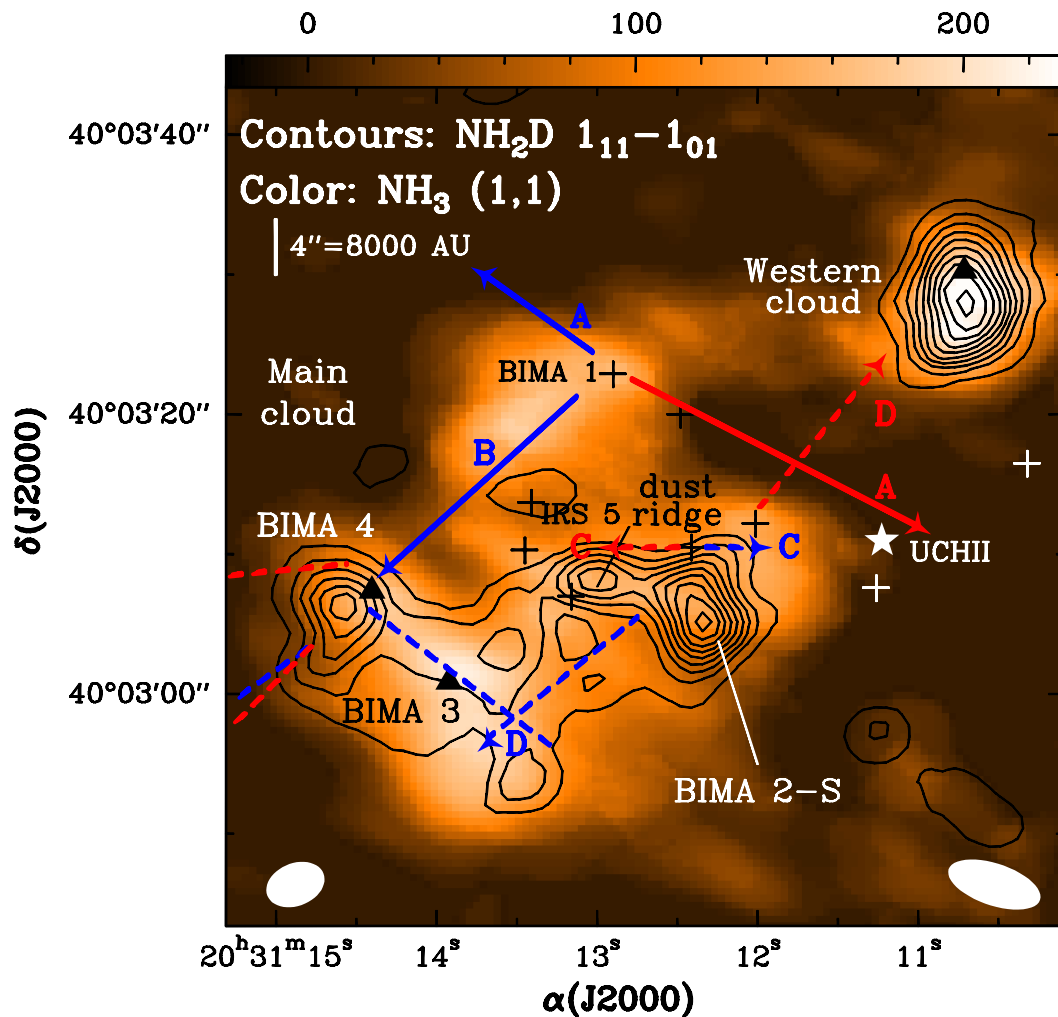


Figure 5.1: Contours:  $\text{NH}_2\text{D}$  zero-order moment. Contours start at 6 %, increasing in steps of 10 % of the peak intensity,  $0.58 \text{ Jy beam}^{-1} \text{ km s}^{-1}$ . Color scale:  $\text{NH}_3(1,1)$  zero-order moment (Palau et al. 2007). The  $\text{NH}_2\text{D}$  synthesized beam,  $4''.32 \times 3''.05$  (P. A. =  $111^\circ$ ), and the  $\text{NH}_3$  synthesized beam are shown in the bottom left and bottom right corners, respectively. White star: position of the UCH II region (IRAS 20293+3952). Plus signs: YSOs embedded in the main cloud. Black triangles:  $\text{NH}_3$  column density peaks in the starless cores BIMA 3, BIMA 4, and the western cloud. Main cores of  $\text{NH}_2\text{D}$  are labeled as western cloud, dust ridge, BIMA 2-S, and BIMA 4. The blue and red continuum/dashed arrows mark the direction of powerful/less powerful molecular outflows, respectively (Beuther et al. 2004a). Outflow B is deflected by BIMA 4 (Palau et al. 2007) and the dashed lines indicate the high-velocity gas around BIMA 4.

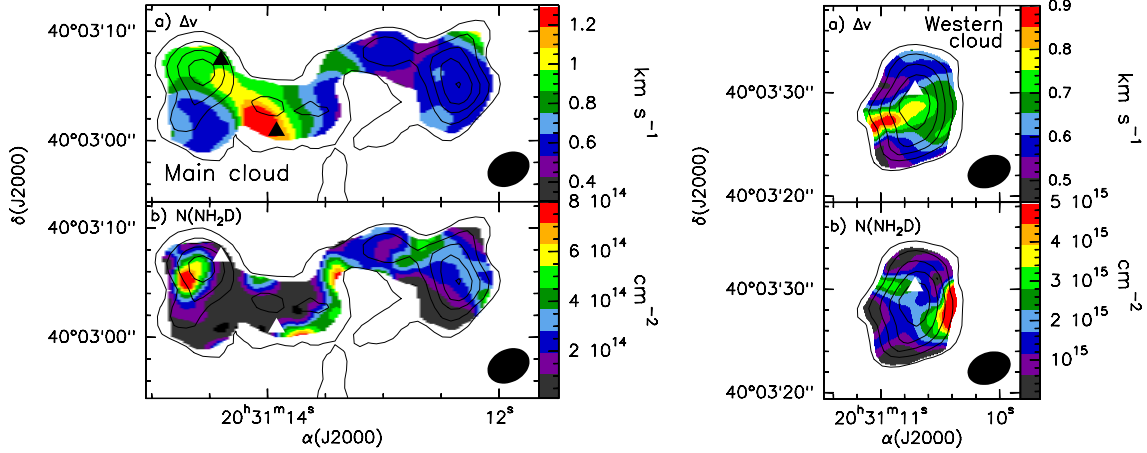


Figure 5.2: Color-scale maps of linewidth and  $N(\text{NH}_2\text{D})$  overlaid on the  $\text{NH}_2\text{D } 1_{11}-1_{01}$  integrated emission (contours) for the main cloud (left panels) and the western cloud (right panels). Triangles mark the  $\text{NH}_3$  column density peaks of BIMA 3, BIMA 4 (left), and the western cloud (right). In all panels the synthesized beam is shown in the bottom right corner.

level ( $E_u = 20.68$  K),  $A_{ul} = 5.8637 \times 10^{-6} \text{ s}^{-1}$  is the Einstein coefficient, and  $J_\nu(T_{\text{ex}}) = (h\nu/k)/(e^{h\nu/kT_{\text{ex}}} - 1)$ , where  $h$  and  $k$  are the Planck and Boltzmann constants, respectively. From the Cologne Database for Molecular Spectroscopy (CDMS; Müller et al. 2001), the upper level degeneracy is  $g_u = 15$ , and the partition function  $Q(T_{\text{ex}})$  is estimated as  $Q(T_{\text{ex}}) = \alpha + \beta T_{\text{ex}}^{3/2}$ , where  $\alpha = 3.899$  and  $\beta = 0.751$  are the best-fit parameters from a fit to the partition function at the different temperatures given in CDMS. The standard ortho/para ratio of 3 (e. g., Walmsley et al. 1987; Tiné et al. 2000) is already included in the partition function.

Figure 5.2 shows a map of the linewidth ( $\Delta v$ ) derived from the hyperfine fit and the total column density  $N(\text{NH}_2\text{D})$  toward the southern side of the main cloud (i. e., dust ridge core, BIMA 2-S, BIMA 3, and BIMA 4, hereafter referred to as the main cloud; see left panels) and the western cloud (right panels). The properties of the western cloud and the main cloud are somewhat different. The total optical depth ( $\tau_{1_{11}-1_{01}} = 2\tau_m$ ) in the western cloud is in the range  $\sim 4$ – $15$ , with a typical uncertainty of  $\sim 1.1$ , whereas the total optical depth is lower toward the main cloud, between 0.5 and 4, with a typical uncertainty of  $\sim 0.5$ . Concerning the linewidth in these clouds (see Fig. 5.2 a), we find line broadening ( $\Delta v \simeq 0.75$ – $0.9 \text{ km s}^{-1}$ ) associated with the western cloud. Toward BIMA 3 and BIMA 4, we also find high

values for the linewidth, around  $\sim 0.8\text{--}1.2\text{ km s}^{-1}$ , while the dust ridge core and BIMA 2-S appear to be more quiescent, with linewidths of  $\sim 0.5\text{--}0.7\text{ km s}^{-1}$ . Since it has been suggested that one of the outflows of the region, outflow B, is interacting with BIMA 4 (Palau et al. 2007), this could produce the line broadening seen in  $\text{NH}_2\text{D}$  in BIMA 3 and BIMA 4. Additionally, the line broadening found in the western cloud is spatially coincident (in projection) with a high-velocity feature of outflow D (Beuther et al. 2004a). Thus, the broad lines seen toward the western cloud, BIMA 3, and BIMA 4, suggest that the deuterated gas is being perturbed by the passage of the outflows (see Fig. 5.1).

The  $\text{NH}_2\text{D}$  column density, corrected for the primary beam response, also presents significant differences between the western cloud and the main cloud. While the column density is, on average,  $N(\text{NH}_2\text{D}) \simeq 25 \times 10^{14}\text{ cm}^{-2}$  in the western cloud, in the main cloud the column density is slightly lower, in the range  $1\text{--}8 \times 10^{14}\text{ cm}^{-2}$ , reaching its maximum value of  $8 \times 10^{14}\text{ cm}^{-2}$  close to the peak position of BIMA 4 (see Fig. 5.2b). The uncertainty of the  $\text{NH}_2\text{D}$  column density is  $\sim 25\text{--}35\%$ .

In order to properly estimate the deuterium fractionation, defined as  $D_{\text{frac}} = N(\text{NH}_2\text{D})/N(\text{NH}_3)$ , we made the  $\text{NH}_3$  VLA images using the same  $uv$  range as the

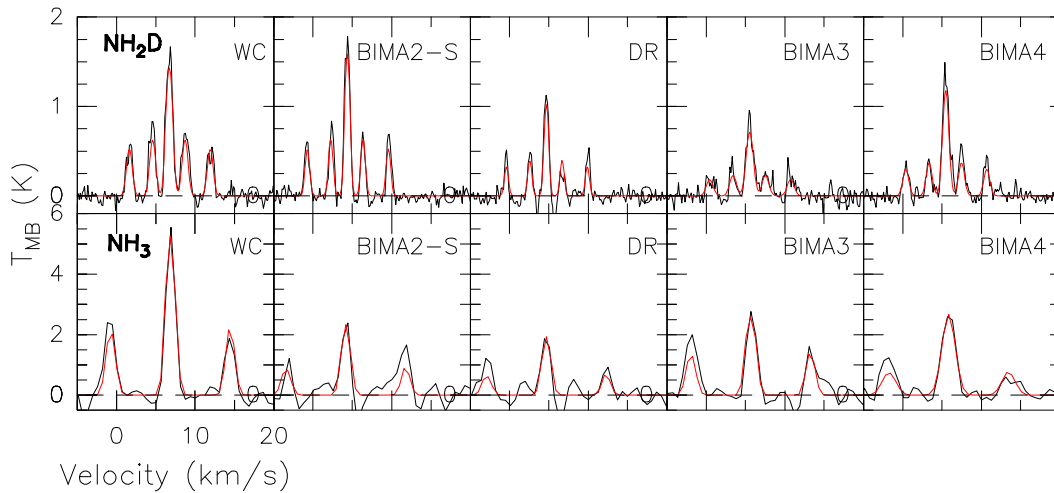


Figure 5.3: Spectra (black line) toward 5 positions of the IRAS 20293+3952 for  $\text{NH}_2\text{D } 1_{11}\text{--}1_{01}$  (top) and  $\text{NH}_3 (1,1)$  (bottom). The 5 positions, which are labeled in the top right corner of each panel, are, from left to right WC (western cloud), BIMA 2-S, DR (dust ridge core), BIMA 3, and BIMA 4. The red lines show the fit to the hyperfine structure obtained as illustrated in Sect. 3.

PdBI data (5–50  $k\lambda$ ), estimating the column densities for both  $\text{NH}_3$  and  $\text{NH}_2\text{D}$  for the same angular scales. Finally, we convolved the  $\text{NH}_2\text{D}$  and  $\text{NH}_3$  emission to a circular beam of  $7''$  (the major axis of the  $\text{NH}_3$  beam). In Fig. 5.3 we present the spectra obtained at the  $\text{NH}_2\text{D}$  emission peak of each condensation (i. e., western cloud, BIMA 2-S, dust ridge core, BIMA 3, and BIMA 4) together with the hyperfine fit obtained toward these positions. In Table 5.1 we list the excitation temperature,  $T_{\text{ex}}$ , the rotational temperature,  $T_{\text{rot}}$ , the  $\text{NH}_2\text{D}$  and  $\text{NH}_3$  column densities,  $D_{\text{frac}}$ , and the  $\text{NH}_3/\text{N}_2\text{H}^+$  ratio for each core and a few YSOs. Toward the YSOs BIMA 1 and IRS 5, we report on upper limits, with  $D_{\text{frac}} < 0.1$ , and we cannot draw any conclusion for the behavior of  $D_{\text{frac}}$  in the protostellar phase. More interestingly, in the western cloud  $D_{\text{frac}}$  is  $\sim 0.8$ , which is the highest value of  $D_{\text{frac}}$  in the region and among the highest reported in the literature (e. g., Crapsi et al. 2007; Pillai et al. 2007; Fontani et al. 2008). In the main cloud,  $D_{\text{frac}}$  presents significant variations among the different cores, with  $D_{\text{frac}}$  decreasing from the northwest ( $D_{\text{frac}} \simeq 0.5$  in BIMA 2-S and the dust ridge core) to the southeast ( $D_{\text{frac}} \simeq 0.1$  in BIMA 3 and BIMA 4). This suggests a chemical differentiation along the main cloud.

## 5.4 Discussion and summary

Our high angular resolution study of the  $\text{NH}_2\text{D}$  toward the massive star-forming region IRAS 20293+3952 reveals strong  $\text{NH}_2\text{D}$  emission toward starless cores, whereas  $\text{NH}_2\text{D}$  is not (or marginally) detected in cores containing YSOs, which suggests that the production of  $\text{NH}_2\text{D}$  is more effective in the pre-protostellar phase than in the protostellar phase. Palau et al. (2007) notice that the starless cores in this region seem to be predominant on the southern side of the main cloud and in the western cloud, while the northern side of the main cloud harbors all the YSOs known in the region, suggestive of the dense gas in the main cloud being progressively more evolved as it moves from south to north. In addition, chemical differentiation among pre-protostellar and protostellar cores was also found by Palau et al. (2007) using the  $\text{NH}_3/\text{N}_2\text{H}^+$  ratio, which was high for pre-protostellar cores and low in protostellar cores (see col. 9 of Table 5.1). Thus, for this region, the behavior of  $D_{\text{frac}}$ , measured from  $\text{NH}_2\text{D}/\text{NH}_3$ , is similar to the behavior of  $\text{NH}_3/\text{N}_2\text{H}^+$  ratio, suggesting that both ratios can be used to distinguish between pre-protostellar and protostellar cores and that both ratios could be related with the evolutionary stage of the dense gas.

Table 5.1: Summary of the main physical properties of selected cores in IRAS 20293+3952

| Core          | $\alpha$ (J2000)<br>(h m s) | $\delta$ (J2000)<br>( $^{\circ}$ ' ") | $T_{\text{ex}}^{\text{a}}$<br>(K) | $\tau_m^{\text{b}}$ | $T_{\text{rot}}^{\text{c}}$<br>(K) | $N(\text{NH}_2\text{D})^{\text{d}}$<br>( $\times 10^{14}$ cm $^{-2}$ ) | $N(\text{NH}_3)^{\text{d}}$<br>( $\times 10^{14}$ cm $^{-2}$ ) | $D_{\text{frac}}^{\text{e}}$ | $\text{NH}_3/\text{N}_2\text{H}^{\text{+c}}$ | Evol.<br>stage $^{\text{f}}$ |
|---------------|-----------------------------|---------------------------------------|-----------------------------------|---------------------|------------------------------------|--|--|------------------------------|--|------------------------------|
| Western cloud | 20:31:10.70                 | 40:03:28.2                            | 4.8 $\pm$ 0.2                     | 1.5                 | 15 $\pm$ 3                         | 10 $\pm$ 2   | 14 $\pm$ 2   | 0.8 $\pm$ 0.2                | 300  | PPC                          |
| BIMA 2-S      | 20:31:12.34                 | 40:03:05.7                            | 5.4 $\pm$ 0.3                     | 1.1                 | 19 $\pm$ 3                         | 2.8 $\pm$ 0.6  | 6.7 $\pm$ 0.8  | 0.4 $\pm$ 0.1                | 90   | PPC                          |
| Dust ridge    | 20:31:12.98                 | 40:03:08.5                            | 4.6 $\pm$ 0.3                     | 1.0                 | 16 $\pm$ 3                         | 2.8 $\pm$ 0.7  | 4.9 $\pm$ 0.9  | 0.6 $\pm$ 0.2                | 90   | PPC                          |
| BIMA 3        | 20:31:13.92                 | 40:03:00.9                            | 5.4 $\pm$ 1.0                     | 0.4                 | 14 $\pm$ 2                         | 1.9 $\pm$ 0.5  | 19 $\pm$ 3   | 0.10 $\pm$ 0.04              | 300  | PPC                          |
| BIMA 4        | 20:31:14.56                 | 40:03:06.8                            | 7.5 $\pm$ 1.6                     | 0.3                 | 14 $\pm$ 2                         | 1.2 $\pm$ 0.4  | 7.4 $\pm$ 0.8  | 0.16 $\pm$ 0.05              | 200  | PPC                          |
| BIMA 1        | 20:31:12.77                 | 40:03:22.6                            | ...                               | ...                 | 24 $\pm$ 3                         | < 1.1 $^{\text{g}}$  | 19 $\pm$ 3   | < 0.06                       | 50   | O, no IR                     |
| IRS 5         | 20:31:13.41                 | 40:03:13.7                            | ...                               | ...                 | 24 $\pm$ 3                         | < 1.5 $^{\text{g}}$  | 11 $\pm$ 2   | < 0.1                        | 50   | IR                           |

**Notes.** <sup>(a)</sup>  $T_{\text{ex}}$  derived from the output parameters of the  $\text{NH}_2\text{D}$   $1_{11}-1_{01}$  hyperfine fit. <sup>(b)</sup> Derived from the fits to the hyperfine structure of  $\text{NH}_2\text{D}$   $1_{11}-1_{01}$ . <sup>(c)</sup> Obtained from Palau et al. (2007). <sup>(d)</sup> Column densities derived using the same  $uv$  range and convolving the images to a circular beam of  $7''$ . <sup>(e)</sup>  $D_{\text{frac}} = N(\text{NH}_2\text{D})/N(\text{NH}_3)$ . <sup>(f)</sup> PPC: pre-protostellar core; O: molecular outflow. <sup>(g)</sup>  $3\sigma$  upper limit estimated adopting  $\Delta v$  from  $\text{NH}_3$  and  $T_{\text{ex}} = 5$  K.

A possible interpretation of the differences in  $D_{\text{frac}}$  seen in the pre-protostellar cores of region could be that they are in different evolutionary stages. According to the study of Crapsi et al. (2005), there is an increasing trend for  $D_{\text{frac}}$  as the starless core approaches the onset of gravitational collapse (from 0.03–0.1 in the youngest cores to 0.1–0.4 toward the most evolved cores). This would indicate that the western cloud is the most evolved pre-protostellar core and that BIMA 3 and BIMA 4 are less evolved. However, in regions of massive star formation, typically associated with clustered environments, other factors, like temperature, UV radiation, and/or molecular outflows, can play important roles in altering the chemistry, and then it is not clear whether this trend is related to the evolutionary stage of pre-protostellar cores.

A comparison of  $D_{\text{frac}}$  between the western cloud and BIMA 3/BIMA 4, all of them having similar temperatures but very different values of  $D_{\text{frac}}$  (see Table 5.1), indicates that temperature is not an important factor in determining  $D_{\text{frac}}$  for temperatures around 15 K. Palau et al. (2007) find evidence that UV radiation from the UCH II region affects the chemistry at the western edge of the main cloud facing the UCH II region, so it could affect BIMA 2-S and the western cloud. In particular, the presence of a cavity between the UCH II region and the western cloud suggests that this cloud could be photo-illuminated by the UCH II region. However, while the western cloud and BIMA 2-S could be locally affected by the UV radiation, this is not the case for BIMA 3 and BIMA 4, for which the high visual extinction in the main cloud prevents UV photons from penetrating. Finally, Fontani et al. (2009) point out that shocks in outflows could modify  $D_{\text{frac}}$ . This could be the case for the western cloud, BIMA 3, and for BIMA 4. While the interaction of an outflow with the western cloud is not evident, Palau et al. (2007) have already proposed that the powerful outflow B is interacting with BIMA 4, producing the deflection of the outflow and thus the ejection of high-velocity material in different directions. This could affect BIMA 4 and BIMA 3 because high-velocity SiO is seen close to these cores (see Fig. 5.1 and Beuther et al. 2004a). This interpretation is reinforced by the line broadening of  $\text{NH}_2\text{D}$  observed towards BIMA 3 and BIMA 4 (see Fig. 5.2). In conclusion, while  $D_{\text{frac}}$  in IRAS 20293+3952 may be locally affected by the interaction of outflows and UV radiation,  $D_{\text{frac}}$  is lower toward YSOs than toward pre-protostellar cores, with a possible evolutionary trend in the pre-protostellar phase, which deserves further study.

# Chapter 6

## General discussion and conclusions

### 6.1 On the behavior of the $\text{NH}_3/\text{N}_2\text{H}^+$ ratio

In the present work we have extended to the high-mass regime the study of the  $\text{NH}_3/\text{N}_2\text{H}^+$  ratio, started by Palau et al. (2007), by performing first a large scale analysis of the IRDC G14.2–0.60 and then high angular resolution observations toward four intermediate/high-mass star-forming regions. Two of the regions harbor a hot molecular core whereas the other two are associated with an UCH II region. A further step to study column density ratios as “chemical clocks” was done by studying the deuterium fractionation and its relation with the  $\text{NH}_3/\text{N}_2\text{H}^+$  ratio toward the pre-protostellar cores surrounding an UCH II region.

We compiled a list of regions from the literature for which the  $\text{NH}_3/\text{N}_2\text{H}^+$  ratio has been estimated. We have included both low- and high-mass star-forming regions and the final list is shown in Table 6.2. It is important to remark that we refer to high-mass protostellar and pre-protostellar cores as those cores associated with cluster environments where at least one of its members is a massive star, whereas low-mass protostellar and pre-protostellar cores are found in isolated regions where only low-mass stellar objects are or will be formed. We note that the sample is not homogenous in the sense that the spatial resolution achieved in low-mass regions is slightly better than in high-mass star-forming regions (5000 AU in front of 10000 AU), and hence this could introduce some distance effects in our analysis. From the table we find that the mean and median values of the  $\text{NH}_3/\text{N}_2\text{H}^+$  ratio in the pre-protostellar phase is 279 and 200, respectively. On the other hand, the mean

Table 6.1: Statistics of the  $\text{NH}_3/\text{N}_2\text{H}^+$  ratio in pre-protostellar and protostellar cores

|                         | $\text{NH}_3/\text{N}_2\text{H}^+$ |        |
|-------------------------|------------------------------------|--------|
|                         | Mean                               | Median |
| <i>pre-protostellar</i> |                                    |        |
| low-mass                | 219                                | 135    |
| high-mass               | 336                                | 290    |
| all                     | 279                                | 200    |
| <i>Protostellar</i>     |                                    |        |
| low-mass                | 144                                | 90     |
| high-mass               | 266                                | 190    |
| all                     | 199                                | 95     |

value of the  $\text{NH}_3/\text{N}_2\text{H}^+$  ratio in the protostellar phase is 199 and median value is 95. We summarized the statistics of the  $\text{NH}_3/\text{N}_2\text{H}^+$  ratio in Table 6.1. Thus, in general terms, the median value of  $\text{NH}_3/\text{N}_2\text{H}^+$  ratio in the pre-protostellar phase is significantly higher than in the protostellar phase, both considering all the sample or separating it in low- and high-mass cores. However, we note that the values of the  $\text{NH}_3/\text{N}_2\text{H}^+$  ratio, for both pre-protostellar and protostellar cores, are systematically higher in cores associated with high-mass star formation.

In an attempt to establish an evolutionary sequence of the  $\text{NH}_3/\text{N}_2\text{H}^+$  ratio, in the following sections we present some of the correlations found by analyzing the sample of dense cores listed in Table 6.2.

### 6.1.1 $\text{NH}_3$ and $\text{N}_2\text{H}^+$ column densities

In Fig. 6.1 we show the  $\text{N}_2\text{H}^+$  column density as a function of the  $\text{NH}_3$  column density for both pre-protostellar and protostellar cores. Indeed, the entire sample does not show a significant correlation between  $N(\text{N}_2\text{H}^+)$  and  $N(\text{NH}_3)$ . However, we find a tight correlation between  $\text{N}_2\text{H}^+$  and  $\text{NH}_3$  column densities during the pre-protostellar phase. The best fit is:

$$N_{\text{pre-protostellar}}(\text{N}_2\text{H}^+) \times 10^{-12} = (3.1 \pm 2.6) + (0.3 \pm 0.1) \times N_{\text{pre-protostellar}}(\text{NH}_3) \times 10^{-14} \text{ cm}^{-2}, \quad (6.1)$$

where the quantities following the plus/minus sign are  $1 \sigma$  uncertainties. The linear correlation coefficient is 0.62.

If we consider only dense cores associated with low-mass star forming regions (blue dots in Fig. 6.1 we found a similar correlation, being the best-fit line:

$$N_{\text{pre-protostellar}}(\text{N}_2\text{H}^+) \times 10^{-12} = (2.2 \pm 1.4) + (0.5 \pm 0.1) \times N_{\text{pre-protostellar}}(\text{NH}_3) \times 10^{-14} \text{ cm}^{-2}, \quad (6.2)$$

with a linear correlation coefficient of 0.61. This result is in complete agreement with the correlation found by Caselli et al. (2002a). On the other hand, we found a similar linear correlation if we consider only the dense cores associated with high-mass star-forming regions, i. e., cores studied in this work plus the regions IRAS 20293+3952 (Palau et al. 2007) and IRAS 05345+3157 (Fontani et al. in preparation). In this case the best-fit line, which is indicated in orange in Fig. 6.1 with a linear correlation coefficient of 0.75, is the following:

$$N_{\text{pre-protostellar}}(\text{N}_2\text{H}^+) \times 10^{-12} = (2.9 \pm 1.2) + (0.2 \pm 0.1) \times N_{\text{pre-protostellar}}(\text{NH}_3) \times 10^{-14} \text{ cm}^{-2}. \quad (6.3)$$

The presence of a young stellar object deeply embedded in the dense gas, specially in regions of high-mass star formation, may produce significant effects on the dense gas, either by increasing the temperature and/or by the presence of powerful molecular outflows. Then, the behavior of these two molecules differs from that found in the pre-protostellar phase and this naturally explains the fact that we do not find any correlation between the  $\text{N}_2\text{H}^+$  and  $\text{NH}_3$  column densities in protostellar cores.

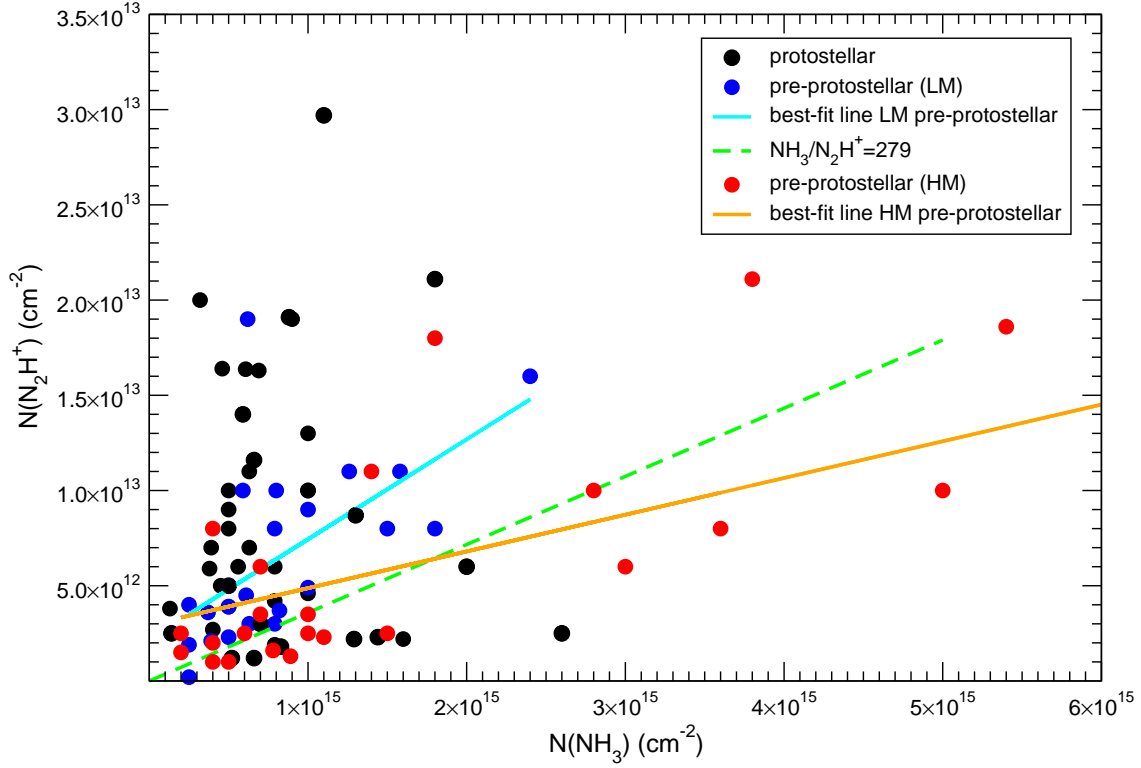


Figure 6.1: Correlation between  $N_2H^+$  and  $NH_3$  column densities. Low-mass pre-protostellar cores are marked with blue dots while the high-mass pre-protostellar cores studied in this work are indicated in red. The best-fit lines for low- and high-mass pre-protostellar cores are indicated by the blue and orange lines, respectively. Protostellar cores, which do not show any significant correlation, are indicated by the black dots. The green dashed line indicates a constant  $NH_3/N_2H^+$  ratio of 279 (the mean value of the sample for pre-protostellar cores).

### 6.1.2 Column densities against temperature

Figure 6.2 shows the  $NH_3$  column density as a function of kinetic temperature for the sample of dense cores listed in Table 6.2. The entire sample does not show correlation between these two physical parameters, but we found, however, some distinct features for both pre-protostellar and protostellar cores. First, we can see a trend during the pre-protostellar phase for high-mass YSOs in which the  $NH_3$  column density decreases as the temperature increases (this trend is barely seen in low-mass pre-protostellar cores). Second, the values of the  $NH_3$  column density in

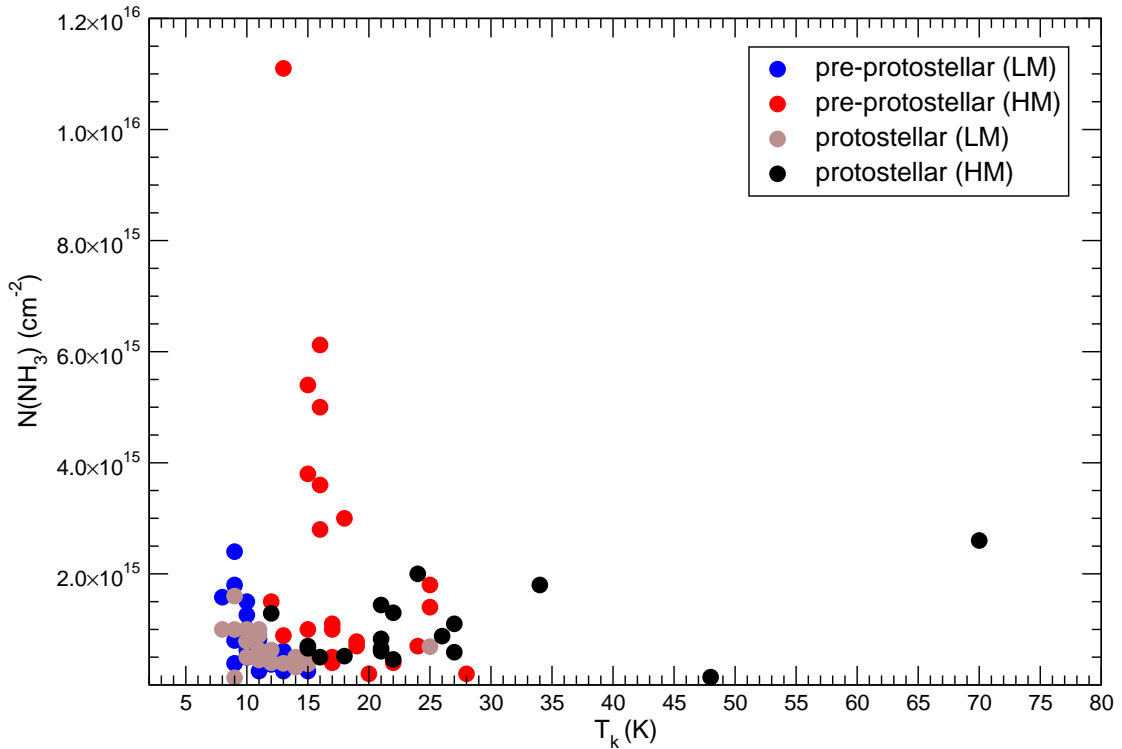


Figure 6.2:  $\text{NH}_3$  column density against kinetic temperature,  $T_k$ , for protostellar cores found in high-mass star-forming regions (black dots), high-mass pre-protostellar cores (red dots), low-mass protostellar cores (brown dots), and low-mass pre-protostellar cores (blue dots).

protostellar cores associated with high-mass star formation are significantly lower compared with those found in pre-protostellar cores, and they present a broader distribution in all the temperature range.

In Figure 6.3 we present the  $\text{N}_2\text{H}^+$  column density as a function of kinetic temperature for the sample of dense cores (pre-protostellar and protostellar), which are found to be associated with clusters forming high-mass stars. While pre-protostellar cores do not show significant correlation between the  $\text{N}_2\text{H}^+$  column density and temperature, we found a good correlation in the protostellar phase. As shown in chapter 4, at high temperatures CO is desorbed from dust mantles favoring the destruction of  $\text{N}_2\text{H}^+$ . Thus, the correlation between the  $\text{N}_2\text{H}^+$  column density and temperature is found only if we consider a temperature range of 10–35 K. As can be seen in Figure 6.3 there are only two points outside this temperature range, which

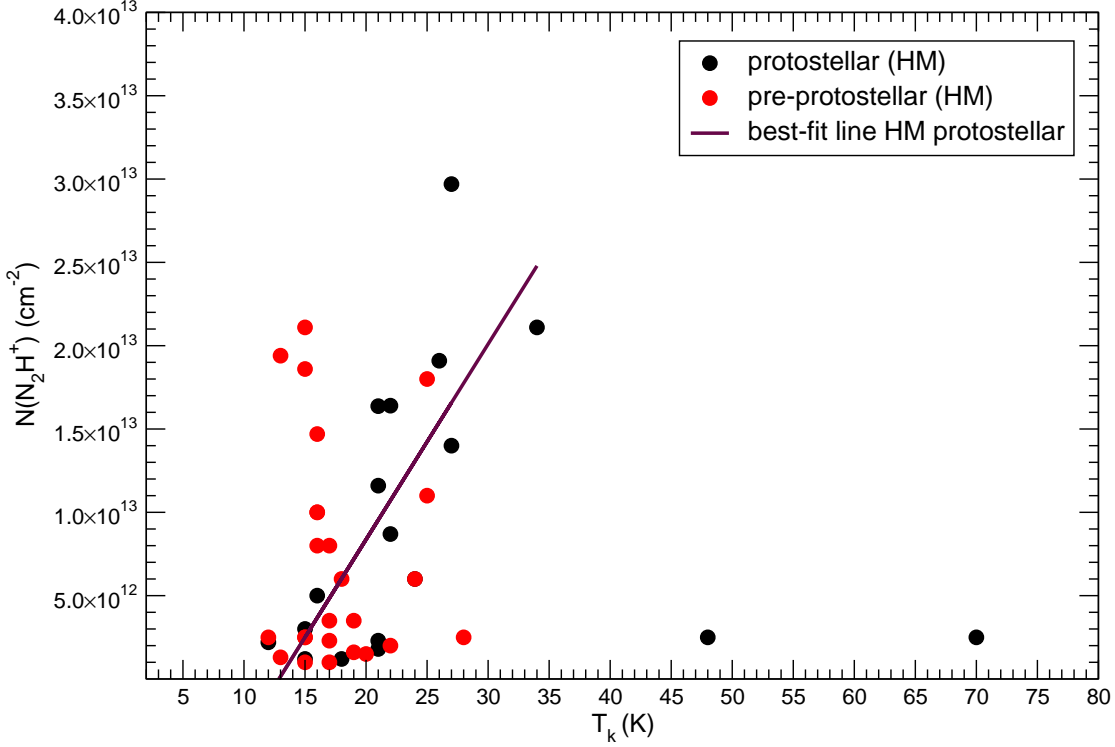


Figure 6.3: Correlation between the  $N_2H^+$  column density and kinetic temperature,  $T_k$ , for protostellar cores found in high-mass star-forming regions (black dots), with the best-fit line marked with the violet line. pre-protostellar cores are indicated by red dots, which do not show significant correlation. Note that the best fit line is only for the temperature range  $\sim 10 - 35$  K (see main text).

correspond to AFGL 5142 hot molecular core, where the temperature is  $\sim 70$  K and the powerful molecular outflows are producing a substantial destruction of the  $N_2H^+$  molecule, and to the UCH II region IRAS 20293+3952, almost devoid of dense gas due to its relatively advanced evolutionary stage.

The best fit obtained for protostellar cores is:

$$N(N_2H^+)_{\text{protostellar}} = (-15.1 \pm 6.1) \times 10^{12} + (1.2 \pm 0.3) \times 10^{12} \times T_k \text{ (cm}^{-2} \text{ K)}, \quad (6.4)$$

with a linear correlation coefficient of 0.75. We emphasize that this relation is only valid for low temperatures, in the range of  $\sim 10 - 35$  K, for which the  $N_2H^+$  column

density increases as the protostellar core evolves. This result suggest that there is golden period of  $\text{N}_2\text{H}^+$  abundance during the protostellar phase just after the onset of star formation.

Thus, the decreasing trend of the  $\text{NH}_3$  column density with the temperature during the pre-protostellar phase suggests that the  $\text{NH}_3/\text{N}_2\text{H}^+$  ratio is mainly determined by the evolution of the  $\text{NH}_3$  molecule (note that we did not find any trend for the  $\text{N}_2\text{H}^+$  column density in the pre-protostellar phase). On the other hand, the lack of a correlation between the  $\text{NH}_3$  column density and temperature during the protostellar phase suggests that the  $\text{NH}_3/\text{N}_2\text{H}^+$  ratio will be mainly determined by the  $\text{N}_2\text{H}^+$  column density. As temperature rises or as the protostar evolves, the  $\text{NH}_3/\text{N}_2\text{H}^+$  ratio decreases until some point where the  $\text{N}_2\text{H}^+$  column density drops drastically because  $\text{N}_2\text{H}^+$  molecule is destroyed by CO, resulting in very high values of the  $\text{NH}_3/\text{N}_2\text{H}^+$  ratio.

### 6.1.3 The $\text{NH}_3/\text{N}_2\text{H}^+$ ratio

In order to explore possible dependencies of the  $\text{NH}_3/\text{N}_2\text{H}^+$  column density ratio we plotted in Fig. 6.4 (left panel) this quantity as a function of the linewidth. Here we do not find any significant correlation between the ratio and the linewidth, neither separating the low-mass cores from the high-mass ones. What is clear from this figure is that the linewidths in cluster environments containing pre-protostellar and protostellar cores are systematically higher compared with low-mass star-forming regions. The median values of the linewidth for low-mass pre-protostellar and protostellar cores are  $0.32 \text{ km s}^{-1}$  and  $0.4 \text{ km s}^{-1}$ , respectively. On the other hand, in regions of massive star formation, the median value of the linewidth for pre-protostellar and protostellar cores is  $1 \text{ km s}^{-1}$  and  $1.5 \text{ km s}^{-1}$ , respectively.

Interestingly, the minimum linewidth observed in high-mass cores is  $\sim 0.5 \text{ km s}^{-1}$ . However, since most of the low-mass regions haven been observed with single-dish telescopes but with higher spectral resolution than the high-mass cores, we should consider the possibility that the differences seen in linewidth may be a consequence of observational effects and not an intrinsic property of regions of massive star formation. The spectral resolution in our sample of high-mass cores varies from  $0.13$  to  $0.6 \text{ km s}^{-1}$ . Despite in some cases of the high-mass regime our spectral resolution would not resolve lines narrower than  $0.5 \text{ km s}^{-1}$ , in other cases we have

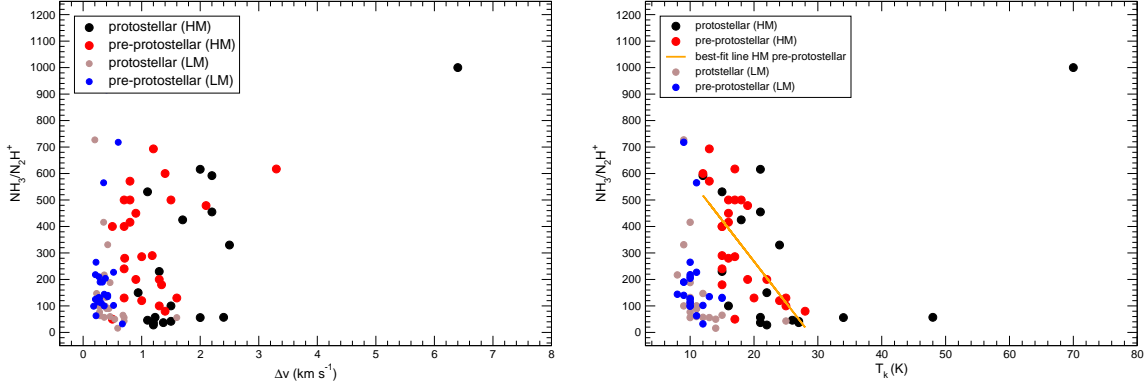


Figure 6.4: *Left panel:*  $\text{NH}_3/\text{N}_2\text{H}^+$  ratio against linewidth. *Right panel:*  $\text{NH}_3/\text{N}_2\text{H}^+$  ratio against kinetic temperature. The best fit-line for high-mass pre-protostellar cores is indicated in orange. In both panels low-mass pre-protostellar cores are marked with blue dots while the high-mass pre-protostellar cores studied in this work are indicated in red. Black dots are protostellar cores associated with high-mass stars and the brown dots indicate low-mass protostellar cores.

enough spectral resolution to resolve them, so spectral resolution is not likely affecting the relatively high values of linewidth in pre-protostellar cores found in regions of massive star formation. Then, we defined an empirical linewidth threshold at  $\Delta v \simeq 0.5 \text{ km s}^{-1}$ , above which we find all the dense cores associated with cluster environments, i. e., with massive star formation, for both pre-protostellar and protostellar cores. The fact that we did not find linewidths smaller than  $0.5 \text{ km s}^{-1}$  is a consequence of these dense cores being more massive than those associated with low-mass star formation and thus, the equipartition will result in more kinetic motions, including turbulence.

Figure 6.4 (right panel) shows the  $\text{NH}_3/\text{N}_2\text{H}^+$  ratio as a function of the kinetic temperature. In this case we found an anticorrelation between the  $\text{NH}_3/\text{N}_2\text{H}^+$  ratio and the kinetic temperature for the pre-protostellar cores studied in this work and considering also the regions analyzed in the same way, like IRAS 20293+3952 (Palau et al. 2007) and IRAS 05345+3157 (Fontani et al. in preparation). The best fit is:

$$\frac{N(\text{NH}_3)_{\text{protostellar}}}{N(\text{N}_2\text{H}^+)_{\text{protostellar}}} = (891 \pm 131) - (31.1 \pm 7.1) \times T_k \text{ (K)}, \quad (6.5)$$

with a linear correlation coefficient of 0.67.

The fact that we found a correlation only for the high-mass pre-protostellar cores could be due to either computational effects (the whole sample has not been analyzed in a similar and consistent way) or a selective effect of high-mass regions only. From Fig. 6.4 we can see that during the pre-protostellar phase the  $\text{NH}_3/\text{N}_2\text{H}^+$  ratio decreases as temperature rises, mainly because the  $\text{NH}_3$  column density decreases too during this phase. This result could be interpreted in terms of chemical evolution of the dense gas during the pre-protostellar phase as the core approaches the onset of star formation. As expected from the results of Fig. 6.1, protostellar cores do not show a correlation between the  $\text{NH}_3/\text{N}_2\text{H}^+$  ratio and the temperature at all. Therefore, we conclude that at least for the pre-protostellar phase there is a golden period of  $\text{NH}_3$  abundance and that the  $\text{NH}_3/\text{N}_2\text{H}^+$  ratio can be used as a “chemical clock”.

In an attempt to establish an evolutionary sequence of the  $\text{NH}_3/\text{N}_2\text{H}^+$  ratio with the stage of evolution of the YSO embedded within the dense core, we present in Fig. 6.5 the  $\text{NH}_3/\text{N}_2\text{H}^+$  column density ratio against the evolutionary stage of the YSO considering independently the low-mass cores (left panel) from the high-mass ones (right panel). While the evolutionary stage of low-mass YSOs is well established (see e. g., Lada 1987; André et al. 1993) the evolutionary sequence for high-mass stars is still unclear mainly because massive stars evolve much faster to the main-sequence than low mass stars and they radiate UV photons while are still accreting matter (see e. g., the review by Zinnecker and Yorke 2007). Then, as a first approximation we have considered three main phases based on their near infrared emission. The first stage would be the stage where no near-infrared emission is detected toward the YSO and the core is still cold. Then, we considered the hot molecular core phase, and finally YSOs associated with near-infrared emission.

As can be seen in Fig. 6.5 (left panel), for low-mass protostellar cores we find small variations in the  $\text{NH}_3/\text{N}_2\text{H}^+$  ratio with the evolutionary stage of the YSO. However, these variations may not be significative, since there is only one object in the transition Class 0/I phase, for which the  $\text{NH}_3/\text{N}_2\text{H}^+$  ratio is very low. Thus, we should increase the number of sources in order to make this variations significative enough to draw any firm conclusion.

Regarding the evolution of the  $\text{NH}_3/\text{N}_2\text{H}^+$  ratio during the high-mass protostellar phase (see right panel of Fig. 6.5) we find some hints of the ratio evolving from low

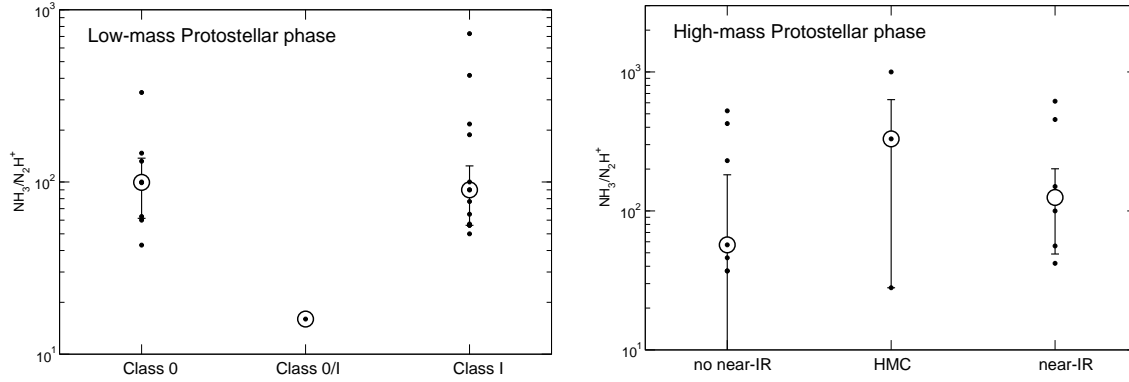


Figure 6.5:  $\text{NH}_3/\text{N}_2\text{H}^+$  ratio against evolutionary stage during the protostellar phase for the sample of low-mass cores (*Left*) and high-mass cores (*Right*). The big dot represents the median value for each evolutionary stage and error bars are the median absolute deviation.

values during the very early stages of star formation to high values in the HMC phase and afterwards. This behavior can be explained in terms of temperature increasing as time goes on, producing the evaporation of CO from grain mantles and hence the destruction of the  $\text{N}_2\text{H}^+$  molecule, that results in a drop of the  $\text{N}_2\text{H}^+$  column density and then the  $\text{NH}_3/\text{N}_2\text{H}^+$  ratio increases. It is important to point out that the sample of high-mass protostellar cores includes those clumps of the IRDC G14.2–0.60 associated with star formation for which we have estimated very high values of the  $\text{NH}_3/\text{N}_2\text{H}^+$  ratio, probably because the spatial resolution (more than 10 times worse than for the other regions) do not allow us to resolve each individual dense core. However, if we take into account only protostellar cores observed with the same spatial resolution we obtained exactly the same trend but with slightly lower values of the median and dispersion.

It is interesting to consider the influence of molecular outflows on the  $\text{NH}_3/\text{N}_2\text{H}^+$  ratio, which could be important both in low-mass and high-mass star-forming regions. As discussed by Chen et al. (2008), who find a strong relationship between the morphology of the  $\text{N}_2\text{H}^+$  emission and the jet/outflow actions, molecular outflows are also playing an important role in the evolution of the dense gas envelope. For example, we would expect to find dense gas envelopes elongated along the outflow direction during the earlier stages of protostellar evolution and the  $\text{NH}_3/\text{N}_2\text{H}^+$  would be low. Eventually, as CO is released from grain mantles it would destroy the

envelope and we should observe the  $\text{N}_2\text{H}^+$  emission with an ‘hour-glass’ morphology and consequently the  $\text{NH}_3/\text{N}_2\text{H}^+$  would be high. Interestingly, in our sample the morphology of the dense gas with respect to the outflow matches well with the evolutionary scenario proposed by Chen et al. (2008) and the evolution of the  $\text{NH}_3/\text{N}_2\text{H}^+$  ratio. For instance, in I00117-MM1 and I20293 (Palau et al. 2007, 2010) we found low values of the  $\text{NH}_3/\text{N}_2\text{H}^+$  ratio and the dense gas is elongated along the outflow direction, whereas in the hot molecular cores of AFGL 5142 and I20126, for which the  $\text{NH}_3/\text{N}_2\text{H}^+$  ratio is very high, the dense gas presents an ‘hour-glass’ morphology. However, to fully confirm this, we should investigate the morphology of the  $\text{N}_2\text{H}^+$  emission with respect to the outflow direction for both low- and high-mass protostellar cores. In summary, while in low-mass protostellar cores the  $\text{NH}_3/\text{N}_2\text{H}^+$  ratio could be affected by the presence of molecular outflows, in regions of high-mass star formation we should additionally consider the increase of temperature, which is a key parameter in determining the  $\text{NH}_3/\text{N}_2\text{H}^+$  ratio, specially in the hot molecular core phase, which at some point produces a significant increase of the  $\text{NH}_3/\text{N}_2\text{H}^+$  ratio.

To summarize, during the pre-protostellar phase the behavior of the  $\text{NH}_3/\text{N}_2\text{H}^+$  ratio is more or less clear, with a decreasing trend of the  $\text{NH}_3/\text{N}_2\text{H}^+$  ratio as the core approaches the onset of gravitational collapse to form a star due to the golden period of  $\text{NH}_3$  seen in this phase. On the other hand, the behavior of the  $\text{NH}_3/\text{N}_2\text{H}^+$  ratio during the protostellar phase is not so obvious. Nevertheless, in this stage we found some hints of dense gas evolution. Initially, the  $\text{NH}_3/\text{N}_2\text{H}^+$  ratio is low, mainly because of the  $\text{N}_2\text{H}^+$  golden period and it progressively increases as the YSOs evolves due to its high temperature and/or the effects of molecular outflows.

Table 6.2: Summary of star-forming regions for which the  $\text{NH}_3/\text{N}_2\text{H}^+$  ratio has been estimated

| Name                          | d<br>(pc) | $L_{\text{bol}}$<br>( $L_{\odot}$ ) | Spat. res.<br>(AU) | $T_{\text{k}}$<br>(K) | $\Delta v$<br>( $\text{km s}^{-1}$ ) | $N(\text{NH}_3)$<br>( $10^{14} \text{ cm}^{-2}$ ) | $N(\text{N}_2\text{H}^+)$<br>( $10^{12} \text{ cm}^{-2}$ ) | Ratio <sup>a</sup> | $M$<br>( $M_{\odot}$ ) | Evolutionary<br>Stage <sup>b</sup> | References   |
|-------------------------------|-----------|-------------------------------------|--------------------|-----------------------|--------------------------------------|---|--|--------------------|------------------------|------------------------------------|--------------|
| <b>Pre-protostellar cores</b> |           |                                     |                    |                       |                                      |   |  |                    |                        |                                    |              |
| L1517B                        | 140       | ...                                 | 7500               | 10                    | 0.27                                 | 6.3   | 3  | 210                | 0.3                    | ...                                | 24, 25       |
| L1498                         | 140       | ...                                 | 7500               | 10                    | 0.18                                 | 7.9   | 8.0  | 99                 | 0.8                    | ...                                | 24, 25       |
| B217-core                     | 140       | ...                                 | 5600               | 9                     | 0.33                                 | 18  | 8.0  | 190                | 1.1                    | ...                                | 1, 11        |
| Oph B1                        | 120       | ...                                 | 2200               | 13                    | 0.42                                 | 6.1   | 4.5  | 135                | 1.1                    | ...                                | 4, 5, 12, 13 |
| L1544                         | 140       | ...                                 | 7500               | 10                    | 0.31                                 | 10  | 9  | 111                | 1.2                    | ...                                | 24, 25       |
| L 723-East arm                | 300       | ...                                 | 3600               | 12                    | 0.52                                 | 3.7   | 3.6  | 102                | 1.8                    | ...                                | 8, 9, 10     |
| IRAS 05405-SMM5               | 450       | ...                                 | 18000              | 11                    | 0.35                                 | 5.9   | 10   | 565                | 1.9                    | ...                                | 14, 15       |
| IRAS 20293-BIMA 4             | 2000      | ...                                 | 14000              | 15                    | 1.34                                 | 38  | 21.1   | 180                | 2.0                    | ...                                | 6            |
| IRAS 20293-BIMA 3             | 2000      | ...                                 | 14000              | 15                    | 1.18                                 | 54  | 18.6   | 290                | 2.2                    | ...                                | 6            |
| IRAS 05405-Ori B9 N           | 450       | ...                                 | 18000              | 13                    | 0.4                                  | 2.5   | 0.2  | 916                | 2.3                    | ...                                | 14, 15       |
| IRAS 05345-S                  | 1800      | ...                                 | 6100               | 16                    | 0.8                                  | 61  | 14.7   | 416                | 2.5                    | ...                                | 21, 22, 23   |
| IRAS 05405-SMM7               | 450       | ...                                 | 18000              | 9                     | 0.6                                  | 8   | 10   | 718                | 3.6                    | ...                                | 14, 15       |
| L 723-West arm                | 300       | ...                                 | 3600               | 11                    | 0.52                                 | 8.2   | 3.7  | 227                | 3.7                    | ...                                | 8, 9, 10     |
| L1512                         | 140       | ...                                 | 7500               | 10                    | 0.22                                 | 7.9   | 3  | 265                | 3.8                    | ...                                | 24, 25       |
| TMC-2A                        | 140       | ...                                 | 7500               | 10                    | 0.25                                 | 12.6  | 11   | 115                | 4.1                    | ...                                | 24, 25       |
| L234A                         | 160       | ...                                 | 8600               | 10                    | 0.21                                 | 5   | 2.3  | 218                | 4.8                    | ...                                | 24, 25       |
| L 1262-core                   | 180       | ...                                 | 7200               | 9                     | 0.42                                 | 24  | 16   | 140                | 5.7                    | ...                                | 8, 3         |
| L1696A                        | 160       | ...                                 | 8600               | 15                    | 0.25                                 | 5.0   | 3.9  | 129                | 6.1                    | ...                                | 24, 25       |
| L63                           | 160       | ...                                 | 8600               | 10                    | 0.21                                 | 15  | 8.0  | 125                | 8.0                    | ...                                | 24, 25       |
| IRAS 05399-SMM1               | 450       | ...                                 | 18000              | 12                    | 0.67                                 | 6.2   | 19   | 32                 | 8.4                    | ...                                | 14, 15       |
| IRAS 05345-N                  | 1800      | ...                                 | 6100               | 13                    | 0.8                                  | 111   | 19.4   | 571                | 8.7                    | ...                                | 21, 22, 23   |
| IRAS 20126-coreC              | 1700      | ...                                 | 12900              | 16                    | 0.8                                  | 50  | 10   | 500                | 12                     | ...                                | 19           |
| L1400K                        | 170       | ...                                 | 9200               | 11                    | 0.22                                 | 2.5   | 4  | 63                 | 14                     | ...                                | 24, 25       |
| TMC-2                         | 140       | ...                                 | 7500               | 10                    | 0.38                                 | 10  | 4.9  | 204                | 16                     | ...                                | 24, 25       |
| TMC-1C                        | 140       | ...                                 | 7500               | 8                     | 0.36                                 | 15.8  | 11   | 144                | 20                     | ...                                | 24, 25       |
| L1155C                        | 440       | ...                                 | 23800              | 10                    | 0.36                                 | 5   | 5  | 100                | 26                     | ...                                | 24, 25       |
| L1536                         | 140       | ...                                 | 7500               | 10                    | 0.28                                 | 5   | 3.9  | 128                | 33                     | ...                                | 24, 25       |

Continued on Next Page...

Table 6.2 – Continued

| Name              | d<br>(pc) | $L_{\text{bol}}$<br>( $L_{\odot}$ ) | Spat. res.<br>(AU) | $T_{\text{k}}$<br>(K) | $\Delta v$<br>( $\text{km s}^{-1}$ ) | $N(\text{NH}_3)$<br>( $10^{14} \text{ cm}^{-2}$ ) | $N(\text{N}_2\text{H}^+)$<br>( $10^{12} \text{ cm}^{-2}$ ) | Ratio <sup>a</sup> | $M$<br>( $M_{\odot}$ ) | Evolutionary<br>Stage <sup>b</sup> | References |
|-------------------|-----------|-------------------------------------|--------------------|-----------------------|--------------------------------------|---|--|--------------------|------------------------|------------------------------------|------------|
| L134A             | 160       | ...                                 | 8600               | 9                     | 0.29                                 | 3.9   | 2.1  | 190                | 83                     | ...                                | 24, 25     |
| G14.2–0.60-S11    | 2300      | ...                                 | 133400             | 13                    | 1.2                                  | 8.9   | 1.3  | 693                | 114                    | ...                                | 19         |
| B28               | 200       | ...                                 | 10800              | 15                    | 0.27                                 | 2.5   | 1.9  | 132                | ...                    | ...                                | 24, 25     |
| IRAS 20293-WCloud | 2000      | ...                                 | 14000              | 16                    | 0.71                                 | 28  | 10   | 280                | ...                    | ...                                | 6          |
| IRAS 22134-coreA  | 2600      | ...                                 | 14300              | 15                    | 0.5                                  | 4   | 1  | 400                | ...                    | ...                                | 19         |
| IRAS 22134-coreB  | 2600      | ...                                 | 14300              | 15                    | 0.7                                  | 6   | 2.5  | 240                | ...                    | ...                                | 19         |
| IRAS 22134-coreC  | 2600      | ...                                 | 14300              | 17                    | 0.7                                  | 5   | 1  | 500                | ...                    | ...                                | 19         |
| IRAS 22134-coreD  | 2600      | ...                                 | 14300              | 15                    | 0.7                                  | 10  | 2.5  | 400                | ...                    | ...                                | 19         |
| IRAS 22134-coreE  | 2600      | ...                                 | 14300              | 22                    | 0.9                                  | 4   | 2  | 200                | ...                    | ...                                | 19         |
| IRAS 22134-coreF  | 2600      | ...                                 | 14300              | 28                    | 1.4                                  | 2   | 2.5  | 80                 | ...                    | ...                                | 19         |
| IRAS 22134-coreG  | 2600      | ...                                 | 14300              | 24                    | 1.0                                  | 7   | 6  | 120                | ...                    | ...                                | 19         |
| IRAS 22134-coreH  | 2600      | ...                                 | 14300              | 20                    | 0.7                                  | 2   | 1.5  | 130                | ...                    | ...                                | 19         |
| IRAS 22134-coreI  | 2600      | ...                                 | 14300              | 19                    | 1.3                                  | 7   | 3.5  | 200                | ...                    | ...                                | 19         |
| IRAS 22134-coreJ  | 2600      | ...                                 | 14300              | 17                    | 0.5                                  | 4   | 8  | 50                 | ...                    | ...                                | 19         |
| IRAS 00117-MM1W   | 1800      | ...                                 | 8800               | 17                    | 1.0                                  | 10  | 3.5  | 286                | ...                    | ...                                | 19         |
| IRAS 00117-MM2W   | 1800      | ...                                 | 8800               | 12                    | 1.4                                  | 15  | 2.5  | 600                | ...                    | ...                                | 19         |
| AFGL 5142-WC      | 1800      | ...                                 | 7200               | 25                    | 1.3                                  | 18  | 18   | 100                | ...                    | ...                                | 19         |
| AFGL 5142-EC      | 1800      | ...                                 | 7200               | 25                    | 1.6                                  | 14  | 11   | 130                | ...                    | ...                                | 19         |
| IRAS 20126-coreA  | 1700      | ...                                 | 12900              | 16                    | 0.9                                  | 36  | 8  | 450                | ...                    | ...                                | 19         |
| IRAS20126-coreB   | 1700      | ...                                 | 12900              | 18                    | 1.5                                  | 30  | 6  | 500                | ...                    | ...                                | 19         |
| G14.2–0.60-S10-E  | 2300      | ...                                 | 133400             | 17                    | 3.3                                  | 11  | 2.3  | 617                | ...                    | ...                                | 19         |
| G14.2–0.60-W12-S  | 2300      | ...                                 | 133400             | 19                    | 2.1                                  | 7.8   | 1.6  | 479                | ...                    | ...                                | 19         |

### Protostellar cores

|                     |      |     |       |    |      |     |      |     |     |                      |          |
|---------------------|------|-----|-------|----|------|-----|------|-----|-----|----------------------|----------|
| L 723-VLA 2         | 300  | 3.4 | 3600  | 25 | 0.7  | 6.9 | 16.3 | 43  | 0.2 | Class 0              | 8, 9, 10 |
| IRAS 20293-NWS      | 2000 | ... | 18000 | 34 | 2.0  | 18  | 21.1 | 56  | 0.7 | Class 0 <sup>c</sup> | 6        |
| IRAS 20293-SWS      | 2000 | ... | 18000 | 22 | 0.94 | 13  | 8.7  | 150 | ... | Class 0 <sup>c</sup> | 6        |
| IRAS 00117-MM2      | 1800 | 600 | 8800  | 15 | 1.3  | 7   | 3    | 230 | 1.7 | Class 0              | 18, 19   |
| B335                | 250  | 3   | 13500 | 10 | 0.39 | 7.9 | 6    | 132 | 2.0 | Class 0              | 24, 25   |
| L1527               | 140  | 1.3 | 7500  | 11 | 0.29 | 5   | 8    | 63  | 2.4 | Class 0              | 24, 25   |
| Orion B9-IRAS 05405 | 450  | 6.4 | 18000 | 11 | 0.32 | 10  | 10   | 100 | 2.8 | Class 0              | 14, 15   |

Continued on Next Page...

Table 6.2 – Continued

| Name                | d<br>(pc) | $L_{\text{bol}}$<br>( $L_{\odot}$ ) | Spat. res.<br>(AU) | $T_{\text{k}}$<br>(K) | $\Delta v$<br>(km s $^{-1}$ ) | $N(\text{NH}_3)$<br>( $10^{14}$ cm $^{-2}$ ) | $N(\text{N}_2\text{H}^+)$<br>( $10^{12}$ cm $^{-2}$ ) | Ratio <sup>a</sup> | $M$<br>( $M_{\odot}$ ) | Evolutionary<br>Stage <sup>b</sup> | References |
|---------------------|-----------|-------------------------------------|--------------------|-----------------------|-------------------------------|--|---|--------------------|------------------------|------------------------------------|------------|
| IRAS 23238-L 1262   | 180       | 2.4                                 | 7200               | 11                    | 0.46                          | 9  | 19  | 60                 | 3.1                    | Class 0                            | 1, 3       |
| IRAS 05345-C1a      | 1800      | ...                                 | 6100               | 21                    | 1.2                           | 6.1  | 16.4  | 37                 | 3.6                    | Class 0                            | 21, 22, 23 |
| IRAS 05399-SMM3     | 450       | 3.5                                 | 18000              | 11                    | 0.38                          | 5.6  | 6.0   | 99                 | 7.8                    | Class 0                            | 14, 15     |
| L1082C              | 440       | 0.6                                 | 23800              | 9                     | 0.42                          | 1.3  | 3.8   | 331                | 24                     | Class 0                            | 24, 25     |
| L158                | 160       | 0.4                                 | 8600               | 12                    | 0.23                          | 4.0  | 2.7   | 147                | 33                     | Class 0                            | 24, 25     |
| IRAS 20293-mm3      | 2000      | ...                                 | 18000              | 21                    | 1.23                          | 6.6  | 11.6  | 57                 | 1.0                    | Class 0/I <sup>c</sup>             | 6, 17      |
| IRAS 20293 -mm2     | 2000      | ...                                 | 14000              | 26                    | 1.10                          | 8.8  | 19.1  | 46                 | 1.3                    | Class 0/I <sup>c</sup>             | 6, 17      |
| Orion B9-IRAS 05399 | 450       | 21                                  | 18000              | 14                    | 0.59                          | 3.2  | 20  | 16                 | 6.1                    | Class 0/I                          | 14, 15     |
| IRAS 20293-mm1      | 2000      | ...                                 | 14000              | 27                    | 1.37                          | 11   | 29.7  | 37                 | 6.3                    | Class 0/I <sup>c</sup>             | 6, 17      |
| IRAS 04248-B217     | 140       | 0.4                                 | 5600               | 11                    | 0.4                           | 4.5  | 5   | 90                 | 0.3                    | Class I                            | 1, 2, 11   |
| Oph B2              | 120       | ...                                 | 2200               | 15                    | 0.68                          | 3.8  | 5.9   | 65                 | 0.6                    | Class I                            | 4, 5, 16   |
| L1524               | 140       | 7                                   | 7500               | 9                     | 0.26                          | 10   | 10  | 100                | 1.2                    | Class I                            | 24, 25     |
| IRAS 20293-IRS 5    | 2000      | ...                                 | 14000              | 27                    | 1.5                           | 5.9  | 14  | 42                 | 1.2                    | Class I <sup>c</sup>               | 6          |
| L1489               | 140       | 2.9                                 | 7500               | 10                    | 0.28                          | 10   | 13  | 77                 | 1.6                    | Class I                            | 24, 25     |
| IRAS 00117-MM1      | 1800      | 560                                 | 8800               | 16                    | 1.5                           | 5  | 5   | 100                | 3.0                    | Class I                            | 18, 19     |
| L1172A              | 440       | 0.9                                 | 23800              | 14                    | 0.54                          | 5  | 10  | 50                 | 8.2                    | Class I                            | 24, 25     |
| L1152               | 440       | 1.4                                 | 23800              | 10                    | 0.46                          | 7.9  | 4.2   | 188                | 12                     | Class I                            | 24, 25     |
| L1534               | 140       | 1.9                                 | 7500               | 8                     | 0.36                          | 10   | 4.6   | 217                | 13                     | Class I                            | 24, 25     |
| L260                | 160       | 0.7                                 | 8600               | 9                     | 0.20                          | 16   | 2.2   | 727                | 21                     | Class I                            | 24, 25     |
| L43                 | 160       | 11.4                                | 8600               | 12                    | 0.36                          | 6.3  | 11  | 57                 | ...                    | Class I                            | 24, 25     |
| L778                | 420       | 2.1                                 | 22700              | 11                    | 0.44                          | 6.3  | 7   | 90                 | 39                     | Class I                            | 24, 25     |
| B361                | 350       | 4.7                                 | 18900              | 10                    | 0.70                          | 5  | 9   | 56                 | 49                     | Class I                            | 24, 25     |
| L1082A              | 440       | 2.3                                 | 23800              | 10                    | 0.35                          | 7.9  | 1.9   | 416                | 160                    | Class I                            | 24, 25     |
| G14.2-0.60-S10-W    | 2300      | ...                                 | 133400             | 12                    | 2.2                           | 12.9   | 2.2   | 592                | ...                    | IRDC                               | 19         |
| G14.2-0.60-W9       | 2300      | ...                                 | 133400             | 15                    | 1.1                           | 6.6  | 1.2   | 531                | 52                     | IRDC                               | 19         |
| G14.2-0.60-W25      | 2300      | ...                                 | 133400             | 18                    | 1.7                           | 5.2  | 1.2   | 425                | 213                    | IRDC                               | 19         |
| L1031B              | 900       | 95                                  | 48600              | 13                    | 1.6                           | 3.9  | 7   | 56                 | 760                    | Class I                            | 24, 25     |
| G14.2-0.60-W12      | 2300      | ...                                 | 133400             | 21                    | 2.2                           | 8.3  | 1.8   | 455                | 778                    | IRDC                               | 19         |
| G14.2-0.60-S10      | 2300      | 3900                                | 133400             | 21                    | 2.0                           | 14.4   | 2.3   | 616                | 1077                   | IRDC                               | 19         |
| IRAS 05345-C1b      | 1800      | 1380                                | 6200               | 22                    | 1.2                           | 4.6  | 16.4  | 28                 | 5.2                    | HMC, early-B                       | 21, 22, 23 |
| AFGL 5142-CC        | 1800      | 4000                                | 7200               | 70                    | 6.4                           | 26   | 2.5   | 1000               | 6                      | HMC, B2                            | 19, 20     |
| IRAS 20126-core     | 1700      | 13000                               | 12900              | 24                    | 2.5                           | 20   | 6   | 330                | 18                     | HMC, B0.2                          | 19         |

Continued on Next Page...

Table 6.2 – Continued

| Name            | d<br>(pc) | $L_{\text{bol}}$<br>( $L_{\odot}$ ) | Spat. res.<br>(AU) | $T_{\text{k}}$<br>(K) | $\Delta v$<br>( $\text{km s}^{-1}$ ) | $N(\text{NH}_3)$<br>( $10^{14} \text{ cm}^{-2}$ ) | $N(\text{N}_2\text{H}^+)$<br>( $10^{12} \text{ cm}^{-2}$ ) | Ratio <sup>a</sup> | $M$<br>( $M_{\odot}$ ) | Evolutionary<br>Stage <sup>b</sup> | References |
|-----------------|-----------|-------------------------------------|--------------------|-----------------------|--------------------------------------|---|--|--------------------|------------------------|------------------------------------|------------|
| IRAS 20293+3952 | 2000      | 6300                                | 14000              | 48                    | 2.4                                  | 1.4   | 2.5  | 57                 | ...                    | UCH II, B1                         | 6          |

<sup>a</sup>Ratio of  $N(\text{NH}_3)$  over  $N(\text{N}_2\text{H}^+)$

<sup>b</sup>IRDC stands for infrared dark cloud; HMC stands for hot molecular core; UCH II: Ultra-compact H II region. Spectral type estimated from centimeter wavelength emission.

<sup>c</sup>Tentative evolutionary stage.

**References.** [1] Hotzel et al. 2004; [2] Hotzel et al. 2001; [3] Launhardt et al. 2010; [4] Friesen et al. 2009; [5] Friesen et al. 2010; [6] Palau et al. 2007; [7] this work; [8] Girart et al. 1997; [9] Masqué 2005; [10] Girart et al. 2009; [11] Motte and André 2001; [12] Motte et al. 1998; [13] Johnstone et al. 2000; [14] Miettinen et al. 2009; [15] Miettinen et al. 2010; [16] Jørgensen et al. 2008; [17] Beuther et al. 2002a; [18] Palau et al. 2010; [19] this work; [20] Zhang et al. 2007; [21] Fontani et al. 2008; [22] Fontani et al. 2009; [23] Fontani et al. in prep.; [24] Benson and Myers 1989; [25] Caselli et al. 2002a

## 6.2 Open questions

In this section, we suggest a few points to take into account for further work aimed at studying column densities ratios as a “chemical clocks” in star-forming regions.

1. Using both interferometers and single-dish telescopes in order to have an accurate picture of the gas content at all spatial scales and assuring spatial resolution down to 5000 AU to separate the contribution of each dense core.
2. Using not only the  $\text{NH}_3/\text{N}_2\text{H}^+$  column density ratio. Here we suggest some column density ratios that can be a good complementary tool to trace the chemical evolution of dense cores. Initially, during the pre-protostellar phase, but before the effects of freeze-out start to be evident the ratio of an early-time molecule over a late-time one, like  $\text{C}^{18}\text{O}/\text{N}_2\text{H}^+$ ,  $\text{CS}/\text{NH}_3$ , and/or  $\text{CS}/\text{N}_2\text{H}^+$ , should be very suitable to trace the very young phases of pre-protostellar cores. Then, once the effects of freeze-out become important, both the  $\text{NH}_3/\text{N}_2\text{H}^+$  and the deuterium fractionation would trace better the evolution before the onset of star formation. After this stage, during the protostellar phase we can use the deuterium fractionation and the  $\text{NH}_3/\text{N}_2\text{H}^+$  ratio too, and as a complementary tool the ratio of S-bearing species, which seems to be well suited to trace the evolution of the hot molecular core phase.
3. Observing molecular outflows and looking for a relation between outflow direction, morphology of the dense gas, and the  $\text{NH}_3/\text{N}_2\text{H}^+$  ratio.

## 6.3 Conclusions

We have extended to high-mass star-forming regions the comparison between the emission of  $\text{NH}_3$  and  $\text{N}_2\text{H}^+$  molecules started by Palau et al. (2007) and previously studied mainly for low-mass star-forming regions. We first performed single-dish observations of the dust emission and dense gas tracers ( $\text{NH}_3$  and  $\text{N}_2\text{H}^+$ ) toward the Infrared Dark Cloud G14.2–0.60 to characterize the physical and chemical properties during the earliest phases of massive star formation, together with high angular resolution  $\text{NH}_3$  data to study the structure and kinematics of the cloud. Moreover, we performed high angular resolution observations with the SMA towards a selected

clump of the cloud to study the initial stages that lead to the formation of massive stars and star clusters and the process of fragmentation. Additionally, we carried out high angular resolution observations of  $\text{NH}_3$  and  $\text{N}_2\text{H}^+$  toward four regions of massive star formation, and complemented the study of column density ratios as good “chemical clocks” by computing the deuterium fractionation in another high-mass star-forming region.

- In the Infrared Dark Cloud G14.2–0.60 we found a very good agreement between the dust and  $\text{NH}_3$  emission, both showing a very clumpy and filamentary structures. These structures appear to be hierarchical from scales of 1 pc to 0.02 pc, so the fragmentation of the cloud takes place at different spatial resolutions. More specifically, we find that a particular clump of G14.2–0.60 is fragmented into 16 millimeter condensations when observed at high angular resolution (0.017 pc), with masses larger than the expected from current theoretical models of massive star formation, suggesting that turbulence and/or magnetic fields could be important.
- In G14.2–0.60 the  $\text{NH}_3/\text{N}_2\text{H}^+$  ratio presents very high values probably due to the poor spatial resolution. We found hints of a possible trend of the  $\text{NH}_3/\text{N}_2\text{H}^+$  ratio with the evolutionary stage, being higher in pre-protostellar clumps than in protostellar clumps. However, we should perform further interferometric observations of the  $\text{N}_2\text{H}^+$  molecule to understand the behavior of the  $\text{NH}_3/\text{N}_2\text{H}^+$  ratio in IRDCs at core scales.
- We studied with interferometers the  $\text{NH}_3/\text{N}_2\text{H}^+$  ratio of four massive star-forming regions. In IRAS00117+6412 the ratio is high in the dense core associated with the youngest object and low for a more evolved, Class 0/I, YSO. In IRAS 22134+5834, an UCH II region with high luminosity, we found important effects of the UV radiation on the dense gas. In this case, although all dense cores appear to be in the pre-protostellar phase, the  $\text{NH}_3/\text{N}_2\text{H}^+$  ratio is relatively low in cores closer to the UCH II region. On the other hand, in IRAS 20126+4104 we found high values of the  $\text{NH}_3/\text{N}_2\text{H}^+$  ratio due to the high temperature reached in the hot molecular core.
- For the massive protostellar cluster AFG 5142 we applied the chemical model UCL\_CHEM and we find that the high  $\text{NH}_3/\text{N}_2\text{H}^+$  ratio are due to the high temperature reached in hot molecular cores. Under these conditions, CO is desorbed from grain mantles, which produces a substantial destruction of the

$\text{N}_2\text{H}^+$  molecule. Thus, in addition to core evolution, the physical properties of the core, like density and in particular the temperature are key parameters in determining the  $\text{NH}_3/\text{N}_2\text{H}^+$  ratio.

- We compiled a list of regions for which the  $\text{NH}_3/\text{N}_2\text{H}^+$  ratio has been estimated. From the list, which includes the regions studied in this work and regions in the literature, we find that the median value of the  $\text{NH}_3/\text{N}_2\text{H}^+$  ratio is higher in pre-protostellar cores than in protostellar cores. What is more, we found an evolutionary sequence of the  $\text{NH}_3/\text{N}_2\text{H}^+$  ratio in both the pre-protostellar and protostellar phase. Initially, there is a golden period of  $\text{NH}_3$  and the  $\text{NH}_3/\text{N}_2\text{H}^+$  ratio is high in young pre-protostellar cores and then it decreases as the core approaches the onset of gravitational collapse. During the protostellar phase, just after the protostar is born, the  $\text{NH}_3/\text{N}_2\text{H}^+$  ratio seems to decrease because there is a golden period of the  $\text{N}_2\text{H}^+$  abundance. At some point, when the temperature is high enough and the effects of molecular outflows are important, the  $\text{NH}_3/\text{N}_2\text{H}^+$  ratio increases considerably.
- In IRAS 20293+3952 the deuterium fractionation,  $D_{\text{frac}} = N(\text{NH}_2\text{D})/N(\text{NH}_3)$ , seems to increase during the pre-protostellar phase until the onset of star formation, although molecular outflows interaction and UV radiations could also play an important role. In addition, both  $\text{NH}_3/\text{N}_2\text{H}^+$  and  $\text{NH}_2\text{D}/\text{NH}_3$  ratios seem to be related with the evolutionary stage of the dense gas, indicating that both ratios are good “chemical clocks” before the onset of gravitational collapse.
- As a result of the present work, we suggest that future observations of dense gas tracers in other massive star-forming regions must be carried out using, in addition to  $\text{NH}_3$  and  $\text{N}_2\text{H}^+$ , deuterated species and also early-time molecules like  $\text{C}^{18}\text{O}$  and  $\text{CS}$  as a complementary ingredient to trace the chemical evolution of the dense gas in the youngest pre-protostellar cores, while the ratio of S-bearing species could be well suitable during the hot molecular core phase.

# Bibliography

- Aikawa, Y., Ohashi, N., and Herbst, E. (2003). Molecular Evolution in Collapsing Prestellar Cores. II. The Effect of Grain-Surface Reactions. *The Astrophysical Journal*, 593:906–924.
- Aikawa, Y., Ohashi, N., Inutsuka, S., Herbst, E., and Takakuwa, S. (2001). Molecular Evolution in Collapsing Prestellar Cores. *The Astrophysical Journal*, 552:639–653.
- Alonso-Albi, T., Fuente, A., Crimier, N., Caselli, P., Ceccarelli, C., Johnstone, D., Planesas, P., Rizzo, J. R., Wyrowski, F., Tafalla, M., Lefloch, B., Maret, S., and Dominik, C. (2010). Chemical study of intermediate-mass (IM) Class 0 protostars. CO depletion and  $\text{N}_2\text{H}^+$  deuteration. *Astronomy and Astrophysics*, 518:A52+.
- André, P., Men'shchikov, A., Bontemps, S., Könyves, V., Motte, F., Schneider, N., Didelon, P., Minier, V., Saraceno, P., Ward-Thompson, D., di Francesco, J., White, G., Molinari, S., Testi, L., Abergel, A., Griffin, M., Henning, T., Royer, P., Merín, B., Vavrek, R., Attard, M., Arzoumanian, D., Wilson, C. D., Ade, P., Aussel, H., Baluteau, J., Benedettini, M., Bernard, J., Blommaert, J. A. D. L., Cambrésy, L., Cox, P., di Giorgio, A., Hargrave, P., Hennemann, M., Huang, M., Kirk, J., Krause, O., Launhardt, R., Leeks, S., Le Penec, J., Li, J. Z., Martin, P. G., Maury, A., Olofsson, G., Omont, A., Peretto, N., Pezzuto, S., Prusti, T., Roussel, H., Russeil, D., Sauvage, M., Sibthorpe, B., Sicilia-Aguilar, A., Spinoglio, L., Waelkens, C., Woodcraft, A., and Zavagno, A. (2010). From filamentary clouds to prestellar cores to the stellar IMF: Initial highlights from the Herschel Gould Belt Survey. *Astronomy and Astrophysics*, 518:L102+.
- André, P., Ward-Thompson, D., and Barsony, M. (1993). Submillimeter continuum observations of Rho Ophiuchi A - The candidate protostar VLA 1623 and prestellar clumps. *The Astrophysical Journal*, 406:122–141.

- Anglada, G., Estalella, R., Mauersberger, R., Torrelles, J. M., Rodriguez, L. F., Canto, J., Ho, P. T. P., and D'Alessio, P. (1995). The molecular environment of the HH 34 system. *The Astrophysical Journal*, 443:682–697.
- Anglada, G., Estalella, R., Pastor, J., Rodriguez, L. F., and Haschick, A. D. (1996). A CS and NH<sub>3</sub> Survey of Regions with H<sub>2</sub>O Maser Emission. *The Astrophysical Journal*, 463:205–+.
- Bachiller, R., Pérez Gutiérrez, M., Kumar, M. S. N., and Tafalla, M. (2001). Chemically active outflow L 1157. *Astronomy and Astrophysics*, 372:899–912.
- Bacmann, A., Lefloch, B., Ceccarelli, C., Steinacker, J., Castets, A., and Loinard, L. (2003). CO Depletion and Deuterium Fractionation in Prestellar Cores. *The Astrophysical Journal, Letters*, 585:L55–L58.
- Belloche, A. and André, P. (2004). Disappearance of N<sub>2</sub>H<sup>+</sup> from the gas phase in the class 0 protostar IRAM 04191. *Astronomy and Astrophysics*, 419:L35–L38.
- Beltrán, M. T., Brand, J., Cesaroni, R., Fontani, F., Pezzuto, S., Testi, L., and Molinari, S. (2006). Search for massive protostar candidates in the southern hemisphere. II. Dust continuum emission. *Astronomy and Astrophysics*, 447:221–233.
- Benson, P. J. and Myers, P. C. (1989). A survey for dense cores in dark clouds. *The Astrophysical Journal Supplement Series*, 71:89–108.
- Bergin, E. A. and Langer, W. D. (1997). Chemical Evolution in Preprotostellar and Protostellar Cores. *The Astrophysical Journal*, 486:316–+.
- Beuther, H. and Henning, T. (2009). Multiple low-turbulence starless cores associated with intermediate- to high-mass star formation. *Astronomy and Astrophysics*, 503:859–867.
- Beuther, H. and Schilke, P. (2004). Fragmentation in Massive Star Formation. *Science*, 303:1167–1169.
- Beuther, H., Schilke, P., and Gueth, F. (2004a). Massive Molecular Outflows at High Spatial Resolution. *The Astrophysical Journal*.
- Beuther, H., Schilke, P., Menten, K. M., Motte, F., Sridharan, T. K., and Wyrowski, F. (2002a). High-Mass Protostellar Candidates. II. Density Structure from Dust Continuum and CS Emission. *The Astrophysical Journal*.

- Beuther, H., Schilke, P., Sridharan, T. K., Menten, K. M., Walmsley, C. M., and Wyrowski, F. (2002b). Massive molecular outflows. *Astronomy and Astrophysics*.
- Beuther, H., Schilke, P., and Wyrowski, F. (2004b). High Spatial Resolution CN and CS Observation of Two Regions of Massive Star Formation. *The Astrophysical Journal*.
- Beuther, H., Sridharan, T. K., and Saito, M. (2005). Caught in the Act: The Onset of Massive Star Formation. *The Astrophysical Journal, Letters*, 634:L185–L188.
- Bisschop, S. E., Fraser, H. J., Öberg, K. I., van Dishoeck, E. F., and Schlemmer, S. (2006). Desorption rates and sticking coefficients for CO and N<sub>2</sub> interstellar ices. *Astronomy and Astrophysics*, 449:1297–1309.
- Boger, G. I. and Sternberg, A. (2005). CN and HCN in Dense Interstellar Clouds. *The Astrophysical Journal*, 632:302–315.
- Bonnell, I. A. and Bate, M. R. (2002). Accretion in stellar clusters and the collisional formation of massive stars. *Monthly Notices of the Royal Astronomical Society*, 336:659–669.
- Bonnell, I. A., Vine, S. G., and Bate, M. R. (2004). Massive star formation: nurture, not nature. *Monthly Notices of the Royal Astronomical Society*, 349:735–741.
- Bottinelli, S., Ceccarelli, C., Williams, J. P., and Lefloch, B. (2007). Hot corinos in NGC 1333-IRAS4B and IRAS2A. *Astronomy and Astrophysics*, 463:601–610.
- Briggs, D. (1995). *High Fidelity Deconvolution of Moderately Resolved Sources*. PhD thesis, New Mexico Inst. of Mining and Technology.
- Bronfman, L., Nyman, L., and May, J. (1996). A CS (2-1) survey of IRAS point sources with color characteristics of ultra-compact HII regions. *Astronomy and Astrophysics Supplement Series*, 115:81–+.
- Busquet, G., Estalella, R., Zhang, Q., Viti, S., Palau, A., Ho, P. T. P., and Sanchez-Monge, A. (2010a). N<sub>2</sub>H<sup>+</sup> depletion in the massive protostellar cluster AFGL 5142. *ArXiv e-prints*.
- Busquet, G., Palau, A., Estalella, R., Girart, J. M., Anglada, G., and Sepúlveda, I. (2009). Low-mass protostars and dense cores in different evolutionary stages in IRAS 00213+6530. *Astronomy and Astrophysics*, 506:1183–1198.

- Busquet, G., Palau, A., Estalella, R., Girart, J. M., Sánchez-Monge, Á., Viti, S., Ho, P. T. P., and Zhang, Q. (2010b). The  $\text{NH}_2\text{D}/\text{NH}_3$  ratio toward pre-protostellar cores around the UC H II region in IRAS 20293+3952. *Astronomy and Astrophysics*.
- Carey, S. J., Clark, F. O., Egan, M. P., Price, S. D., Shipman, R. F., and Kuchar, T. A. (1998). The Physical Properties of the Midcourse Space Experiment Galactic Infrared-dark Clouds. *The Astrophysical Journal*, 508:721–728.
- Carpenter, J. M., Snell, R. L., and Schloerb, F. P. (1990). Molecular clouds associated with luminous far-infrared sources in the outer Galaxy. *The Astrophysical Journal*, 362:147–164.
- Caselli, P., Benson, P. J., Myers, P. C., and Tafalla, M. (2002a). Dense Cores in Dark Clouds. XIV.  $\text{N}_2\text{H}^+$  (1-0) Maps of Dense Cloud Cores. *The Astrophysical Journal*, 572:238–263.
- Caselli, P., Myers, P. C., and Thaddeus, P. (1995). Radio-astronomical Spectroscopy of the Hyperfine Structure of  $\text{N}_2\text{H}^+$ . *The Astrophysical Journal, Letters*, 455:L77+.
- Caselli, P., van der Tak, F. F. S., Ceccarelli, C., and Bacmann, A. (2003). Abundant  $\text{H}_2\text{D}^+$  in the pre-stellar core L1544. *Astronomy and Astrophysics*, 403:L37–L41.
- Caselli, P., Walmsley, C. M., Zucconi, A., Tafalla, M., Dore, L., and Myers, P. C. (2002b). Molecular Ions in L1544. II. The Ionization Degree. *The Astrophysical Journal*, 565:344–358.
- Ceccarelli, C., Castets, A., Loinard, L., Caux, E., and Tielens, A. G. G. M. (1998). Detection of doubly deuterated formaldehyde towards the low-luminosity protostar IRAS 16293-2422. *Astronomy and Astrophysics*, 338:L43–L46.
- Cesaroni, R. (2005). Hot molecular cores. In R. Cesaroni, M. Felli, E. Churchwell, & M. Walmsley, editor, *Massive Star Birth: A Crossroads of Astrophysics*, volume 227 of *IAU Symposium*, pages 59–69.
- Cesaroni, R., Felli, M., Jenness, T., Neri, R., Olmi, L., Robberto, M., Testi, L., and Walmsley, C. M. (1999a). Unveiling the disk-jet system in the massive (proto)star IRAS 20126+4104. *Astronomy and Astrophysics*, 345:949–964.
- Cesaroni, R., Felli, M., Testi, L., Walmsley, C. M., and Olmi, L. (1997). The disk-outflow system around the high-mass (proto)star IRAS 20126+4104. *Astronomy and Astrophysics*, 325:725–744.

- Cesaroni, R., Felli, M., and Walmsley, C. M. (1999b). High density molecular clumps around protostellar candidates. *Astronomy and Astrophysics Supplement Series*, 136:333–361.
- Cesaroni, R., Neri, R., Olmi, L., Testi, L., Walmsley, C. M., and Hofner, P. (2005). A study of the Keplerian accretion disk and precessing outflow in the massive protostar IRAS 20126+4104. *Astronomy and Astrophysics*.
- Cesaroni, R., Palagi, F., Felli, M., Catarzi, M., Comoretto, G., di Francos, Giovannardi, C., and Palla, F. (1988). A catalogue of H<sub>2</sub>O maser sources north of delta = - 30 deg. *Astronomy and Astrophysics Supplement Series*, 76:445–458.
- Charnley, S. B. (1997). Sulfuretted Molecules in Hot Cores. *The Astrophysical Journal*, 481:396–+.
- Chen, H., Liu, S., Su, Y., and Zhang, Q. (2010). Deuterium Fractionation as an Evolutionary Probe in the Infrared Dark Cloud G28.34+0.06. *The Astrophysical Journal, Letters*, 713:L50–L54.
- Chen, X., Launhardt, R., Bourke, T. L., Henning, T., and Barnes, P. J. (2008). ATCA and Spitzer Observations of the Binary Protostellar Systems CG 30 and BHR 71. *The Astrophysical Journal*, 683:862–875.
- Chen, Y., Yao, Y., Yang, J., Zeng, Q., and Sato, S. (2005). Near-Infrared Imaging of the Star Formation Region AFGL 5142. *The Astrophysical Journal*, 629:288–298.
- Chini, R., Ward-Thompson, D., Kirk, J. M., Nielbock, M., Reipurth, B., and Sievers, A. (2001). Mm/Submm images of Herbig-Haro energy sources and candidate protostars. *Astronomy and Astrophysics*, 369:155–169.
- Codella, C., Lefloch, B., Ceccarelli, C., Cernicharo, J., Caux, E., Lorenzani, A., Viti, S., Hily-Blant, P., Parise, B., Maret, S., Nisini, B., Caselli, P., Cabrit, S., Pagani, L., Benedettini, M., Boogert, A., Gueth, F., Melnick, G., Neufeld, D., Pacheco, S., Salez, M., Schuster, K., Bacmann, A., Baudry, A., Bell, T., Bergin, E. A., Blake, G., Bottinelli, S., Castets, A., Comito, C., Coutens, A., Crimier, N., Dominik, C., Demyk, K., Encrenaz, P., Falgarone, E., Fuente, A., Gerin, M., Goldsmith, P., Helmich, F., Hennebelle, P., Henning, T., Herbst, E., Jacq, T., Kahane, C., Kama, M., Klotz, A., Langer, W., Lis, D., Lord, S., Pearson, J., Phillips, T., Saraceno, P., Schilke, P., Tielens, X., van der Tak, F., van der Wiel, M., Vastel, C., Wakelam, V., Walters, A., Wyrowski, F., Yorke, H., Borys, C., Delorme, Y., Kramer, C.,

- Larsson, B., Mehdi, I., Ossenkopf, V., and Stutzki, J. (2010). The CHESSE spectral survey of star forming regions: Peering into the protostellar shock L1157-B1. I. Shock chemical complexity. *Astronomy and Astrophysics*, 518:L112+.
- Collings, M. P., Anderson, M. A., Chen, R., Dever, J. W., Viti, S., Williams, D. A., and McCoustra, M. R. S. (2004). A laboratory survey of the thermal desorption of astrophysically relevant molecules. *Monthly Notices of the Royal Astronomical Society*, 354:1133–1140.
- Collings, M. P., Dever, J. W., Fraser, H. J., and McCoustra, M. R. S. (2003a). Laboratory studies of the interaction of carbon monoxide with water ice. *Astrophysics and Space Science*, 285:633–659.
- Collings, M. P., Dever, J. W., Fraser, H. J., McCoustra, M. R. S., and Williams, D. A. (2003b). Carbon Monoxide Entrapment in Interstellar Ice Analogs. *The Astrophysical Journal*, 583:1058–1062.
- Comito, C., Schilke, P., Phillips, T. G., Lis, D. C., Motte, F., and Mehringer, D. (2005). A Molecular Line Survey of Orion KL in the 350 Micron Band. *The Astrophysical Journal Supplement Series*, 156:127–167.
- Comoretto, G., Palagi, F., Cesaroni, R., Felli, M., Bettarini, A., Catarzi, M., Curioni, G. P., Curioni, P., di Franco, S., Giovanardi, C., Massi, M., Palla, F., Panella, D., Rossi, E., Speroni, N., and Tofani, G. (1990). The Arcetri atlas of H<sub>2</sub>O maser sources. *Astronomy and Astrophysics Supplement Series*, 84:179–225.
- Connelley, M. S., Reipurth, B., and Tokunaga, A. T. (2007). Infrared Nebulae around Young Stellar Objects. *The Astronomical Journal*, 133:1528–1559.
- Crapsi, A., Caselli, P., Walmsley, C. M., Myers, P. C., Tafalla, M., Lee, C. W., and Bourke, T. L. (2005). Probing the Evolutionary Status of Starless Cores through N<sub>2</sub>H<sup>+</sup> and N<sub>2</sub>D<sup>+</sup> Observations. *The Astrophysical Journal*, 619:379–406.
- Crapsi, A., Caselli, P., Walmsley, M. C., and Tafalla, M. (2007). Observing the gas temperature drop in the high-density nucleus of L 1544. *Astronomy and Astrophysics*, 470:221–230.
- Daniel, F., Cernicharo, J., and Dubernet, M. (2006). The Excitation of N<sub>2</sub>H<sup>+</sup> in Interstellar Molecular Clouds. I. Models. *The Astrophysical Journal*, 648:461–471.
- Di Francesco, J., André, P., and Myers, P. C. (2004). Quiescent Dense Gas in Protostellar Clusters: The Ophiuchus A Core. *The Astrophysical Journal*, 617:425–438.

- Dobashi, K., Nozawa, S., Hayashi, Y., Sato, F., and Fukui, Y. (1994). A molecular cloud and a CO outflow associated with IRAS 22134+5834. *The Astronomical Journal*, 107:2148–2152.
- Dobashi, K. and Uehara, H. (2001). A CO Outflow and a Molecular Cloud Core Associated with a Young Massive Star IRAS 22134+5834. *Publications of the Astronomical Society of Japan*, 53:799–809.
- Egan, M. P., Shipman, R. F., Price, S. D., Carey, S. J., Clark, F. O., and Cohen, M. (1998). A Population of Cold Cores in the Galactic Plane. *The Astrophysical Journal, Letters*, 494:L199+.
- Eiroa, C., Torrelles, J. M., Miranda, L. F., Anglada, G., and Estalella, R. (1994). Optical nebulosities associated with IRAS sources in dense cloud cores. *Astronomy and Astrophysics Supplement Series*, 108:73–78.
- Emprechtinger, M., Caselli, P., Volgenau, N. H., Stutzki, J., and Wiedner, M. C. (2009). The  $\text{N}_2\text{D}^+/\text{N}_2\text{H}^+$  ratio as an evolutionary tracer of Class 0 protostars. *Astronomy and Astrophysics*, 493:89–105.
- Enoch, M. L., Lee, J., Harvey, P., Dunham, M. M., and Schnee, S. (2010). A Candidate Detection of the First Hydrostatic Core. *The Astrophysical Journal, Letters*, 722:L33–L38.
- Estalella, R., Mauersberger, R., Torrelles, J. M., Anglada, G., Gomez, J. F., Lopez, R., and Muders, D. (1993). The Molecular Cores in the L1287, AFGL 5142, and IRAS 20126+4104 Regions. *The Astrophysical Journal*, 419:698+.
- Evans, N. J., Shirley, Y. L., Mueller, K. E., and Knez, C. (2002). The Formation and Early Evolution of Massive Stars. In P. Crowther, editor, *Hot Star Workshop III: The Earliest Phases of Massive Star Birth*, volume 267 of *Astronomical Society of the Pacific Conference Series*, pages 17+.
- Fallscheer, C., Beuther, H., Zhang, Q., Keto, E., and Sridharan, T. K. (2009). Rotational structure and outflow in the infrared dark cloud 18223-3. *Astronomy and Astrophysics*, 504:127–137.
- Faúndez, S., Bronfman, L., Garay, G., Chini, R., Nyman, L., and May, J. (2004). SIMBA survey of southern high-mass star forming regions. I. Physical parameters of the 1.2 mm/IRAS sources. *Astronomy and Astrophysics*, 426:97–103.

- Flower, D. R., Pineau Des Forêts, G., and Walmsley, C. M. (2006). The abundances of nitrogen-containing molecules during pre-protostellar collapse. *Astronomy and Astrophysics*, 456:215–223.
- Fontani, F., Caselli, P., Bourke, T. L., Cesaroni, R., and Brand, J. (2008). Highly deuterated pre-stellar cores in a high-mass star formation region. *Astronomy and Astrophysics*, 477:L45–L48.
- Fontani, F., Caselli, P., Crapsi, A., Cesaroni, R., Molinari, S., Testi, L., and Brand, J. (2006). Searching for massive pre-stellar cores through observations of  $\text{N}_2\text{H}^+$  and  $\text{N}_2\text{D}^+$ . *Astronomy and Astrophysics*, 460:709–720.
- Fontani, F., Zhang, Q., Caselli, P., and Bourke, T. L. (2009). Linking pre- and proto-stellar objects in the intermediate-/high-mass star forming region IRAS 05345+3157. *Astronomy and Astrophysics*, 499:233–247.
- Friesen, R. K., Di Francesco, J., Shimajiri, Y., and Takakuwa, S. (2010). The Initial Conditions of Clustered Star Formation. II.  $\text{N}_2\text{H}^+$  Observations of the Ophiuchus B Core. *The Astrophysical Journal*, 708:1002–1024.
- Friesen, R. K., Di Francesco, J., Shirley, Y. L., and Myers, P. C. (2009). The Initial Conditions of Clustered Star Formation. I.  $\text{NH}_3$  Observations of Dense Cores in Ophiuchus. *The Astrophysical Journal*, 697:1457–1480.
- Fuente, A., Martin-Pintado, J., Cernicharo, J., and Bachiller, R. (1993). A chemical study of the photodissociation region NGC 7023. *Astronomy and Astrophysics*, 276:473–+.
- Fuente, A., Neri, R., and Caselli, P. (2005a). Detection of a hot core in the intermediate-mass Class 0 protostar NGC 7129-FIRS 2. *Astronomy and Astrophysics*.
- Fuente, A., Rizzo, J. R., Caselli, P., Bachiller, R., and Henkel, C. (2005b). Chemical evolution in the environment of intermediate mass young stellar objects. *Astronomy and Astrophysics*.
- Fuller, G. A., Williams, S. J., and Sridharan, T. K. (2005). The circumstellar environment of high mass protostellar objects. III. Evidence of infall? *Astronomy and Astrophysics*, 442:949–959.

- Fuller, G. A. and Wootten, A. (2000). Small-Scale Structure of the Circumstellar Gas around the Very Young Outflow-Driving Source L483-FIR. *The Astrophysical Journal*, 534:854–869.
- Garay, G. and Lizano, S. (1999). Massive Stars: Their Environment and Formation. *Publications of the Astronomical Society of the Pacific*, 111:1049–1087.
- Girart, J. M., Estalella, R., Anglada, G., Torrelles, J. M., Ho, P. T. P., and Rodriguez, L. F. (1997). The Ammonia Core in L723: Hot Spots at the Center of the Quadrupolar Molecular Outflow. *The Astrophysical Journal*, 489:734–+.
- Girart, J. M., Rao, R., and Estalella, R. (2009). The L723 Low-Mass Star Forming Protostellar System: Resolving a Double Core. *The Astrophysical Journal*, 694:56–68.
- Goddi, C. and Moscadelli, L. (2006). Tracing the base of protostellar wind(s) towards the high-mass star forming region AFGL 5142: VLA continuum and VLBA H<sub>2</sub>O maser observations. *Astronomy and Astrophysics*, 447:577–587.
- Goddi, C., Moscadelli, L., Sanna, A., Cesaroni, R., and Minier, V. (2007). Associations of H<sub>2</sub>O and CH<sub>3</sub>OH masers at milli-arcsec angular resolution in two high-mass YSOs. *Astronomy and Astrophysics*, 461:1027–1035.
- Goldsmith, P. F., Heyer, M., Narayanan, G., Snell, R., Li, D., and Brunt, C. (2008). Large-Scale Structure of the Molecular Gas in Taurus Revealed by High Linear Dynamic Range Spectral Line Mapping. *The Astrophysical Journal*, 680:428–445.
- Goodwin, S. P., Kroupa, P., Goodman, A., and Burkert, A. (2007). The Fragmentation of Cores and the Initial Binary Population. *Protostars and Planets V*, pages 133–147.
- Harju, J., Walmsley, C. M., and Wouterloot, J. G. A. (1993). Ammonia clumps in the Orion and Cepheus clouds. *Astronomy and Astrophysics Supplement Series*, 98:51–75.
- Hatchell, J. (2003). High NH<sub>2</sub>D/NH<sub>3</sub> ratios in protostellar cores. *Astronomy and Astrophysics*, 403:L25–L28.
- Hatchell, J., Thompson, M. A., Millar, T. J., and MacDonald, G. H. (1998). Sulphur chemistry and evolution in hot cores. *Astronomy and Astrophysics*, 338:713–722.

- Herpin, F., Marseille, M., Wakelam, V., Bontemps, S., and Lis, D. C. (2009). S-bearing molecules in massive dense cores. *Astronomy and Astrophysics*, 504:853–867.
- Hildebrand, R. H. (1983). The Determination of Cloud Masses and Dust Characteristics from Submillimetre Thermal Emission. *Quarterly Journal of the Royal Astronomical Society*, 24:267–+.
- Hill, T., Burton, M. G., Minier, V., Thompson, M. A., Walsh, A. J., Hunt-Cunningham, M., and Garay, G. (2005). Millimetre continuum observations of southern massive star formation regions - I. SIMBA observations of cold cores. *Monthly Notices of the Royal Astronomical Society*, 363:405–451.
- Ho, P. T. P. (1977). *Study of the ammonia molecule in the interstellar medium*. PhD thesis, Massachusetts Institute of Technology.
- Ho, P. T. P., Moran, J. M., and Lo, K. Y. (2004). The Submillimeter Array. *The Astrophysical Journal, Letters*, 616:L1–L6.
- Ho, P. T. P. and Townes, C. H. (1983). Interstellar ammonia. *Annual Review of Astronomy and Astrophysics*, 21:239–270.
- Hofner, P., Cesaroni, R., Olmi, L., Rodríguez, L. F., Martí, J., and Araya, E. (2007). Sub-arcsecond resolution radio continuum observations of IRAS 20126+4104. *Astronomy and Astrophysics*, 465:197–205.
- Hofner, P., Cesaroni, R., Rodríguez, L. F., and Martí, J. (1999). A double system of ionized jets in IRAS 20126+4104. *Astronomy and Astrophysics*, 345:L43–L46.
- Hosking, J. G. and Whitworth, A. P. (2004). Fragmentation of magnetized cloud cores. *Monthly Notices of the Royal Astronomical Society*, 347:1001–1010.
- Hotzel, S., Harju, J., Lemke, D., Mattila, K., and Walmsley, C. M. (2001). Dense gas and cold dust in the dark core B217. *Astronomy and Astrophysics*, 372:302–316.
- Hotzel, S., Harju, J., and Walmsley, C. M. (2004). The  $\text{NH}_3/\text{N}_2\text{H}^+$  abundance ratio in dense cores. *Astronomy and Astrophysics*, 415:1065–1072.
- Hunter, T. R., Testi, L., Taylor, G. B., Tofani, G., Felli, M., and Phillips, T. G. (1995). A multiwavelength picture of the AFGL 5142 star-forming region. *Astronomy and Astrophysics*, 302:249–+.

- Hunter, T. R., Testi, L., Zhang, Q., and Sridharan, T. K. (1999). Molecular Jets and H<sub>2</sub>O Masers in the AFGL 5142 Hot Core. *The Astronomical Journal*, 118:477–487.
- Jackson, J. M., Finn, S. C., Chambers, E. T., Rathborne, J. M., and Simon, R. (2010). The ‘Nessie’ Nebula: Cluster Formation in a Filamentary Infrared Dark Cloud. *The Astrophysical Journal, Letters*, 719:L185–L189.
- Jaffe, D. T., Guesten, R., and Downes, D. (1981). New H<sub>2</sub>O masers associated with far-infrared sources. *The Astrophysical Journal*, 250:621–630.
- Jaffe, D. T., Stier, M. T., and Fazio, G. G. (1982). A high resolution far-infrared survey of a section of the galactic plane. I. The nature of the sources. *The Astrophysical Journal*, 252:601–609.
- Jenness, T., Scott, P. F., and Padman, R. (1995). Studies of Embedded Far Infrared Sources in the Vicinity of H<sub>2</sub>O Masers - I. Observations. *Monthly Notices of the Royal Astronomical Society*, 276:1024–+.
- Johnstone, D., Rosolowsky, E., Tafalla, M., and Kirk, H. (2010). Dense Gas Tracers in Perseus: Relating the N<sub>2</sub>H<sup>+</sup>, NH<sub>3</sub>, and Dust Continuum Properties of Pre- and Protostellar Cores. *The Astrophysical Journal*, 711:655–670.
- Johnstone, D., Wilson, C. D., Moriarty-Schieven, G., Joncas, G., Smith, G., Gregersen, E., and Fich, M. (2000). Large-Area Mapping at 850 Microns. II. Analysis of the Clump Distribution in the  $\rho$  Ophiuchi Molecular Cloud. *The Astrophysical Journal*, 545:327–339.
- Jørgensen, J. K. (2004). Imaging chemical differentiation around the low-mass protostar L483-mm. *Astronomy and Astrophysics*, 424:589–601.
- Jørgensen, J. K., Johnstone, D., Kirk, H., Myers, P. C., Allen, L. E., and Shirley, Y. L. (2008). Current Star Formation in the Ophiuchus and Perseus Molecular Clouds: Constraints and Comparisons from Unbiased Submillimeter and Mid-Infrared Surveys. II. *The Astrophysical Journal*, 683:822–843.
- Jørgensen, J. K., Schöier, F. L., and van Dishoeck, E. F. (2004). Molecular inventories and chemical evolution of low-mass protostellar envelopes. *Astronomy and Astrophysics*, 416:603–622.
- Kauffmann, J. and Pillai, T. (2010). How Many Infrared Dark Clouds Can form Massive Stars and Clusters? *The Astrophysical Journal, Letters*, 723:L7–L12.

- Kauffmann, J., Pillai, T., Shetty, R., Myers, P. C., and Goodman, A. A. (2010a). The Mass-Size Relation from Clouds to Cores. I. A New Probe of Structure in Molecular Clouds. *The Astrophysical Journal*.
- Kauffmann, J., Pillai, T., Shetty, R., Myers, P. C., and Goodman, A. A. (2010b). The Mass-size Relation from Clouds to Cores. II. Solar Neighborhood Clouds. *The Astrophysical Journal*.
- Kawamura, J. H., Hunter, T. R., Tong, C., Blundell, R., Zhang, Q., Katz, C. A., Papa, D. C., and Sridharan, T. K. (1999). First Image with the CfA Superconductive HEB Receiver: The Protostellar Outflow from IRAS 20126+4104 in CO (J=7-6). *Publications of the Astronomical Society of the Pacific*, 111:1088–1094.
- Keto, E. and Zhang, Q. (2010). The standard model of star formation applied to massive stars: accretion discs and envelopes in molecular lines. *Monthly Notices of the Royal Astronomical Society*, 406:102–111.
- Kim, K. and Kurtz, S. E. (2006). Occurrence Frequency of CO Outflows in Massive Protostellar Candidates. *The Astrophysical Journal*, 643:978–984.
- Kirk, H., Johnstone, D., and Tafalla, M. (2007). Dynamics of Dense Cores in the Perseus Molecular Cloud. *The Astrophysical Journal*, 668:1042–1063.
- Klessen, R. S. (2001). The Formation of Stellar Clusters: Mass Spectra from Turbulent Molecular Cloud Fragmentation. *The Astrophysical Journal*, 556:837–846.
- Kramer, C., Stutzki, J., Rohrig, R., and Corneliussen, U. (1998). Clump mass spectra of molecular clouds. *Astronomy and Astrophysics*, 329:249–264.
- Krumholz, M. R. (2006). Radiation Feedback and Fragmentation in Massive Protostellar Cores. *The Astrophysical Journal, Letters*, 641:L45–L48.
- Krumholz, M. R., Klein, R. I., and McKee, C. F. (2007). Radiation-Hydrodynamic Simulations of Collapse and Fragmentation in Massive Protostellar Cores. *The Astrophysical Journal*, 656:959–979.
- Krumholz, M. R. and McKee, C. F. (2008). A minimum column density of  $1 \text{ g cm}^{-2}$ s for massive star formation. *Nature*, 451:1082–1084.
- Kumar, M. S. N., Keto, E., and Clerkin, E. (2006). The youngest stellar clusters. Clusters associated with massive protostellar candidates. *Astronomy and Astrophysics*, 449:1033–1041.

- Kumar, M. S. N., Ojha, D. K., and Davis, C. J. (2003). A Ring-shaped Embedded Young Stellar (Proto)Cluster. *The Astrophysical Journal*, 598:1107–1111.
- Kurtz, S., Cesaroni, R., Churchwell, E., Hofner, P., and Walmsley, C. M. (2000). Hot Molecular Cores and the Earliest Phases of High-Mass Star Formation. *Protostars and Planets IV*, pages 299–+.
- Lada, C. J. (1987). Star formation - From OB associations to protostars. In M. Peimbert & J. Jugaku, editor, *Star Forming Regions*, volume 115 of *IAU Symposium*, pages 1–17.
- Launhardt, R., Nutter, D., Ward-Thompson, D., Bourke, T. L., Henning, T., Khanzadyan, T., Schmalzl, M., Wolf, S., and Zylka, R. (2010). Looking Into the Hearts of Bok Globules: Millimeter and Submillimeter Continuum Images of Isolated Star-forming Cores. *The Astrophysical Journal Supplement Series*, 188:139–177.
- Lee, J., Bergin, E. A., and Evans, II, N. J. (2004). Evolution of Chemistry and Molecular Line Profiles during Protostellar Collapse. *The Astrophysical Journal*, 617:360–383.
- Leurini, S., Rolffs, R., Thorwirth, S., Parise, B., Schilke, P., Comito, C., Wyrowski, F., Güsten, R., Bergman, P., Menten, K. M., and Nyman, L. (2006). APEX 1 mm line survey of the Orion Bar. *Astronomy and Astrophysics*, 454:L47–L50.
- Li, D., Goldsmith, P. F., and Menten, K. (2003). Massive Quiescent Cores in Orion. I. Temperature Structure. *The Astrophysical Journal*, 587:262–277.
- Linsky, J. L., Draine, B. T., Moos, H. W., Jenkins, E. B., Wood, B. E., Oliveira, C., Blair, W. P., Friedman, S. D., Gry, C., Knauth, D., Kruk, J. W., Lacour, S., Lehner, N., Redfield, S., Shull, J. M., Sonneborn, G., and Williger, G. M. (2006). What Is the Total Deuterium Abundance in the Local Galactic Disk? *The Astrophysical Journal*, 647:1106–1124.
- Lis, D. C., Roueff, E., Gerin, M., Phillips, T. G., Coudert, L. H., van der Tak, F. F. S., and Schilke, P. (2002). Detection of Triply Deuterated Ammonia in the Barnard 1 Cloud. *The Astrophysical Journal, Letters*, 571:L55–L58.
- López-Sepulcre, A., Cesaroni, R., and Walmsley, C. M. (2010). A comparative study of high-mass cluster forming clumps. *Astronomy and Astrophysics*, 517:A66+.
- Mac Low, M. and Klessen, R. S. (2004). Control of star formation by supersonic turbulence. *Reviews of Modern Physics*, 76:125–194.

- Machida, M. N., Matsumoto, T., Hanawa, T., and Tomisaka, K. (2005). Collapse and fragmentation of rotating magnetized clouds - II. Binary formation and fragmentation of first cores. *Monthly Notices of the Royal Astronomical Society*, 362:382–402.
- Maret, S., Bergin, E. A., and Lada, C. J. (2006). A low fraction of nitrogen in molecular form in a dark cloud. *Nature*, 442:425–427.
- Masqué, J. M. (2005). BIMA 3 mm observations of L723. Master’s thesis, Universitat de Barcelona.
- Matsuyanagi, I., Itoh, Y., Sugitani, K., Oasa, Y., Mukai, T., and Tamura, M. (2006). Sequential Formation of Low-Mass Stars in the BRC 14 Region. *Publications of the Astronomical Society of Japan*, 58:L29–L34.
- Matthews, B. C., Hogerheijde, M. R., Jørgensen, J. K., and Bergin, E. A. (2006). The Rotating Molecular Core and Precessing Outflow of the Young Stellar Object Barnard 1c. *The Astrophysical Journal*, 652:1374–1389.
- McKee, C. F. and Tan, J. C. (2002). Massive star formation in 100,000 years from turbulent and pressurized molecular clouds. *Nature*, 416:59–61.
- McKee, C. F. and Tan, J. C. (2003). The Formation of Massive Stars from Turbulent Cores. *The Astrophysical Journal*, 585:850–871.
- Menten, K. M., Pillai, T., and Wyrowski, F. (2005). Initial conditions for massive star birth-Infrared dark clouds. In R. Cesaroni, M. Felli, E. Churchwell, & M. Walmsley, editor, *Massive Star Birth: A Crossroads of Astrophysics*, volume 227 of *IAU Symposium*, pages 23–34.
- Miettinen, O., Harju, J., Haikala, L. K., and Juvela, M. (2010). Physical properties of dense cores in Orion B9. *ArXiv e-prints*.
- Miettinen, O., Harju, J., Haikala, L. K., Kainulainen, J., and Johansson, L. E. B. (2009). Prestellar and protostellar cores in Orion B9. *Astronomy and Astrophysics*, 500:845–860.
- Molinari, S., Brand, J., Cesaroni, R., and Palla, F. (1996). A search for precursors of ultracompact HII regions in a sample of luminous IRAS sources. I. Association with ammonia cores. *Astronomy and Astrophysics*, 308:573–587.

- Moscadelli, L., Cesaroni, R., and Rioja, M. J. (2000). Tracing the root of the bipolar jet in IRAS 20126+4104: VLBA observations of H<sub>2</sub>O masers. *Astronomy and Astrophysics*, 360:663–670.
- Moscadelli, L., Cesaroni, R., and Rioja, M. J. (2005). Water masers in the massive protostar IRAS 20126+4104: ejection and deceleration. *Astronomy and Astrophysics*, 438:889–898.
- Motte, F. and André, P. (2001). The circumstellar environment of low-mass protostars: A millimeter continuum mapping survey. *Astronomy and Astrophysics*, 365:440–464.
- Motte, F., André, P., and Neri, R. (1998). The initial conditions of star formation in the rho Ophiuchi main cloud: wide-field millimeter continuum mapping. *Astronomy and Astrophysics*, 336:150–172.
- Müller, H. S. P., Thorwirth, S., Roth, D. A., and Winnewisser, G. (2001). The Cologne Database for Molecular Spectroscopy, CDMS. *Astronomy and Astrophysics*, 370:L49–L52.
- Öberg, K. I., van Broekhuizen, F., Fraser, H. J., Bisschop, S. E., van Dishoeck, E. F., and Schlemmer, S. (2005). Competition between CO and N<sub>2</sub> Desorption from Interstellar Ices. *The Astrophysical Journal, Letters*, 621:L33–L36.
- Olberg, M., Bester, M., Rau, G., Pauls, T., Winnewisser, G., Johansson, L. E., and Hjalmarson, A. (1985). A new search for and discovery of deuterated ammonia in three molecular clouds. *Astronomy and Astrophysics*, 142:L1–L4.
- Oliveira, C. M., Hébrard, G., Howk, J. C., Kruk, J. W., Chayer, P., and Moos, H. W. (2003). Interstellar Deuterium, Nitrogen, and Oxygen Abundances toward GD 246, WD 2331-475, HZ 21, and Lanning 23: Results from the FUSE Mission. *The Astrophysical Journal*, 587:235–255.
- Ossenkopf, V. and Henning, T. (1994). Dust opacities for protostellar cores. *Astronomy and Astrophysics*, 291:943–959.
- Palagi, F., Cesaroni, R., Comoretto, G., Felli, M., and Natale, V. (1993). Classification and Statistical Properties of Galactic H<sub>2</sub>O Masers. *Astronomy and Astrophysics Supplement Series*, 101:153–+.

- Palau, A., Estalella, R., Girart, J. M., Ho, P. T. P., Zhang, Q., and Beuther, H. (2007). Star formation in a clustered environment around the UCH {II} region in IRAS 20293+3952. *Astronomy and Astrophysics*, 465:219–233.
- Palau, A., Sánchez-Monge, Á., Busquet, G., Estalella, R., Zhang, Q., Ho, P. T. P., Beltrán, M. T., and Beuther, H. (2010). Three intermediate-mass young stellar objects with different properties emerging from the same natal cloud in IRAS 00117+6412. *Astronomy and Astrophysics*, 510:A5+.
- Parise, B., Ceccarelli, C., Tielens, A. G. G. M., Castets, A., Caux, E., Lefloch, B., and Maret, S. (2006). Testing grain surface chemistry: a survey of deuterated formaldehyde and methanol in low-mass class 0 protostars. *Astronomy and Astrophysics*, 453:949–958.
- Parise, B., Ceccarelli, C., Tielens, A. G. G. M., Herbst, E., Lefloch, B., Caux, E., Castets, A., Mukhopadhyay, I., Pagani, L., and Loinard, L. (2002). Detection of doubly-deuterated methanol in the solar-type protostar IRAS 16293-2422. *Astronomy and Astrophysics*, 393:L49–L53.
- Pauls, A., Wilson, T. L., Bieging, J. H., and Martin, R. N. (1983). Clumping in Orion KL - 2-arcsecond maps of ammonia. *Astronomy and Astrophysics*, 124:23–38.
- Perault, M., Omont, A., Simon, G., Seguin, P., Ojha, D., Blommaert, J., Felli, M., Gilmore, G., Guglielmo, F., Habing, H., Price, S., Robin, A., de Batz, B., Cesarsky, C., Elbaz, D., Epchtein, N., Fouque, P., Guest, S., Levine, D., Pollock, A., Prusti, T., Siebenmorgen, R., Testi, L., and Tiphene, D. (1996). First ISOCAM images of the Milky Way. *Astronomy and Astrophysics*, 315:L165–L168.
- Peretto, N. and Fuller, G. A. (2009). The initial conditions of stellar protocluster formation. I. A catalogue of Spitzer dark clouds. *Astronomy and Astrophysics*, 505:405–415.
- Pillai, T., Wyrowski, F., Carey, S. J., and Menten, K. M. (2006a). Ammonia in infrared dark clouds. *Astronomy and Astrophysics*.
- Pillai, T., Wyrowski, F., Hatchell, J., Gibb, A. G., and Thompson, M. A. (2007). Probing the initial conditions of high mass star formation. I. Deuteration and depletion in high mass pre/protocluster clumps. *Astronomy and Astrophysics*, 467:207–216.

- Pillai, T., Wyrowski, F., Menten, K. M., and Krügel, E. (2006b). High mass star formation in the infrared dark cloud G11.11-0.12. *Astronomy and Astrophysics*.
- Pineau des Forêts, G., Roueff, E., Schilke, P., and Flower, D. R. (1993). Sulphur-bearing molecules as tracers of shocks in interstellar clouds. *Monthly Notices of the Royal Astronomical Society*, 262:915–928.
- Pirogov, L., Zinchenko, I., Caselli, P., and Johansson, L. E. B. (2007). Chemical differentiation in regions of high-mass star formation. CS, dust, and  $\text{N}_2\text{H}^+$  in southern sources. *Astronomy and Astrophysics*, 461:523–535.
- Pirogov, L., Zinchenko, I., Caselli, P., Johansson, L. E. B., and Myers, P. C. (2003).  $\text{N}_2\text{H}^+(1-0)$  survey of massive molecular cloud cores. *Astronomy and Astrophysics*, 405:639–654.
- Plume, R., Jaffe, D. T., and Evans, II, N. J. (1992). A survey of CS  $J = 7 - 6$  in regions of massive star formation. *The Astrophysical Journal Supplement Series*, 78:505–515.
- Qiu, K., Zhang, Q., Megeath, S. T., Gutermuth, R. A., Beuther, H., Shepherd, D. S., Sridharan, T. K., Testi, L., and De Pree, C. G. (2008). Spitzer IRAC and MIPS Imaging of Clusters and Outflows in Nine High-Mass Star Forming Regions. *The Astrophysical Journal*, 685:1005–1025.
- Ragan, S. E., Bergin, E. A., and Gutermuth, R. A. (2009). Detection of Structure in Infrared-Dark Clouds with Spitzer: Characterizing Star Formation in the Molecular Ring. *The Astrophysical Journal*, 698:324–349.
- Rathborne, J. M., Jackson, J. M., and Simon, R. (2006). Infrared Dark Clouds: Precursors to Star Clusters. *The Astrophysical Journal*, 641:389–405.
- Rathborne, J. M., Jackson, J. M., Zhang, Q., and Simon, R. (2008). Submillimeter Array Observations of Infrared Dark Clouds: A Tale of Two Cores. *The Astrophysical Journal*, 689:1141–1149.
- Rathborne, J. M., Simon, R., and Jackson, J. M. (2007). The Detection of Protostellar Condensations in Infrared Dark Cloud Cores. *The Astrophysical Journal*, 662:1082–1092.
- Rawlings, J. M. C., Hartquist, T. W., Menten, K. M., and Williams, D. A. (1992). Direct diagnosis of infall in collapsing protostars. I - The theoretical identification

- of molecular species with broad velocity distributions. *Monthly Notices of the Royal Astronomical Society*, 255:471–485.
- Reid, M. A. and Matthews, B. C. (2008). Deconstructing the High-Mass Star-Forming Region IRAS 23033+5951. *The Astrophysical Journal*, 675:1343–1351.
- Reid, M. A. and Wilson, C. D. (2006). High-Mass Star Formation. II. The Mass Function of Submillimeter Clumps in M17. *The Astrophysical Journal*, 644:990–1005.
- Richards, P. J., Little, L. T., Heaton, B. D., and Toriseva, M. (1987). HCO(+) survey of unassociated compact molecular clouds in the IRAS Point Source Catalog. *Monthly Notices of the Royal Astronomical Society*, 228:43–54.
- Rieke, G. H. and Lebofsky, M. J. (1985). The interstellar extinction law from 1 to 13 microns. *The Astrophysical Journal*, 288:618–621.
- Roberts, H., Herbst, E., and Millar, T. J. (2003). Enhanced Deuterium Fractionation in Dense Interstellar Cores Resulting from Multiply Deuterated H<sub>3</sub><sup>+</sup>. *The Astrophysical Journal, Letters*, 591:L41–L44.
- Roberts, H. and Millar, T. J. (2000). Modelling of deuterium chemistry and its application to molecular clouds. *Astronomy and Astrophysics*, 361:388–398.
- Rodón, J. A. (2009). *The fragmentation of massive star-forming regions*. PhD thesis, Max-Planck-Institut für Astronomie.
- Roueff, E., Lis, D. C., van der Tak, F. F. S., Gerin, M., and Goldsmith, P. F. (2005). Interstellar deuterated ammonia: from NH<sub>3</sub> to ND<sub>3</sub>. *Astronomy and Astrophysics*, 438:585–598.
- Saito, S., Ozeki, H., Ohishi, M., and Yamamoto, S. (2000). Observations of NH<sub>2</sub>D toward Dark Molecular Clouds. *The Astrophysical Journal*, 535:227–230.
- Sakai, T., Sakai, N., Kamegai, K., Hirota, T., Yamaguchi, N., Shiba, S., and Yamamoto, S. (2008). A Molecular Line Observation toward Massive Clumps Associated with Infrared Dark Clouds. *The Astrophysical Journal*, 678:1049–1069.
- Salpeter, E. E. (1955). The Luminosity Function and Stellar Evolution. *The Astrophysical Journal*, 121:161–+.

- Sánchez-Monge, A. (2011). *Massive Star Formation: ionized and molecular gas emission in the first evolutionary stages*. PhD thesis, Universitat de Barcelona.
- Sánchez-Monge, Á., Palau, A., Estalella, R., Beltrán, M. T., and Girart, J. M. (2008). Survey of intermediate/high mass star-forming regions at centimeter and millimeter wavelengths. *Astronomy and Astrophysics*, 485:497–515.
- Sánchez-Monge, Á., Palau, A., Estalella, R., Kurtz, S., Zhang, Q., Di Francesco, J., and Shepherd, D. (2010). IRAS 22198+6336: Discovery of an Intermediate-mass Hot Core. *The Astrophysical Journal, Letters*, 721:L107–L111.
- Sandell, G. and Wright, M. (2010). A Detailed Study of the Accretion Disk Surrounding the High-mass Protostar NGC 7538 S. *The Astrophysical Journal*, 715:919–938.
- Sault, R. J., Teuben, P. J., and Wright, M. C. H. (1995). A Retrospective View of MIRIAD. In R. A. Shaw, H. E. Payne, & J. J. E. Hayes, editor, *Astronomical Data Analysis Software and Systems IV*, volume 77 of *Astronomical Society of the Pacific Conference Series*, pages 433–+.
- Schilke, P., Benford, D. J., Hunter, T. R., Lis, D. C., and Phillips, T. G. (2001). A Line Survey of Orion-KL from 607 to 725 GHz. *The Astrophysical Journal Supplement Series*, 132:281–364.
- Scoville, N. Z., Carlstrom, J. E., Chandler, C. J., Phillips, J. A., Scott, S. L., Tilanus, R. P. J., and Wang, Z. (1993). The relational database and calibration software for the Caltech millimeter array. *Publications of the Astronomical Society of the Pacific*, 105:1482–1494.
- Shepherd, D. S., Yu, K. C., Bally, J., and Testi, L. (2000). The Molecular Outflow and Possible Precessing Jet from the Massive Young Stellar Object IRAS 20126+4104. *The Astrophysical Journal*, 535:833–846.
- Skrutskie, M. F., Cutri, R. M., Stiening, R., Weinberg, M. D., Schneider, S., Carpenter, J. M., Beichman, C., Capps, R., Chester, T., Elias, J., Huchra, J., Liebert, J., Lonsdale, C., Monet, D. G., Price, S., Seitzer, P., Jarrett, T., Kirkpatrick, J. D., Gizis, J. E., Howard, E., Evans, T., Fowler, J., Fullmer, L., Hurt, R., Light, R., Kopan, E. L., Marsh, K. A., McCallon, H. L., Tam, R., Van Dyk, S., and Wheelock, S. (2006). The Two Micron All Sky Survey (2MASS). *The Astronomical Journal*, 131:1163–1183.

- Snell, R. L., Huang, Y., Dickman, R. L., and Claussen, M. J. (1988). Molecular outflows associated with bright far-infrared sources. *The Astrophysical Journal*, 325:853–863.
- Sofia, U. J. and Meyer, D. M. (2001). Interstellar Abundance Standards Revisited. *The Astrophysical Journal, Letters*, 554:L221–L224.
- Sridharan, T. K., Beuther, H., Schilke, P., Menten, K. M., and Wyrowski, F. (2002). High-Mass Protostellar Candidates. I. The Sample and Initial Results. *The Astrophysical Journal*, 566:931–944.
- Su, Y., Liu, S., Chen, H., Zhang, Q., and Cesaroni, R. (2007). The Outflow from the Luminous Young Stellar Object IRAS 20126+4104: From 4000 AU to 0.4 pc. *The Astrophysical Journal*, 671:571–580.
- Sweitzer, J. S. (1978). On the excitation of interstellar ammonia in the Kleinmann-Low nebula. *The Astrophysical Journal*, 225:116–129.
- Tafalla, M., Myers, P. C., Caselli, P., and Walmsley, C. M. (2004). On the internal structure of starless cores. I. Physical conditions and the distribution of CO, CS, N<sub>2</sub>H<sup>+</sup>, and NH<sub>3</sub> in L1498 and L1517B. *Astronomy and Astrophysics*, 416:191–212.
- Tafalla, M., Myers, P. C., Caselli, P., Walmsley, C. M., and Comito, C. (2002). Systematic Molecular Differentiation in Starless Cores. *The Astrophysical Journal*, 569:815–835.
- Tafalla, M. and Santiago, J. (2004). L1521E: The first starless core with no molecular depletion. *Astronomy and Astrophysics*, 414:L53–L56.
- Tafalla, M., Santiago-García, J., Myers, P. C., Caselli, P., Walmsley, C. M., and Crapsi, A. (2006). On the internal structure of starless cores. II. A molecular survey of L1498 and L1517B. *Astronomy and Astrophysics*, 455:577–593.
- Testi, L. and Sargent, A. I. (1998). Star Formation in Clusters: A Survey of Compact Millimeter-Wave Sources in the Serpens Core. *The Astrophysical Journal, Letters*, 508:L91–L94.
- Tielens, A. G. G. M. (1983). Surface chemistry of deuterated molecules. *Astronomy and Astrophysics*, 119:177–184.

- Tiné, S., Roueff, E., Falgarone, E., Gerin, M., and Pineau des Forêts, G. (2000). Deuterium fractionation in dense ammonia cores. *Astronomy and Astrophysics*, 356:1039–1049.
- Torrelles, J. M., Gomez, J. F., Anglada, G., Estalella, R., Mauersberger, R., and Eiroa, C. (1992). The powering sources of the molecular outflows in the AFGL 437, AFGL 5142, and AFGL 5157 regions. *The Astrophysical Journal*, 392:616–621.
- Trinidad, M. A., Curiel, S., Migenes, V., Patel, N., Torrelles, J. M., Gómez, J. F., Rodríguez, L. F., Ho, P. T. P., and Cantó, J. (2005). Very Large Array Simultaneous 1.3 cm Continuum and H<sub>2</sub>O Maser Observations toward IRAS 20126+4104. *The Astronomical Journal*, 130:2206–2211.
- Ungerechts, H., Winnewisser, G., and Walmsley, C. M. (1986). Ammonia observations and temperatures in the S140/L1204 molecular cloud. *Astronomy and Astrophysics*, 157:207–216.
- van der Tak, F. F. S., Schilke, P., Müller, H. S. P., Lis, D. C., Phillips, T. G., Gerin, M., and Roueff, E. (2002). Triply deuterated ammonia in NGC 1333. *Astronomy and Astrophysics*, 388:L53–L56.
- van Dishoeck, E. F. and Blake, G. A. (1998). Chemical Evolution of Star-Forming Regions. *Annual Review of Astronomy and Astrophysics*, 36:317–368.
- Verdes-Montenegro, L., Torrelles, J. M., Rodriguez, L. F., Anglada, G., Lopez, R., Estalella, R., Canto, J., and Ho, P. T. P. (1989). Further studies of the role of dense molecular clouds around outflow sources. *The Astrophysical Journal*, 346:193–200.
- Viti, S., Caselli, P., Hartquist, T. W., and Williams, D. A. (2001). Chemical signatures of shocks in hot cores. *Astronomy and Astrophysics*, 370:1017–1025.
- Viti, S., Collings, M. P., Dever, J. W., McCoustra, M. R. S., and Williams, D. A. (2004). Evaporation of ices near massive stars: models based on laboratory temperature programmed desorption data. *Monthly Notices of the Royal Astronomical Society*, 354:1141–1145.
- Viti, S. and Williams, D. A. (1999). Time-dependent evaporation of icy mantles in hot cores. *Monthly Notices of the Royal Astronomical Society*, 305:755–762.

- Vogel, S. N., Wright, M. C. H., Plambeck, R. L., and Welch, W. J. (1984). Interaction of the outflow and quiescent gas in Orion - HCO<sup>+</sup> aperture synthesis maps. *The Astrophysical Journal*, 283:655–667.
- Wagenblast, R. and Hartquist, T. W. (1989). Non-equilibrium level populations of molecular hydrogen. II - Models of the Zeta OPH cloud. *Monthly Notices of the Royal Astronomical Society*, 237:1019–1025.
- Walmsley, C. M., Hermsen, W., Henkel, C., Mauersberger, R., and Wilson, T. L. (1987). Deuterated ammonia in the Orion hot core. *Astronomy and Astrophysics*, 172:311–315.
- Wang, Y., Zhang, Q., Pillai, T., Wyrowski, F., and Wu, Y. (2008). NH<sub>3</sub> Observations of the Infrared Dark Cloud G28.34+0.06. *The Astrophysical Journal, Letters*, 672:L33–L36.
- Wang, Y., Zhang, Q., Rathborne, J. M., Jackson, J., and Wu, Y. (2006). Water Masers Associated with Infrared Dark Cloud Cores. *The Astrophysical Journal, Letters*, 651:L125–L128.
- Wilking, B. A., Blackwell, J. H., Mundy, L. G., and Howe, J. E. (1989). A millimeter-wave spectral-line and continuum survey of cold IRAS sources. *The Astrophysical Journal*, 345:257–264.
- Williams, J. P., Blitz, L., and McKee, C. F. (2000). The Structure and Evolution of Molecular Clouds: from Clumps to Cores to the IMF. *Protostars and Planets IV*, pages 97–+.
- Wiseman, J. J. and Ho, P. T. P. (1998). Large-Scale Structure, Kinematics, and Heating of the Orion Ridge. I. VLA NH<sub>3</sub> (1,1) and (2,2) Mosaics. *The Astrophysical Journal*, 502:676.
- Wood, D. O. S. and Churchwell, E. (1989). Massive stars embedded in molecular clouds - Their population and distribution in the galaxy. *The Astrophysical Journal*, 340:265–272.
- Woodall, J., Agúndez, M., Markwick-Kemper, A. J., and Millar, T. J. (2007). The UMIST database for astrochemistry 2006. *Astronomy and Astrophysics*, 466:1197–1204.

- Wouterloot, J. G. A., Brand, J., and Fiegle, K. (1993). IRAS sources beyond the solar circle. III - Observations of H<sub>2</sub>O, OH, CH<sub>3</sub>OH and CO. *Astronomy and Astrophysics Supplement Series*, 98:589–636.
- Zhang, Q., Hunter, T. R., Beuther, H., Sridharan, T. K., Liu, S., Su, Y., Chen, H., and Chen, Y. (2007). Multiple Jets from the High-Mass (Proto)stellar Cluster AFGL 5142. *The Astrophysical Journal*, 658:1152–1163.
- Zhang, Q., Hunter, T. R., Brand, J., Sridharan, T. K., Cesaroni, R., Molinari, S., Wang, J., and Kramer, M. (2005). Search for CO Outflows toward a Sample of 69 High-Mass Protostellar Candidates. II. Outflow Properties. *The Astrophysical Journal*, 625:864–882.
- Zhang, Q., Hunter, T. R., and Sridharan, T. K. (1998). A Rotating Disk around a High-Mass Young Star. *The Astrophysical Journal, Letters*, 505:L151–L154.
- Zhang, Q., Hunter, T. R., Sridharan, T. K., and Cesaroni, R. (1999). Shock-heated NH<sub>3</sub> in a Molecular Jet Associated with a High-Mass Young Star. *The Astrophysical Journal, Letters*, 527:L117–L120.
- Zhang, Q., Hunter, T. R., Sridharan, T. K., and Ho, P. T. P. (2002). A Disk/Jet System toward the High-Mass Young Star in AFGL 5142. *The Astrophysical Journal*, 566:982–992.
- Zhang, Q., Wang, Y., Pillai, T., and Rathborne, J. (2009). Fragmentation at the Earliest Phase of Massive Star Formation. *The Astrophysical Journal*, 696:268–273.
- Zinchenko, I., Caselli, P., and Pirogov, L. (2009). Chemical differentiation in regions of high-mass star formation - II. Molecular multiline and dust continuum studies of selected objects. *Monthly Notices of the Royal Astronomical Society*, 395:2234–2247.
- Zinnecker, H. and Yorke, H. W. (2007). Toward Understanding Massive Star Formation. *Annual Review of Astronomy and Astrophysics*, 45:481–563.



# Appendix

## Derivation of $T_{\text{rot}}$ and $N(\text{NH}_3)$ from $\text{NH}_3$ (1,1) and (2,2) observations

$T_{\text{MB}}(1, 1; m)$  and  $N(1, 1)$ :

The  $\text{NH}_3$  (1,1) method of CLASS fits the magnetic hyperfine structure of  $\text{NH}_3$  (1,1). The output parameters for the fit to the hyperfine structure are:  $A\tau_{\text{m}}$ , the velocity of the reference line, the intrinsic line width, and the optical depth of the (1,1) main line,  $\tau_{\text{m}}$  (sum of the optical depths of the magnetic hyperfine components of the main line),  $\tau_{\text{m}} = \tau(1, 1)/2$ . The parameter  $A$ , according to Pauls et al. (1983), is defined as  $A = f[J_{\nu}(T_{\text{ex}}) - J_{\nu}(T_{\text{bg}})]$ , where  $f$  is the filling factor. Then, from the output parameters, and applying the radiative transfer equation, one can obtain the (1,1) main line temperature  $T_{\text{MB}}(1, 1; m)$ ,

$$T_{\text{MB}}(1, 1; m) = A\tau_{\text{m}} \frac{1 - e^{-\tau_{\text{m}}}}{\tau_{\text{m}}}. \quad (\text{A.1})$$

The excitation temperature  $T_{\text{ex}}$  is *not* directly obtained from the fit, but is isolated from the output parameter  $A\tau_{\text{m}}$ ,

$$T_{\text{ex}} = \frac{1.14}{\ln \left( 1 + 1.14 / [A\tau_{\text{m}}/\tau_{\text{m}} + J_{\nu}(T_{\text{bg}})] \right)}. \quad (\text{A.2})$$

Note that no assumption is made concerning  $T_{\text{ex}}$  with respect to the background temperature  $T_{\text{bg}}$ .

The beam averaged column density in the (1,1) level (Anglada et al. 1995),

$$\left[ \frac{N(1, 1)}{\text{cm}^{-2}} \right] = 1.58 \times 10^{13} f \frac{e^{1.14/T_{\text{ex}}} + 1}{e^{1.14/T_{\text{ex}}} - 1} \tau_{\text{m}} \left[ \frac{\Delta v}{\text{km s}^{-1}} \right], \quad (\text{A.3})$$

the filling factor  $f$  being assumed to be 1 for our VLA observations.

To derive Eq. (A.3),  $N(1, 1)$  is not approximated to  $2N_{+}(1, 1)$ , but is taken as  $N(1, 1) = N_{+}(1, 1)[1 + \exp(h\nu_{11}/kT_{\text{ex}})]$  (see Harju et al. (1993) for more details).

$T_{\text{MB}}(2, 2; m)$ :

For  $\text{NH}_3(2,2)$  we fitted one single Gaussian, with the (2,2) main line temperature,  $T_{\text{MB}}(2, 2; m)$ , being an output parameter of the fit.

$T_{\text{rot}}^{21}$ :

The rotational temperature derived from  $\text{NH}_3(1,1)$  and  $\text{NH}_3(2,2)$  can be estimated, following Ho & Townes (1983, Eq. 4), by assuming that the transitions between the metastable inversion doublets are approximated as a two-level system, and that the excitation temperature  $T_{\text{ex}}$  and line width  $\Delta v$  are the same for both  $\text{NH}_3(1,1)$  and  $\text{NH}_3(2,2)$ . Then,

$$T_{\text{rot}}^{21} = \frac{-41.5}{\ln \left( -\frac{0.283}{\tau_{\text{m}}} \ln \left[ 1 - \frac{T_{\text{MB}}(2,2;m)}{T_{\text{MB}}(1,1;m)} \cdot (1 - e^{-\tau_{\text{m}}}) \right] \right)}, \quad (\text{A.4})$$

Note that we did *not* assume that the emission is optically thin. The assumption of a two-level system is reasonable because transitions between the metastable inversion doublets are usually much faster than those of other rotational states (Ho and Townes 1983). If the density and temperature were high enough to populate the

upper non metastable states, multilevel statistical calculations would be required (e. g., Sweitzer 1978).

An estimate of the gas kinetic temperature can be obtained by correcting the rotational temperature derived from  $\text{NH}_3$ , using the expression given in Tafalla et al. (2004),

$$T_k = \frac{T_{\text{rot}}^{21}}{1 - \frac{T_{\text{rot}}^{21}}{42} \ln [1 + 1.1e^{-16/T_{\text{rot}}^{21}}]}, \quad (\text{A.5})$$

which is almost independent of core density and size. This relation is recommended for the range  $T_k = 5\text{--}20$  K.

### $N(\text{NH}_3)$ :

The  $\text{NH}_3$  column density was derived by following Ungerechts et al. (1986), and Harju et al. (1993). The main assumptions are: *i*) only metastable levels are populated; *ii*)  $T_{\text{rot}}$  is the same for each pair of rotational levels; *iii*) the ratio of the column densities of each rotational level is the same as the ratio of the column densities of upper inversion levels; *iv*) the contribution to the total  $\text{NH}_3$  column density comes essentially from levels with  $J \leq 3$ ; *v*) the relative population of all metastable levels of both ortho and para- $\text{NH}_3$  is that given by thermal equilibrium at temperature  $T_{\text{rot}}$ ; and *vi*) the frequencies for the  $\text{NH}_3(1,1)$  and  $\text{NH}_3(2,2)$  transitions are very similar. With these assumptions,

$$N(\text{NH}_3) = N(1, 1) \left[ \frac{1}{3}e^{23.4/T_{\text{rot}}^{21}} + 1 + \frac{5}{3}e^{-41.5/T_{\text{rot}}^{21}} + \frac{14}{3}e^{-101.2/T_{\text{rot}}^{21}} \right]. \quad (\text{A.6})$$

### Uncertainty in $T_{\text{rot}}^{21}$ :

In order to estimate the uncertainties associated with  $T_{\text{rot}}$  and  $N(\text{NH}_3)$  introduced by this method, we did the following.

The error of  $T_{\text{rot}}s^{21}$  was estimated by assuming optically thin emission and that the main sources of error come from  $T_{\text{MB}}(1, 1; m)$  and  $T_{\text{MB}}(2, 2; m)$ . Defining  $R \equiv$

$T_{\text{MB}}(2, 2; m)/T_{\text{MB}}(1, 1; m)$ , the relative error is  $\frac{\delta R}{R} = \sqrt{\left(\frac{\delta T_{\text{MB}}(1, 1; m)}{T_{\text{MB}}(1, 1; m)}\right)^2 + \left(\frac{\delta T_{\text{MB}}(2, 2; m)}{T_{\text{MB}}(2, 2; m)}\right)^2}$ , with  $\delta T_{\text{MB}}(1, 1; m)$  and  $\delta T_{\text{MB}}(2, 2; m)$  given directly by the hyperfine fit. Then, the error in the rotational temperature was estimated as

$$\delta T_{\text{rot}}^{21} = \frac{-41.5}{\ln^2(0.283R)} \frac{\delta R}{R}. \quad (\text{A.7})$$

As a test for the previous estimate of the error in  $T_{\text{rot}}$ , we estimated the opacity from the ratio of the main line intensity to the inner satellite average intensity,  $T_{\text{MB}}(1, 1, is)$ , following Ho & Townes (1983),

$$\frac{T_{\text{MB}}(1, 1; m)}{T_{\text{MB}}(1, 1; is)} = \frac{1 - e^{-\tau_m}}{1 - e^{-\tau_m/3.6}}, \quad (\text{A.8})$$

and derived  $T_{\text{rot}}$  with this estimate of the opacity. The opacities derived from this method are systematically lower than but compatible to the values derived from the hyperfine fit, and the rotational temperature obtained agrees with the values derived from the  $\text{NH}_3(1,1)$  hyperfine method used in this work. We note that the opacity inferred from the hyperfine fit seems to be more reliable than the opacity from the ratio of the main line to the satellites *when* the width of the magnetic hyperfine components is comparable to the their separation in velocity (e. g., Anglada et al. 1995), which is 0.11–0.53  $\text{km s}^{-1}$ . This is probably the case of our region. However, since the observations reported here were carried out with a spectral resolution in some cases lower than the intrinsic line width, the hyperfine fits must be regarded with caution and for this reason we compared them with the ratio of the main line to the satellite method.